-

ON-STATE RELIABILITY STUDY OF ALGAN/GAN HIGH ELECTRON MOBILITY TRANSISTOR ON SILICON

GOVINDO JOANNESHA SYARANAMUAL

SCHOOL OF MATERIALS SCIENCE AND ENGINEERING

2018

ON-STATE RELIABILITY STUDY OF ALGAN/GAN HIGH ELECTRON MOBILITY TRANSISTOR ON SILICON

GOVINDO JOANNESHA SYARANAMUAL

SCHOOL OF MATERIALS SCIENCE AND ENGINEERING

A thesis submitted to the Nanyang Technological University
in partial fulfilment of the requirement for the degree of
Doctor of Philosophy

2018

Statement of Originality

I hereby certify that the work embodied in this thesis is the result of original research and has not been submitted for a higher degree to any other University or Institution.

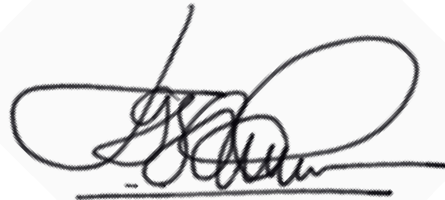

25 August 2017	
. . . .	. . . .
Date	Govindo Joannesha Syaranamual

Abstract

Monolithic integration of AlGaN/GaN high electron mobility transistor (HEMT) into silicon (Si) platform is very attractive as this is a cost-effective solution to extend the capabilities of silicon technology especially for high power and high frequency applications. It is not only that Si substrate is cheaper than other commonly used substrates for GaN epitaxy such as Sapphire and SiC but growing on Si substrate also allows integration with current Si technology in the industry. Unfortunately, this technology is still very limited by its associated reliability issues. This study focused on depletion-mode (D-mode) AlGaN/GaN HEMT devices on Si with negative threshold voltage (V_{TH}) of about −3 V.

AlGaN/GaN HEMT reliability can be divided into OFF-state and ON-state reliabilities. AlGaN/GaN HEMT ON-state reliability is not as well reported as OFF-state reliability. Therefore, this thesis aims to fill up the knowledge gap in AlGaN/GaN HEMT ON-state reliability. This study has three main objectives. The first objective is to comprehend the electrical and physical degradation mechanism in AlGaN/GaN HEMT devices stressed under ON-state condition. The second objective is to understand the effects of stressing and process parameters on AlGaN/GaN HEMT ON-state degradation. Finally, this study aims to develop a reliability model based on the degradation mechanism in AlGaN/GaN HEMT stressed under ON-state condition.

OFF-state and ON-state degradations were compared in Chapter 4. It was observed that devices stressed under ON-state condition degraded faster than similar devices stressed under OFF-state condition with higher stressing temperature. This is because of the occurrence of electro-chemical oxidation of AlGaN away from the gate edge during ON-state stressing. Dark features containing gallium, aluminum and oxygen were found at the AlGaN/Si_xN_{1-x} interface away from the gate edge on the drain side of the ON-state-stressed devices. These oxidized portions of AlGaN were etched away during metallization and passivation layer etching leaving behind pits at the drain-gate access region. The total area

of pits in the drain-gate access region correlated well with I_{D-max} degradation. It was concluded that 2DEG electrons contributed to the AlGaN oxidation away from the gate edge during ON-state stressing. A qualitative model for ON-state degradation was proposed based on the electro-chemical oxidation mechanism.

In Chapter 5, fast and slow degradation modes were observed for devices stressed under ON-state condition. These two degradation modes were characterized by the dominant source of oxygen. In fast degradation mode, the dominant source of oxygen was the pre-existing oxygen at the AlGaN/Si_xN_{1-x} interface whereas the dominant source of oxygen in slow degradation mode was oxygen from the ambient which diffused through the Si_xN_{1-x} passivation. In addition, it was established that the maximum distance for pit formation from the gate edge correlated with the stressing current density.

In Chapter 6, effect of passivation density on AlGaN/GaN HEMT ON-state degradation was investigated. High passivation density will mitigate the passivation layer degradation and hinder oxygen diffusion from ambient to the AlGaN/Si_xN_{1-x} interface. Once the passivation degrades, oxygen from the ambient will diffuse through and oxidize AlGaN layer. Mathematical relationship between stressing temperature and I_{D-max} in slow mode degradation was derived based on oxygen diffusion through the Si_xN_{1-x} passivation.

In the final chapter, the thesis was summarized and its implications and limitations were discussed. Finally, possible future works were proposed to further advance the knowledge of AlGaN/GaN HEMT ON-state reliability.

Acknowledgements

First of all, I would like to thank God for His providence and blessings throughout my PhD journey. I would like to express my sincere gratitude to my two supervisors, Professor Gan Chee Lip and Professor Carl V. Thompson for their invaluable guidance and advice throughout the project. I also want to thank SMART-LEES sub-group members, Dr. Wardhana Aji Sasangka, Dr. I Made Riko, and Gao Yu, for the support and invaluable discussion about the project.

I would like to thank the people in Professor Gan Chee Lip's group: Dr. Khoo Chee Ying, Dr. Eric Phua, Dr. Liu Qing, Eric Tan, Chung Tah and Wahyuaji who have contributed throughout the project in one way or another. I would like to acknowledge Professor Ng Geok Ing, Dr S. Arulkumaran and Foo Siew Chuen for providing samples used in this project. I also want to thank Mr Choo Kok Fah and Dr. Joyce Ling Huey Lin for their help with thermo-reflectance experiment and thermal simulation. I would like to thank Vinod Kumar Murugan who always reminds me to have fun in between lab sessions.

Special thanks to Christiyani Kabul, Pdt Budianto Lim, Lydia Siah and my other friends in Bukit Batok Presbyterian Church (BBPC) Singapore for their prayer and support throughout my PhD journey.

I owe my deepest gratitude to my family for their support. Finally, I would like to dedicate this work to my mom, Andini Emmiati and my dad, Frederik Jones Syaranamual who always believe in me and pray for me from Indonesia.

Table of Contents

Abstract .... **i**

Acknowledgements .... **iii**

Table of Contents .... **v**

Table Captions .... **xi**

Figure Captions .... **xiii**

Abbreviations .... **xxv**

Chapter 1 Introduction **1**

1.1 Background 2

1.1.1 AlGaN/GaN HEMT Working Principle 3

1.1.2 AlGaN/GaN HEMT on Various Substrates 5

1.2 Hypothesis/Problem Statement 6

1.3 Objectives and Scope 7

1.4 Dissertation Overview 8

1.5 Findings and Outcomes/Originality 9

Chapter 2 Literature Review **11**

2.1 Introduction 12

2.2 OFF-State Reliability 12

2.2.1 Inverse Piezoelectric Stress 12

2.2.2 Electro-Chemical Oxidation 15

2.2.3 Percolation Path Mechanism....18

2.3 ON-State Reliability....21

2.3.1 Hot Electron Degradation....22

2.3.2 Electro-Chemical Oxidation....24

2.3.2 Ohmic Contact Degradation....27

2.4 Thesis in Context to Knowledge Gaps....30

Chapter 3 Experimental Methodology....31

3.1 Device Description....32

3.2 Electrical Characterization and Stressing....33

3.2.1 Electrical Characterization....35

3.2.2 Electrical Stressing....37

3.3 Junction Temperature Measurement....38

3.3.1 Thermo-Reflectance....38

3.3.2 Finite Element Simulation....40

3.4 Electric Field Finite Element Simulation....42

3.5 Etching....44

3.5.1 Metal Contacts and Passivation Layer Etching....45

3.5.2 Dislocation Etching....46

3.6 Microstructure Characterization....47

3.6.1 Scanning Electron Microscopy....47

3.6.2 Focused Ion Beam....49

3.6.3 Transmission Electron Microscopy....51

3.6.3.1 Scanning Transmission Electron Microscopy....52

3.6.3.2 Energy Dispersive X-ray Spectroscopy....52

3.6.3.3 Weak Beam Dark Field Technique for Threading Dislocation Analysis 53

3.6.3.4 Electron Energy Loss Spectroscopy 55

3.6.3.5 Relative Density Measurement of Si_xN_{1-x} Passivation Layer using EELS 57

3.6.3.6 Absolute Composition of Si_xN_{1-x} Passivation Layer 58

3.6.4 X-Ray Reflectometry 59

3.6.4.1 Film Density Measurement 61

3.6.4.2 Film Thickness Measurement 62

3.6.4.3 Surface Roughness Measurement 63

3.6.4.4 X-ray Reflectivity Measurement of Si_xN_{1-x} Passivation Layer 63

3.6.5 Pit Counting Method 64

Chapter 4 Comparative Study of AlGaN/GaN High Electron Mobility Transistor Degradation Mechanism under OFF-state and ON-state Stressing 67

4.1 Introduction 68

4.2 Experimental Details 68

4.2.1 Junction Temperature Measurement 68

4.2.2 Electrical Stressing 72

4.2.3 Microstructure Characterization 73

4.3 Results and Discussions 73

4.3.1 Electrical Stressing Results 73

4.3.2 Microstructure Characterization Results 76

4.3.3 Electrical Stressing with Substrate Bias Results 82

4.3.4 Proposed Model for ON-state Degradation 84

4.4 Summary 87

Chapter 5 Effect of Current Density on AlGaN/GaN High Electron Mobility Transistor Degradation under ON-State Stressing......89

5.1 Introduction......90

5.2 Experimental Details......90

5.2.1 Thermo-reflectance Measurement......91

5.2.2 Thermal Finite Element Simulation......92

5.2.3 Electric Field Finite Element Simulation......93

5.2.4 Electrical Stressing......94

5.2.5 Microstructural Characterization......96

5.3 Results and Discussions......96

5.3.1 Stressing Condition Determination......96

5.3.2 Current Density Stressing......102

5.3.3 Two ON-State Degradation Modes......105

5.3.4 Role of Current Density in ON-state Degradation......109

5.3.5 Fast Degradation Mode Analysis......115

5.3.6 Proposed Degradation Mechanism Based on Current Density......118

5.4 Summary......120

Chapter 6 Effect of Passivation Density on AlGaN/GaN High Electron Mobility Transistor Degradation under ON-State Stressing......123

6.1 Introduction......124

6.2 Experimental Details......124

6.2.1 Material Properties of Low and High Density Passivation Layers......125

6.2.2 Electrical Stressing......126

6.3 Results and Discussions......128

6.3.1 Si_xN_{1-x} Degradation......128

6.3.2 Electrical Stressing Results 131
6.3.2.1 Conversion Time 132
6.3.2.2 Slow Mode Slope 134
6.4 ON-State Degradation Model 135
6.4.1 I_{D-max} Degradation and Pit Volume Correlation 136
6.4.2 Electro-chemical Oxidation Reaction 138
6.4.3 Oxygen Diffusion through Si_xN_{1-x} Passivation 141
6.4.4 Temperature Dependence of I_{D-max} Degradation 146
6.5 Summary 148

Chapter 7 Summary and Future Works 151
7.1 Summary 152
7.2 Implications and Limitations 155
7.3 Future Works 156
7.4 List of Publication 158

References 159

Appendix 177

Table Captions

Table 1.1 Properties of different substrates with the respect to GaN epitaxy [1-7]

Table 3.1 Material parameters used in the thermal finite simulation

Table 3.2 WBDF tilting conditions for threading dislocation (TD) characterization

Table 3.3 EELS ionization edges of the elements used in AlGaN/GaN HEMT reliability study [8]

Table 4.1 Junction temperature measurement parameters by thermo-reflectance method

Table 4.2 ON-state and OFF-state electrical stressing parameters

Table 4.3 ON-state and OFF-state electrical stressing results and parameters

Table 5.1 Device dimensions and parameters used in thermo-reflectance measurements

Table 5.2 Power density calculation for thermal finite element simulation

Table 5.3 Device dimensions and parameters used in ON-state stressing

Table 5.4 Device dimensions and parameters for electric field finite element simulation

Table 5.5 Stressing parameters for different current density

Table 5.6 Stressing parameters for additional experiment under ON-state condition

Table 5.7 Stressing parameters and results for devices stressed under ON-state condition with different current densities

Table 5.8 Avrami exponent for devices stressed under high and low current densities

Table 6.1 Parameters extracted from XRR measurements for low and high density Si_xN_{1-x} passivation

Table 6.2 Device dimensions used in the experiment and the simulated maximum electric field under ON-state condition V_{DS} = 20 V and V_{GS} = 0 V

Table 6.3 Stressing parameters for different temperatures and passivation densities

Table 6.4 Degradation pit radius/height (r/h) ratio from cross-sectional TEM images

Table 6.5 Concentration gradients for all three stressing batches under ON-state condition V_{DS} = 20 V, V_{GS} = 0 V with 2 different Si_xN_{1-x} densities

Table 6.6 Activation energy Q_d and pre-exponent factor D_0 for O_2 diffusivity through Si_xN_{1-x} passivation layer

Figure Captions

Figure 1.1 Performance comparison between GaN-, GaAs- and Si-based transistors assuming all transistors have the same packaging [9]

Figure 1.2 Schematics of (a) Ga-polar GaN crystal structure, (b) spontaneous and piezoelectric polarization in Ga-polar system with the 2DEG located at the lower AlGaN/GaN interface [10]

Figure 1.3 Energy band diagram and charge distribution of Ga-polar AlGaN/GaN HEMT without any bias applied [11]

Figure 2.1 Change in device characteristics when the device undergoes step-voltage stress at V_{DS} = 0 V and V_{GS} was swept from -10 to -40 V with 1-V step at T = 150°C [12]

Figure 2.2 Degradation pit at the gate-edge on the drain side for devices stressed at V_{DS} = 0 V and V_{DG} sweep from V_{DG} = -10 V to V_{DG} = (a) 37 V, (b) 25 V, (c) 17 V, (d) 16 V, (e) 15 V and (e) 0 V at 150°C [12]

Figure 2.3 (a) Vertical electric field distribution and (b) elastic energy density for a device operating under OFF-state condition V_{GS} = -5 V and V_{DS} = 33 V [13]

Figure 2.4 Pit/groove evolutions at (a) unstressed, $V_{DGstress}$ = (b) 15 V (below critical voltage), (c) 20 V, (d) 42 V, (e) 57 V and (f) average AFM depth profile over a gate width of 2 μm for $V_{DGstress}$ = 57 V at T_{Base} = 150°C [14]

Figure 2.5 Top-view SEM images of the devices stressed under OFF-state condition V_{DS} = 0 V and V_{GS} = -40 V for 100 minutes in (a) ambient air and (b) vacuum of 3×10^{-5} Torr after metallization layer removal [15]

Figure 2.6 Degradation pit formation at the gate edge of the drain side by electro-chemical oxidation mechanism under OFF-state condition [16]

Figure 2.7 I_G evolution over time for the device stressed under OFF-state condition $V_D = V_S = 0$ V and $V_{GS} = -30$ V (below critical voltage = -35 V) [17]

Figure 2.8 Electroluminescence (EL) measurements at different stressing time for the device stressed under OFF-state condition $V_D = V_S = 0$ V and $V_{GS} = -30$ V (below critical voltage = -35 V) [17]

Figure 2.9 (a) Electroluminescence image of OFF-state stressed device $V_{GS} = -15$ V, $V_{DS} = 40$ V for 4 mins, (b) and (c) AFM images for the areas inside the squares after metallization and passivation layer removal; (d) zoomed in version of one of the pit at (b) and (e) the depth profile of the pit along the 3 lines in (d) [18]

Figure 2.10 Percolation path degradation mechanism at (a) $t < t_{BD}$ and (b) $t > t_{BD}$ [19]

Figure 2.11 (a) EL vs gate voltage plots at different stressing time for a device stressed at $V_{DS} = 30$ V and $V_{GS} = -1$ V. (b) Drain current and (c) EL/drain current ratio measured on the same device over time [20]

Figure 2.12 Hot electron trapping mechanism in AlGaN/GaN HEMT surface under ON-state condition [21]

Figure 2.13 Cross-sectional TEM images for devices with (a) 19% and (b) 58% $I_{D\text{-}max}$ degradation at the gate edge on the drain side (c) Change in drain current (I_{DQ}) during stressing and $I_{D\text{-}max}$ recorded every hour for the device stressed under ON-state condition $V_{DS} = 40$ V and $I_{D\text{-}initial} = 250$ mA/mm over time [22]

Figure 2.14 Top-view SEM images for the devices stressed under V_{DS} = 40 or 50 V and I_{DQ} = 100 mA/mm with different I_{D-max} degradation levels after metallization and passivation layer removal [23]

Figure 2.15 Distribution of pit/trench depth at the gate edge on the drain side and erosion depth under the gate along half of the gate width for device with 21.6% I_{D-max} degradation [23]

Figure 2.16 Cross-sectional TEM image of the device stressed under ON-state and EDX results at point A and B [22]

Figure 2.17 (a) Cross-sectional TEM image of the degraded Ohmic contact showing a void with Al-Ga-Au allow surrounding it and layer of Al-Au penetrating AlGaN layer; (b) EDX line scan from blue arrow in (a) [24]

Figure 2.18 Cross-sectional SEM image shows extrusion of Au-Al IMC (red circle) in degraded Ohmic contact for a device stressed under DC condition V_{DS} = 50 V, I_{DS} 50 mA/mm and $T_{junction}$ = 275^0 C for 2000 hours [25]

Figure 3.1 Cross-sectional schematics of AlGaN/GaN HEMT on Si device

Figure 3.2 Top-view SEM image of the AlGaN/GaN HEMT

Figure 3.3 Probe station used to test and stress the device at wafer level

Figure 3.4 (a) In-house-built system to test and stress device under high vacuum or high humidity. (b) Wire-bonded chip to dual in-line package (DIP) used in this system

Figure 3.5 32-SMU National Instrument modified EM system

Figure 3.6 I_D-V_{DS} plot of AlGaN/GaN HEMT on Si substrate

Figure 3.7 I_D-V_{GS} and I_G-V_{GS} plot of AlGaN/GaN HEMT on Si substrate

Figure 3.8 One characterization and stressing cycle during electrical stressing of AlGaN/GaN HEMT

Figure 3.9 Thermo-reflectance (a) measurement setup and (b) calibration setup [26]

Figure 3.10 Schematics of AlGaN/GaN HEMT used for thermal finite element simulation (a) cross-sectional view at the left gate finger and (b) top-view of the whole device

Figure 3.11 Input and output system of Silvaco Atlas device simulator [27]

Figure 3.12 Typical contour map obtained from TonyPlot

Figure 3.13 SEM image of AlGaN/GaN HEMT device (a) before and (b) after passivation/metallization layer removal

Figure 3.14 SEM image of GaN film after dislocation etching using 85% H_3PO_4 for 100 minutes at 80^oC

Figure 3.15 FEI Nova 600 NanoLab DualBeam™ SEM/FIB system used for microstructure characterization and cross-sectional TEM sample preparation

Figure 3.16 Electron-sample interaction volume within the sample [28]

Figure 3.17 Schematic diagram of SEM/FIB dual beam system [29]

Figure 3.18 Cross-sectional TEM sample preparation using FIB system: (a) trenches are made to expose the lamellar, (b) the lamellar is picked using a nanoprobe, (c) the lamellar is transferred and attached to TEM copper grid and (d) the lamellar is thinned down to about 100 nm thick

Figure 3.19 (a) JEOL 2100F TEM with (b) double-tilt sample holder located in FACTS lab [30]

Figure 3.20 X-ray generation in EDX under STEM mode: (a) Incident electron hit the sample atom and knock some electrons from the inner shell to the outer shell, (b) X-rays are generated with these excited electrons return to the inner shell [31]

Figure 3.21 WBDF images of the same sample at (a) g = [1120] to show pure edge TD labelled as E, (b) g = [0002] to show pure screw TD labelled as S. Mixed TDs are visible in both conditions and labelled as M

Figure 3.22 Electron energy-loss spectrum of $YBa_2Cu_3O_7$ showing zero-loss peak and ionization edges from each element [32]

Figure 3.23 EELS spectrum needed to determine specimen thickness using log-ratio method [33]

Figure 3.24 (a) Schematics of EELS line-scan to determine relative density of Si_xN_{1-x} passivation layer (b) side-view of the TEM lamellar

Figure 3.25 Experimental setup for X-ray reflectivity (XRR) measurement [34]

Figure 3.26 A typical XRR measurement plot

Figure 3.27 Bruker D8 Discover HR-XRD system used for XRR measurement [35]

Figure 3.28 One of **t**op-view SEM images of an AlGaN/GaN HEMT device stressed under ON-state condition after passivation and metallization layer removal

Figure 4.1 (a) Top-view image of the AlGaN/GaN HEMT taken by light microscope, ΔT distribution of the device under (b) ON-state condition V_{DS} = 20 V, V_{GS} = 0 V and (c) OFF-state condition V_{DS} = 10 V, V_{GS} = -10 V at base temperature 25°C

Figure 4.2 Maximum junction temperatures at the drain-gate access region for device 1-3 under ON-state condition V_{DS} = 20 V, V_{GS} = 0 V at four different base temperatures

Figure 4.3 Normalized I_{D-max} evolution of AlGaN/GaN HEMTs under OFF-state (V_{DS} = 10 V, V_{GS} = -10 V, T_{base} = 250°C) and ON-state (V_{DS} = 20 V, V_{GS} =0 V, Max $T_{junction}$ = 217°C)

Figure 4.4 Simulated (a) vertical and (b) horizontal electric field for AlGaN/GaN HEMTs under OFF-state (V_{DS} = 10 V, V_{GS} = -10 V, T_{base} = 250°C) and ON-state (V_{DS} = 20 V, V_{GS} =0 V, Max $T_{junction}$ = 217°C) condition

Figure 4.5 Top-view SEM image of the stressed device under (a) OFF-state (V_{DS} = 10 V, V_{GS} = -10 V, T_{base} = 250°C) and (b) ON-state (V_{DS} = 20 V, V_{GS} =0 V, max $T_{junction}$ = 216.6^{o}C) conditions after Si_xN_{1-x} passivation and metallization layers removal

Figure 4.6 Pit distribution for the OFF-state (V_{DS} = 10 V, V_{GS} = -10 V, T_{base} = 250°C) and ON-state (V_{DS} = 20 V, V_{GS} =0 V, Max $T_{junction}$ = 217°C) stressed devices

Figure 4.7 Correlation between I_{D-max} degradation and total pit area at drain-gate access region for devices stressed under ON-state condition

Figure 4.8 Cross-sectional TEM images of device stressed under ON-state condition before Si_xN_{1-x} passivation and metallization removal. Images taken at (a) the drain side gate edge, (b) 260 nm and (c) 1000 nm from gate edge in the drain-gate access region; (d) at the source side gate edge, (e) 300 nm and (f) 1000 nm from the gate edge in the gate-source access region Dark features were observed at the AlGaN/Si_xN_{1-x} interface at the drain side. These dark features will be removed together with a portion of oxidized AlGaN layer during passivation and metallization removal to form degradation pits.

Figure 4.9 Elemental characterization by EELS and EDX line-scans along (a) A-A' (Figure 4.8b) and (b) B-B' (Figure 4.8e) for aluminum, gallium and oxygen. Zero distance is taken at the initial AlGaN/Si_xN_{1-x} interface

Figure 4.10 $I_{D\text{-}max}$ degradation vs. stressing time under UV (254 nm) exposure with and without substrate bias (V_{DS} = 10 V, V_{GS} = floating, T_{Base} = 200°C)

Figure 4.11 Pit distribution of the unstressed device and stressed devices under UV (254 nm) exposure and ON-state bias V_{DS} = 10 V, V_{GS} = floating with/without substrate bias = -20 V

Figure 4.12 Proposed model for ON-state degradation based on electro-chemical oxidation mechanism

Figure 4.13 Device schematics used in Silvaco 2D finite element simulation for (a) N-polar and (b) Ga-polar AlGaN/GaN HEMT

Figure 4.14 Electron concentration and energy band diagram for (a) N-polar and (b) Ga-polar $Al_{0.30}Ga_{0.70}N$/GaN HEMT under ON-state condition V_{DS} = 20 V, V_{GS} = 0 V obtained from 2D finite element simulation taken at 50 nm away from the gate edge in the gate-drain access region

Figure 4.15 Maximum electric field distribution in (a) vertical direction and (b) lateral direction across the Ga-polar and N-polar AlGaN/GaN HEMT device under ON-state bias V_{DS} = 20 V and V_{GS} = 0 V

Figure 5.1 Temperature increase distribution under V_{DS} = 20 V, V_{GS} = 0 V, I_{DS} = 21.3 mA and T_{Base} = 25°C measured by thermo-reflectance method

Figure 5.2 Comparison between maximum junction temperatures obtained by thermo-reflectance (TR) measurement and thermal simulation at different current densities and base temperatures

Figure 5.3 Calculated maximum temperature for different current densities at base temperature 200°C and 175°C

Figure 5.4 Vertical electric field distribution for V_{DS} = 20 V and different V_{GS} at the top AlGaN layer

Figure 5.5 Horizontal electric field distribution for V_{DS} = 20 V and different V_{GS} at the top AlGaN layer

Figure 5.6 Maximum (a) vertical and (b) horizontal electric field for V_{DS} = 20 V and different V_{GS} at various locations

Figure 5.7 $I_{D\text{-}max}$ versus time for the devices stressed under ON-state condition V_{DS} = 20 V high (J_{DS}-initial = 0.168 A/mm, T_{base} = 175^{0} C), low current densities (J_{DS}-initial = 0.089 A/mm, T_{base} = 200^{0} C) and temperature only (T_{base} = 260^{0} C) stressing.

Figure 5.8 (a) Typical $I_{D\text{-}max}$ vs. time graph and (b) second derivative graph with the two degradation modes

Figure 5.9 (a) schematics of AlGaN/GaN HEMT device at the drain side and STEM-EELS line-scans at location (b) 1, (c) 2, (d) 3 and (e) 4 to characterize nitrogen, oxygen and carbon.

Figure 5.10 $I_{D\text{-}max}$ evolutions of AlGaN/GaN HEMT devices stressed under ON-state condition V_{DS} = 30 V, V_{GS} = 0 V with high vacuum (1 × 10^{-5} Torr) and ambient at T_{base} = 150^0 C for 500 hours

Figure 5.11 Average slow mode slopes of AlGaN/GaN HEMT devices stressed under ON-state condition with different current densities.

Figure 5.12 Average (a) conversion point degradation and (b) conversion point time of AlGaN/GaN HEMT devices stressed under ON-state condition with different current densities.

Figure 5.13 (a) Total pit area per unit device width as a function of distance from the gate edge and (b) top-view SEM image of the device stressed under V_{DS} = 20 V, V_{GS} = 0 V, T_{Base} = 150^0 C with average J_{DS} = 0.194 A/mm for 20 h after metallization/passivation removal

Figure 5.14 Maximum pit distance vs. average current density plot for devices stressed under ON-state condition for 20 h with different current densities at various base temperatures

Figure 5.15 Total pit areas at the drain-gate access region plotted against $I_{D\text{-}max}$ degradation of the devices stressed under different current densities. $I_{D\text{-}max}$ degradation is normalized to individual device regardless of the stressing current density

Figure 5.16 (a) Top view of the drain-gate access region and oxygen diffuses towards the activated region. (b) Each pit is assumed to have conical shape

Figure 5.17 (a) $I_{D\text{-}max}$ vs time plot for one of the devices stressed under different current density and (b) $Ln\left(Ln\left(1-\frac{I_{D-max}\, degradation\,(\%)}{100}\right)\right)$ vs $Ln\, t$ plot to extract Avrami exponent

Figure 5.18 Electroluminescence (EL) intensity distributions in AlGaN/GaN HEMT before and after electrical stressing which represent drain current degradation [36]

Figure 5.19 Proposed degradation model to illustrate the effect of (a) high current density and (b) low current density in AlGaN/GaN HEMT ON-state degradation

Figure 6.1 XRR measurement plots for low and high density Si_xN_{1-x} passivation layers

Figure 6.2 Top-view schematics of AlGaN/GaN HEMT device to show cross-sectional TEM sample cut directions

Figure 6.3 (a) Cross-sectional TEM image along the gate width from the OFF-state stressed device V_{DS} = 0 V, V_{GS} = –50 V at 200^0 C with 24% $I_{D\text{-}max}$ degradation; (b) relative density, oxygen line-scan and nitrogen line-scan obtained by EELS analysis from line C-C'; oxygen and nitrogen line-scan obtained by EELS analysis from line (c) E-E' and (d) D-D'

Figure 6.4 Typical $I_{D\text{-}max}$ vs time plot for device stressed under ON-state condition V_{DS} = 20 V, V_{GS} = 0 V for 200 hours in this experiment

Figure 6.5 Second derivative plot from $I_{D\text{-}stress}$ vs time plot of the device stressed under ON-state condition V_{DS} = 20 V, V_{GS} = 0 V

Figure 6.6 Average conversion time vs surrounding temperature for devices with high and low density passivation stressed under ON-state condition V_{DS} = 20 V, V_{GS} = 0 V

Figure 6.7 Average slow mode slope vs surrounding temperature for devices with high and low density passivation stressed under ON-state condition V_{DS} = 20 V, V_{GS} = 0 V

Figure 6.8 Modeling map for AlGaN/GaN HEMT slow degradation mode under ON-state stressing condition

Figure 6.9 (a) Top-view SEM image and (b) cross-sectional TEM image of the degradation pits at the drain-gate access region

Figure 6.10 I_{D-max} degradation plotted against normalized total pit volume calculated from the stressed devices

Figure 6.11 Total numbers of moles O_2 used in electro-chemical oxidation plotted as a function of I_{D-max} degradation for all the stressed devices

Figure 6.12 O_2 concentration profile in the steady-state diffusion through Si_xN_{1-x} passivation

Figure 6.13 Number of moles O_2 distribution plot for AlGaN/GaN HEMT device stressed under ON-state condition

Figure 6.14 Top-view schematic of AlGaN/GaN HEMT device to show the distance L where the Si_xN_{1-x} passivation is likely to degrade due to high electric field

Figure 6.15 Arrhenius plot of the O_2 diffusivity through degraded Si_xN_{1-x} passivation layer

Figure 7.1 (a) Unit cell of GaN hexagonal-wurzite structure [37], (b) top view of the unit cell, and AlGaN/GaN HEMT devices grown in the same chip in (c) [1100], (d) [1120] orientations

Abbreviations

2DEG	Two-Dimensional Electron Gas
ADF	Annular Dark Field
AFM	Atomic Force Microscopy
BF	Bright Field
CCD	Charge Coupled Device
DIP	Dual In-line Package
EDX	Energy Dispersive X-ray Spectroscopy
EELS	Electron Energy Loss Spectroscopy
EL	Electroluminescence
FET	Field Effect Transistor
FIB	Focused Ion Beam
HEMT	High Electron Mobility Transistor
IR	Infra-Red
IC	Integrated Circuit
JMAK	Johnson-Mehl-Avrami-Kolmogorov
LED	Light Emitting Diode
MBE	Molecular Beam Epitaxy
MOCVD	Metal-Organic Chemical Vapor Deposition
MOSFET	Metal-Oxide-Semiconductor Field Effect Transistor
PECVD	Plasma-Enhanced Chemical Vapor Deposition
RIE	Reactive Ion Etching
SEM	Scanning Electron Microscopy
TR	Thermo-Reflectance
TEM	Transmission Electron Microscopy
WBDF	Weak Beam Dark Field
XRR	X-ray Reflectometry

Chapter 1

Introduction

AlGaN/GaN high electron mobility transistor (HEMT) on Si substrate has the potential to extend the capabilities of Si-based devices for high power and high frequency applications. However, market adaptation of this technology is still limited by its reliability issues. Thus, it is important to study the reliability of AlGaN/GaN HEMT on Si substrate. This chapter covers the rationale, objectives and the scope of the reliability study. This chapter also contains the overview of each chapter in this thesis.

1.1 Background

Semiconductor technology has improved dramatically in the past decades in terms of device performance and function. This is mainly due to miniaturization of the field effect transistor (FET) based on silicon semiconductor technology. As predicted by Moore's law, an advanced integrated circuit (IC) doubles in the number of transistors and gives better performance for each technology node. Unfortunately, silicon technology cannot cater to the high power and high frequency applications such as radar, power amplifier, and microwave communications due to its small band-gap [38, 39]. Thus, other materials and transistor structures are needed in order to complement the silicon-based semiconductor in this area.

The device that is used in electronics for these applications today is the high electron mobility transistor (HEMT). Figure 1.1 shows five key characteristics that make HEMT more suitable for high power and high frequency applications compared to silicon metal-oxide-semiconductor field effect transistor (Si-MOSFET). HEMT has higher operating temperature and higher breakdown voltage than Si-MOSFET due to its higher energy band-gap i.e. 1.43 eV for GaAs, 3.42 eV for GaN and 1.12 eV for Si [40]. This makes HEMT apt for high power application especially AlGaN/GaN HEMT [41]. Si-MOSFET operates based on inversion-channel from doped semiconductor whereas HEMT operates based on two-dimensional electron gas (2DEG). The charge carriers in the inversion-channel of Si-MOSFET have lower mobility than the 2DEG of HEMT [42]. Therefore, HEMT is much faster than Si-MOSFET, making it appropriate as a switching device with high cut-off frequency [43, 44].

The first HEMT was invented by T. Mimura from Fujitsu in the late 1970s and it was made of AlGaAs/GaAs [45]. The latest HEMT technology is fabricated using AlGaN/GaN, with the first AlGaN/GaN HEMT demonstrated by Khan *et al*. [46]. AlGaN/GaN HEMT has drawn a lot of interest as it gives better performance than AlGaAs/GaAs HEMT especially for high power applications due to its higher energy band-gap and larger spontaneous polarization [10, 47]. AlGaN/GaN HEMT can operate up to 400°C [9] and have 5-12

W/mm [48] power density while AlGaAs/GaAs HEMT can only operate up to 200°C and 1.5 W/mm.

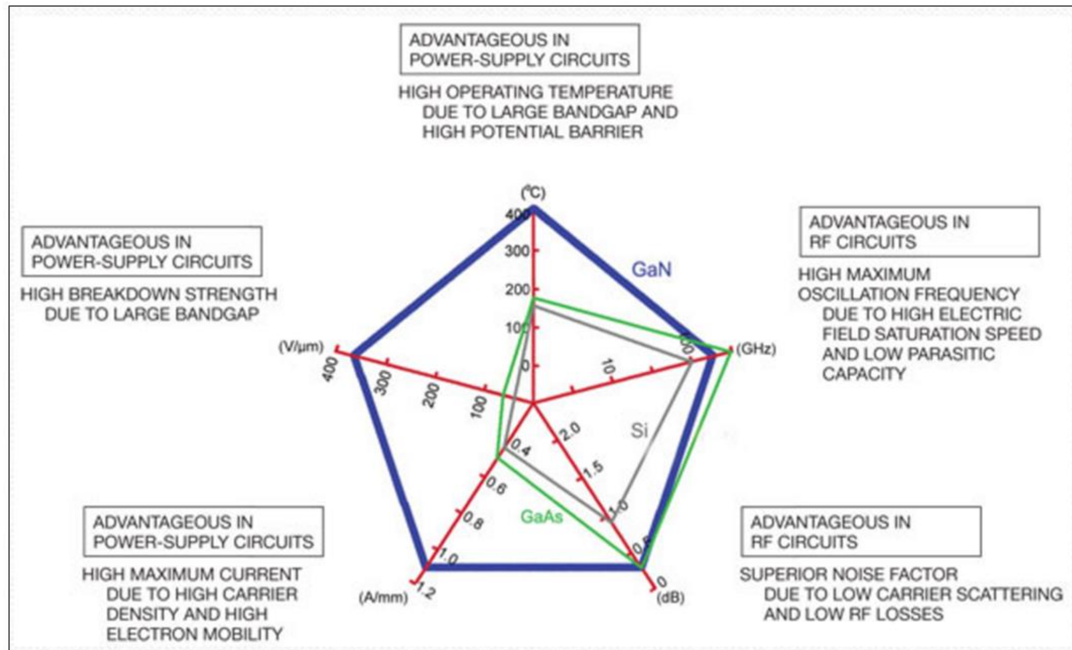

Figure 1.1 Performance comparison between GaN-, GaAs- and Si-based transistors assuming all transistors have the same packaging [9]

1.1.1 AlGaN/GaN HEMT Working Principle

AlGaN/GaN HEMT epitaxy can be grown by both molecular beam epitaxy (MBE) [49-53] and metal-organic chemical vapor deposition (MOCVD) [54-58]. The performance of the MBE-grown device is comparable to the MOCVD-grown device [59]. However, in the long run, MBE is more costly than MOCVD. Therefore, MOCVD is preferred over MBE to grow AlGaN/GaN HEMT commercially.

AlN and GaN have a wurtzite-type hexagonal crystal structure [60]. Two types of GaN epitaxy can be grown depending on the cut-face of the GaN i.e. Ga-polar and N-polar. Ga-polar film is usually grown by MOCVD whereas N-polar film is usually grown by MBE under certain conditions [61]. The devices used in this study are Ga-polar AlGaN/GaN HEMTs.

Strong spontaneous polarization occurs in GaN and AlN since nitrogen has higher electronegativity than gallium and aluminum. The spontaneous polarization for GaN and AlN are 0.029 and 0.081 C/m^2, respectively [62]. On top of spontaneous polarization, GaN and AlN have piezoelectric polarization as they are piezoelectric material. When a thin layer of $Al_xGa_{1-x}N$ is grown on top of Ga-polar GaN, it will experience tensile strain. This tensile strain will generate piezoelectric polarization in the same direction with the spontaneous polarization (Figure 1.2b). This strong polarization generates electric field within the AlGaN layer. In the case of unintentionally-doped AlGaN, it is assumed that there are surface donor states at the top of AlGaN layer. When the AlGaN layer is thick enough such that the Fermi level will reach these states, electrons will be stimulated to jump into conduction band. These electrons are then swept towards AlGaN/GaN interface by the electric field. Upon contact with GaN layer, these electrons will flow into GaN side because GaN has a lower Fermi level. Electrons will continue to flow until the Fermi level is equalized and 2-dimensional electron gas (2DEG) is formed at the AlGaN/GaN interface [63-68]. These electrons are energetically confined at the AlGaN/GaN interface (Figure 1.3) but they are highly mobile along the AlGaN/GaN interface.

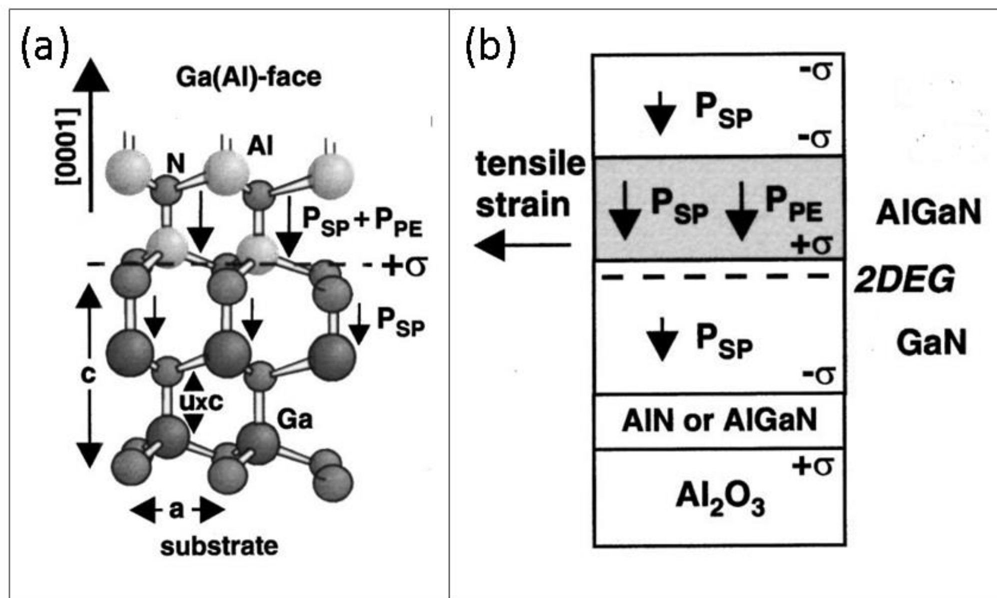

Figure 1.2 Schematics of (a) Ga-polar GaN crystal structure, (b) spontaneous and piezoelectric polarization in Ga-polar system with the 2DEG located at the lower AlGaN/GaN interface [10]

The carrier sheet density and carrier mobility in the 2DEG can be further enhanced by fine-tuning Al molar fraction *x* and the $Al_xGa_{1-x}N$ thickness. Increasing Al molar fraction and $Al_xGa_{1-x}N$ thickness will increase the carrier sheet density since the piezoelectric polarization will increase. However, the carrier mobility will decrease due to increasing scattering when carrier density increases [69].

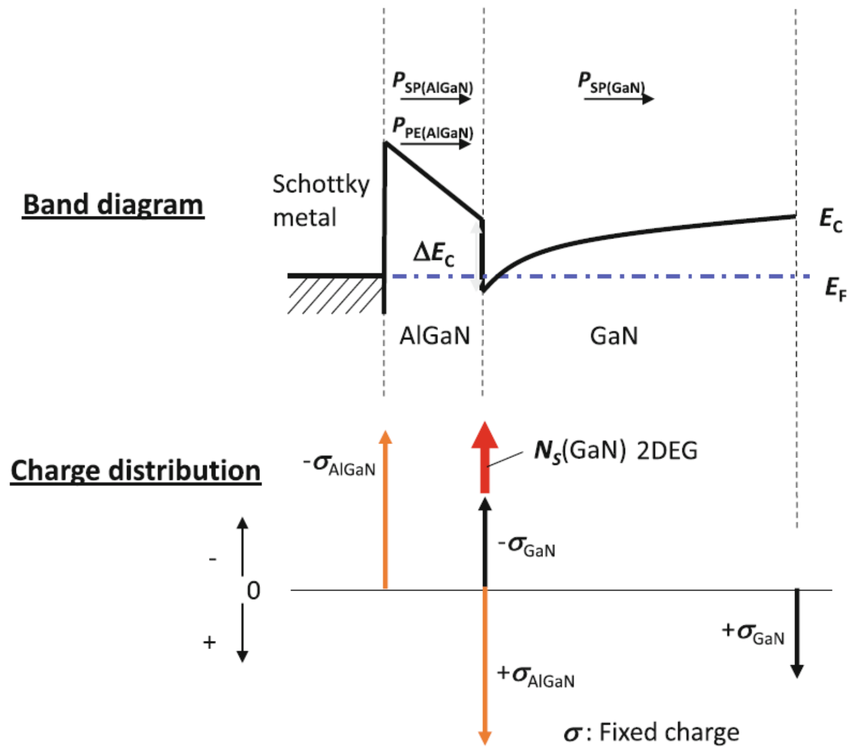

Figure 1.3 Energy band diagram and charge distribution of Ga-polar AlGaN/GaN HEMT without any bias applied [11]

1.1.2 AlGaN/GaN HEMT on Various Substrates

Since GaN substrate is very expensive, AlGaN/GaN HEMT is usually grown on foreign substrates. The common foreign substrates are sapphire, SiC and Si. The properties of each substrate with respect of GaN epitaxy are shown in Table 1.1. Out of these three foreign substrates, SiC shows the best compatibility with AlGaN/GaN epitaxy. However, it is the most expensive among the foreign substrates. The cheaper alternatives will be sapphire or Si. Among these two substrates, Si substrate has a better prospect than sapphire. Si substrate is available up to 12” and it has less wafer-bow management problem than

sapphire [70]. AlGaN/GaN epitaxy is typically grown on (111) Si due to its trigonal symmetry that supports the epitaxial growth of (0001) GaN [3].

Table 1.1 Properties of different substrates with the respect to GaN epitaxy [1-7]

	Sapphire	SiC	Si	GaN
Lattice mismatch (%)	16	3.1	-17	0
Linear thermal expansion coefficient ($\times10^{-6}$ K^{-1})	7.5	4.4	2.6	5.6
Thermal conductivity (W cm^{-1} K^{-1})	0.25	4.9	1.6	2.3
Cost	Cheap	Expensive	Cheap	Very expensive
Dislocation density of GaN film (cm^{-2})	10^8	10^8	10^9	10^4-10^6

Furthermore, growing AlGaN/GaN on Si allows monolithic integration between AlGaN/GaN HEMT and Si-based semiconductors [71-73]. This allows cost-efficient large scale production and opens up new applications. Despite this promising potential, there are still many reliability issues to be addressed [74]. Therefore, this project aims to improve the knowledge on AlGaN/GaN HEMT-on-Si reliability.

1.2 Hypothesis/Problem Statement

Normally-ON AlGaN/GaN HEMT operates both in OFF- and ON-state conditions. Under OFF-state condition, large negative voltage is applied to prevent current from flowing in 2DEG channel. Maximum drain current (I_{D-max}) of the device decreases over time upon stressing under OFF-state condition. This phenomenon correlates well with the formation of physical defects such as pits [75], cracks [13] and grooves [14] via electro-chemical oxidation process [16]. The formation of these defects is dependent on various factors such as threading dislocation [75, 76], applied bias [14], temperature [77] and stressing duration [78].

Despite the extensive studies that have been done for AlGaN/GaN HEMT OFF-state reliability, there are very limited studies done on ON-state reliability even for the

AlGaN/GaN HEMT on other substrates such as SiC and sapphire. Therefore, this study addresses the knowledge gap on AlGaN/GaN HEMT-on-Si degradation under ON-state condition. The study aims at understanding the degradation mechanisms and developing the reliability model which will ultimately allow us to predict the life-time of AlGaN/GaN HEMT-on-Si devices.

1.3 Objectives and Scope

There are three main objectives for this reliability study. They are as follows:

a) Understand the electrical and physical degradation mechanism in AlGaN/GaN HEMT-on-Si devices stressed under ON-state condition.

b) Understand the effects of various stressing and process parameters on AlGaN/GaN HEMT ON-state degradation

c) Develop a reliability model for the degradation mechanism in AlGaN/GaN HEMT-on-Si devices stressed under ON-state condition.

This study covers ON-state degradation due to decreasing $I_{D\text{-}max}$ over time. This is because $I_{D\text{-}max}$ is the most common parameter used to evaluate the performance of a transistor. The $I_{D\text{-}max}$ degradation is then correlated with the pit formation at the drain-gate access region because the pits are readily observed and reproduced.

There are other electrical parameters that can be used to analyze the degradation such as $I_{G\text{-}leak}$ [17], V_{TH} [79] and transconductance (g_m) [80]. However, these parameters do not show a consistent correlation with pit formation across the devices used in this study. These parameters might be related to other physical degradations that are not readily observable. Therefore, these parameters are not included in this thesis.

The devices that are used in this experiment have a long gate (around 2 μm) as only these

samples are available from our collaborators. Therefore, the analysis here may not be applicable to devices with sub-micron gate length. Furthermore, statistical analysis is out of the scope of this thesis because of the limited number of samples available.

1.4 Dissertation Overview

The thesis addresses ON-state reliability problem of AlGaN/GaN HEMT-on-Si devices. This thesis consists of seven chapters. These seven chapters can be summarized as follow:

Chapter 1 provides the rationale for the research and outlines the goals and scope.

Chapter 2 reviews the literature concerning AlGaN/GaN HEMT reliability. This chapter reviews the previous studies done on AlGaN/GaN HEMT reliability. It starts with the review on the OFF-state degradation mechanisms and proposed degradation models. Then it continues with the review on AlGaN/GaN HEMT degradation under ON-state condition. This chapter concludes with thesis relevance on the knowledge gap.

Chapter 3 discusses tools and techniques used to investigate the ON-state reliability problem of AlGaN/GaN HEMT-on-Si devices. This chapter consists of three parts. The first part discusses about the tools and methods used to test and to stress the devices electrically. The next part talks about simulation tools used to determine the junction temperature and electric-field distribution in the device. Lastly, tools and techniques used to characterize device microstructure are explained. The working principle and rationale of each method or tool is thoroughly explained.

Chapter 4 covers the results and discussions on the comparative studies between OFF-state and ON-state degradations. At the end of this chapter, a qualitative ON-state degradation model based on electro-chemical oxidation mechanism is proposed.

Chapter 5 elaborates on the effects of current density on AlGaN/GaN HEMT-on-Si ON-state degradation. Thermal simulation is used to determine the appropriate stressing

conditions. The effect of current density on AlGaN/GaN HEMT devices stressed under ON-state condition is analyzed and discussed. ON-state degradation mechanism is proposed based on current density difference.

Chapter 6 explains about the effect of Si_xN_{1-x} passivation density on AlGaN/GaN HEMT-on-Si degradation under ON-state stressing. Devices with two different Si_xN_{1-x} passivation densities were stressed under ON-state condition and the results are compared. After that, a quantitative degradation model is proposed based on oxygen diffusion through Si_xN_{1-x} passivation layer for slow mode degradation.

Chapter 7 covers the summary, implications and limitations of the thesis. The key findings of the study are summarized. The implications and limitations of the research are discussed. Finally, the opportunities and strategies for future work are discussed.

1.5 Findings and Outcomes/Originality

This research has led to several novel outcomes by:

1. Explaining the differences between OFF-state and ON-state degradations of AlGaN/GaN HEMT-on-Si devices.

2. Understanding the effects of current density, passivation density and temperature on AlGaN/GaN HEMT-on-Si ON-state degradation.

3. Developing qualitative and quantitative degradation model based on electro-chemical oxidation mechanism.

Chapter 2

Literature Review

This chapter reviews the previous work on AlGaN/GaN HEMT reliability. The first part focuses on OFF-state reliability, which covers electrical and microstructure characterization of OFF-state degradation using various techniques and parameters. Then three reported OFF-state degradation mechanisms are discussed in detail. They are the inverse-piezoelectric mechanism, electro-chemical oxidation and percolation path mechanism. The second part of this chapter covers available literature for AlGaN/GaN HEMT ON-state reliability. ON-state reliability is not as well reported as OFF-state reliability. The current understanding of ON-state degradation mechanism is discussed. There are two mechanisms, i.e. hot electrons degradation and electro-chemical oxidation mechanism. However, the correlation between current and physical degradation under ON-state condition is still unclear especially for AlGaN/GaN HEMT on Si. The last part of this chapter discusses about how this thesis fills the knowledge gaps in AlGaN/GaN HEMT-on-Si ON-state reliability.

2.1 Introduction

AlGaN/GaN HEMT has a lot of potential to complement Si-based semiconductor especially for high power and high frequency applications. However, this technology is still limited by reliability issues [74]. Typical AlGaN/GaN HEMT is a normally-ON device with negative threshold voltage. It operates in both ON- and OFF-state conditions. In this chapter, previous reliability studies on AlGaN/GaN HEMT are reviewed in order to understand the current gaps in the knowledge of reliability issues in AlGaN/GaN HEMT.

2.2 OFF-State Reliability

OFF-state stressing is usually done by applying large negative V_{GS}. Upon electrical stressing, the device will degrade that is characterized by a decrease in maximum drain current (I_{D-max}) and/or increase in gate leakage current (I_{G-leak}) [19, 81].

Three major mechanisms have been proposed to explain the OFF-state device degradation. They are:

1) Inverse piezoelectric stress
2) Electro-chemical oxidation
3) Percolation path mechanism

Previous studies about these mechanisms will be reviewed in the following subsections.

2.2.1 Inverse Piezoelectric Stress

Piezoelectric effect is the phenomenon which certain materials generate electric charge when subjected to mechanical stress. The amount of electric charge generated is proportional to the mechanical stress applied. Inverse piezoelectric effect is that the same materials experience mechanical strain when an electric field is applied to the materials. Both AlGaN and GaN are piezoelectric materials.

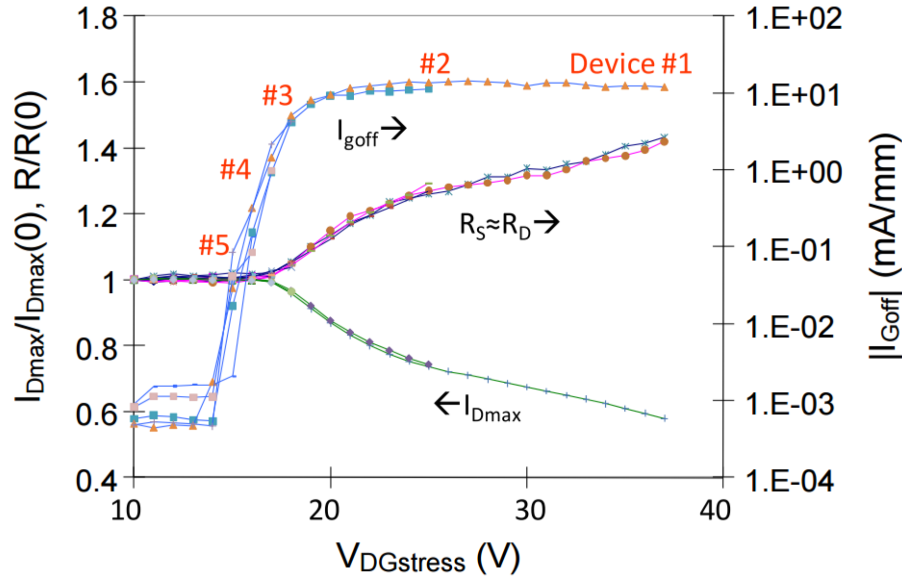

Figure 2.1 Change in device characteristics when the device undergoes step-voltage stress at V_{DS} = 0 V and V_{GS} was swept from -10 to -40 V with 1-V step at T = 150°C [12]

Inverse piezoelectric mechanism was first proposed by Joh *et al.* [82]. Figure 2.1 shows the evolution of I_{D-max}, I_{G-off} and source/drain resistance (R_S/R_D) for the device stressed under OFF-state condition V_{DS} = 0 V, V_{GS} was swept from -10 to -40 V (1-V step) at 150°C. The I_{D-max}, I_{G-off} and R_S/R_D were constant up to about V_{DG} = 17 V. At V_{DG} = 17 V, I_{D-max} started to decrease while R_S/R_D started to increase steadily. I_{G-off}, on the other hand, showed an abrupt increase at V_{DG} = 17 V. This voltage is the critical voltage at which the device starts to degrade [12, 13, 81].

The experiment was repeated for a few times using identical devices. Each device was stressed with V_{DS} = 0 V and V_{DG} sweep from V_{DG} = -10 V to a certain V_{DG} as numbered in Figure 2.1 in order to investigate the different stages of degradation. Figure 2.2 shows pit formed at gate edge on the drain side for six different stages of degradation:

(a) Device #1: Highest degradation (V_{DG} = 37 V)
(b) Device #2: Medium degradation (V_{DG} = 25 V)
(c) Device #3: Onset of I_{D-max} and R_S/R_D degradation with large I_{G-off} (V_{DG} = 17 V)
(d) Device #4: Mild I_{G-off} degradation (V_{DG} = 16 V)
(e) Device #5: Onset of I_{G-off} degradation
(f) Device #6: Unstressed device as reference

Pit was formed at the gate edge on the drain side for device #1 to #5. There is no pit formed for device #6 which showed that pit was formed because of the electrical stressing. The degradation at the gate edge on the drain side got more severe as V_{DG} increases.

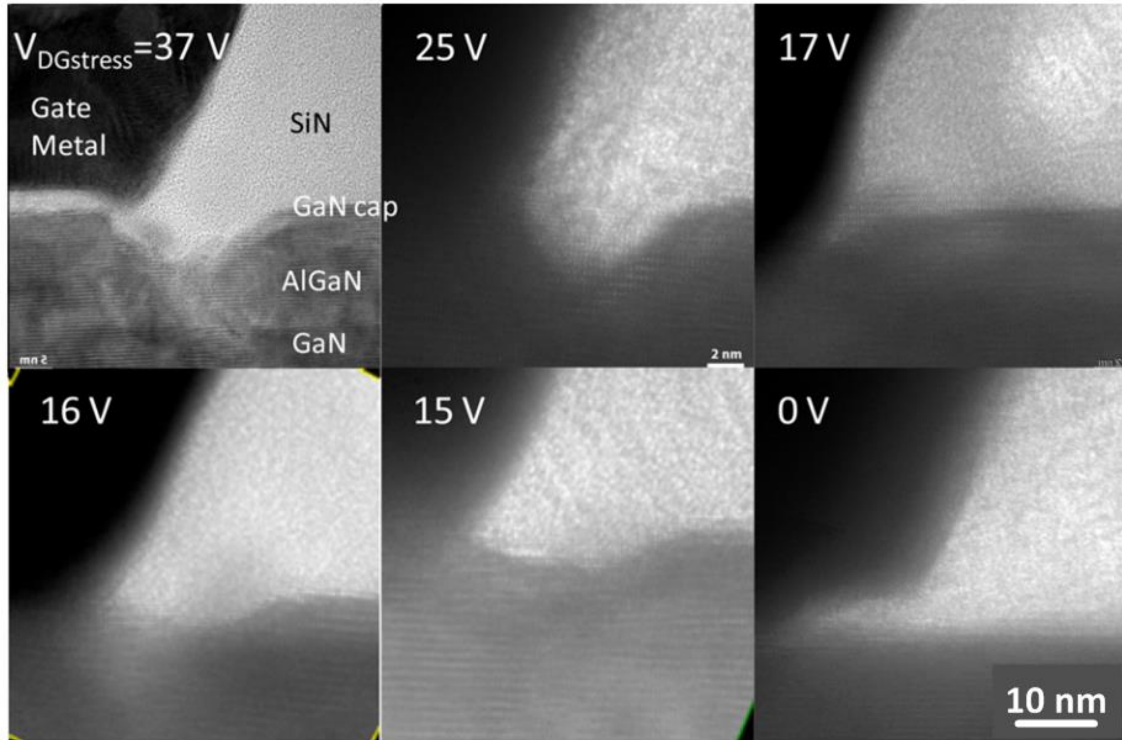

Figure 2.2 Degradation pit at the gate-edge on the drain side for devices stressed at V_{DS} = 0 V and V_{DG} sweep from V_{DG} = -10 V to V_{DG} = (a) 37 V, (b) 25 V, (c) 17 V, (d) 16 V, (e) 15 V and (e) 0 V at 150°C [12]

Figure 2.3 shows the electric field and elastic energy density for the device operating under V_{GS} = -5 V and V_{DS} = 33 V. It shows that the highest vertical electric field is at gate edge on the drain side of the device. This corresponds to the location where pits were found (Figure 2.2a-e). Joh *et al.* proposed that the vertical electric field increases as the V_{DG} increases [13]. The vertical electric field generates inverse piezoelectric stress which will increase the elastic energy of the material. At the critical voltage, the elastic energy density reaches its critical value at gate edge on the drain side. This leads to pit formation at the same location.

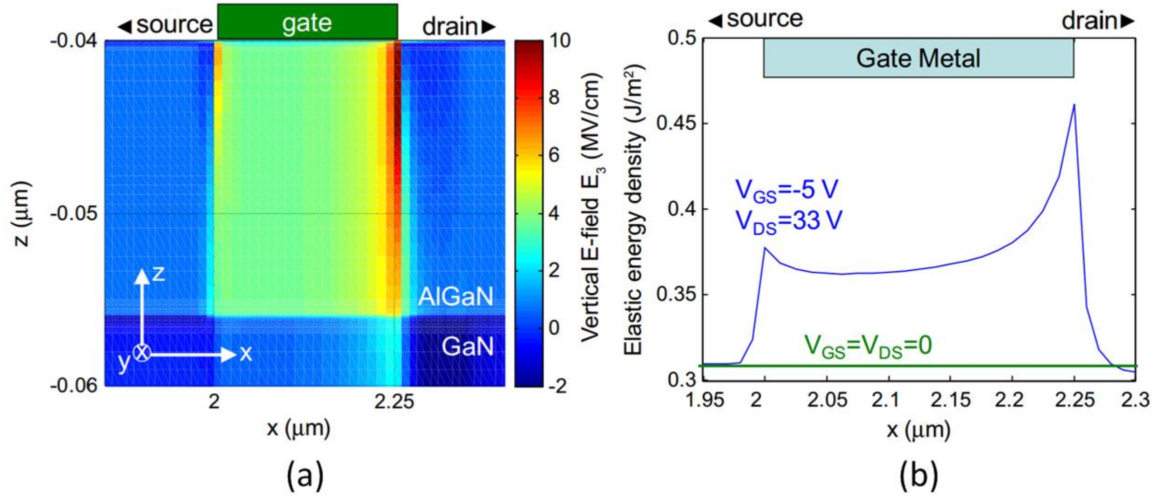

Figure 2.3 (a) Vertical electric field distribution and (b) elastic energy density for a device operating under OFF-state condition V_{GS} = -5 V and V_{DS} = 33 V [13]

2.2.2 Electro-Chemical Oxidation

Makaram *et al.* observed physical degradation for the device stressed below the critical voltage [14]. They stressed the device under OFF-state condition V_{GS} = -7 V and V_{DS} sweep from 8 to 50 V at 150°C. It was found that the critical voltage of the device was around 20 V. After electrical stressing, the metallization layer and SiN passivation were removed using chemical etching method. SiN passivation layer was removed using HF etch (1: 10 HF: H_2O) and metallization layer was removed using aqua regia (3:1 HCl: HNO_3) at 80°C for 20 minutes. After that, the device surface was cleaned with piranha solution (H_2SO_4:H_2O_2) for 5 minutes at 115°C. The physical degradation was analyzed using atomic force microscope (AFM).

Figure 2.4 shows the physical degradation evolution for devices stressed at different V_{DG}, V_{GS} = -7 V at 150°C. V-shaped groove at the gate edge extending the entire length device starting from V_{DG} = 15 V and the groove got wider and deeper as V_{DG} increases (Figure 2.4b-e). No groove was observed in the unstressed device (Figure 2.4a) which suggests that the groove was caused by electrical stressing. The groove was observed at V_{DG} = 15 V (Figure 2.4b) which was lower than the critical voltage (V_{DG} = 20 V). This suggests that

there is another mechanism that causes the degradation and it is not inverse-piezoelectric mechanism. They suggested electro-chemical oxidation as an alternative degradation mechanism [14].

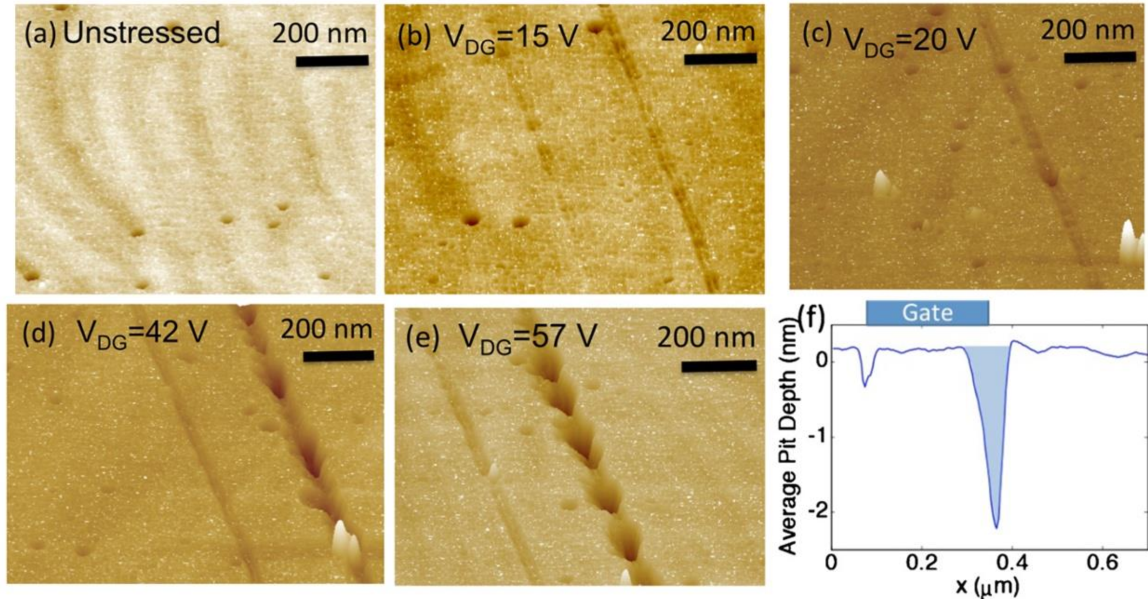

Figure 2.4 Pit/groove evolutions at (a) unstressed, $V_{DGstress}$ = (b) 15 V (below critical voltage), (c) 20 V, (d) 42 V, (e) 57 V and (f) average AFM depth profile over a gate width of 2 μm for $V_{DGstress}$ = 57 V at T_{Base} = 150°C [14]

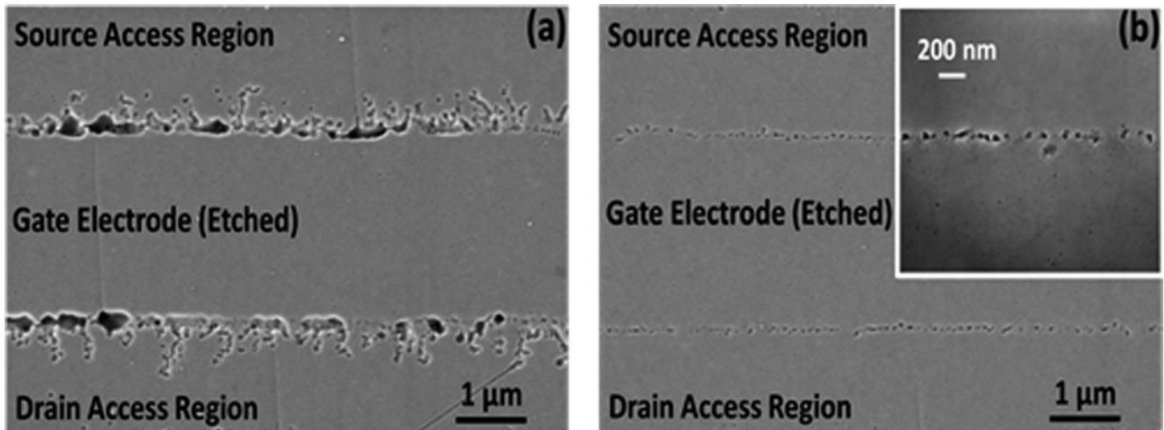

Figure 2.5 Top-view SEM images of the devices stressed under OFF-state condition V_{DS} = 0 V and V_{GS} = -40 V for 100 minutes in (a) ambient air and (b) vacuum of 3 × 10^{-5} Torr after metallization layer removal [15]

Feng *et al.* followed up to investigate the electro-chemical oxidation mechanism [15, 16]. Figure 2.5 shows the top-view SEM images of the devices stressed under OFF-state

condition V_{DS} = 0 V and V_{GS} = -40 V for 100 minutes in ambient and vacuum (3×10^{-5} Torr) after metallization layer removal. It was observed that the device stressed in ambient air showed larger pits at the gate edges as compared to the device stressed under vacuum. They suggested that oxygen in the ambient air led to larger degradation pit [15]. The smaller pits formed for the device stressed in vacuum might be due to native oxygen on GaN cap surface [83-87].

Feng *et al.* proposed an OFF-state degradation model based on electro-chemical oxidation mechanism [16], as illustrated in Figure 2.6. Oxygen, in the form of water vapor, penetrates through the silicon nitride passivation layer. Upon reaching the AlGaN surface at the gate edge, the oxygen reacts with electrons from the gate to form oxygen ions. These ions oxidize AlGaN in the presence of holes generated from inter-band tunneling in AlGaN/GaN HEMT to form pits. The pits are formed preferably at threading dislocations as the energy required for the pit formation is reduced at dislocations [36, 75, 88]. They also pointed out that the pits formed by electro-chemical oxidation correlated well with I_{D-max} degradation but not with I_G [16]. This might be because I_G degradation has a different mechanism as I_{D-max} degradation [87, 89-91].

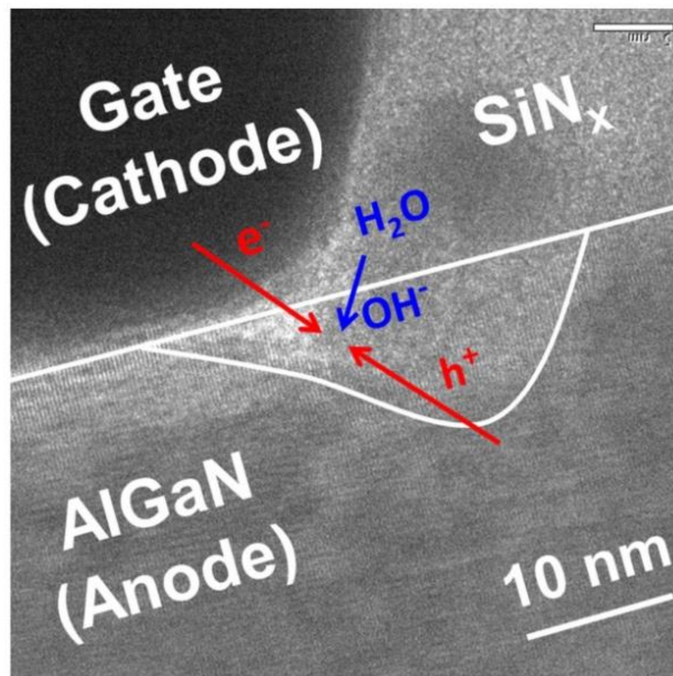

Figure 2.6 Degradation pit formation at the gate edge of the drain side by electro-chemical oxidation mechanism under OFF-state condition [16]

2.2.3 Percolation Path Mechanism

Marcon *et al.* and Meneghini *et al.* also found that AlGaN/GaN HEMT degradation occurred below critical voltage when the device is stressed for a long time under OFF-state condition [17, 92]. This OFF-state degradation is characterized by an increase in I_G. Figure 2.7 shows I_G over time for the device stressed at V_{DS} = 0 V and V_{GS} = -30 V. The critical voltage for this particular device is V_{GS} = -35 V. This result suggests that a device stressed below critical voltage will degrade if it is stressed for a long time. Therefore, inverse piezoelectric mechanism cannot explain the degradation.

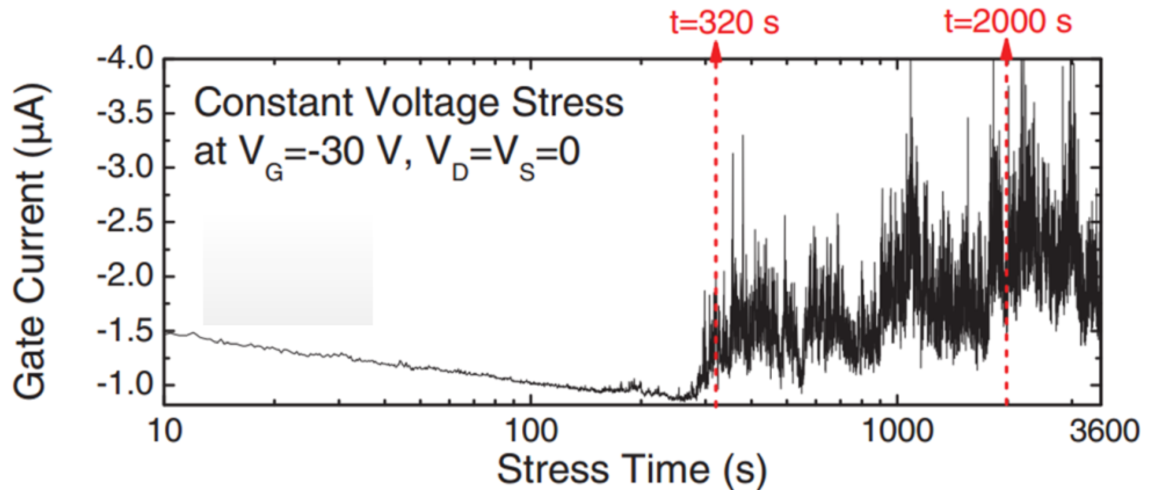

Figure 2.7 I_G evolution over time for the device stressed under OFF-state condition $V_D = V_S$ = 0 V and V_{GS} = -30 V (below critical voltage = -35 V) [17]

Figure 2.8 shows electroluminescence (EL) measurements for the same device shown in Figure 2.7. It was observed that hot spots appeared after the stressing and the number of hot spot increased over time. The number of hot spot correlates well with the I_G increase [17, 19, 89, 92, 93].

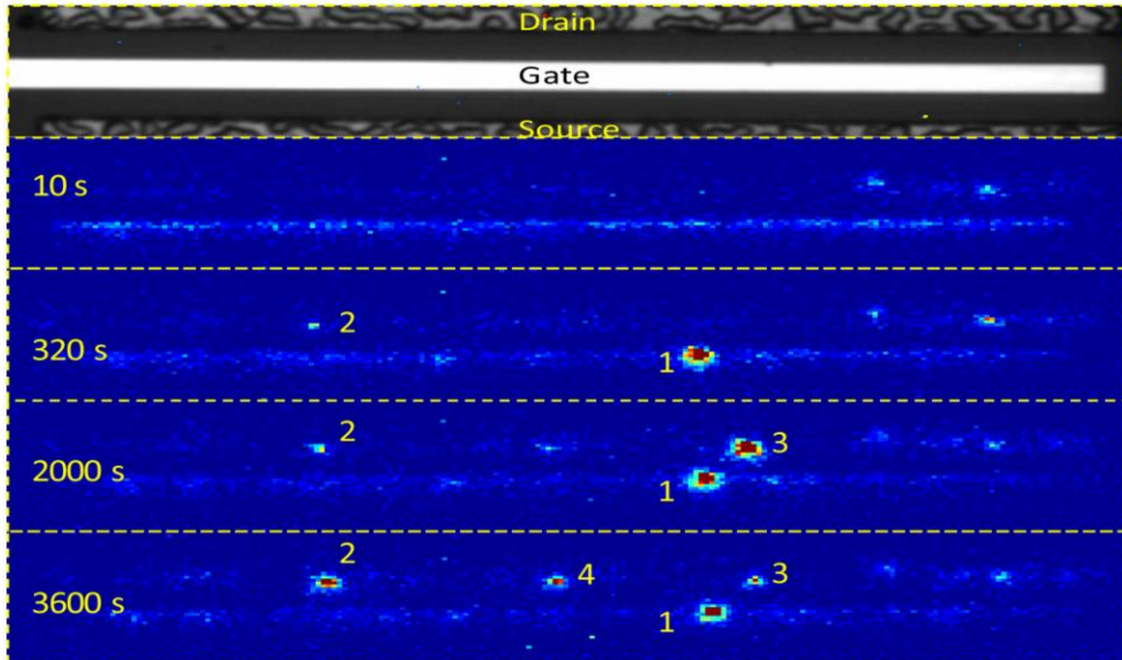

Figure 2.8 Electroluminescence (EL) measurements at different stressing time for the device stressed under OFF-state condition $V_D = V_S = 0$ V and $V_{GS} = -30$ V (below critical voltage = -35 V) [17]

Figure 2.8 shows electroluminescence (EL) measurements for the same device shown in Figure 2.7. It was observed that hot spots appeared after the stressing and the number of hot spot increased over time. The number of hot spot correlates well with the I_G increase [17, 19, 89, 92, 93].

Bajo *et al.* did microstructure characterization on the stressed devices. Figure 2.9 shows the microstructure characterization of the device stressed under OFF-state condition V_{GS} = -15 V, V_{DS} = 40 V for 4 minutes. Figure 2.9a shows the EL measurement before metallization and passivation layer removal. Figure 2.9b-d shows the top-view AFM images of the stressed device after metallization and passivation layer removal and Figure 2.9e shows the depth profile of the pit shown in Figure 2.9d. The result showed that there is a correlation between hot spot and big degradation pit. Conductive AFM measurement showed that these pits were current leakage path [18].

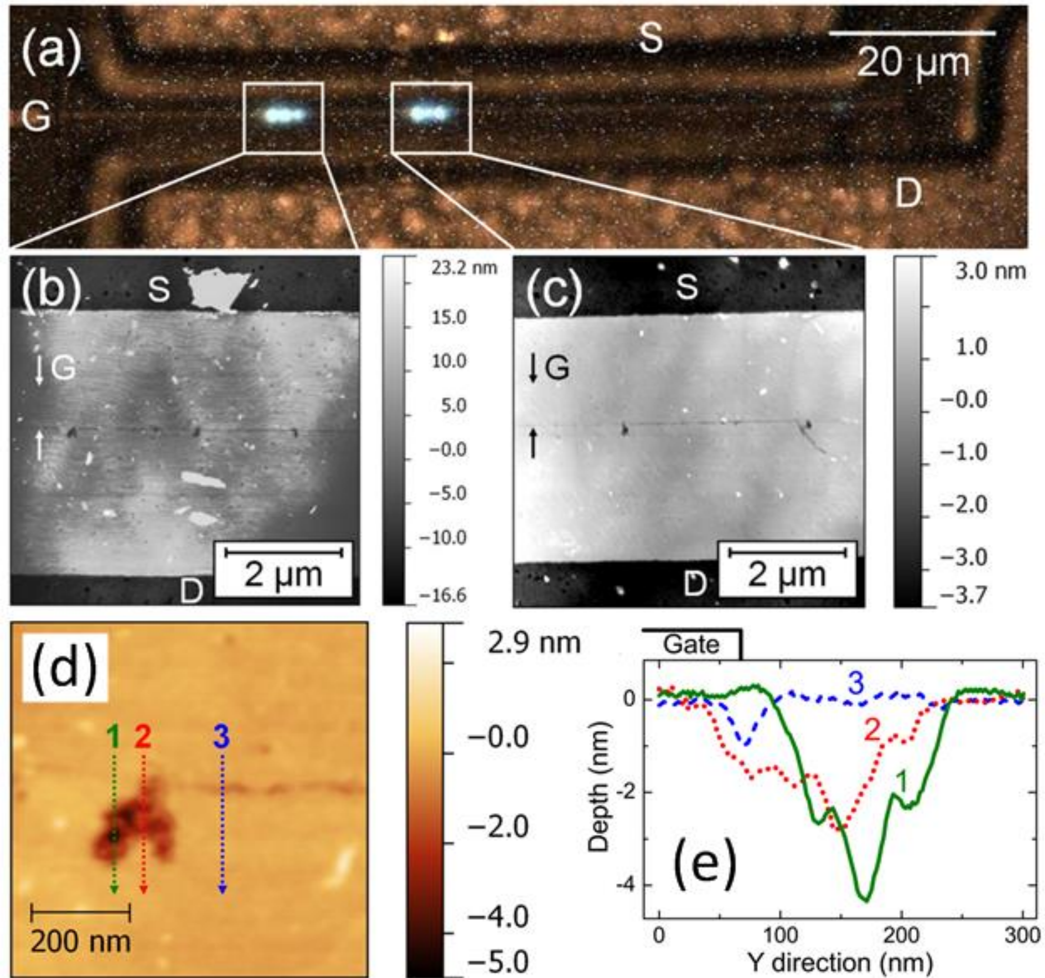

Figure 2.9 (a) Electroluminescence image of OFF-state stressed device V_{GS} = -15 V, V_{DS} = 40 V for 4 mins, (b) and (c) AFM images for the areas inside the squares after metallization and passivation layer removal; (d) zoomed in version of one of the pit at (b) and (e) the depth profile of the pit along the 3 lines in (d) [18]

Meneghini *et al.* proposed a degradation model based on percolation path mechanism [17]. Figure 2.10 illustrates the percolation path model. Defects with activation energy of 0.5 eV were generated within AlGaN layer when the device was stressed under OFF-state condition [94]. Defects start to form at the gate side of AlGaN (Figure 2.10a) and extend across AlGaN layer as stressing time increases. When the defects reach AlGaN/GaN interface, a percolation path is formed (Figure 2.10b). This string of defects across AlGaN layer provides a conductive path which leads to sudden increase in I_G (Figure 2.7). This location will then appear as a hot spot in EL measurement and correlate with a large pit. The time at which I_G suddenly increases is called breakdown time (t_{BD}). It is worth noting

that the pits at hot spots are scarcer but bigger size compared to the pits for $I_{D\text{-}max}$ degradation under similar bias condition. This suggests there are two different mechanisms for the pit formation.

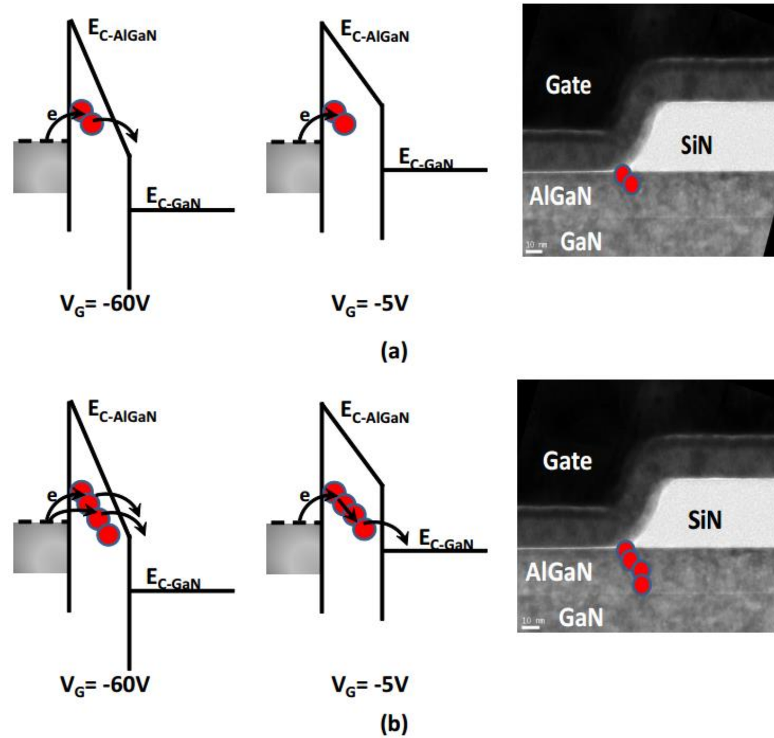

Figure 2.10 Percolation path degradation mechanism at (a) $t < t_{BD}$ and (b) $t > t_{BD}$ [19]

2.3 ON-State Reliability

During ON-state operation, drain current (I_D) at 2DEG channel flows from drain to source terminal and the energetic electrons will flow in the opposite direction. These energetic electrons in 2DEG may cause degradation during ON-state operation. Unfortunately, ON-state reliability is not as well reported as OFF-state reliability. In this section, previous studies on ON-state reliability will be reviewed.

2.3.1 Hot Electron Degradation

Sozza *et al.* stressed AlGaN/GaN HEMT on SiC substrate under constant power dissipation at 6 W/mm (V_{DS} = 25 V) at ambient temperature of 100°C, 120°C and 140°C for 3000 hours [95]. They observed that $I_{D\text{-}max}$ decreased over time. This phenomenon was also observed in AlGaN/GaN HEMT grown on Si substrate [21, 96]. They attributed this degradation to hot electrons degradation [95, 97]. Meneghini *et al.* used electroluminescence (EL) to characterize the hot electron degradation [20]. Figure 2.11a shows the EL vs. gate voltage curves at different time for the device stressed under ON-state condition V_{DS} = 30 V and V_{GS} = -1 V.

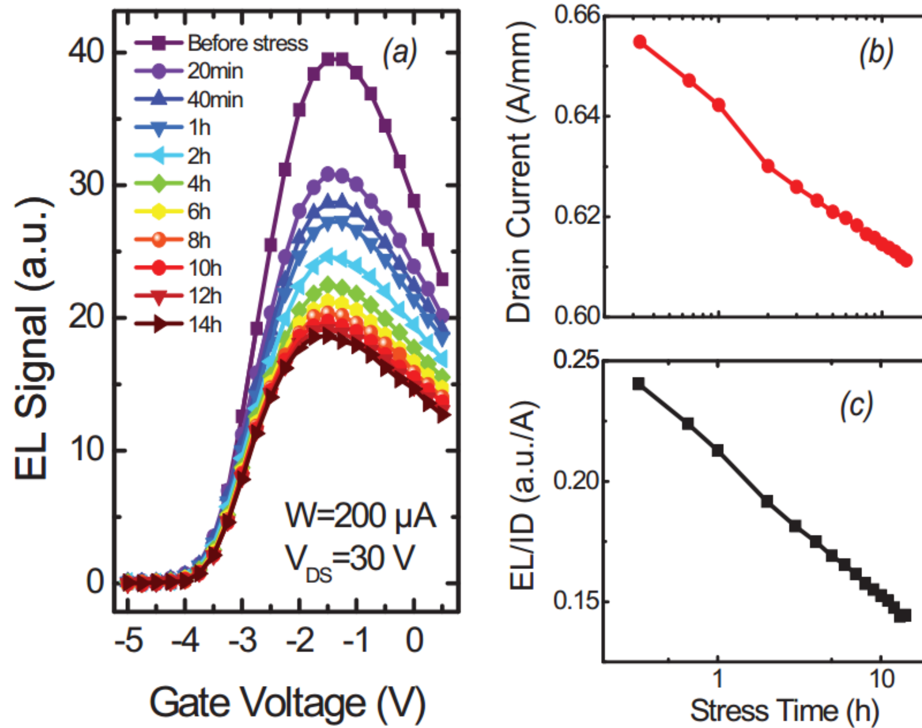

Figure 2.11 (a) EL vs gate voltage plots at different stressing time for a device stressed at V_{DS} = 30 V and V_{GS} = -1 V. (b) Drain current and (c) EL/drain current ratio measured on the same device over time [20]

The amplitude of EL signal is dependent on the magnitude of electric field and the concentration of electrons in 2DEG channel. The EL signal increased beyond threshold voltage because of increasing number of hot electrons in the 2DEG channel. However, at

higher gate voltages, EL signal decreased because of decreasing electric field [20]. Figure 2.11c shows the EL/I_D ratio over time. This ratio gives a qualitative measure of electric field in the channel [98]. EL/I_D ratio decreased over time and this correlated well with I_D degradation (Figure 2.11b). This suggests that ON-state stressing leads to decrease in electric field.

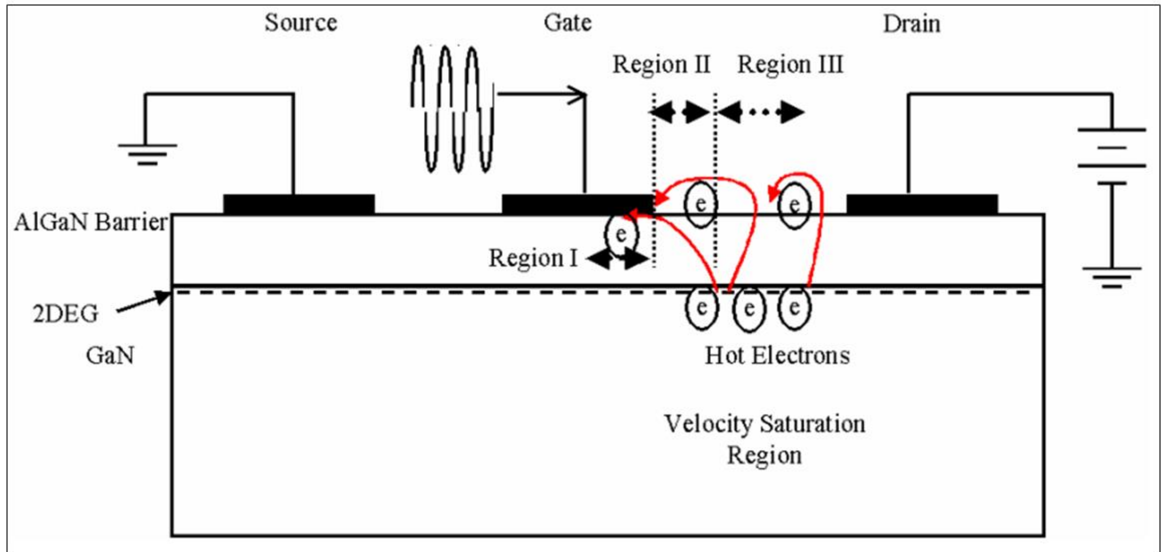

Figure 2.12 Hot electron trapping mechanism in AlGaN/GaN HEMT surface under ON-state condition [21]

Figure 2.12 illustrates the hot electron trapping in AlGaN/GaN HEMT surface during ON-state operation. Meneghini *et al.* and Pavlidis *et al.* proposed an ON-state degradation mechanism based on hot electron trapping [20, 21]. During ON-state stressing, electrons in 2DEG channel are accelerated at the drain-gate access region due to the high electric field at this region. These hot electrons can be injected into AlGaN layer, AlGaN/SiN interface or SiN layers and trapped there. As a result, less electrons are available in the 2DEG channel. These trapped electrons also act as virtual gate at the drain-gate access region which repels electrons away from 2DEG channel. Therefore, I_D will decrease. Anand *et al.* reported six different trap activation energies for AlGaN/GaN HEMT on Si stressed under ON-state condition i.e. 0.44 eV, 0.51 eV, 0.54 eV, 0.58 eV, 0.65 eV and 0.73 eV [99]. However, there is no microstructure evidence which can be related to this degradation mechanism.

2.3.2 Electro-Chemical Oxidation

Park *et al.* also did ON-state reliability study for AlGaN/GaN HEMT grown on SiC substrate [22]. They stressed the device under ON-state condition V_{DS} = 40 V and $I_{D\text{-}initial}$ = 250 mA/mm at base temperature of 82°C, 112°C and 142°C for 250 hours. $I_{D\text{-}max}$ was measured every hour at V_{DS} = 5 V and V_{GS} = 1 V.

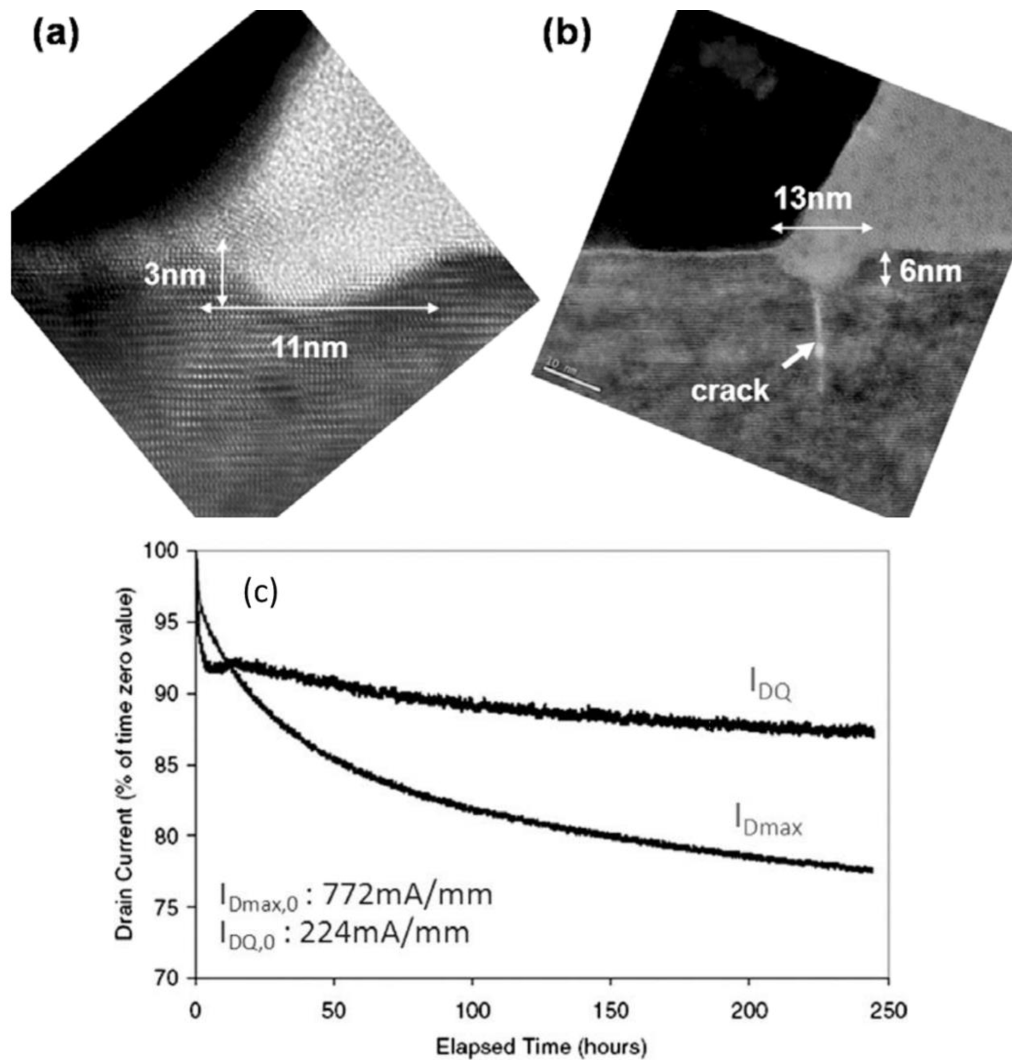

Figure 2.13 Cross-sectional TEM images for devices with (a) 19% and (b) 58% $I_{D\text{-}max}$ degradation at the gate edge on the drain side (c) Change in drain current (I_{DQ}) during stressing and $I_{D\text{-}max}$ recorded every hour for the device stressed under ON-state condition V_{DS} = 40 V and $I_{D\text{-}initial}$ = 250 mA/mm over time [22]

Figure 2.13a and 2.13b show the cross-sectional TEM images for the devices with 19% and 58% $I_{D\text{-}max}$ degradation, respectively. Figure 2.13c shows the evolution in drain current

(I_{DQ}) and $I_{D\text{-}max}$ over time for the ON-state stressed device. Pit was found at the gate edge on the drain side and the size of the pit correlated with $I_{D\text{-}max}$ degradation. However, this may not represent the whole width of the device because the cross-sectional TEM images are too localized.

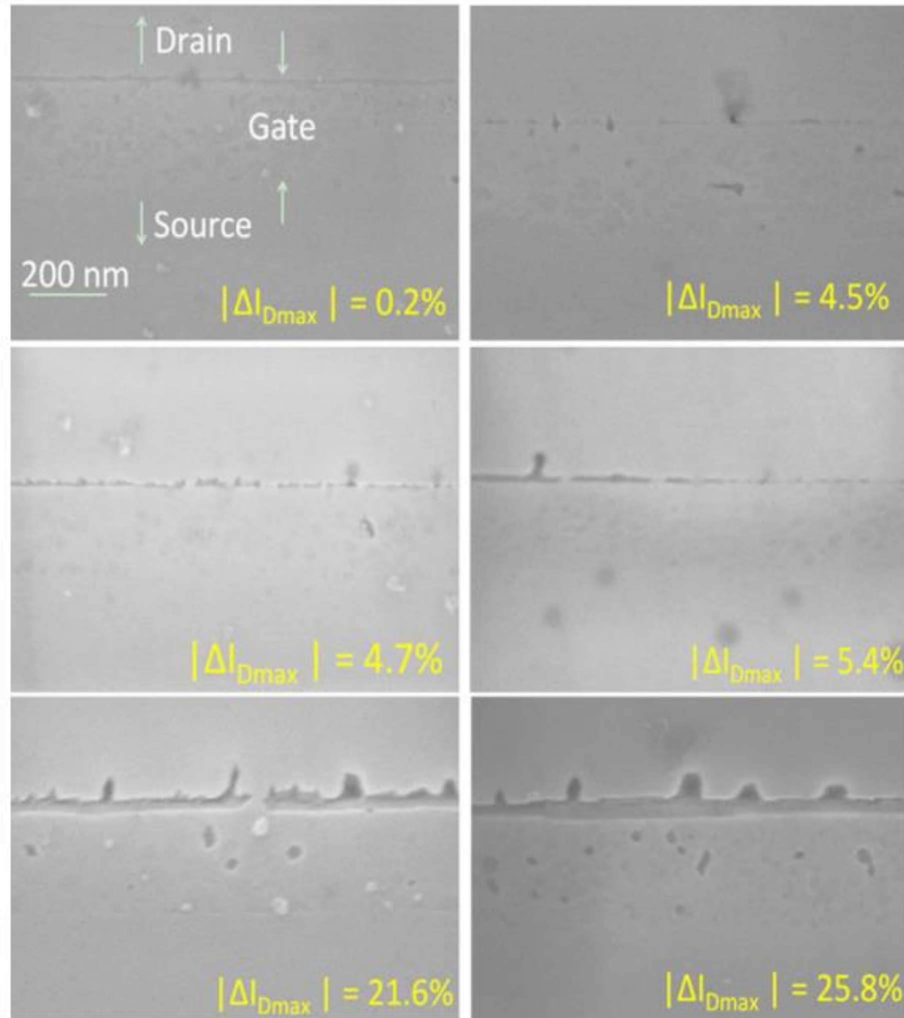

Figure 2.14 Top-view SEM images for the devices stressed under V_{DS} = 40 or 50 V and I_{DQ} = 100 mA/mm with different $I_{D\text{-}max}$ degradation levels after metallization and passivation layer removal [23]

Figure 2.14 shows the top-view SEM images for devices stressed under ON-state condition V_{DS} = 40 or 50 V and I_{DQ} = 100 mA/mm with different $I_{D\text{-}max}$ degradation levels after metallization and passivation layer removal by Wu *et al.* [23]. Pits/grooves were observed at the gate edge on the drain side of the device and their size correlated with $I_{D\text{-}max}$

degradation. The physical degradation was found across the gate width. This supports the study by Park *et al.* [22]. In addition, Wu *et al.* also observed eroded portion of AlGaN under the gate, which originated from the fabrication process and enhanced during electrical stressing [23].

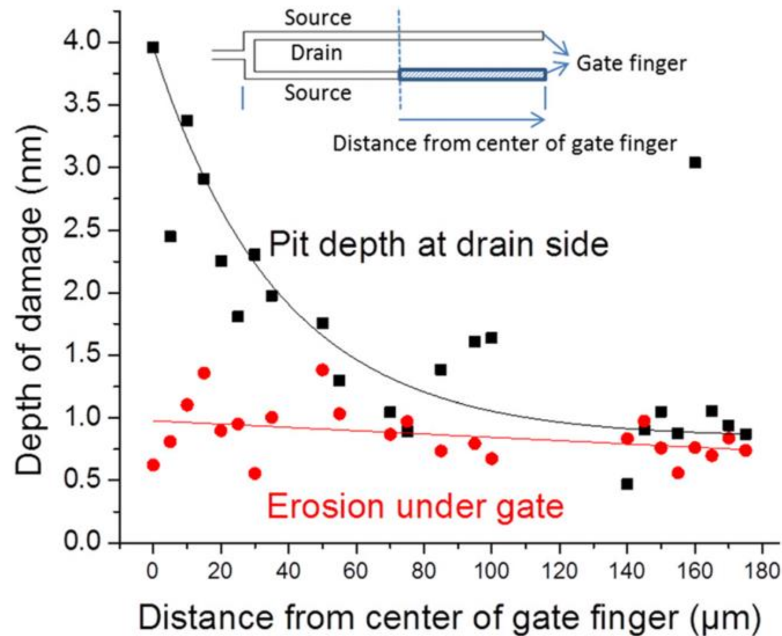

Figure 2.15 Distribution of pit/trench depth at the gate edge on the drain side and erosion depth under the gate along half of the gate width for device with 21.6% $I_{D\text{-}max}$ degradation [23]

Figure 2.15 shows the distribution of pit/trench depth and erosion depth along half of the gate width for a device stressed under ON-state condition with 21.6% $I_{D\text{-}max}$ degradation. The pit size became smaller for location further from the center of gate finger because of better heat dissipation at this location. On the other hand, erosion under the gate showed no correlation with distance from center of gate finger. This suggests that pit formation is a thermally activated process [22, 77, 100].

Figure 2.16 shows the cross-sectional TEM image for a degraded device and EDX results at point A (inside the pit) and point B (in the normal AlGaN surface). Oxygen, silicon and carbon were found in the pit. This suggests that oxidation could have occurred during the ON-state degradation and the pit was filled with SiN passivation material. Wu *et al.* proposed that ON-state degradation mechanism is similar to electro-chemical oxidation in

OFF-state degradation with activation energy ranging between 0.83 eV and 1.04 eV [101]. It is worth noting that the I_{D-max} degradation does not correlate with I_{G-leak} degradation in this ON-state study.

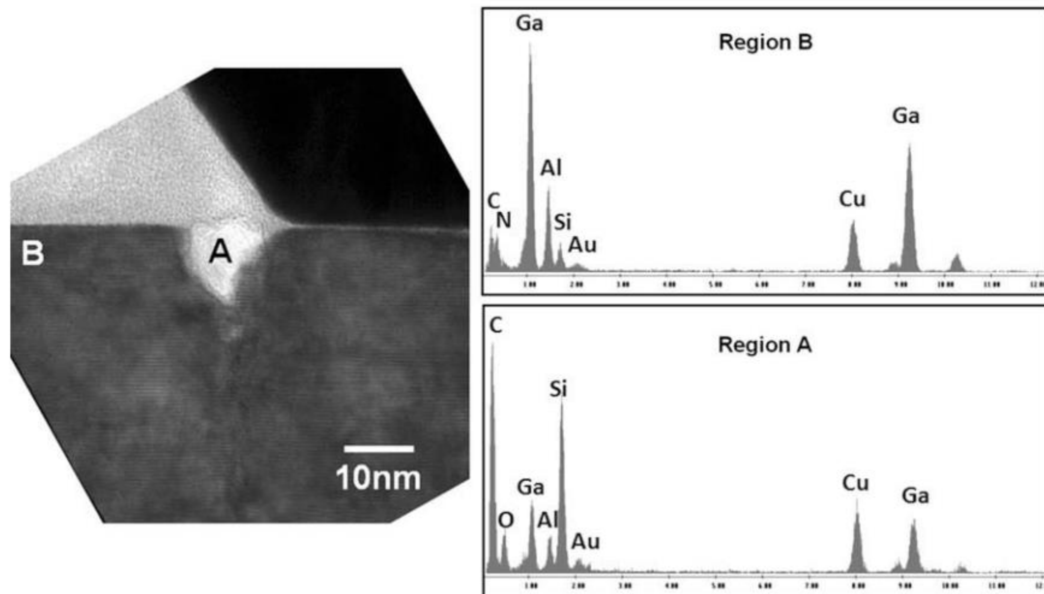

Figure 2.16 Cross-sectional TEM image of the device stressed under ON-state and EDX results at point A and B [22]

2.3.3 Ohmic Contact Degradation

A typical Ohmic contact in AlGaN/GaN HEMT is formed by rapid thermal annealing (RTA) of Ti/Al/Ni/Au metal stacks because of its low Ohmic resistance [102-105]. This is important for device with low sheet resistance (R_{sh}) like AlGaN/GaN HEMT because high contact resistance will limit its extrinsic gain and current density. Also, the Ohmic contact has to be stable as AlGaN/GaN HEMT is commonly used in high temperature applications because of its wide energy band-gap. Therefore, it is important to understand the Ohmic contact degradation under high temperature which will be discussed in this sub-section.

Dong *et al.* investigated the Ohmic contact degradation using circular transmission line model (CTLM). The CTLM structures were stressed under 400, 500 and 600°C in pure N_2

atmosphere for 120 h without any bias [24]. I-V characteristics of the Ohmic contacts were measured periodically during the thermal stressing. Total resistance of the Ohmic contacts were relatively stable after 120-h stressing under 400 and 500°C which shows that there is no Ohmic contact degradation. However, for contacts stressed under 600°C, the total resistance increased from 15 Ω to 80 Ω after the first 24 hours.

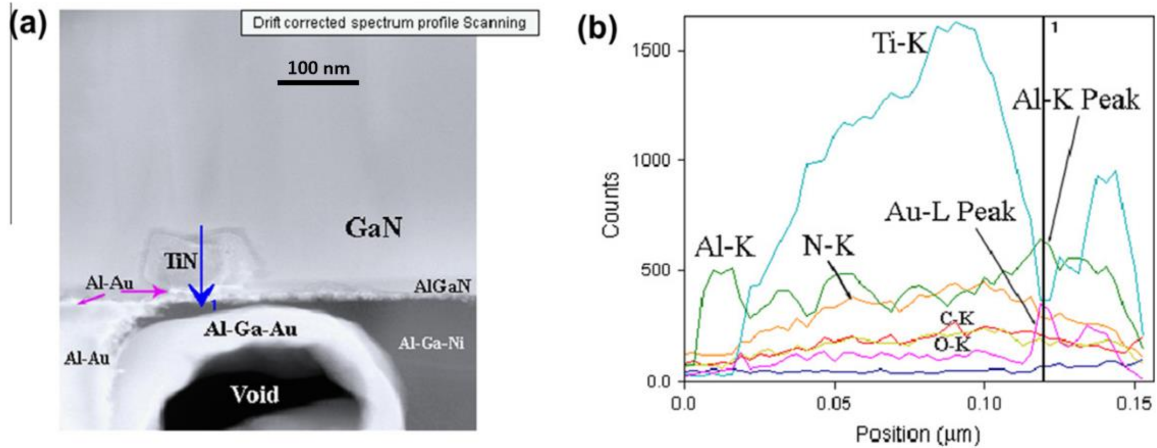

Figure 2.17 (a) Cross-sectional TEM image of the degraded Ohmic contact showing a void with Al-Ga-Au allow surrounding it and layer of Al-Au penetrating AlGaN layer; (b) EDX line scan from blue arrow in (a) [24]

Figure 2.17a and b shows cross-sectional TEM and the EDX line scan of the blue arrow in Figure 2.17a, respectively for the degraded Ohmic contact after being stressed under 600°C for 24 hours. A void surrounded by Al-Ga-Au was found at the contact area and Al-Au was observed at the AlGaN layer on top of the TiN area. The author proposed that the Al-Au melts when the device is thermally stressed at 600°C because 525°C is the lowest eutectic temperature in Al-Au phase diagram. After the Al-Au alloy melts, it penetrated the AlGaN layer which leads to decreasing 2DEG density and increasing contact resistance. As Al-Au penetrates the AlGaN layer, void is formed at the contact area and Ga out diffuses into the Ohmic contact area. This explains the presence of Ga surrounding the void in the Ohmic contact area in Figure 2.17a.

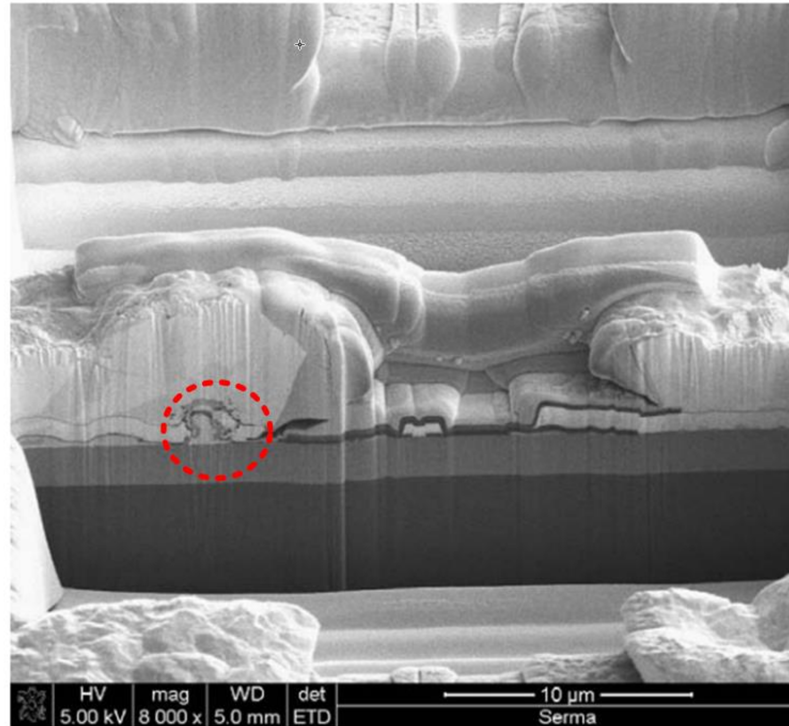

Figure 2.18 Cross-sectional SEM image shows extrusion of Au-Al IMC (red circle) in degraded Ohmic contact for a device stressed under DC condition V_{DS} = 50 V, I_{DS} 50 mA/mm and $T_{junction}$ = 275°C for 2000 hours [25]

Piazza *et al.* reported Ohmic contact degradation occurred even for devices thermally stressed at 340°C for 2000 hours. They also proposed Ga out-diffusion and Au inter-diffusion as the degradation mechanism [25]. The same author observed Ohmic contact degradation in the actual device stressed under DC condition V_{DS} = 50 V, I_{DS} = 50 mA/mm and estimated $T_{junction}$ = 275°C for 2000 hours. There was local extrusion of Au-Al inter-metallic compound (IMC) observed in cross-sectional SEM picture (Figure 2.18) [25]. Wu *et al.* who did DC stressing on Au-free Ohmic contact, proposed that there is nitrogen out-diffusion from TiN or Si_3N_4 passivation into the Ohmic metal which causes increase in contact resistance [106].

2.4 Thesis in Context to Knowledge Gaps

The literature review shows that extensive study has been done for OFF-state reliability. For OFF-state reliability, it was found that the physical defect formation depends on various factors such as applied voltage [81], threading dislocation [75, 76], environment [15], and stressing duration [78]. Several mechanisms have been proposed to explain the OFF-state degradation such as inverse piezoelectric [13], electro-chemical oxidation [16] and percolation path-induced degradation [17].

Unlike OFF-state reliability study, ON-state reliability study is not readily available. Sozza *et al.* and Meneghini *et al*. correlated $I_{D\text{-}max}$ degradation with hot electron trapping on the surface at the drain-gate access region [20, 97]. EL was used to characterize ON-state degradation and Anand *et al.* proposed six different trap activation energies [99]. However, there is no clear connection between the hot electrons and 2DEG electrons. This thesis will discuss the role of current flow in 2DEG channel and provide physical evidence of ON-state degradation.

Wu *et al.* found that ON-state stressing led to pit formation at the gate edge on drain side of the device. The pit formation is a thermally activated process with activation energy ranging between 0.83 eV and 1.04 eV [100, 101]. They proposed that the ON-state degradation mechanism is the same as that of OFF-state degradation mechanism proposed by Feng *et al.* i.e. electro-chemical oxidation. However, this study did not show a direct comparison between ON-state and OFF-state degradations. Also, this study was done using AlGaN/GaN HEMT on SiC devices [22, 23, 77]. Sasangka *et al.* reported the correlation between threading dislocation and pit formation for OFF-state degradation in AlGaN/GaN HEMT on Si [75]. This correlation may not be readily observed in SiC substrate as AlGaN/GaN HEMT on SiC has 1 to 2 order lower threading dislocation density than AlGaN/GaN HEMT on Si [1, 7]. This correlation might lead to different results for ON-state degradation in AlGaN/GaN HEMT on Si devices. This thesis will compare OFF-state and ON-state directly and all the devices used in this thesis are grown on (111) Si substrate.

Chapter 3

Experimental Methodology

Reliability study of AlGaN/GaN high electron mobility transistor (HEMT) on Si requires two stages of experiments. The first part is stressing the device under various accelerated conditions and the second part is the failure analysis. AlGaN/GaN HEMT device is electrically stressed and its characteristics such as maximum drain current ($I_{D\text{-}max}$), gate leakage current ($I_{G\text{-}leak}$) and threshold voltage (V_{TH}) are monitored. After electrical stressing, the device is then analyzed using various failure analysis techniques in order to understand the degradation mechanism and develop a reliability model to estimate the lifetime of the device. This chapter starts with description of the devices used in this study. Then, the working principle and theory behind all the tools and techniques used for electrical stressing and failure analysis are describe and discussed.

3.1 Device Description

AlGaN/GaN HEMT devices used in the study are grown on Si (111) substrate by metal-organic chemical vapor deposition (MOCVD) [107]. The GaN used in this study is Ga-polar film. Figure 3.1 shows the cross-section schematics of the AlGaN/GaN HEMT on Si device. First AlN/GaN superlattice is grown on Si (111) substrate to reduce the stress due to the large lattice mismatch between AlGaN/GaN and Si [108]. (111) Si is commonly used for GaN epitaxy because it has trigonal symmetry which supports the epitaxial growth of (0001) GaN [3]. This superlattice consists of alternating AlN (7 nm) and GaN (18 nm) with total thickness of 1.54 µm. The next layers are the GaN buffer, AlGaN barrier and GaN capping layer with thickness of 840 nm, 18 nm and 2 nm, respectively. GaN capping layer is used to improve the device performance [109, 110]. This capping layer has to be kept thin because thick capping layer can decrease the 2DEG density [111].

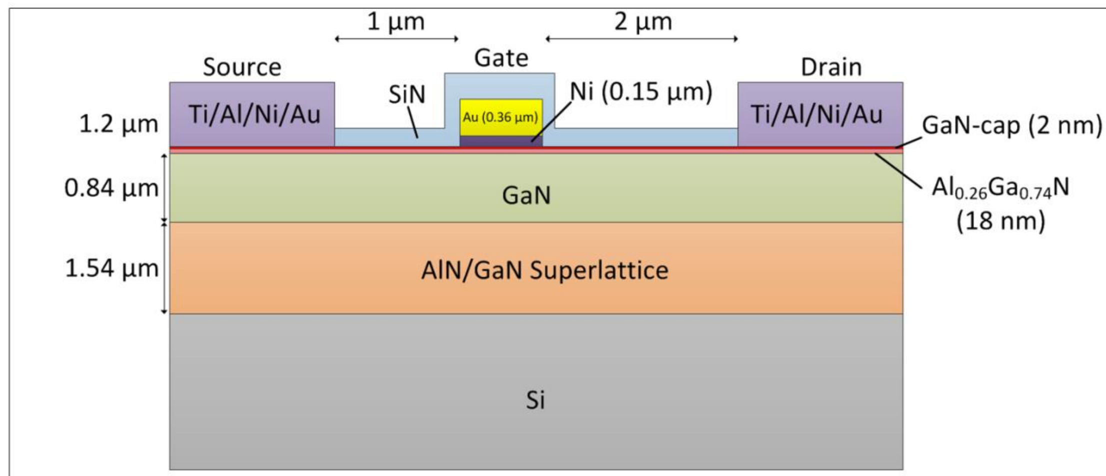

Figure 3.1 Cross-sectional schematics of AlGaN/GaN HEMT on Si device

After the epitaxy growth, the device goes through fabrication process. The Schottky gate length of device is 2-µm and it consists of 0.15 µm-thick Ni and 0.36 µm-thick Au. The ohmic contacts at drain and source side are made of Ti/Al/Ni/Au (20/120/40/50 nm) which was annealed at 825°C for 30 s with a contact resistance of R_c = 0.12 Ω mm [107]. All of these devices are double-gate devices with L_{GD} = 2 µm, L_{SG} = 1 µm and W_G = 25 - 150 µm with no field plate as shown in Figure 3.2. Then 120-nm-thick SiN layer was deposited using plasma-enhanced chemical vapor deposition (PECVD) to passivate the devices. XRR

measurement showed that the Si:N = 43: 57 with density of 2.26 g/cm^3. These AlGaN/GaN HEMTs are Ga-polar and normally-ON devices. Only one gate is turned on during the electrical stressing. Once a gate is stressed, the other gate will not be used as it might have also degraded during the stressing.

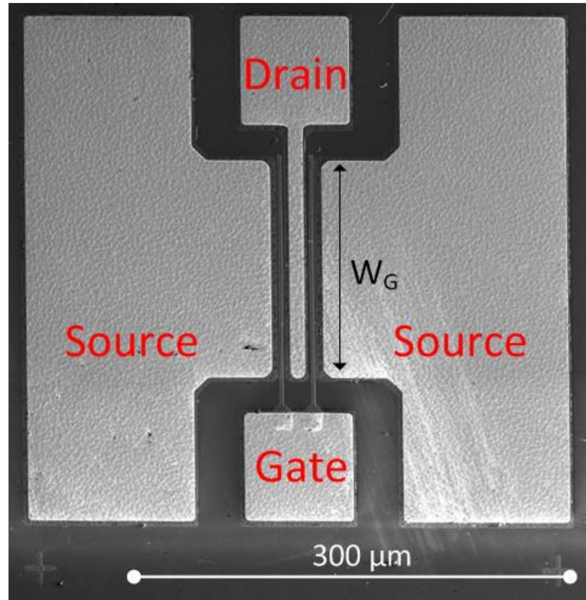

Figure 3.2 Top-view SEM image of the AlGaN/GaN HEMT

3.2 Electrical Characterization and Stressing

Electrical characterization and stressing are done using various systems in the lab. Figure 3.3 shows the probe station used to characterize and stress devices at wafer level. This probe station is connected to Keithley 4200 parameter analyzer. The stage of this probe station can be heated up to 300°C.

Secondly, an in-house built system shown in Figure 3.4a is also used to stress and characterize the devices. In this system, the tested device has to be wire-bonded to a dual in-line package (DIP) as shown in Figure 3.4b. This system is connected to Keithley 2612 source meter and the package can be heated up to 300°C. Furthermore, this system allows us to stress the device in high vacuum or high humidity conditions. The vacuum level can reach about 1×10^{-5} Torr.

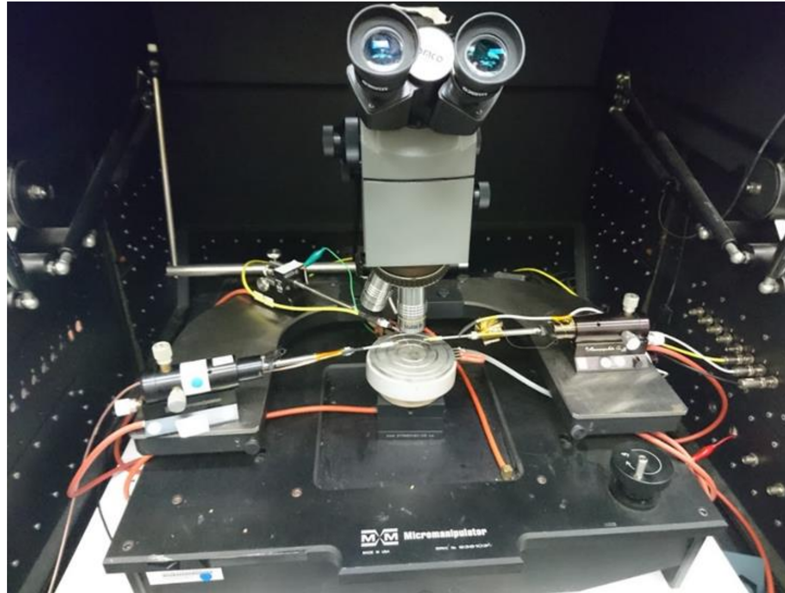

Figure 3.3 Probe station used to test and stress the device at wafer level

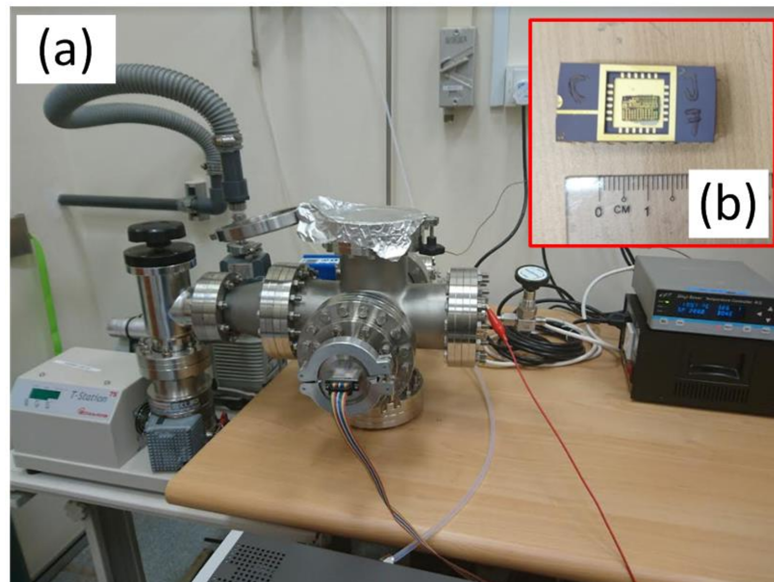

Figure 3.4 (a) In-house-built system to test and stress device under high vacuum or high humidity. (b) Wire-bonded chip to dual in-line package (DIP) used in this system

Lastly, Figure 3.5 shows the modified electromigration (EM) system that can be used to stress multiple devices at once at a maximum temperature of 300^0C. This system is connected to 32-SMU National Instrument (NI). So, 16 devices can be stressed or tested simultaneously at the same base temperature with different bias conditions. The devices have to be wire-bonded to the DIPs as well in this system.

Figure 3.5 32-SMU National Instrument modified EM system

3.2.1 Electrical Characterization

The electrical characteristics of the AlGaN/GaN HEMT can be monitored by the I-V curve. In this experiment, I_D-V_{DS} characteristic is obtained by sweeping V_{DS} from 0 V to 21 V for different V_{GS} from -4 V to 1 V at 1 V/step rate. A typical I_D-V_{DS} graph can be seen in Figure 3.6. Secondly, I_D-V_{GS} characteristic is obtained by biasing the V_{DS} at 10 V and sweeping V_{GS} from -10 V to 2 V. The drain current (I_D) and gate current (I_G) are monitored. A typical I_D-V_{GS} and I_G-V_{GS} graphs are shown in Figure 3.7. From I_D-V_{GS} graph, drain current saturation (I_{D-max}) which is a commonly used parameter to monitor the device degradation can be obtained [14, 75, 76, 81, 112, 113]. Also, drain leakage current and gate leakage current can be obtained from Figure 3.7. Some literature show that the leakage currents increase as the device degrades [17, 114, 115]. In addition, threshold voltage (V_{TH}) can be obtained by taking a linear fit of the slope portion of I_D-V_{GS} graph. These electrical characteristics are important for AlGaN/GaN HEMT reliability analysis. This transistor works in 2 different regimes, i.e. OFF- and ON-state. ON-state is the regime where there is current flowing in the 2DEG channel and when the V_{GS} is higher than V_{TH} whereas OFF-

state is the regime where no current is flowing in 2DEG channel and when the V_{GS} is lower than V_{TH} (Figure 3.7).

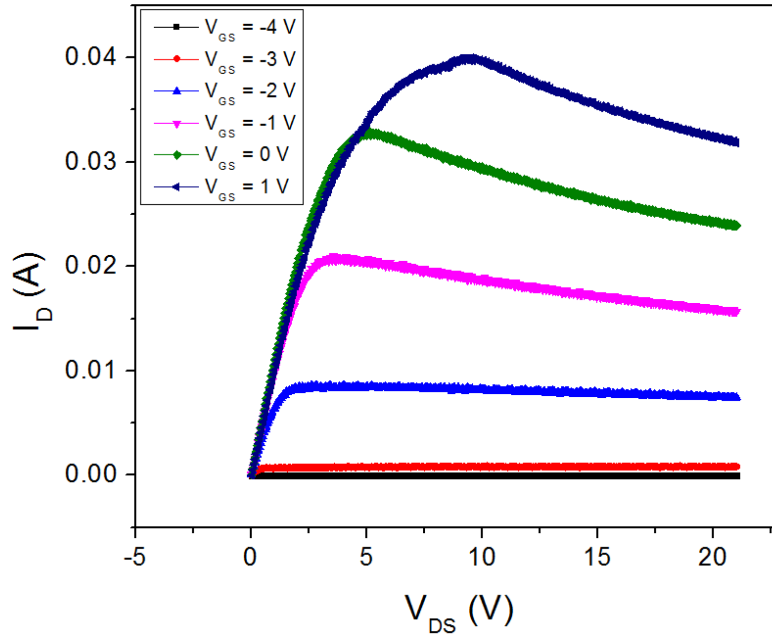

Figure 3.6 I_D-V_{DS} plot of AlGaN/GaN HEMT on Si substrate

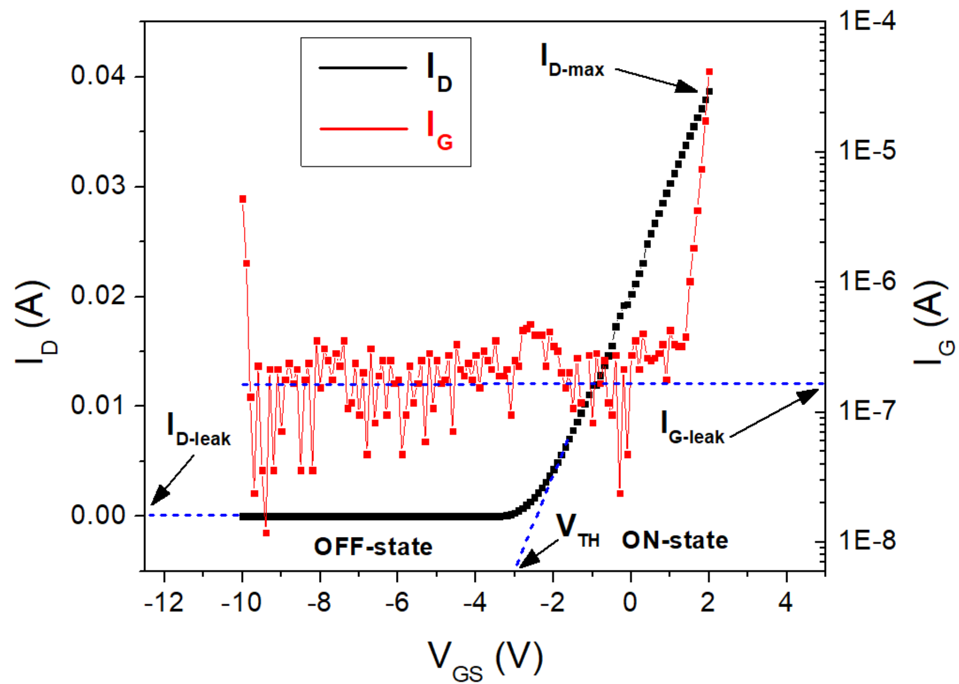

Figure 3.7 I_D-V_{GS} and I_G-V_{GS} plot of AlGaN/GaN HEMT on Si substrate

3.2.2 Electrical Stressing

AlGaN/GaN HEMT is commonly used as a switching device. It operates in both ON-state and OFF-state conditions. Since the AlGaN/GaN HEMT devices used are normally ON devices, bias needs to be applied to turn off the device, i.e. OFF-state condition. During OFF-state condition, a large negative bias is applied at the gate to repel all electrons away from the channel. Thus, there is no current flowing during OFF-state. On the other hand, during ON-state condition, the gate is biased above the threshold voltage and the current is flowing from the source to drain.

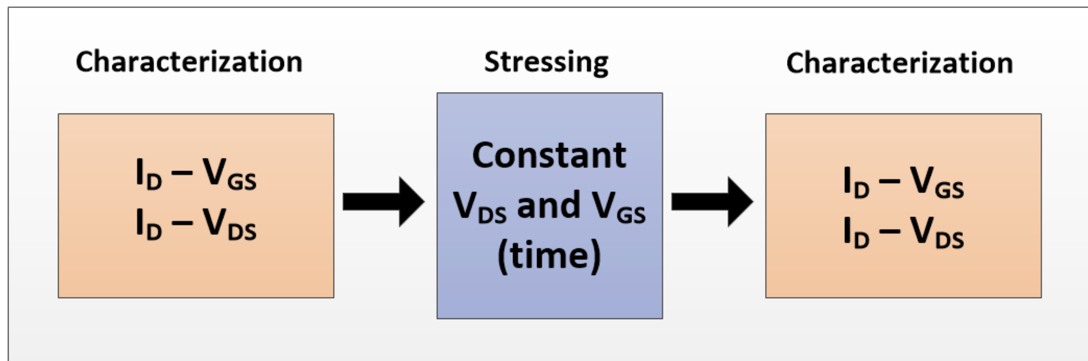

Figure 3.8 One characterization and stressing cycle during electrical stressing of AlGaN/GaN HEMT

In this experiment, devices are stressed at constant voltage condition. The stressing configuration consists of many of stressing cycles. One stressing cycle starts with a characterization step followed by stressing step and another characterization step (Figure 3.8). For example, to stress a device for 20 hours, it is split into 20 stressing cycles with 1 hour stressing time for each cycle. The device characteristics will be extracted during the characterization steps in each cycle and the device degradation will be monitored throughout the total stressing time. The characterization step used is the same step explained in section 3.2.1. The characterization and stressing steps are done at the same temperature as the stressing temperature.

The devices are stressed under various conditions depending on the requirement of the experiment. The test system used also depends on the experiment requirement as each

electrical stressing system mentioned above has unique capabilities. The details of the stressing condition will be mentioned in each chapter.

3.3 Junction Temperature Measurement

Temperature is a crucial factor in determining microelectronics reliability. Temperature causes lattice vibration and charge carrier scattering which may accelerate degradation. Under ON-state condition, the energetic electrons in 2DEG channel flow from source to drain generating drain current. The electrons will interact with the lattice atoms and generate joule heating. This joule heating will accelerate degradation. Therefore, it is important to obtain the junction temperature and the thermal distribution of the device. The thermal distribution is used to locate the hot spots on the device due to joule heating and then can be correlated to the physical degradation. In this study, the junction temperature is computed using thermal finite element simulation. This thermal model is verified by thermo-reflectance measurement.

3.3.1 Thermo-Reflectance

In this thesis, the junction temperature was obtained using thermo-reflectance method. Thermo-reflectance is a non-contact experimental technique for thermal profiling of semiconductor device surface. Thermo-reflectance offers a better spatial resolution than infrared (IR) measurement [116]. This technique is based on the change in sample’s relative reflectivity as a function of temperature change of the sample surface [117]. The change in reflectivity is directly proportional to the change in temperature of the sample [117, 118]. In this experiment, thermo-reflectance measurement was done using Microsanj NT200 thermal imaging system [119].

Figure 3.9a shows the experimental setup for thermo-reflectance. The surface of the tested device is illuminated using a light-emitting diode (LED). The reflected light is then collected through the light microscope connected to a CCD camera. The system uses blue (470 nm) LED and a 100x, NA = 0.8 microscope objective to get an optical spatial

resolution of 150 nm. A pulsing voltage is applied to generate the current which then induces joule heating. The CCD camera will capture the different reflectivity during the pulsing and translate this difference into a thermal image. The thermal image will show the distribution of change in temperature (ΔT) due to current flow, i.e. joule heating.

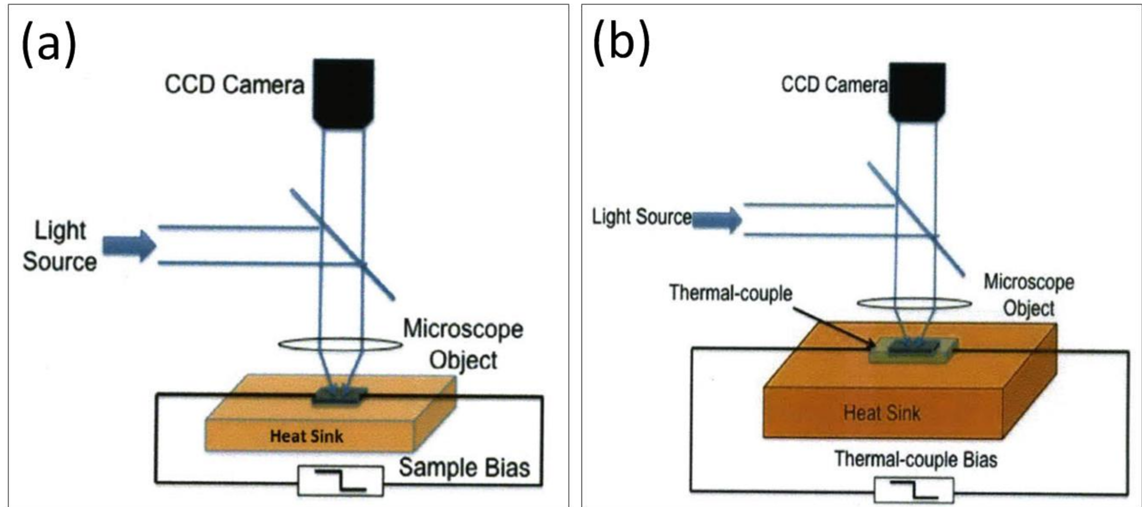

Figure 3.9 Thermo-reflectance (a) measurement setup and (b) calibration setup [26]

Thermo-reflectance coefficient is required in order to obtain an accurate thermal measurement of the device. The calibration setup is shown in Figure 3.9b. A flat GaN film is placed on the stage and connected to the small thermocouple. The stage is heated up to a certain temperature and is recorded by the thermocouple. The CCD camera obtains the thermo-reflectance amplitude on the material of interest. Then, the thermo-reflectance coefficient is obtained by dividing the thermo-reflectance amplitude by the amplitude of the temperature oscillation recorded by the thermocouple [118]. The thermo-reflectance coefficient obtained from this experiment for GaN is 1.95×10^{-4} /^{o}C.

AlGaN/GaN HEMT on Si devices with different dimension were measured at different base temperature from 25°C to 100°C. The tested device was biased at V_{DS} = 20 V and V_{GS} was used to control the drain current. The measured temperature was obtained from the thermal image. Power density is required for the input in the finite element simulation, and can be obtained by the formula below.

$$Power\ density = \frac{V_{DS} \times I_D}{L_G \times W_G \times H_G} \tag{3.1}$$

where V_{DS}, I_D, L_G, W_G and H_G are drain voltage, drain current, gate length, gate width and gate height respectively.

3.3.2 Finite Element Simulation

Finite element analysis (FEA) based thermal simulation was used to compute the junction temperature of the AlGaN/GaN HEMT during ON-state operating condition. In this experiment, the finite element simulation was done using Thermal Analysis System (TAS) by ANSYS [120].

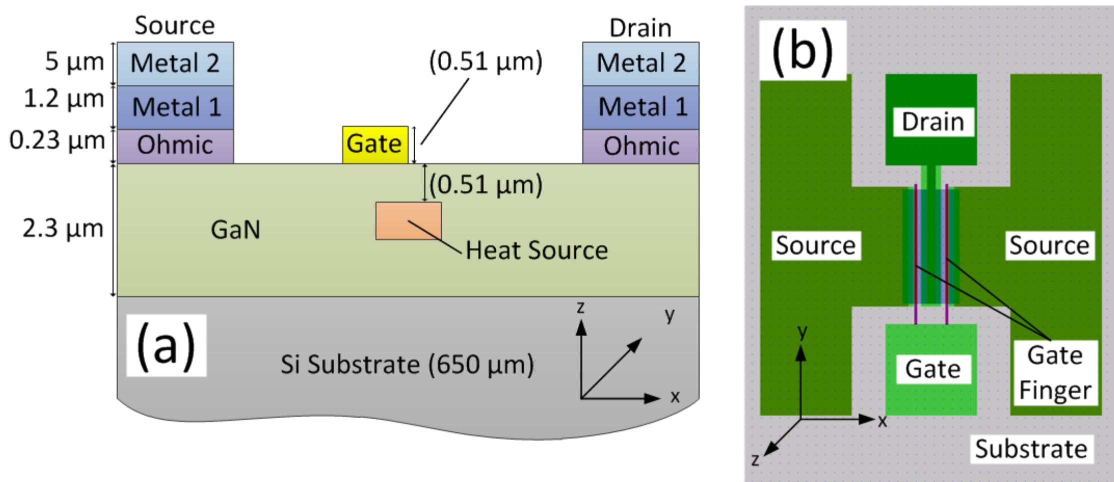

Figure 3.10 Schematics of AlGaN/GaN HEMT used for thermal finite element simulation (a) cross-sectional view at the left gate finger and (b) top-view of the whole device

Figure 3.10a shows the cross-section device geometry at the left gate finger area used in the TAS. Figure 3.10b shows the top-view of the whole device that is drawn according to the real device dimensions. Heat source is defined as a volumetric heat source which has the same dimension as the gate and located 0.51 µm under the gate edge of the drain side (Figure 3.10a) where 0.51 µm is the gate height. This location was determined during the model calibration using thermoreflectance measurement. This location has the highest electron scattering due to maximum electric field which leads to highest heat generation.

The material properties, thickness and slice count for each feature are shown in Table 3.1. Slice count is defined as the number of division through the thickness for a particular feature. This parameter is important to obtain a good mesh.

Secondly, mesh refinement was done to ensure that the mesh is sufficiently fine to get an accurate simulation reading especially around the region of interest. The auto-region option was used to ensure that there is no missing node or discontinuous feature, and then followed by polygon extrusion to make the 3D model. The extrusion was done in the negative z-direction (Figure 3.10b).

Table 3.1 Material parameters used in the thermal finite simulation

Features	Material	Thermal Conductivity (W/mK)		Thickness (μm)	Slice count
		In-plane	Through thickness		
Gate	Au	315.0		0.51	3
Metal 1	Ti/Ni/Au	259.8	110.2	1.20	7
Metal 2	Au	315.0		5.00	7
Ohmic metal	Ti/Al/Ni/Au	279.5	192.9	0.23	6
Isolation	GaN	$141.39\ (298/T)^{1.2112}$		0.15	5
GaN layer	GaN	$141.39\ (298/T)^{1.2112}$		2.30	13
Heat source	GaN	$141.39\ (298/T)^{1.2112}$		0.51	3
Si substrate	Si	$152.59\ (298/T)^{1.334}$		650.00	24

The next step is to define the thermal interface resistance between GaN layer and Si substrate. This thermal interface resistance is defined as a 0.25 μm layer with heat transfer coefficient of 3.03×10^{-5} W/^{0}C.μm^2, while the base temperature is set at the bottom of Si substrate. Lastly, the equivalence and model check steps were done to ensure that there is no missing part on the model. For each simulation, base temperature and power density for the volumetric heat source were varied. Power density was obtained from equation (3.1). In this simulation, only left side of the gate was used so that it is consistent with the electrical stressing condition.

The assumptions used in this simulation are:

- The AlGaN layers are assumed to have the same thermal properties as GaN. The Al% in AlGaN is below 30% and the AlGaN layers are relatively thinner than the other layers. Thus, this will not affect the junction temperature much. Moreover, this will reduce the simulation time as the meshing complexity will be reduced.
- The gate metal is assumed to be gold instead of gold with a thin nickel layer at the bottom. The junction temperature difference is negligible.
- The SiN passivation layer is not included in the model as the effect of this layer on the junction temperature is negligible.
- The relationship between measured and simulated junction temperatures remains the same for higher temperatures.

3.4 Electric Field Finite Element Simulation

Electric field is one of the factors that affects the AlGaN/GaN HEMT reliability [79, 115, 121, 122]. Thus, it is very important to analyze the electric field distribution on the AlGaN/GaN HEMT device during OFF- or ON-state operations. In this study, the electric field is simulated by using Silvaco Atlas device simulator [27]. Silvaco Atlas is a two- or three-dimensional device simulator which predicts the electrical behavior of semiconductor devices.

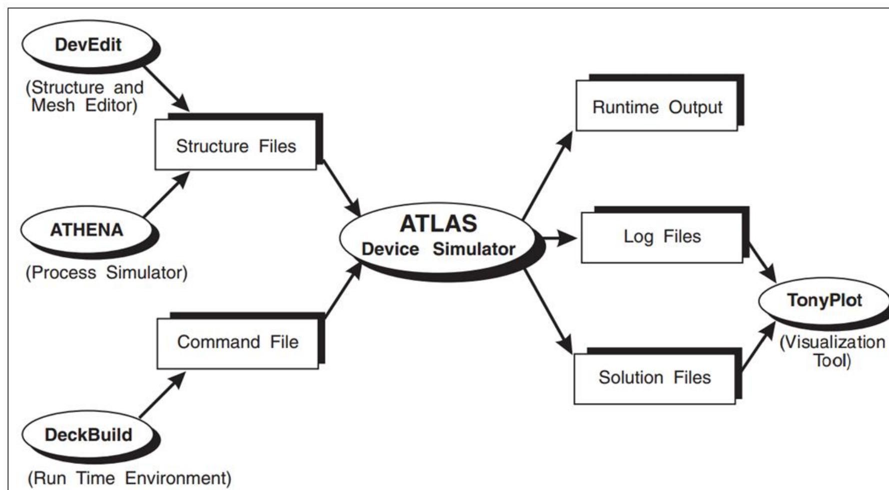

Figure 3.11 Input and output system of Silvaco Atlas device simulator [27]

Figure 3.11 shows the general simulation steps in Silvaco Atlas. There are two input files i.e. structure files and command file. Structure file contains the device structure that is going to be simulated while command file contains commands for the software to execute. The output files are run-time output, log file and solution file. Run-time output shows the simulation progress and error messages during the execution. Log file contains all terminal voltages and currents from device analysis. Lastly, solution file contains the solution values within the device structure for a given bias condition. The solution can be extracted and plotted from solution and log files using TonyPlot.

An extension of Silvaco Atlas called Blaze is needed to simulate compound semiconductors. Blaze takes into account the band structure of heterojunction which is dependent on the material composition and position of the compound semiconductors. In this study, the electric simulation of AlGaN/GaN HEMT uses one of the examples from Silvaco website. The example used is “AlGaN/GaN HEMT Id-Vgs and Id-Vds Characterization” under GANFET Application Examples section [123]. A small modification was done to extract the electric-field distribution. The following lines were added in the command file line 85,

```
solve previous
solve vgate=1
solve vsource=0
solver vdrain=20
save outf=GaN_EField.str
```

The Al composition used in the actual $Al_xGa_{1-x}N$ layer is 0.30 with thickness of 18 nm. The AlN/GaN superlattice is regarded as GaN layer in this simulation. The GaN buffer and the AlN/GaN superlattice have a total thickness of 2.2 μm. The other device dimensions (L_G, L_{GD} and L_{SG}) and bias condition are keyed according to the device used in each chapter. After all the parameters are have been entered, the script in DeckBuild is run. After it finishes, the GaN_EField.str file is opened in TonyPlot where the electric field values and distribution can be obtained.

Figure 3.12 shows a typical contour map obtained from TonyPlot. The cut-lines are then drawn at the region of interest. For example, cutline A-A’ was drawn in Figure 3.12 to extract the electron concentration at 2DEG across the device. In this thesis, the region of interest is at the device surface.

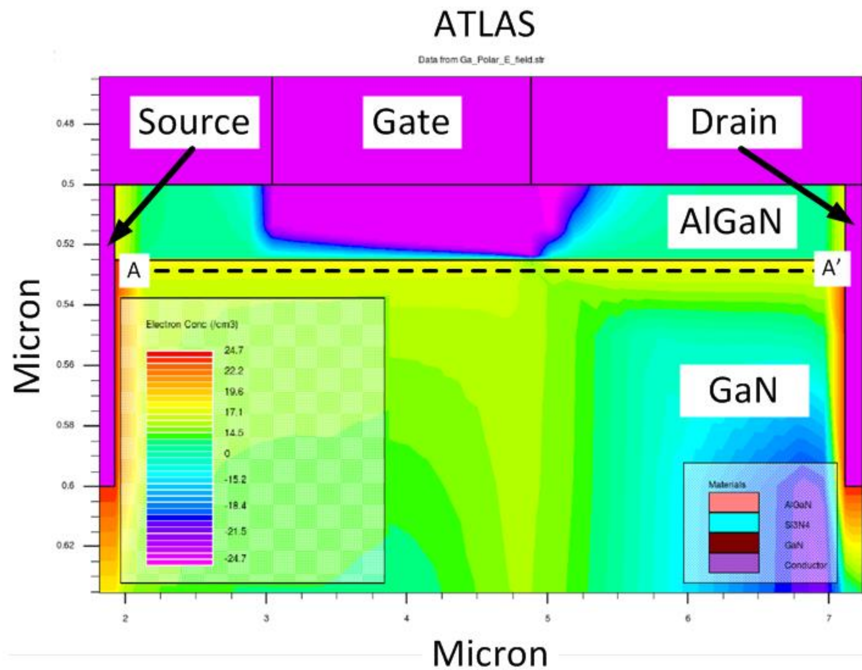

Figure 3.12 Typical contour map obtained from TonyPlot

3.5 Etching

In this thesis, most of the physical degradation observed was pit at AlGaN layer. One way to characterize this pit is using cross-sectional TEM. The drawback of using TEM is that the result is highly localized, only about 100 nm of the gate width. Therefore, another method was adopted to get a larger view, which is to use top-view analysis in SEM. However, the metallization and passivation layers have to be removed first by etching method before the pits can be seen in SEM. Furthermore, dislocation etching can also be done to calculate the threading dislocation density in the GaN layer.

3.5.1 Metal Contacts and Passivation Layer Etching

This etching technique is used to remove the metal contacts and passivation layers [14]. The Si_xN_{1-x} passivation and oxide layers were removed using isotropic reactive ion etching (RIE). The metal contacts were then removed using aqua regia (3:1 HCl : HNO_3). Finally, the surface was cleaned using isopropyl alcohol (IPA) and acetone mixture. The detailed steps are as follow:

1) Soak in IPA for 5 minutes
2) Isotropic RIE for 4 minutes
3) Soak in IPA for 5 minutes
4) Soak in aqua regia solution at 80°C for 60 minutes
5) Soak in IPA and acetone mixture at 80°C for 10 minutes
6) Dry the chip

All the steps except RIE were done in ultrasonic bath. After these layers were removed, the physical degradation of AlGaN/GaN HEMT device can be observed under SEM. Figure 3.13 shows the top-view SEM image of a AlGaN/GaN HEMT device before and after etching.

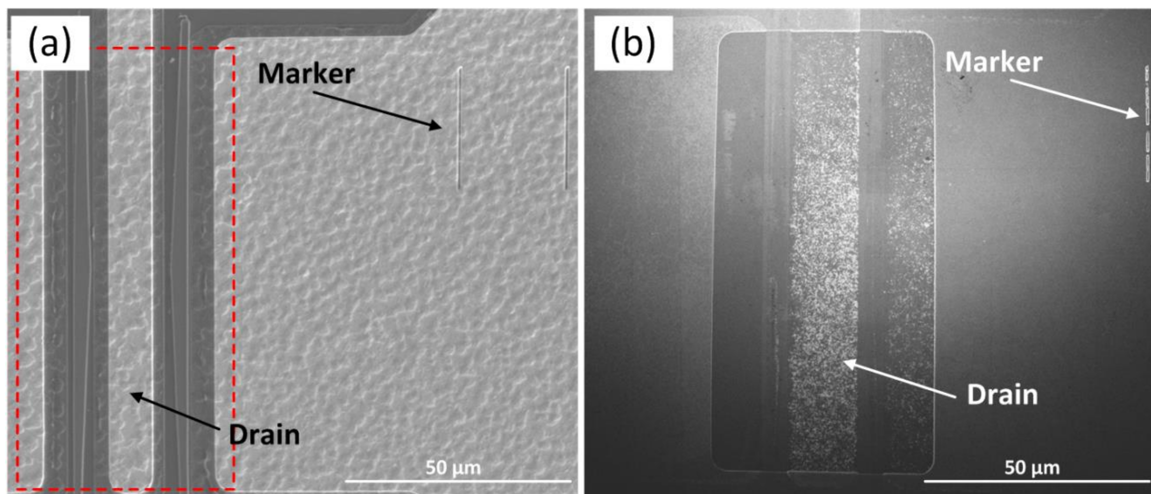

Figure 3.13 SEM image of AlGaN/GaN HEMT device (a) before and (b) after passivation/metallization layer removal

3.5.2 Dislocation Etching

This etching method is used to characterize threading dislocations on the AlGaN/GaN device. 85% phosphoric acid (H_3PO_4) was used to selectively etch dislocation in GaN film [124-126]. The crystal containing dislocation will be etched faster due to the lattice distortion and strain field of the dislocation [127]. The device was immersed in the 85% H_3PO_4 at 80^oC for 100 minutes followed by cleaning using IPA. 100 minutes was found to be the optimum condition because beyond 100 minutes the pits would merge with the neighboring pits. As the result, the etch pit density calculation will not be accurate. The etching was done inside ultrasonic bath.

Figure 3.14 shows the result of the dislocation etching under SEM. Different types of dislocations can be differentiated by the size of the etch pits. The large and the small etch pits are associated with screw/mixed and edge threading dislocations, respectively [124]. This is a simple method to obtain the threading dislocation density and the distribution of different types of dislocations in GaN film.

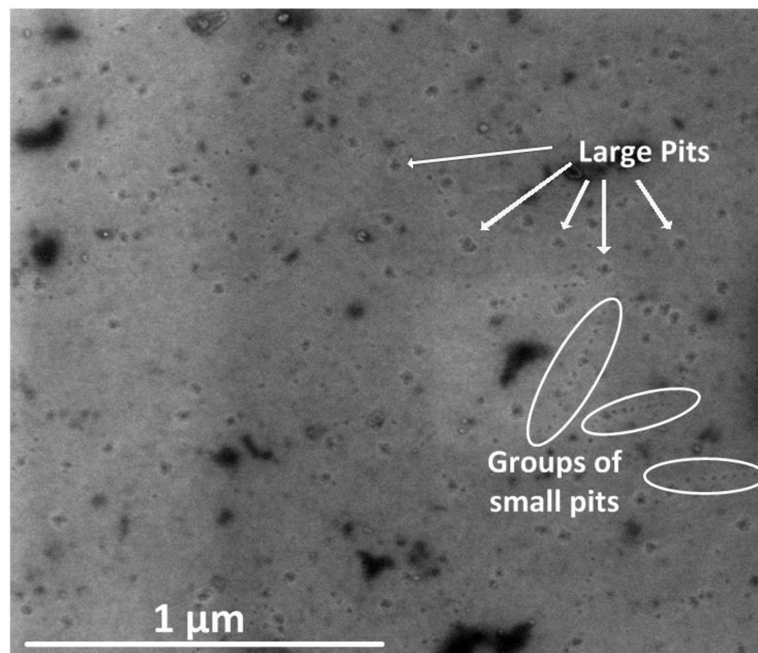

Figure 3.14 SEM image of GaN film after dislocation etching using 85% H_3PO_4 for 100 minutes at 80^oC

3.6 Microstructure Characterization

Microstructure characterization is critical in this study to observe the physical defects caused by the electrical stressing. Scanning electron microscope (SEM) is mainly used for top-view device analysis especially before and after wet etching. Focused ion beam (FIB) is used for cross-sectional transmission electron microscope (TEM) sample preparation. Lastly, TEM and its various techniques are used to analyze the cross-section of the device. The techniques used are scanning-transmission electron microscopy (STEM), energy dispersive X-ray spectroscopy (EDX), electron energy loss spectroscopy (EELS) and weak beam dark field (WBDF).

3.6.1 Scanning Electron Microscopy

Scanning electron microscope (SEM) is one of the common characterization tools. It is used to characterize the topography and texture of the sample with a magnification up to 500,000X. FEI Nova 600 NanoLab DualBeam^{TM} SEM/FIB system was used in this study (Figure 3.15).

SEM image is generated by sweeping a focused electron beam across the specimen surface. The signals from the electron-sample interactions will generate important information of the specimen. Electron-sample interaction can be schematically represented by Figure 3.16. Different signals are used for different purposes. Secondary electrons are useful to obtain the topography and morphology of the sample whereas back-scattered electrons are useful to display contrast in composition in a multiphase sample. The characteristic X-rays are important for the elemental analysis, while the diffracted back-scattered electrons are important to determine the crystalline structure and material orientation in the sample [128]. The device is analyzed under SEM before and after the electrical stressing to observe for microstructural changes on the device.

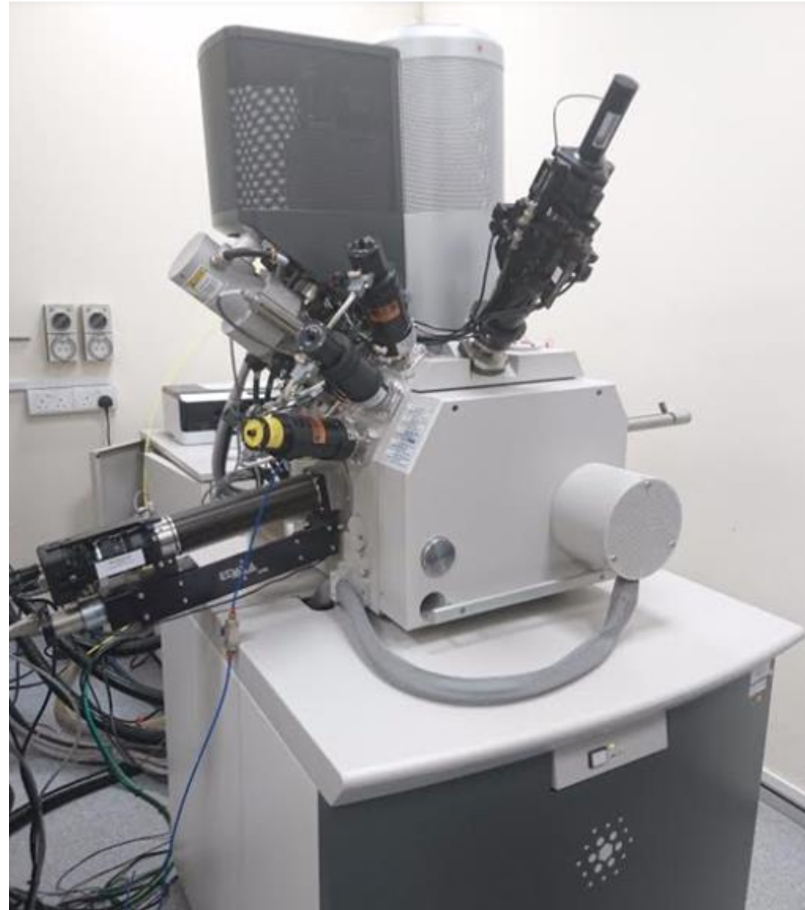

Figure 3.15 FEI Nova 600 NanoLab DualBeam™ SEM/FIB system used for microstructure characterization and cross-sectional TEM sample preparation

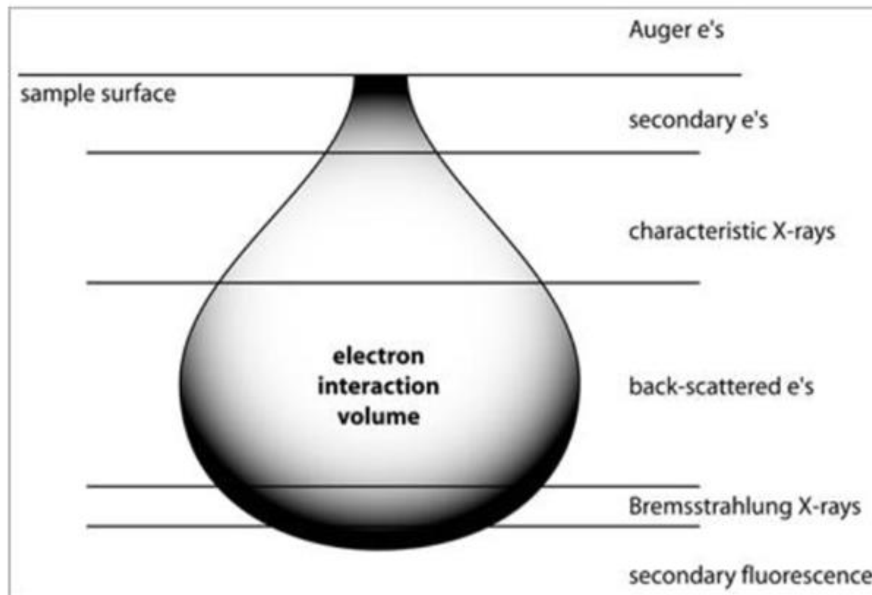

Figure 3.16 Electron-sample interaction volume within the sample [28]

3.6.2 Focused Ion Beam

Focused ion beam (FIB) is another powerful characterization tool. It has similar imaging principle as SEM but instead of using an electron beam, FIB uses a focused beam of gallium ions for imaging. In addition to imaging, the focused beam can be used for sputtering or milling at a specific spot depending on the current used. When the gallium (Ga^+) ions hit the sample surface, secondary and sputtered ions are produced. These ions are collected to form an image. When a large current is used, the Ga^+ ions can be used to etch away material from the sample's surface.

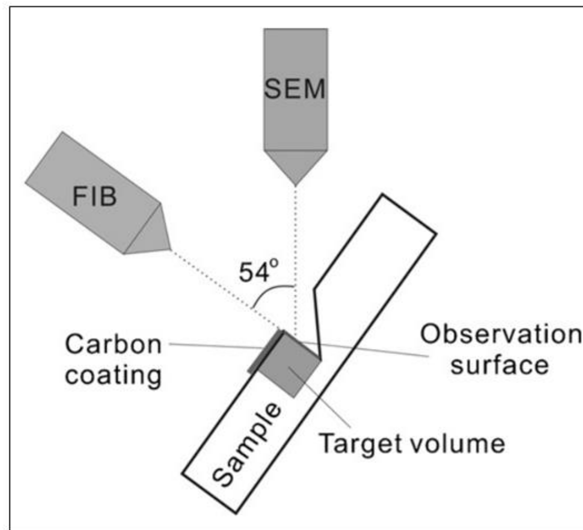

Figure 3.17 Schematic diagram of SEM/FIB dual beam system [29]

FEI Nova 600 NanoLab DualBeam™ SEM/FIB system (Figure 3.15) was used in this to prepare the cross sectional TEM sample [129, 130]. Figure 3.17 shows the diagram inside the SEM/FIB dual beam system. The ion beam source is perpendicular to the sample surface while the electron source is at 36° from the sample surface. This setup allows direct monitoring of the milling process from the SEM mode. This is very crucial especially during the thinning down step of the TEM sample.

Figure 3.18 shows the necessary steps to prepare a TEM lamellar.

(a) Trenches are created by ion milling to expose the lamellar.

(b) The lamellar is then cut and picked using a nanoprobe and transferred onto a copper grid.

(c) The lamellar is attached to the copper grid by Pt deposition.

(d) Finally, the lamellar is thinned down and cleaned using ion beam to about 100 nm thin so that it can be examined under TEM. When the lamellar thickness is getting closer to 100 nm, low kV milling at about 1-2 kV should be used to prevent FIB-induced damage [131]. During the thinning down step, SEM mode is used to monitor the lamellar thickness.

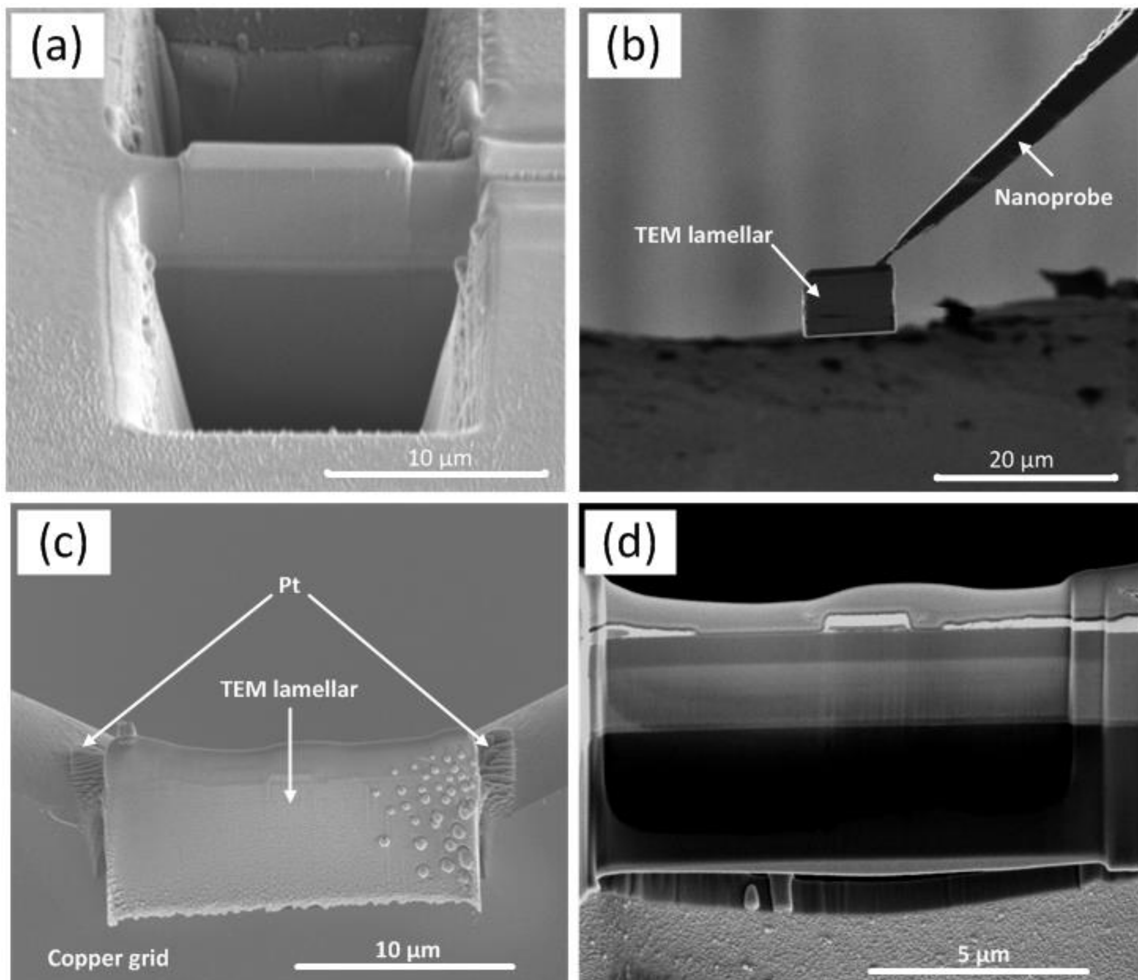

Figure 3.18 Cross-sectional TEM sample preparation using FIB system: (a) trenches are made to expose the lamellar, (b) the lamellar is picked using a nanoprobe, (c) the lamellar is transferred and attached to TEM copper grid and (d) the lamellar is thinned down to about 100 nm thick

3.6.3 Transmission Electron Microscopy

Transmission Electron Microscope (TEM) is a tool that can characterize a material down to atomic level. TEM is able to give a very high resolution, i.e. atomic level resolution (< 2 Å). TEM is able to give information about the morphology, crystal structure, defects, crystal composition, and magnetic microstructure [132]. In this study, TEM is used to characterize the microstructure of the AlGaN/GaN HEMT cross-section. Various techniques are used to characterize the device cross-section such as scanning transmission electron microscopy (STEM), energy-dispersive X-ray spectroscopy (EDX) and electron energy loss spectroscopy (EELS). In addition, weak beam dark field (WBDF) technique is used to characterize the threading dislocations.

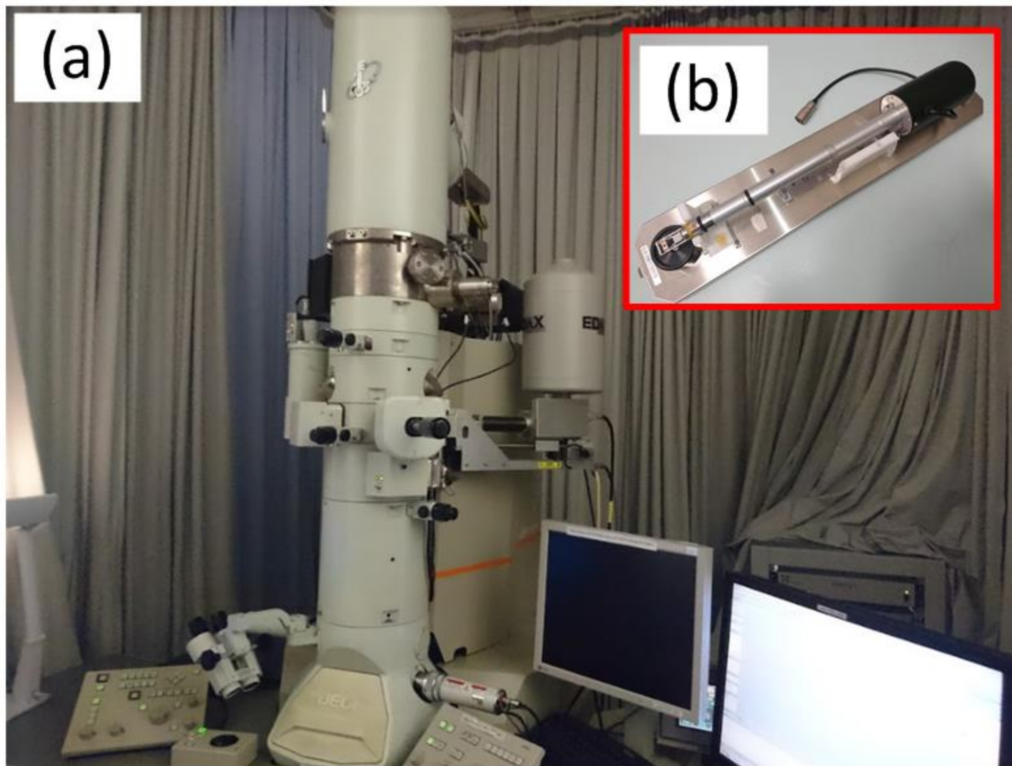

Figure 3.19 (a) JEOL 2100F TEM with (b) double-tilt sample holder located in FACTS lab [30]

Figure 3.19a shows the TEM that was used for the analysis in this study i.e. JEOL 2100F. Double-tilt sample holder (Figure 3.19b) was used which allows the samples to be tilted in both x- and y-axis. One main drawback of TEM characterization is that it is highly localized.

Thus, the results may not represent the bulk material. After the device is electrically stressed, cross-sectional TEM sample is prepared using FIB to observe any microstructural defect on the device before and after the passivation and metallization layers removal.

3.6.3.1 Scanning Transmission Electron Microscopy

Scanning transmission electron microscopy (STEM) is one mode in TEM that scans the sample lamellar using focused electron beam. When the electrons pass through atoms they will be scattered. On the other hand, when they pass through an empty space, they will be transmitted. The heavier the atoms, the larger electron scattering angle will be. These scattered and transmitted electrons can be used for imaging and elemental analysis. There are two imaging modes and two elemental analysis techniques that are commonly used in STEM. The two imaging modes are bright field (BF) and annular dark field (ADF), while the two elemental analysis techniques are energy-dispersive X-ray spectroscopy (EDX) and electron energy loss spectroscopy (EELS) [133]. In addition, as this STEM mode is done in TEM with 200 kV accelerating voltage, this will increase the sample penetration. This means that not only thicker samples can be used, but more importantly higher spatial resolution can be achieved compared to normal SEM [134].

3.6.3.2 Energy Dispersive X-ray Spectroscopy

Energy dispersive X-ray spectroscopy (EDX) is one of the most commonly used chemical analysis tools in failure analysis. EDX is usually attached to SEM or TEM. In TEM, EDX is usually done in STEM mode. As discussed in section 3.6.1, the electron-sample interaction gives out various signals such as secondary electrons, backscattered electrons and characteristic X-rays. EDX analysis uses the characteristic X-rays. When energetic electrons hit the sample atom, some electrons are knocked out from the inner shell and get excited to the outer shell (Figure 3.20a). When the excited electrons from the outer shell come back to the inner shell, X-ray will be generated [31] (Figure 3.20b). The X-ray energy corresponds to the energy difference between the outer and inner shell. This energy is

unique for each element and thus, it can be used to characterize different elements in the sample.

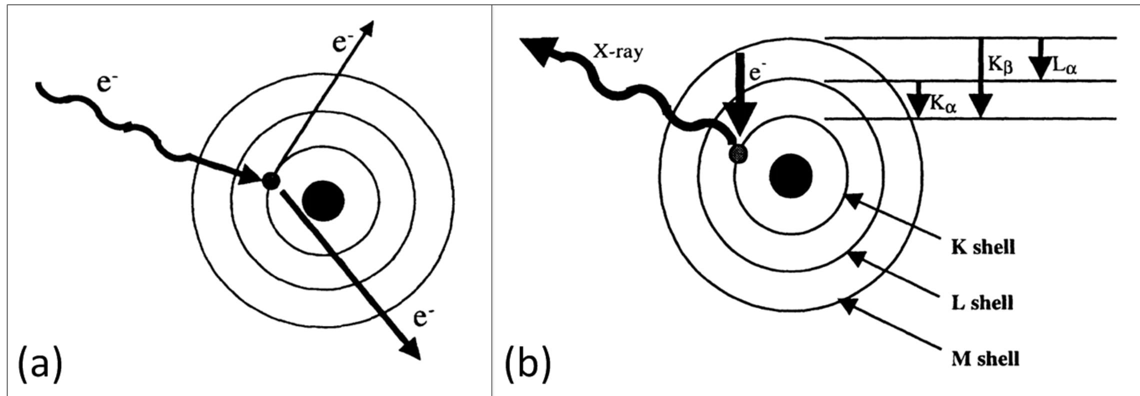

Figure 3.20 X-ray generation in EDX under STEM mode: (a) Incident electron hit the sample atom and knock some electrons from the inner shell to the outer shell, (b) X-rays are generated with these excited electrons return to the inner shell [31]

STEM-EDX in TEM gives a better spatial resolution as compared to EDX in SEM because of the high accelerating voltage used (200 kV) [135]. The X-ray signals are collected using EDAX EDX detector. Various scan modes are used in this experiment such as point scan, line scan and elemental mapping. During the EDX signal collection, the sample has to be tilted 15° in the positive x-direction in order to ensure no signal blockage by the copper grid. The spot size and camera length used are 1 nm and 20 cm respectively. STEM-EDX will be used for analyzing heavy elements such as aluminum, gallium, titanium, gold and nickel.

3.6.3.3 Weak Beam Dark Field Technique for Threading Dislocation Analysis

Weak beam dark field (WBDF) technique is commonly used to characterize different types of dislocation [136]. In WBDF image, dislocations will appear bright whereas other areas will appear dark. Correct tilting has to be fulfilled in order to obtain this contrast. The condition is $\mathbf{g} \cdot \mathbf{b} = 0$, where $\mathbf{g}$ is the reciprocal lattice vector and $\mathbf{b}$ is the burger vector of the dislocation. If this condition is fulfilled, it will give a weak/zero contrast, i.e. the dislocation which has burger vector $\mathbf{b}$ will not be visible in the image.

In this project, the AlGaN/GaN epitaxy is grown in [0001] direction on (111) Si substrate. Therefore, the threading dislocations are in [0001] direction as well. The burger vectors of pure screw and pure edge threading dislocation are [0001] and [1120], respectively [137]. Table 3.2 summarizes the WBDF conditions to characterize different types of threading dislocation in AlGaN/GaN epitaxy.

Table 3.2 WBDF tilting conditions for threading dislocation (TD) characterization

g	**b**	Pure Screw TD	Pure Edge TD	Mixed TD
[0002]	[1120]	Visible	Invisible	Visible
[1120]	[0002]	Invisible	Visible	Visible

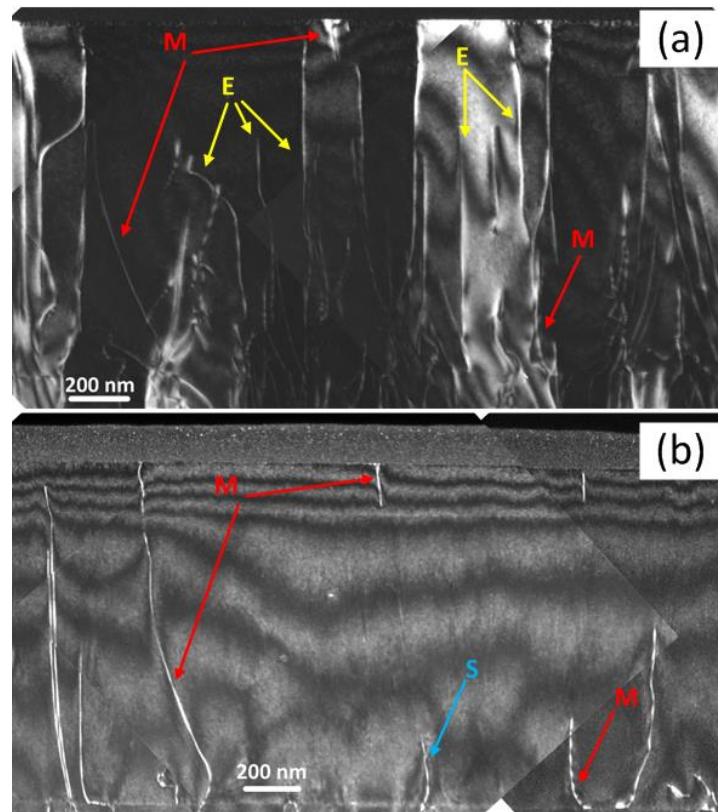

Figure 3.21 WBDF images of the same sample at (a) g = [1120] to show pure edge TD labelled as E, (b) g = [0002] to show pure screw TD labelled as S. Mixed TDs are visible in both conditions and labelled as M

Figure 3.21a shows the WBDF image at **g** = [1120]. Under this condition, edge dislocations will appear as bright lines whereas screw dislocations will be invisible. On the other hand, when **g** = [0002] as shown in Figure 3.21b, screw dislocations will be visible and edge dislocations will be invisible. Some of the dislocations are visible in both conditions. These dislocations are mixed dislocations.

3.6.3.4 Electron Energy Loss Spectroscopy

Electron energy loss spectroscopy (EELS) is another analytical technique used in STEM mode. EELS measures the electrons' energy loss after they interact with the sample. STEM-EELS has a spatial resolution down to atomic level and energy resolution down to 0.1-1 eV [138]. This makes STEM-EELS a precise characterization technique.

In the STEM mode, electrons are bombarded to the sample with 200 kV accelerating voltage. The electrons interact with core electrons in the sample atoms and lose some of their energy due to inelastic scattering. These transmitted electrons are then collected by the EELS detector. The energy loss during the inelastic scattering corresponds to binding energy of the core electrons. Since the binding energy is unique for every element, the energy loss can be used to characterize the chemical composition of the sample.

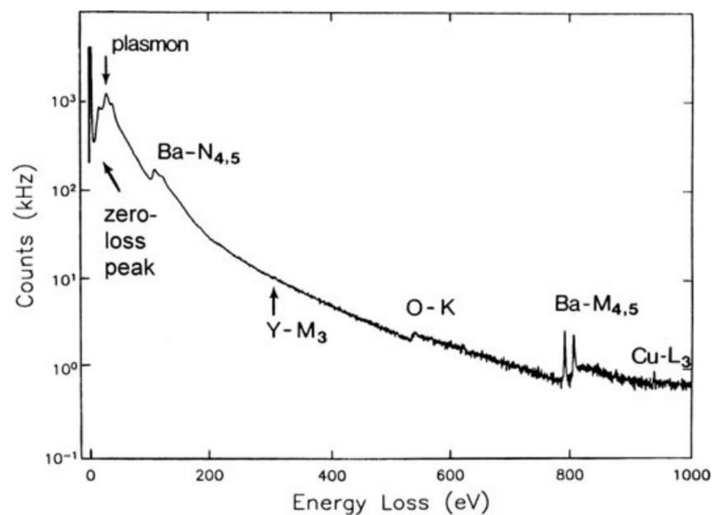

Figure 3.22 Electron energy-loss spectrum of $YBa_2Cu_3O_7$ showing zero-loss peak and ionization edges from each element [32]

When the transmitted electrons are collected by the EELS detector, the spectrometer will separate the electrons according to the energy loss and an electron energy-loss spectrum is produced. An electron energy-loss spectrum shows the number of electrons as a function of decrease in their kinetic energy. One example is the electron energy-loss spectrum of $YBa_2Cu_3O_7$ by Shin *et al.* [32] shown in Figure 3.22. This plot shows the zero-loss peak which represents the intensity of electrons that go through elastic scattering or no energy loss. Ionization edges shown as sharp peaks at higher energy loss represent the binding energy of core electrons from specific elements. In this particular example, the elements are Ba, O, Y and Cu.

In this study, EELS is used to characterize the elements in AlGaN/GaN HEMT device especially the light elements. This is because EELS detection efficiency is much higher than EDX and peak-to-background ratio for EELS is much lower than EDX [139]. For heavier elements, EDX will be used as it requires shorter collection time than EELS. This is important because the longer the collection time, it will be more prone to sample drifting which may compromise the data accuracy. The elements of interest and their ionization edges used in this study are summarized in Table 3.3.

Table 3.3 EELS ionization edges of the elements used in AlGaN/GaN HEMT reliability study [8]

Element	Ionization Edge (eV)
Si	99
C	284
N	401
O	532
Ni	855
Ga	1115
Al	1560

3.6.3.5 Relative Density Measurement of Si_xN_{1-x} Passivation Layer using EELS

First and foremost, the thickness of a specific region in the sample can be estimated using log-ratio method [33]. The incident beam is shone on the region of interest and low-loss spectrum from this region is collected. The area under the zero-loss peak (I_0) is then compared with the total area under the curve for the whole spectrum (I_t) as shown in Figure 3.23.

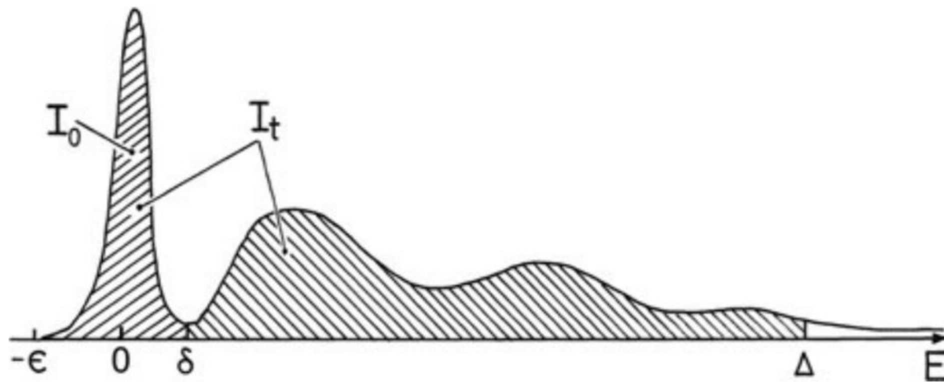

Figure 3.23 EELS spectrum needed to determine specimen thickness using log-ratio method [33]

The thickness (t) of the specimen then can be calculated using the formula below:

$$t = \lambda \ln \frac{I_t}{I_0} \tag{3.2}$$

$$\lambda \propto \frac{1}{\rho^{0.3}} \tag{3.3}$$

$$t\rho^{0.3} \propto \ln \frac{I_t}{I_0} \tag{3.4}$$

where λ and ρ are the total mean free path for all inelastic scattering and density of the specimen, respectively. This total mean free path is inversely proportional to $\rho^{0.3}$. Thus, the $\ln(I_t/I_0)$ is proportional to $\rho^{0.3}$ and thickness of the film.

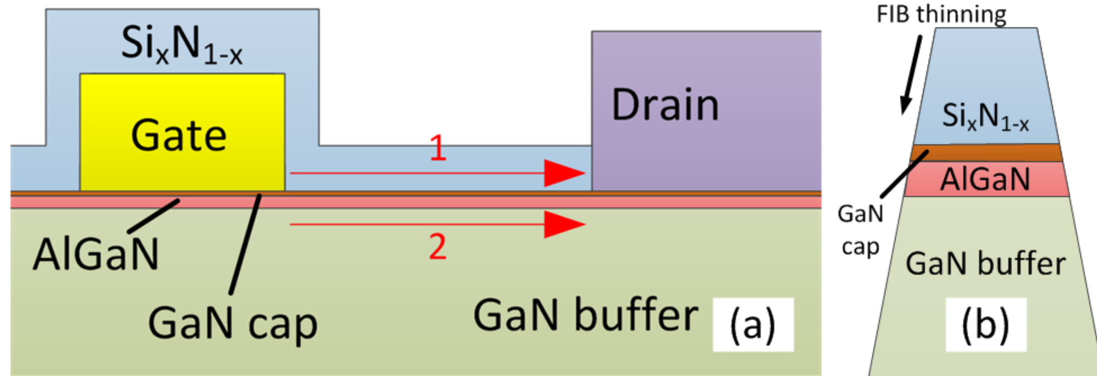

Figure 3.24 (a) Schematics of EELS line-scan to determine relative density of Si_xN_{1-x} passivation layer (b) side-view of the TEM lamellar

In this experiment, EELS line-scan is used to determine the relative local density of the Si_xN_{1-x} passivation layer along the line by using the log-ratio method. One problem with this approach is to separate between the effect of thickness difference and density difference. In order to solve this issue, the EELS signal from line 1 and 2 are collected and the I_t/I_0 ratio is extracted. Although the thickness of GaN buffer layer is not the same as the Si_xN_{1-x} passivation layer (Figure 3.24b), it is expected that the thickness variation along line 1 and 2 is the same. This is a fair assumption as the Si_xN_{1-x} and GaN buffer layers are thinned down simultaneously during the sample preparation in FIB. Secondly, it is assumed that the density of GaN buffer layer along line 2 is constant. Therefore, any fluctuation in $\ln(I_t/I_0)$ along line 2 is due to the thickness difference and not density difference. This is then compared with the $\ln(I_t/I_0)$ along line 1. Any fluctuation observed in line 1 but not in line 2 will be the result of density difference.

3.6.3.6 Absolute Composition of Si_xN_{1-x} Passivation Layer

In this experiment, it is important to get the absolute composition of Si_xN_{1-x} passivation layer. This information can also be obtained using EELS. When another element is added to a host material, the lattice parameter and valency may change. This leads to a change in valence electron density and plasmon energy. This plasmon energy can be used to obtain the absolute composition of Si_xN_{1-x}. Firstly, Si_xN_{1-x} sample with known composition is scanned using EELS. EELS spectra are from 0 eV (zero-loss) to 401 eV (nitrogen peak).

This range contains silicon peak at 99 eV. In practice, the range has to be split into 4 smaller ranges due to detector limitation. The ranges are 0 – 100 eV, 101 – 200 eV, 201 – 300 eV and 301- 401 eV. All the measurement parameters are kept constant for the 4 ranges. These measurements are then combined to get the whole range from 0 eV to 401 eV. This is done by using splice function in Gatan DigitalMicrograph software [140]. Then, the plasmon energy for Si_xN_{1-x} sample with known composition can be extracted from the low-loss energy peaks. These steps are repeated for the two different Si_xN_{1-x} passivation layers. The relative composition of the two samples is then normalized against the Si_xN_{1-x} sample with a known chemical composition in order to get the absolute composition. The EELS settings and collection time are kept the same for all measurements to ensure consistency.

3.6.4 X-Ray Reflectometry

X-ray reflectometry (XRR) is a non-destructive and non-contact method to measure thickness, density and surface roughness [141-144] of thin film with a precision of about 1-3 Å [145].

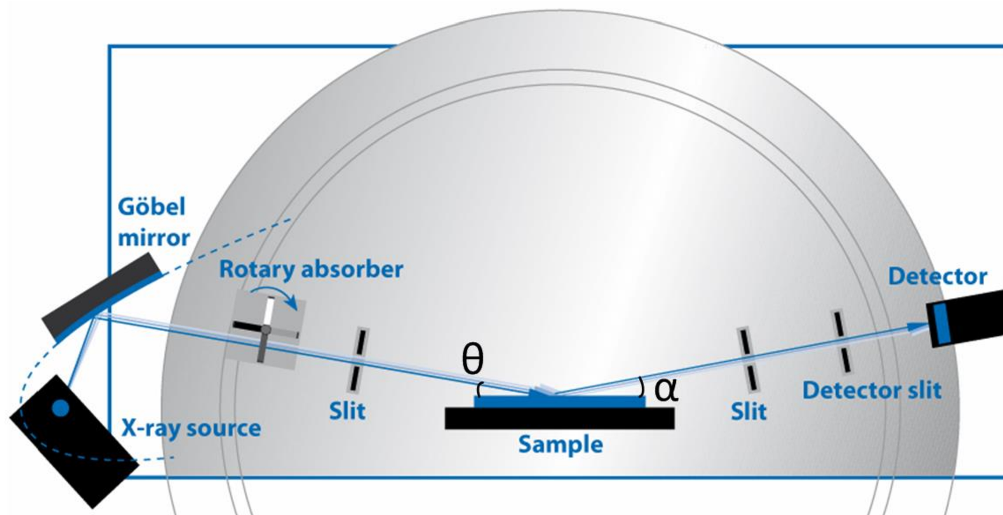

Figure 3.25 Experimental setup for X-ray reflectivity (XRR) measurement [34]

The XRR setup is shown in Figure 3.25. A monochromatic X-ray beam with a wavelength λ is shone on the thin film surface at an incident angle θ. Upon contact with the sample surface, X-rays will be reflected. This reflection corresponds to the electron density in the

sample. This information can be translated into refractive index in the classical optics. The reflected intensity at angle $\alpha = 2\theta$ is recorded by the detector. This setup demonstrates specular reflection where grazing angle (ω) = $2\theta/2$ condition is satisfied. Reflected intensity will be recorded for incident angle θ from 0 to 4 degree. During all the measurements, the incident angle is always half of the angle of reflection ($\theta = 0.5\alpha$).

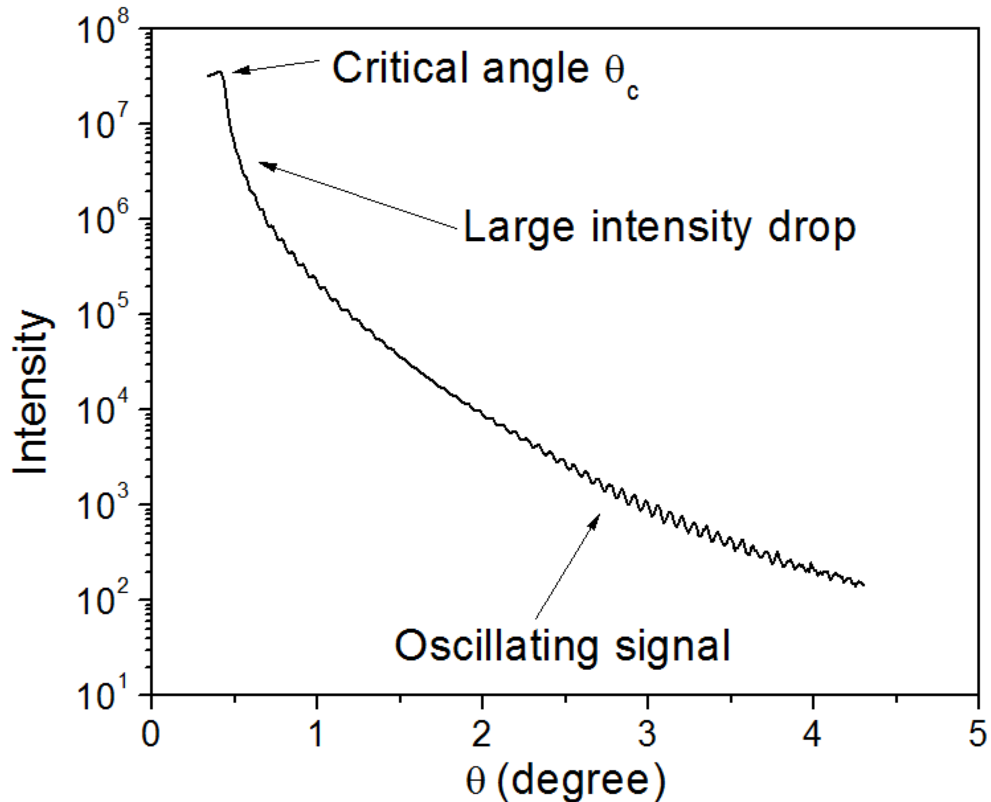

Figure 3.26 A typical XRR measurement plot

Figure 3.26 shows a typical XRR measurement plot. The density of the thin film can be determined from the critical angle θ_c. Critical angle is the maximum angle where total internal reflection occurs. When the incident angle θ increases above the critical angle θ_c, interference fringes will be produced as reflection from different interfaces start to interfere. Thickness of the thin film will be determined from the period of the interference fringes (oscillating signal) and the layer roughness will be determined from the fall in the intensity.

3.6.4.1 Film Density Measurement

Film density is related to the refractive index of the thin film. The complex refractive index (n) is given by

$$n = 1 - \delta + i\beta \tag{3.5}$$

where δ and β represent the dispersion and absorption, respectively. When the frequencies are much larger than the atomic resonance frequencies, δ can be expressed by

$$\delta = \frac{r_0\lambda^2}{2\pi} N_e \tag{3.6}$$

Where r_0 is the Bohr's radius, λ is the wavelength of the monochromatic X-ray source and N_e is the electron density. N_e is given by

$$N_e = Z \times N_{atom} \tag{3.7}$$

$$N_{atom} = \frac{N_A}{A}\rho \tag{3.8}$$

Where Z is the number of electrons per atom, N_A is Avogadro's number, A is the atomic weight and ρ is film density. In order to express the dispersion, absorption and X-ray absorption edge more accurately, Z is often replaced by complex atom form factor. δ and β can be expressed as

$$\delta = \frac{r_0\lambda^2}{2\pi}(Z + f')N_{atom} \tag{3.9}$$

$$\beta = \frac{r_0\lambda^2}{2\pi} f'' N_{atom} \tag{3.10}$$

where f' and f'' are complex atom form factors that describe X-ray absorption edge.

Substituting equation (3.7) and (3.8) into (3.9) and (3.10), δ and β can be obtained as a function of film density. For a reflection at an interface between air (n_{air} = 1) and another material, the refractive index is $n = 1 - \delta$. The critical angle is usually very small about 0.3° and when the incident angle is lower than the critical angle, total reflection occurs. By applying Snell's law and small angle approximations, the critical angle θ_c can be expressed as

$$\begin{aligned} 1 - \delta &= \cos\theta_C \\ &\approx 1 - \frac{\theta_C}{2} \\ \theta_C &\approx \sqrt{2\delta} \\ &= \sqrt{\frac{r_0\lambda^2}{\pi} N_A \frac{(Z + f')}{A} \rho} \end{aligned} \tag{3.11}$$

θ_c is determined by the sudden fall in the reflected intensity in the XRR measurement curve (Figure 3.26) and the thin film density can be calculated using equation (3.11).

3.6.4.2 Film Thickness Measurement

The X-ray will penetrate into the film when the incident angle is greater than the critical angle θ_c. For this condition, the reflection occurs at both top and bottom surfaces of the film. This leads to formation of interference fringes. These fringes are angle dependent and not frequency dependent like in the case of optical spectroscopy. The p-th interference maximum for a path difference $\Delta = p\lambda$ is located at

$$p\lambda = \Delta = 2d\check{N}_{X,1}(\theta_p) \tag{3.12}$$

$$\approx 2d\sqrt{\theta_p^2 - 2\delta} \qquad p \in \mathbb{N}$$

$$\theta_p^2 \approx p^2 \frac{\lambda}{4d^2} + 2\delta \tag{3.13}$$

$$= p^2 \frac{\lambda}{4d^2} + \theta_C^2 \tag{3.14}$$

In this case, the contributions of multiply reflected beams can be neglected because of low amplitude reflection coefficient. If the substrate is optically denser than the film, a phase difference of π occurs at the reflection film/substrate interface and p is substituted with p + 0.5. Using the difference between two neighboring maxima and minima and equation (3.13), the film thickness can be calculated by

$$d \approx \frac{\lambda}{2} \frac{1}{\sqrt{\theta_{p+1}^2 - \theta_C^2} - \sqrt{\theta_p^2 - \theta_C^2}} \tag{3.15}$$

$$d \approx \frac{\lambda}{2} \frac{1}{\theta_{p+1} - \theta_p} \qquad for\ \theta_p \gg \theta_C \tag{3.16}$$

3.6.4.3 Surface Roughness Measurement

XRR measurements also give information on the surface roughness of the thin film. The incident X-ray will be scattered when it hits a rough surface. This leads to lower intensity in the reflected beam signal collected by the detector. From Figure 6.2, the sudden drop in the intensity will provide information on the surface roughness. Nevot and Croce assumed roughness as non-homogenous thickness with a Gaussian distribution with a mean d and a standard deviation σ. With this assumption, the Frensel coefficients of reflection becomes

$$\rho_{v,h} \cdot \exp\left(-\frac{d}{2\sigma^2}\right) \tag{3.17}$$

3.6.4.4 X-ray Reflectivity Measurement of Si_xN_{1-x} Passivation Layer

The equipment used for XRR measurement is Bruker D8 Discover HR-XRD [146] shown in Figure 6.3 below. This equipment uses Cu-Kα radiation operated at 40 kV and 40 mA with a stage that can accommodate up to 4-inch wafer and scintillation counter as the detector.

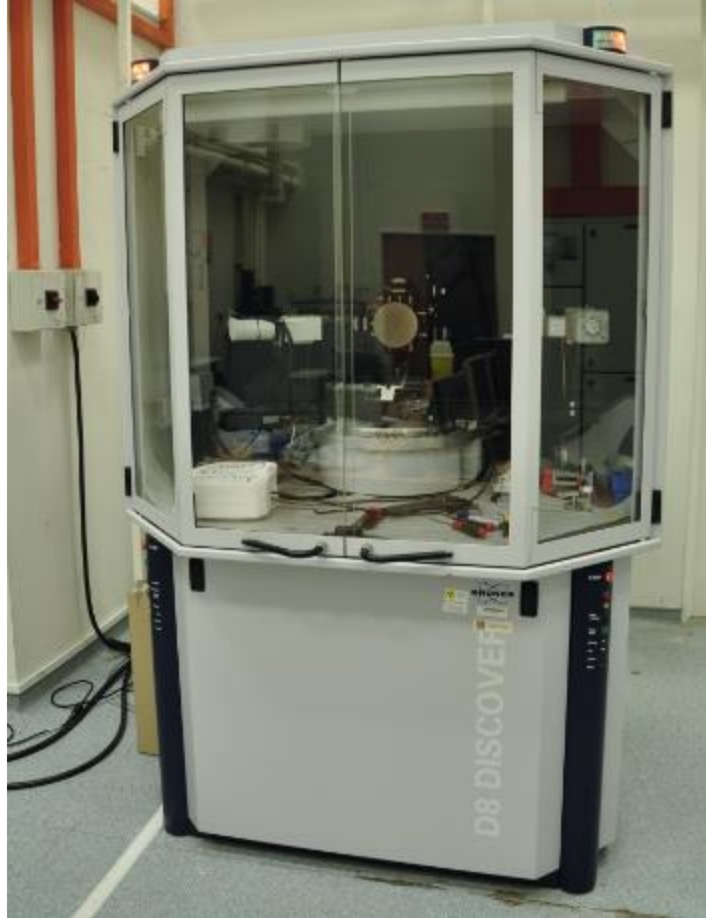

Figure 3.27 Bruker D8 Discover HR-XRD system used for XRR measurement [35]

The reflected ray intensity was collected for incident angle from 0° to 4.5° for two different Si_xN_{1-x} passivation samples. The measurement results were then evaluated using Leptos software [147]. Once the simulation curve fits the XRR measurement results, the film thickness, density and surface roughness of the samples can be extracted.

3.6.5 Pit Counting Method

In this project, ImageJ software [148] was used to count the pits from top-view SEM image, in order to obtain the number of pits and pit area on AlGaN/GaN HEMT devices after passivation and metallization layer removal. Multiple SEM images of the device were taken at 15,000x magnification so that the pits could be clearly seen. This step was repeated for the whole device width and the images were stitched together.

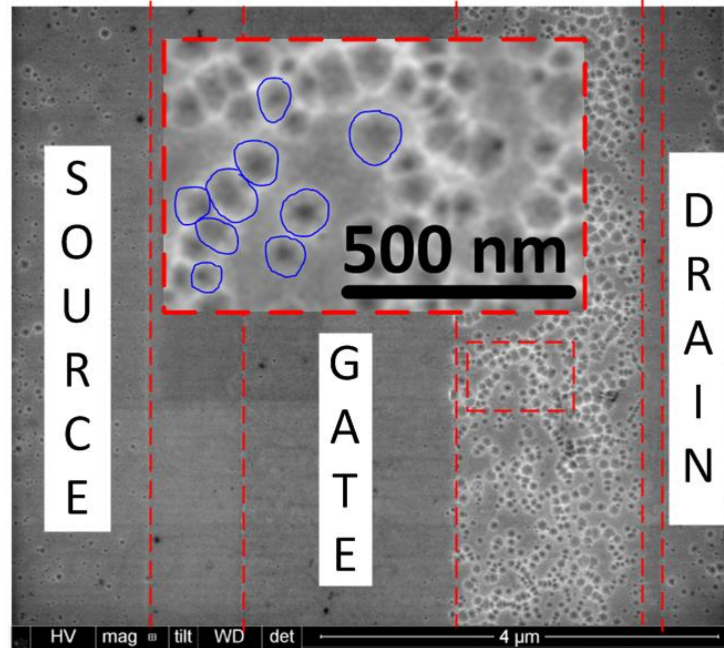

Figure 3.28 One of **t**op-view SEM images of an AlGaN/GaN HEMT device stressed under ON-state condition after passivation and metallization layer removal

Figure 3.28 shows one of the SEM images taken from a device stressed under ON-state condition after passivation and metallization layer removal. Pits were circled one by one using ImageJ for the entire device width. Individual pit area was recorded by the software. After all the pits were circled, total number of pits and total pit area were calculated for this particular device.

Chapter 4*

Comparative Study of AlGaN/GaN High Electron Mobility Transistor Degradation Mechanism under OFF-state and ON-state Stressing

Extensive study has been done for OFF-reliability but not for ON-state reliability. In this chapter, OFF-state degradation was compared with ON-state degradation to investigate the role of current flow in 2DEG channel. It was found that devices stressed under ON-state condition degraded faster than under OFF-state condition. Microstructural analysis showed dark features containing aluminum, gallium and oxygen at AlGaN/Si_xN_{1-x} interface away from the gate edge. These dark features turned into pits in drain-gate access region after Si_xN_{1-x} passivation and metallization layers removal. These pits away from the gate edge are likely to be the reason for higher degradation under ON-state condition. Finally, it was proposed that hot electrons in 2DEG channel contribute to ON-state degradation by promoting electro-chemical oxidation of AlGaN away from the gate edge.

*This section has been published substantially as G. Syaranamual, W. Sasangka, R. Made, S. Arulkumaran, G. Ng, S. Foo, *et al.*, "Role of two-dimensional electron gas (2DEG) in AlGaN/GaN high electron mobility transistor (HEMT) ON-state degradation," *Microelectronics Reliability,* vol. 64, pp. 589-593, 2016.

4.1 Introduction

Under ON-state condition, drain current flows from the drain to the source. In AlGaN/GaN HEMT, the current is generated from the movement of mobile electrons at 2DEG channel. Wu *et al.* proposed that ON-state degradation has the same mechanism as OFF-state degradation, i.e. electro-chemical oxidation [23]. However, there is no direct comparison between devices stressed under ON- and OFF-state conditions. They also found that ON-state degradation is thermally-activated process [77, 100, 101]. The current flow generates joule heating that causes higher degradation.

In this chapter, devices stressed under ON- and OFF-state conditions will be compared. The difference between ON- and OFF-state degradations will be discussed. This chapter focuses on the effect of drain current during ON-state operation. The starting hypothesis is that the role of 2DEG in ON-state degradation is only to elevate the device temperature via joule heating which accelerates the degradation.

4.2 Experimental Details

In order to prove this hypothesis, devices stressed under ON-state condition were compared to devices stressed under OFF-state condition with higher base temperature. The purpose of the higher temperature was to compensate the temperature increase from joule heating during ON-state stressing. ON-state junction temperature was measured using thermo-reflectance method. The devices were electrically stressed and followed by microstructure characterization.

4.2.1 Junction Temperature Measurement

During OFF-state stressing, there is no drain current flow across the device. Therefore, the stressing temperature is taken as the applied base temperature. On the other hand, for ON-state stressing, the drain current flows from drain to source. This current induced joule heating. Therefore, increase in temperature due to joule heating has to be calculated in

order to obtain a more accurate stressing temperature. The junction temperature measurement is obtained using thermo-reflectance method. The experimental setup and working principle of thermo-reflectance are explained in section 3.3.

Table 4.1 Junction temperature measurement parameters by thermo-reflectance method

Device Number	Mode	V_{DS} (V)	V_{GS} (V)	Base Temperature (°C)
1	ON-state	20	0	25, 50, 60, 80, 100
2	ON-state	20	0	50, 60, 80, 100
3	ON-state	20	0	50, 60, 80, 100
1	OFF-state	10	-10	25

Table 4.1 shows different parameters used in the junction temperature measurements using thermo-reflectance method. The collection time for each measurement was 5 minutes. During collection time, the devices did not show degradation. The first set of measurements was done on device 1 to compare the temperature distribution between ON-state and OFF-state operations. This was to ensure that there was no current flow and joule heating during OFF-state operation. The voltage between drain and gate (V_{DG} = 20 V) was kept constant to ensure that the electric field between drain and gate was constant for both OFF-state and ON-state conditions. The second set of measurements was to measure the junction temperature of the device under ON-state condition. The ON-state stressing was done with bias V_{DS} = 20 V and V_{GS} = 0 V at 150°C base temperature. Unfortunately, the maximum base temperature that could be applied in the thermo-reflectance system was 100°C. Therefore, measurements were taken at four different temperatures i.e. 50, 60, 80 and 100°C and then the measurements were extrapolated to 150°C in order to obtain the junction temperature during ON-state stressing. This linear extrapolation is reasonable because Martin-Horcajo *et al.* had reported that junction temperature increases linearly when ambient temperature varies from 25°C to 225°C [149]. The measurements were repeated for 3 devices with similar dimensions.

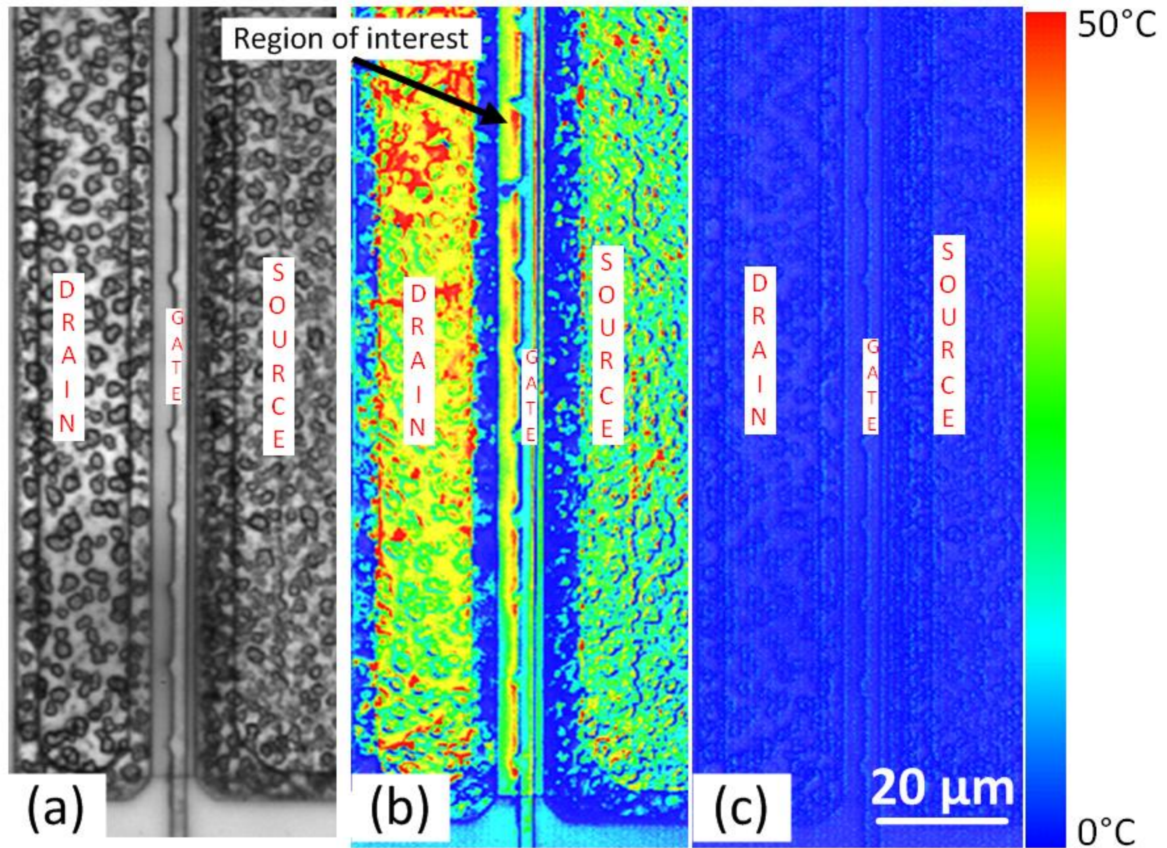

Figure 4.1 (a) Top-view image of the AlGaN/GaN HEMT taken by light microscope, ΔT distribution of the device under (b) ON-state condition V_{DS} = 20 V, V_{GS} = 0 V and (c) OFF-state condition V_{DS} = 10 V, V_{GS} = -10 V at base temperature 25°C

Figure 4.1a shows the top-view image of device 1 under optical microscope. Figure 4.1b and c show the distribution of temperature change (ΔT) for device under ON-state (V_{DS} = 20 V, V_{GS} = 0 V) and OFF-state (V_{DS} = 10 V, V_{GS} = -10 V) conditions, respectively. The measurements were done at base temperature 25°C. There was significant difference between ON-state and OFF-state due to the current flow under ON-state condition. The device temperature increased up to 50°C under ON-state condition whereas there was negligible increase in temperature under OFF-state condition. Therefore, the maximum junction temperature was 75°C under ON-state. On the other hand, the device temperature under OFF-state condition was 25°C, which was the base temperature. In this study, the region of interest is the drain-gate access region shown by the arrow in Figure 4.1(b).

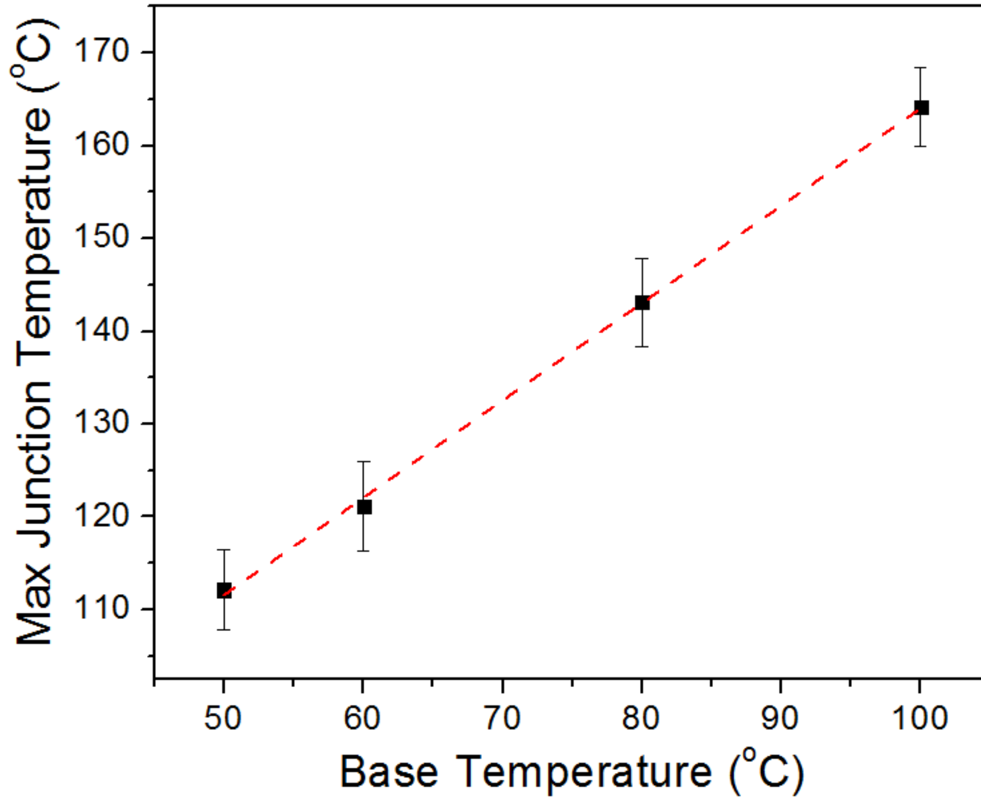

Figure 4.2 Maximum junction temperatures at the drain-gate access region for device 1-3 under ON-state condition V_{DS} = 20 V, V_{GS} = 0 V at four different base temperatures

$$Max\ Junction\ Temperature\ = M\ \times\ Base\ Temperature +\ C \tag{4.1}$$

Figure 4.2 shows the result for the second set of measurements. The maximum temperature at the region of interest was taken to estimate the junction temperature of the device under ON-state condition V_{DS} = 20 V, V_{GS} = 0 V. The measurements were taken from 3 different devices with similar dimensions at 4 different base temperatures. The result was linearly fitted into equation 4.1 with M = 1.05 and C = 59 ^{o}C.

The junction temperature for the device under the same bias condition at 150°C was obtained by extrapolating the result in Figure 4.2. Maximum junction temperature of 217°C was obtained for a base temperature of 150°C. This result will be used for the electrical stressing in the next section.

4.2.2 Electrical Stressing

This experiment was done in probe station using Keithley 4200 parameter analyzer. Each device underwent ten I_D-V_{GS} sweep cycles at room temperature before the stressing to ensure that the device was stable and had no early degradation. I_D-V_{GS} and I_D-V_{DS} sweeps were done every 1 hour during the electrical stressing at the stressing temperatures.

Table 4.2 ON-state and OFF-state electrical stressing parameters

Stressing code	1	2	3	4
Mode	OFF-state	ON-state	ON-state	ON-state
V_{DS} (V)	10	20	10	10
V_{GS} (V)	-10	0	Floating	Floating
V_{DG} (V)	20	20	-	-
$V_{Substrate}$ (V)	-	-	-	-20
Stressing duration (hr)	20	20	20	20
Base temperature (^oC)	250	150	200	200
Max junction temperature (^oC)	250	217*	269*	269*
UV-light	-	-	Yes	Yes
Number of samples	3	3	3	3

*max junction temperatures calculated using equation (4.1)

Table 4.2 shows the electrical stressing parameters for the experiments in this chapter. The first experiment was comparing between ON-state and OFF-state stressing. The OFF- and ON-state stressing parameters are shown in Table 4.2 stressing code 1 and 2, respectively. The V_{DG} was kept constant to ensure that the electric field at the drain-gate access region was constant. The OFF-state base temperature was 100°C higher than ON-state base temperature. This was to compensate the joule heating during ON-state stressing. The maximum junction temperature was 217°C for the ON-state stressing. The device characteristics such as I_{D-max}, I_{G-leak} and V_{TH} were monitored every hour during the 20 hour-stressing.

Another set of experiment was done to identify the role of 2DEG electrons in ON-state degradation. The stressing parameters are listed in Table 4.2 stressing code 3 and 4. UV light (254 nm) was shone on the device during the stressing to ensure abundant holes were available. This particular wavelength was used to ensure that UV light had enough energy (4.88 eV) to produce photo-generated holes in AlGaN layer (band-gap about 4.09 eV). The holes are needed in electro-chemical oxidation of AlGaN [16]. The negative substrate bias was applied to force the 2DEG electrons to move towards the AlGaN surface where physical degradation have been reported after ON-state stressing [22, 23, 77].

4.2.3 Microstructure Characterization

Microstructural characterization was done for all the stressed devices after the electrical stressing. Cross-sectional TEM analysis was done to analyze the physical degradation. EDX and EELS analysis were used for elemental analysis on the physical degradation. Some of the stressed devices were de-processed by etching method. The metallization and passivation layers were removed in order to observe the physical degradation from top-view in the SEM.

4.3 Results and Discussion

4.3.1 Electrical Stressing Results

The starting hypothesis was the role of 2DEG in ON-state degradation is to elevate the device temperature via joule heating. Devices stressed under ON-state condition were compared to devices stressed under OFF-state condition with 100°C higher base temperature. The purpose of the higher temperature was to compensate the temperature increase from joule heating during ON-state stressing. The increase in temperature was found to be 67°C by thermo-reflectance measurement. If the hypothesis is true, the devices stressed under OFF-state should degrade more than the devices stressed under ON-state condition. This is because the OFF-state stressing temperature is higher than the maximum junction temperature of the devices under ON-state condition.

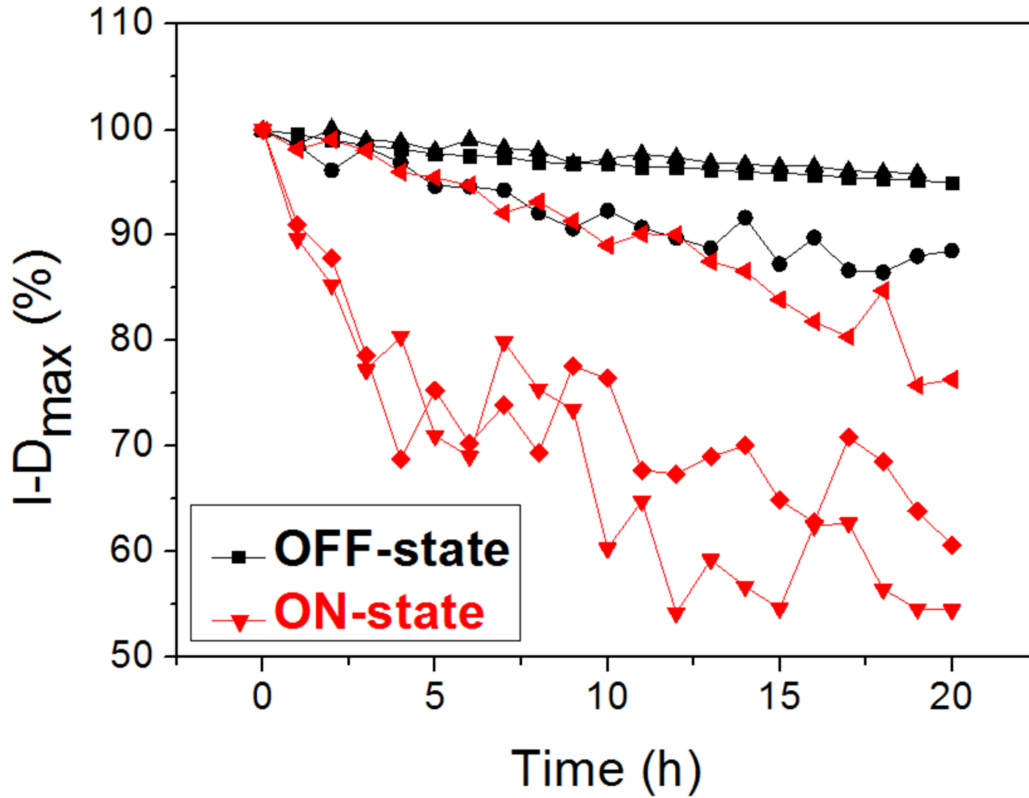

Figure 4.3 Normalized I_{D-max} evolution of AlGaN/GaN HEMTs under OFF-state (V_{DS} = 10 V, V_{GS} = -10 V, T_{base} = 250°C) and ON-state (V_{DS} = 20 V, V_{GS} =0 V, Max $T_{junction}$ = 217°C) conditions

Table 4.3 ON-state and OFF-state electrical stressing results and parameters

Stressing Parameters	OFF-state	ON-state
V_{DS} (V)	10	20
V_{GS} (V)	-10	0
V_{DG} (V)	20	20
Stressing duration (hr)	20	20
Base temperature (^{o}C)	250	150
Actual temperature (^{o}C)	250	217
Average I_{D-max} degradation (%)	6.8 ± 4.0	36.2 ± 11.2

Figure 4.3 shows the normalized I_{D-max} evolution over stressing time and Table 4.3 shows the stressing parameters and results for devices stressed under ON-state and OFF-state condition. It was observed that ON-state stressed devices on average degraded 30% more as compared to OFF-state stressed devices despite the fact that the OFF-state stressing base

temperature was 33°C higher than maximum stressing junction temperature in the ON-state. This suggests that the effect of drain current is more than just increasing device temperature via joule heating during ON-state stressing. The difference between ON-state and OFF-state degradation is not induced by electric field since V_{DG} was kept constant during the stressing. Figure 4.4 shows the vertical and horizontal electric field obtained by Silvaco simulation. It shows that there is almost no difference in the electric field between ON- and OFF-state stressing condition at the region between gate and drain. In the next section, microstructural characterization is discussed in order to understand more about the role of 2DEG in ON-state degradation.

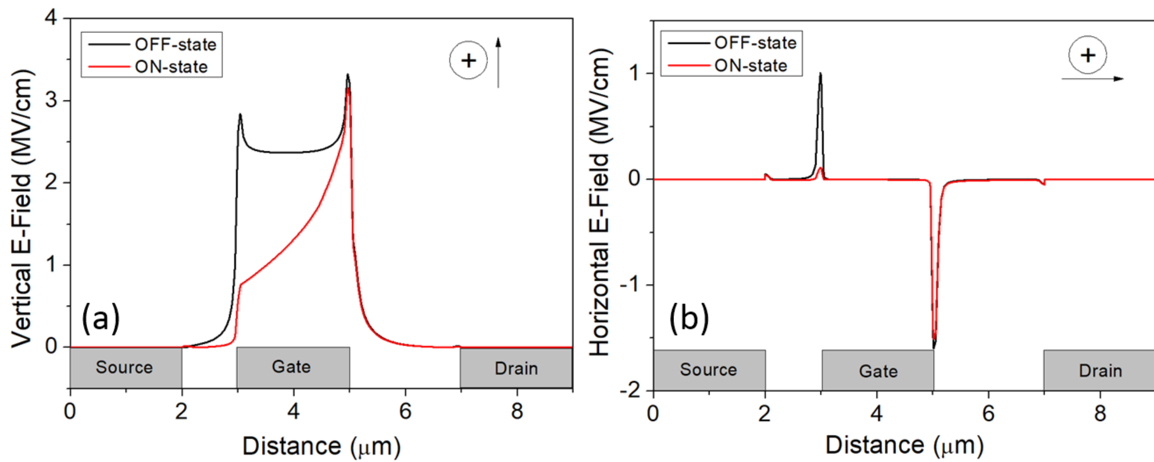

Figure 4.4 Simulated (a) vertical and (b) horizontal electric field for AlGaN/GaN HEMTs under OFF-state (V_{DS} = 10 V, V_{GS} = -10 V, T_{base} = 250°C) and ON-state (V_{DS} = 20 V, V_{GS} =0 V, Max $T_{junction}$ = 217°C) condition

4.3.2 Microstructure Characterization Results

After 20 hours electrical stressing, ON-state stressed devices showed higher $I_{D\text{-}max}$ degradation than OFF-state stressed devices. Microstructural characterization was done to analyze the physical degradation caused by electrical stressing. Si_xN_{1-x} passivation and metallization layer of the stressed devices were removed by etching method and analyzed under SEM.

Figure 4.5 shows the top-view SEM image of the devices stressed under OFF-state condition V_{DS} = 10 V, V_{GS} = -10 V at base temperature of 250°C and under ON-state condition V_{DS} = 20 V, V_{GS} =0 V at maximum junction temperature of 217°C. Degradation pits were observed at the gate edge on the drain side for the device stressed under OFF-state condition (Figure 4.5a). This result is consistent with the previous studies on OFF-state degradation [14-16, 75, 78]. On the other hand, for ON-state stressed devices, degradation pits extended from the gate edge region into large portion of the drain-gate access region (Figure 4.5b). This is likely to be the reason for 30% higher $I_{D\text{-}max}$ degradation of the ON-state devices than OFF-state devices on average. Figure 4.6 shows the pit distribution for the OFF- and ON-state-stressed devices. The pits were counted using ImageJ software [148]. The counting method has been explained in section 3.6.5. The total pit area was obtained by summing all the individual pit area in the drain-gate access region.

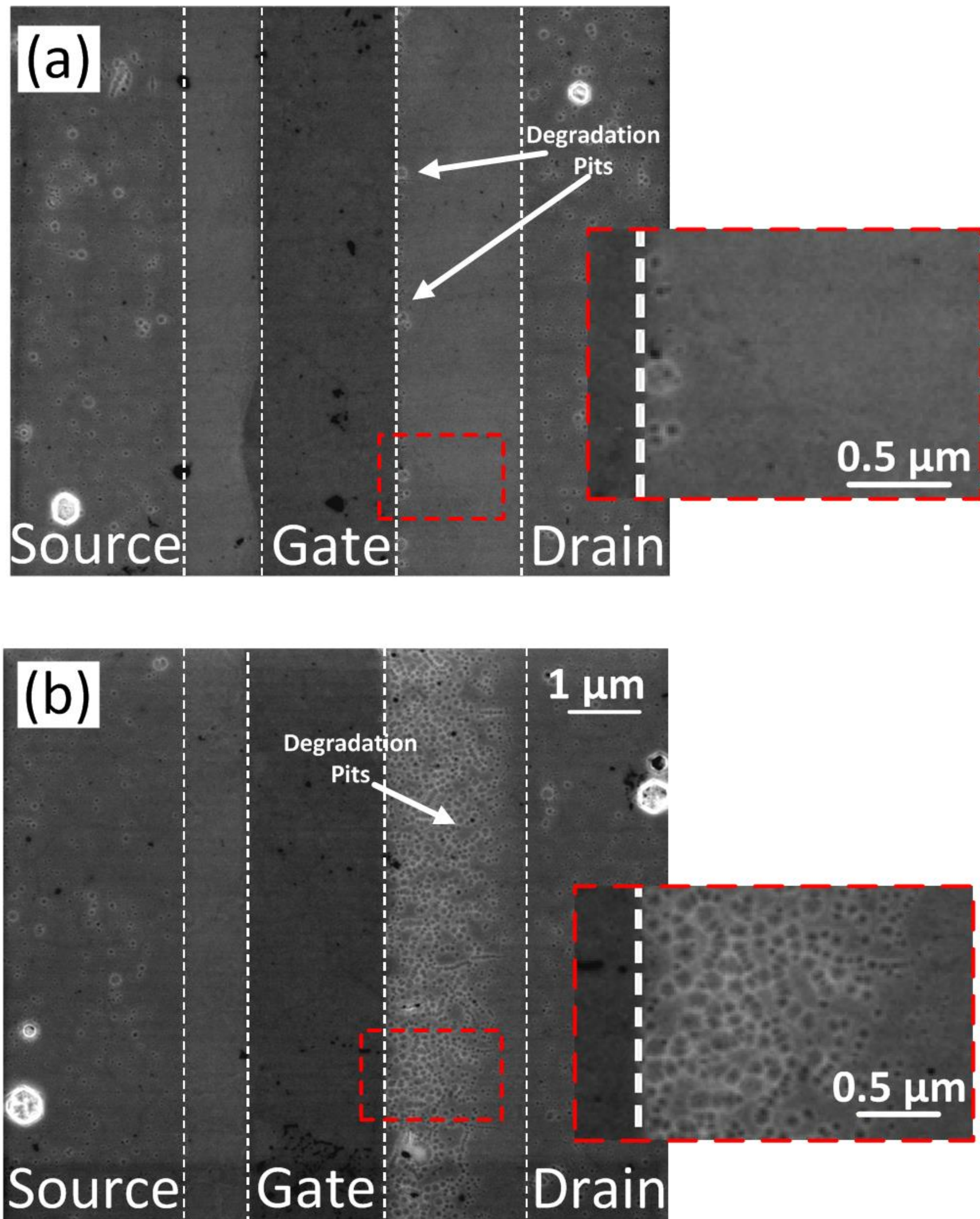

Figure 4.5 Top-view SEM image of the stressed device under (a) OFF-state (V_{DS} = 10 V, V_{GS} = -10 V, T_{base} = 250°C) and (b) ON-state (V_{DS} = 20 V, V_{GS} =0 V, max. $T_{junction}$ = 217°C) conditions after Si_xN_{1-x} passivation and metallization layers removal

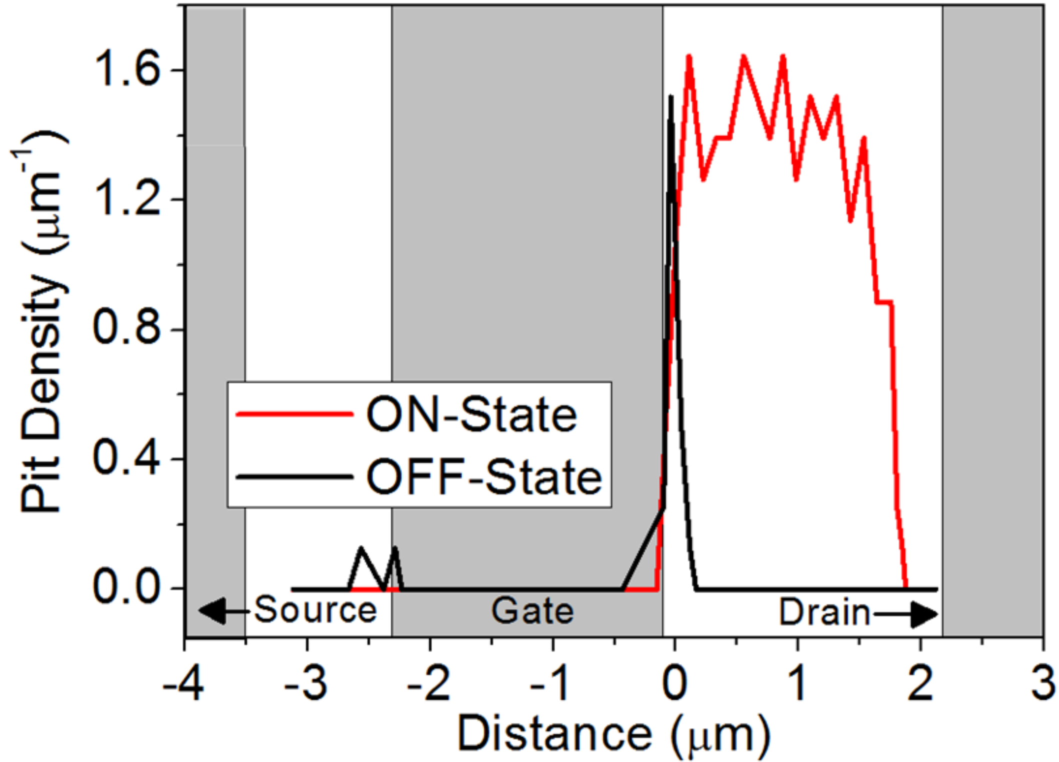

Figure 4.6 Pit distribution for the OFF-state (V_{DS} = 10 V, V_{GS} = -10 V, T_{base} = 250°C) and ON-state (V_{DS} = 20 V, V_{GS} =0 V, Max $T_{junction}$ = 217°C) stressed devices

Figure 4.7 shows the correlation between $I_{D\text{-}max}$ degradation and total pit area at the drain-gate access region for the devices stressed under ON-state condition. It was observed that $I_{D\text{-}max}$ degradation increases as the total pit area at drain-gate access region increases. This supports the electrical stressing results that ON-state stressed devices show higher $I_{D\text{-}max}$ degradation than OFF-state stressed devices due to more pits at drain-gate access region. This is because pitting makes AlGaN layer thinner and thinner AlGaN barrier layer will decrease the 2DEG density [68]. Therefore, the $I_{D\text{-}max}$ decreases as more pits formed at the drain-gate access region. Moreover, the pit density calculated from Figure 4.5b is 8.18×10^9 cm^{-2}. This pit density is comparable with the threading dislocation density of the chip (8.52×10^9 cm^{-2}) calculated from cross-sectional TEM. This suggests that pit formation is correlated with threading dislocation which is consistent with report on OFF-state degradation [75].

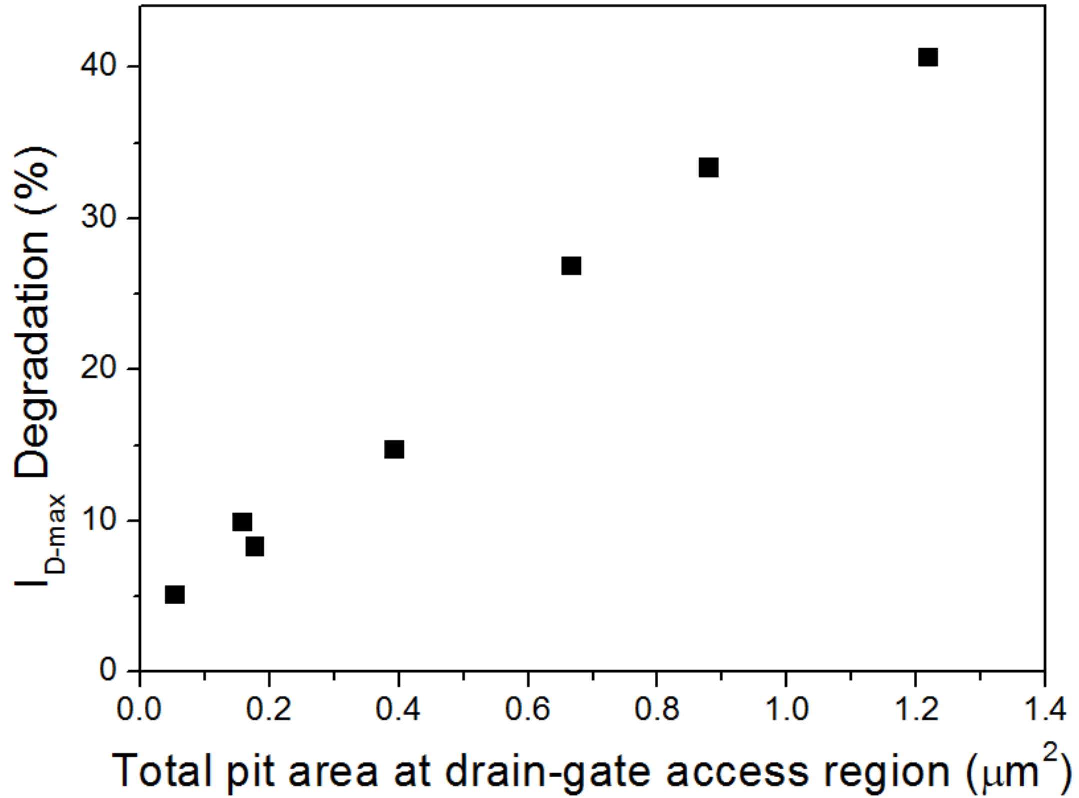

Figure 4.7 Correlation between $I_{D\text{-}max}$ degradation and total pit area at drain-gate access region for devices stressed under ON-state condition

Further analysis was done in order to understand the origin of the degradation pits located away from the gate-edge during ON-state stressing. Cross-sectional TEM was done on the ON-state stressed device without Si_xN_{1-x} passivation and metallization layer removal. Figure 4.8 shows the cross-sectional TEM images from both source and drain side of the ON-state-stressed device. Dark features were observed at the AlGaN/Si_xN_{1-x} interface at the drain side (Figure 4.8b and c). These features got smaller in size as the distance from the gate edge increases. The features decreases in size from 4.5 nm in height for location 260 nm away from gate edge (Figure 4.8b) to 2.2 nm in height for location 1000 nm (Figure 4.8c) from the gate edge. On the other hand, the dark feature was not observable at the source side (Figure 4.8d-f). This is consistent with Figure 4.5b that degradation pits were only observable at the drain side and fewer pits were found at locations further away from the gate edge.

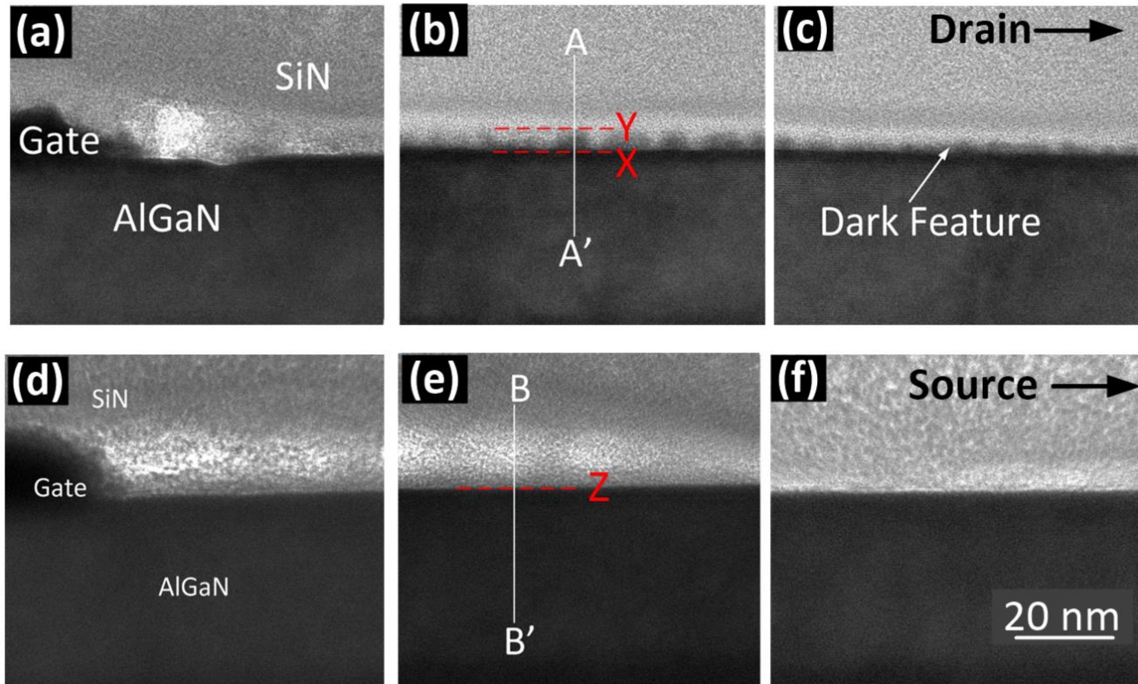

Figure 4.8 Cross-sectional TEM images of device stressed under ON-state condition before Si_xN_{1-x} passivation and metallization removal. Images taken at (a) the drain side gate edge, (b) 260 nm and (c) 1000 nm from gate edge in the drain-gate access region; (d) at the source side gate edge, (e) 300 nm and (f) 1000 nm from the gate edge in the gate-source access region. Dark features were observed at the AlGaN/Si_xN_{1-x} interface at the drain side. These dark features will be removed together with a portion of oxidized AlGaN layer during passivation and metallization removal to form degradation pits.

Elemental analysis was done on the dark features to characterize the elements present. EELS was used to characterize oxygen whereas EDX was used to characterize gallium and aluminum as EELS is more sensitive for light elements while EDX is more sensitive for heavy elements [138, 139]. Figure 4.9a and b shows the EELS/EDX line-scan for line A-A' in Figure 4.8b and line B-B' in Figure 4.8e, respectively. The dark feature contained gallium, aluminum and oxygen as shown in Figure 4.9a. Oxygen was also found in the AlGaN layer below the dark features (Figure 4.9a). This suggests that AlGaN layer has been partially oxidized and the oxidized AlGaN was removed together with Si_xN_{1-x} passivation layer during the passivation layer removal step, leaving behind degradation pits away from the gate edge. Figure 4.9b shows a sharp increase of aluminum and gallium and a sharp decrease of oxygen in the AlGaN layer. This suggests that no AlGaN was oxidized.

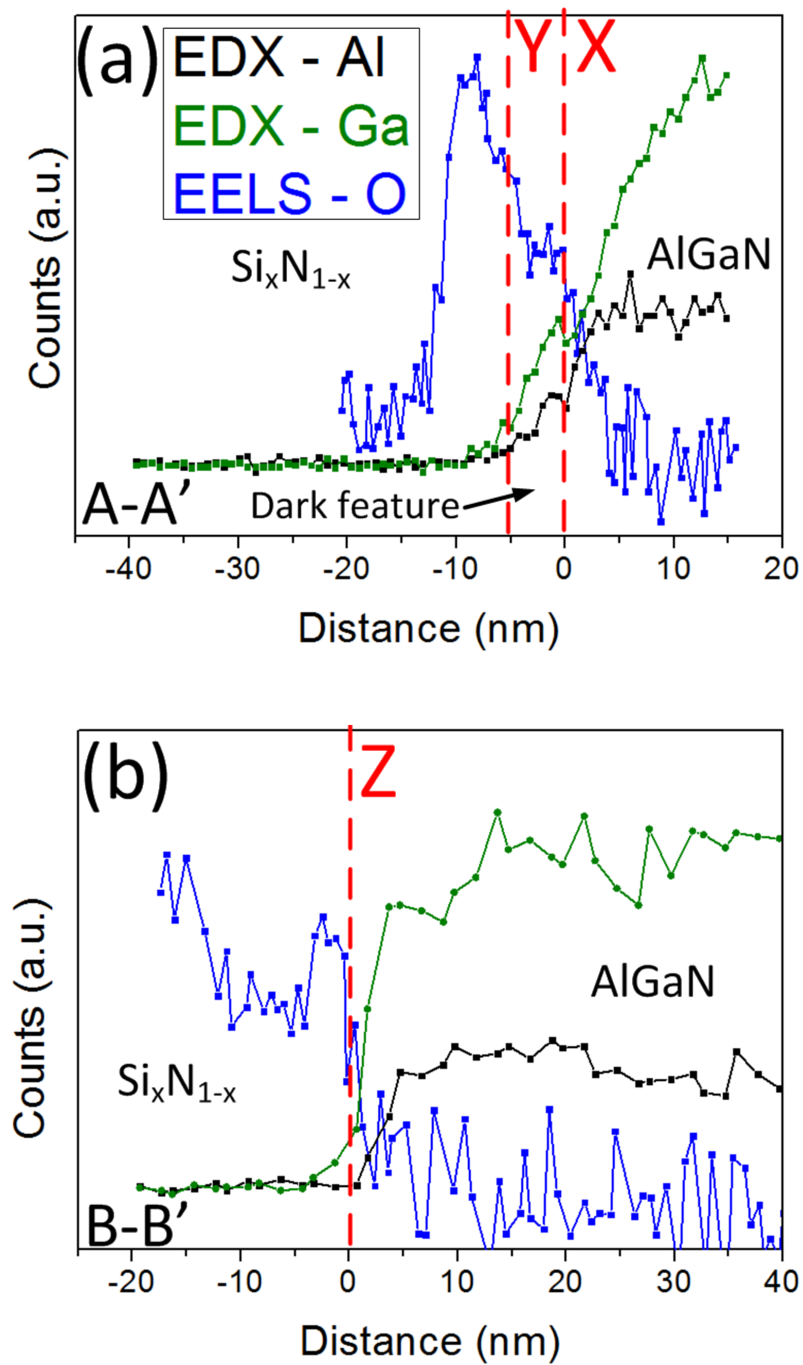

Figure 4.9 Elemental characterization by EELS and EDX line-scans along (a) A-A' (Figure 4.8b) and (b) B-B' (Figure 4.8e) for aluminum, gallium and oxygen. Zero distance is taken at the initial AlGaN/Si_xN_{1-x} interface

4.3.4 Electrical Stressing with Substrate Bias Results

Up to this point, it has been shown that the role of ON-state current is more than just increasing the device temperature via joule heating. Microstructural analysis shows the evidence of AlGaN oxidation at the region away from the gate edge on the drain side of the device. In the OFF-state degradation model proposed by Feng *et al.*, the electrons needed to reduce the water molecules come from the gate metal [16]. This leads to pit formation at the gate edge. In the ON-state, however, pits were observed away from the gate edge. This suggests that there might be another source of electrons that causes electro-chemical oxidation of AlGaN away from the gate edge. The hypothesis is that the electrons come from 2DEG in the AlGaN/GaN interface. This experiment was designed to prove this hypothesis. Devices were stressed under ON-state condition with negative substrate bias and UV exposure. Negative bias was applied to drive more electrons from 2DEG channel toward the AlGaN layer. The UV (254 nm) exposure was to ensure abundant holes being generated in the AlGaN layer for electro-chemical oxidation. Devices used for substrate bias experiment had comparable current density with the devices stressed without substrate bias.

Figure 4.10 shows the I_{D-max} degradation of ON-state-stressed devices with and without substrate bias. The I_{D-max} evolution for fresh device is also shown for comparison. It was observed that the device stressed with -20 V substrate bias degraded 14% more compared to device stressed without substrate bias. This means that the device stressed with substrate bias has larger total pit area at the drain-gate access region.

Figure 4.11 shows the pit distribution of the stressed and fresh devices after Si_xN_{1-x} passivation and metallization layers were removed. The pit density for device stressed with -20 V substrate bias (2.90×10^7 cm^{-2}) was three times higher than device stressed without substrate bias (1.03×10^7 cm^{-2}). It was also found that more pits were formed further from the gate edge for the device stressed with substrate bias. These results further support the correlation between hot electrons and pit formation. The negative bias forces more electrons from 2DEG channel to move up toward the AlGaN layer. This leads to more

AlGaN being oxidized which translates into more degradation pits and higher $I_{D\text{-}max}$ degradation.

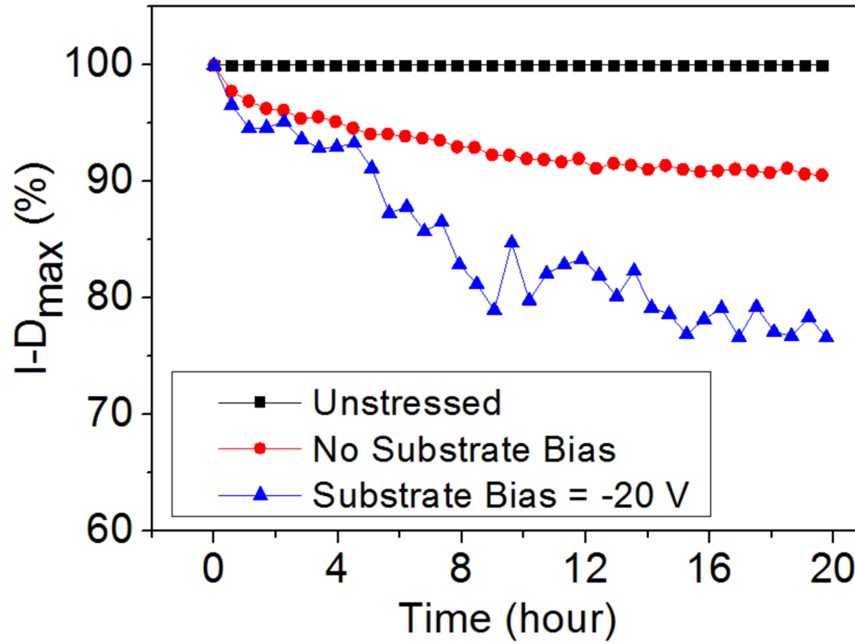

Figure 4.10 $I_{D\text{-}max}$ degradation vs. stressing time under UV (254 nm) exposure with and without substrate bias (V_{DS} = 10 V, V_{GS} = floating, T_{Base} = 200°C)

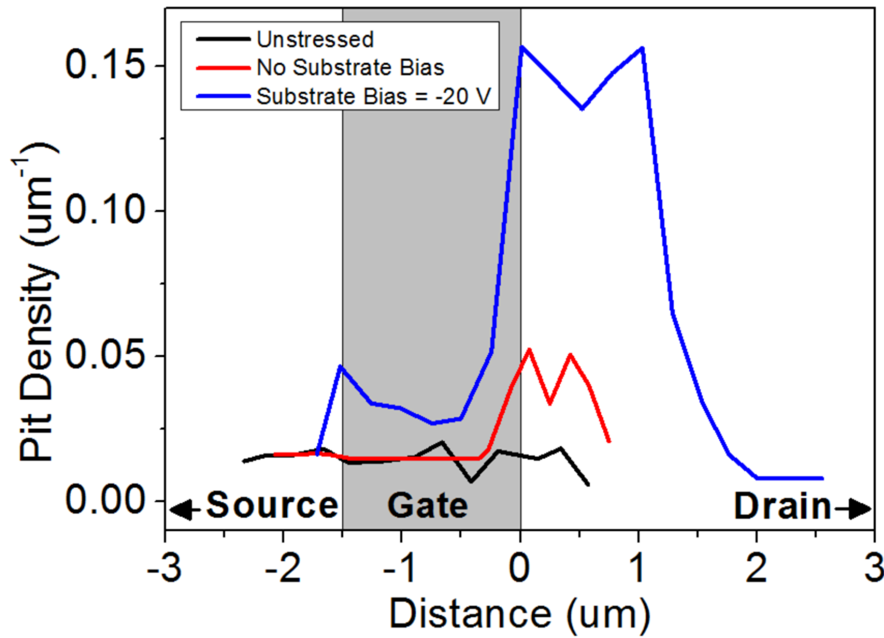

Figure 4.11 Pit distribution of the unstressed device and stressed devices under UV (254 nm) exposure and ON-state bias V_{DS} = 10 V, V_{GS} = floating with/without substrate bias = -20 V

4.3.5 Proposed Model for ON-State Degradation

In the previous section, it has been shown that hot electrons from 2DEG channel can move up to the AlGaN layer and contribute to electro-chemical oxidation of AlGaN. In this section, a model for ON-state degradation based on electro-chemical oxidation mechanism is proposed.

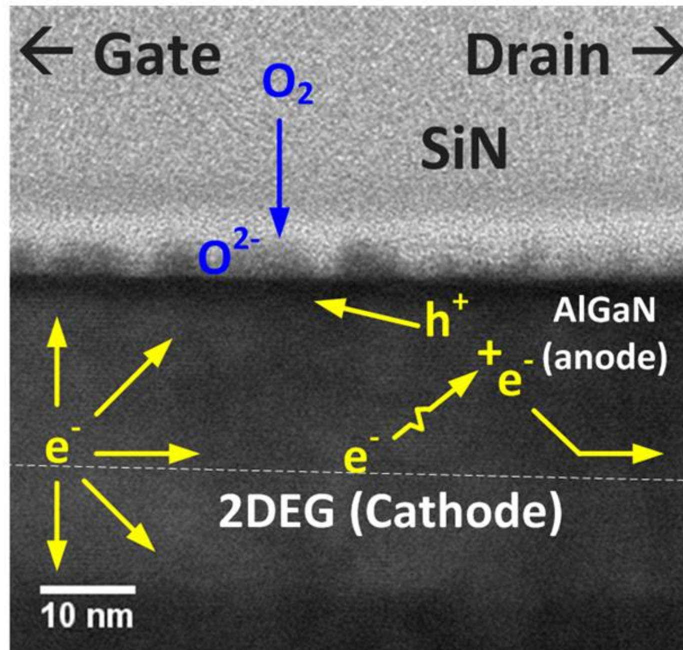

Figure 4.12 Proposed model for ON-state degradation based on electro-chemical oxidation mechanism

Figure 4.12 shows the proposed model for ON-state degradation. The hot electrons from 2DEG channel scatter toward AlGaN/Si_xN_{1-x} interface to reduce oxygen molecules to O^{2-} ions. The oxygen molecules penetrate through the Si_xN_{1-x} passivation to reach AlGaN/Si_xN_{1-x} interface. These electrons also might have enough energy to generate holes via impact ionization as holes are needed for the electro-chemical process [16]. The holes move toward AlGaN/Si_xN_{1-x} interface and react with AlGaN to form Al^{3+} and Ga^{3+} ions. Finally, Al^{3+} and Ga^{3+} ions react with O^{2-} ions to form aluminum and gallium oxides at the AlGaN/Si_xN_{1-x} interface, which was observed as dark features under TEM.

Killat *et al.* reported that impact ionization is possible on N-polar AlGaN/GaN HEMT under ON-state condition (V_{GS} = -0.5 V, V_{DS} = 10 V to 40 V) [150]. However, the devices used in this study are Ga-polar AlGaN/GaN HEMT. 2D finite element simulation was done to compare between Ga-polar and N-polar devices using Silvaco TCAD.

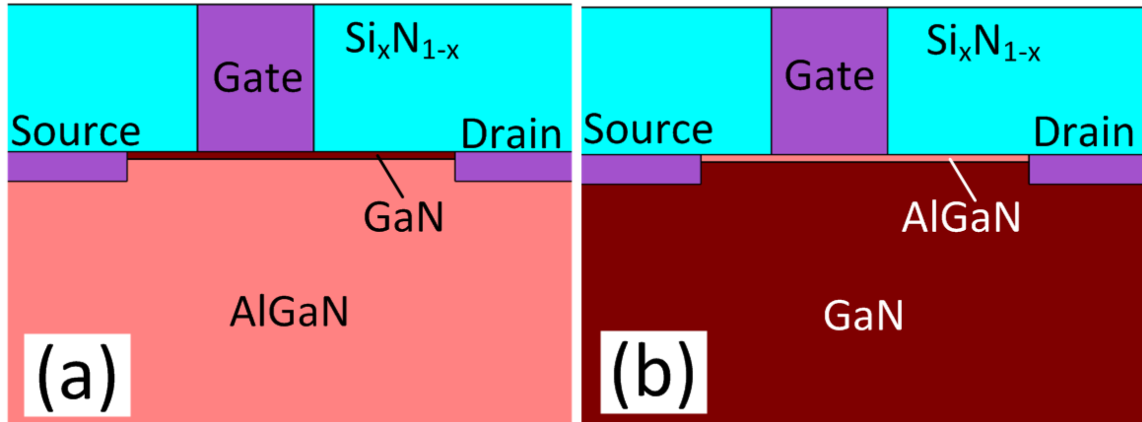

Figure 4.13 Device schematics used in Silvaco 2D finite element simulation for (a) N-polar and (b) Ga-polar AlGaN/GaN HEMT

Figure 4.13 shows the device schematics for Ga-polar and N-polar AlGaN/GaN HEMT devices. The same dimensions were used in this simulation for both N-polar and Ga-polar simulation i.e. L_G = 2 µm, L_{GD} = 2 µm and L_{SG} = 1 µm. In N-polar device, the GaN layer was 25 nm below the gate followed by 1.5 µm $Al_{0.3}Ga_{0.7}N$ whereas in Ga-polar device, the 25 nm and 1.5 µm layers were $Al_{0.3}Ga_{0.7}N$ and GaN, respectively. The bias condition was V_{DS} = 20 V and V_{GS} = 0 V.

Figure 4.14 shows the electron concentration and energy band diagram for both devices with ON-state bias condition V_{DS} = 20 V, V_{GS} = 0 V located 50 nm from the gate edge in the drain-gate access region. It is worth noting that the electron concentration and energy band diagram trends are for all locations along the drain-gate access region. The electron concentration is the highest at 2DEG. The highest electron concentration was located at the left and right side of the AlGaN/GaN interface for N-polar and Ga-polar devices, respectively. This is because the direction of spontaneous and piezoelectric polarizations of N-polar AlGaN/GaN HEMT is in opposite direction of that of Ga-polar AlGaN/GaN HEMT. This is consistent with the literature by Ambacher *et al.* [47].

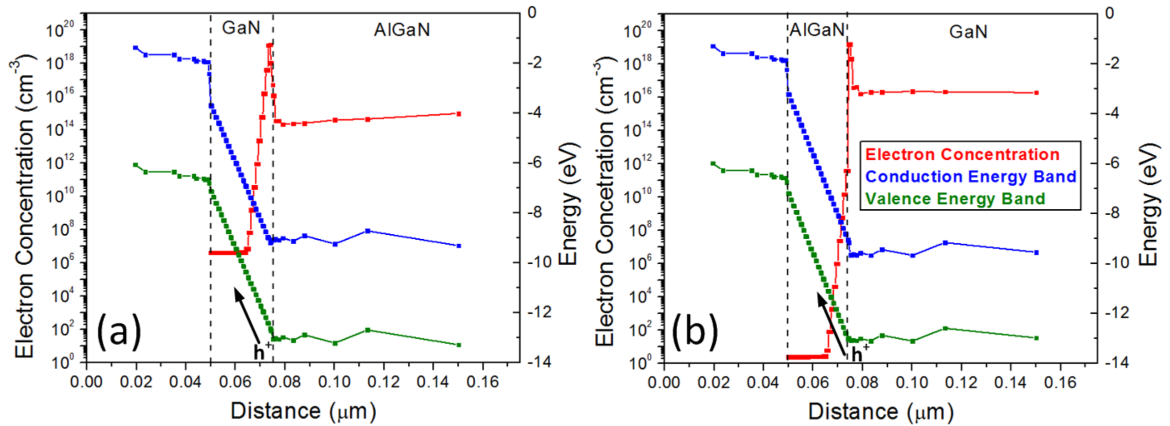

Figure 4.14 Electron concentration and energy band diagram for (a) N-polar and (b) Ga-polar $Al_{0.30}Ga_{0.70}N$/GaN HEMT under ON-state condition V_{DS} = 20 V, V_{GS} = 0 V obtained from 2D finite element simulation taken at 50 nm away from the gate edge in the gate-drain access region

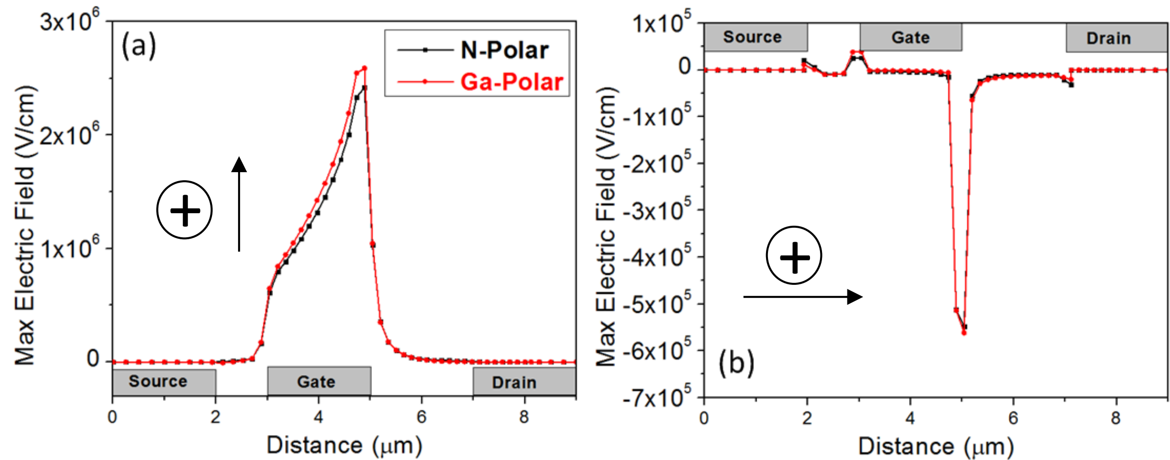

Figure 4.15 Maximum electric field distribution in (a) vertical direction and (b) lateral direction across the Ga-polar and N-polar AlGaN/GaN HEMT device under ON-state bias V_{DS} = 20 V and V_{GS} = 0 V

Figure 4.15 shows the maximum electric field distribution of both devices in vertical and lateral directions for Ga- and N-polar AlGaN/GaN HEMT devices under ON-state bias V_{DS} = 20 V, V_{GS} = 0 V. In vertical direction, Ga-polar device has a higher maximum electric field than N-polar. In lateral direction, the maximum electric field of Ga-polar device was comparable with that of N-polar device. The magnitude of electric field for N-polar device is comparable with Killat *et al.* (inset of Figure 4 in [150]). This suggests that the hot electrons in the 2DEG channel have a comparable energy for both types of AlGaN/GaN HEMT. Therefore, the impact ionization is also possible in Ga-polar devices used in this

study. Another study by Killat *et al.* reported impact ionization in Ga-polar HEMTs with InGaN back-barrier operating under ON-state condition V_{DS} = 20 V, V_{GS} = 0 V and current density = 0.9 mA/mm [151]. They reported that the impact ionization in InGaN layer is more significant than in AlGaN/GaN interface. Although, the devices used in this study have no InGaN back-barrier layer, they were stressed at 3 order higher current density (about 250 mA/mm) than Killat *et al.* for the same bias condition. Therefore, the impact ionization in AlGaN/GaN interface becomes more significant for devices used in this study.

In addition, Figure 4.14 shows that it is energetically favorable for the impact-ionization-generated holes to move towards the surface for both Ga-polar and N-polar devices. Similar trend was reported by Park *et al.* [152]. This means that the holes generated by impact ionization in Ga-polar AlGaN/GaN HEMT are able to reach the surface and contribute to the electro-chemical oxidation of AlGaN.

4.4 Summary

In this chapter, ON-state and OFF-state degradations were compared with a starting hypothesis that the role of 2DEG current in ON-state degradation is only to increase the junction temperature via joule heating that accelerates the degradation. OFF-state devices were stressed at 100°C higher to compensate the joule heating in ON-state stressing. ON-state-stressed devices showed 30% higher degradation despite being at 33°C lower stressing temperature measured by thermo-reflectance method. This result suggests that the role of 2DEG in ON-state degradation is more than increasing the junction temperature via joule heating.

Passivation layer and metallization layers of the stressed devices were removed using etching method and studied under SEM. Pits were found at the drain-gate access region in the device stressed under ON-state condition. On the other hand, pits were only found at the gate edge on the drain side of the OFF-state-stressed device. Cross-sectional TEM was done for device stressed under ON-state condition. EELS and EDX analysis in TEM showed dark features containing aluminum, gallium and oxygen at the AlGaN/Si_xN_{1-x}

interface only at the drain-gate access region of the ON-state-stressed devices. This suggests that AlGaN has been partially oxidized and it was removed during Si_xN_{1-x} passivation and metallization etching, and leaving behind degradation pits at the drain-gate access region. These degradation pits in the drain-gate access region are likely to be the reason of higher I_{D-max} degradation as compared to OFF-state-stressed devices. Also, the pit density was comparable with the threading dislocation of the chip. This further emphasizes the importance of threading dislocation density in AlGaN/GaN HEMT reliability.

ON-state stressing with negative substrate bias was done to investigate further the role of 2DEG electrons in ON-state degradation. Negative substrate bias was used to push electrons from 2DEG channel to AlGaN/Si_xN_{1-x} interface. The device stressed with negative substrate bias showed larger I_{D-max} degradation and more pits at the drain-gate access region compared to the device stressed without substrate bias. This result also further supports the correlation between hot electrons and pit formation which translates into higher I_{D-max} degradation. This result confirms that 2DEG electrons play a role in the electro-chemical oxidation of AlGaN under ON-state condition beyond joule heating. Finally, ON-state degradation model was proposed based on electro-chemical oxidation. Hot electrons are being injected from 2DEG channel to at AlGaN/Si_xN_{1-x} interface and reduce the oxygen molecules to O^{2-}. Then O^{2-} ions oxidize the AlGaN in the presence of impact-ionization-generated holes.

In reliability, the most damaging factor has to be solved first. The findings in this chapter highlight the importance of understanding ON-state reliability for AlGaN/GaN HEMT devices as ON-state degradation is more severe than OFF-state degradation.

Chapter 5

Effect of Current Density on AlGaN/GaN High Electron Mobility Transistor Degradation under ON-State Stressing

2DEG electrons play a significant role in AlGaN/GaN HEMT degradation under ON-state condition. The amount of electrons in the 2DEG channel increases proportionally with current density. In this chapter, the effect of current density on AlGaN/GaN HEMT degradation under ON-state condition is studied. The first part of the chapter discusses about the determination of stressing condition with the help of thermal and electric field simulations to eliminate the effect of joule heating from higher current density. The second part of the chapter discusses about the effect of current density on the device degradation. It is shown that $I_{D\text{-}max}$ *degradation consists of two parts i.e. fast and slow degradation modes. These two modes are differentiated by the source of oxygen that contributes to the electro-chemical oxidation of AlGaN at the AlGaN/*Si_xN_{1-x} *interface. It was also found that higher current density stressing results in higher* $I_{D\text{-}max}$ *degradation and it has a strong correlation with the maximum distance for pit formation at drain-gate access region. Finally, the ON-state degradation mechanism is proposed based on the different current densities.*

5.1 Introduction

In the previous chapter, it has been shown that hot electrons in 2DEG channel contribute to the AlGaN/GaN HEMT degradation under ON-state condition which leads to higher I_{D-max} degradation as compared to OFF-state condition. I_{D-max} degradation correlates well with the total pit area at the drain-gate access region for devices stressed under ON-state condition. However, the effect of different current density on I_{D-max} degradation and pit formation at the drain-gate access region is still unclear.

In this chapter, the effect of different current density on AlGaN/GaN HEMT degradation under ON-state condition was investigated. In order to do this, the effect of other factors that may cause device degradation i.e. temperature [77], threading dislocation [75, 76] and applied bias [81, 114, 153] have to be minimized. The first part of the chapter discusses about how to decouple the effect of current density from temperature and electric field during ON-state degradation. The second part of the chapter discusses about the results of ON-state stressing with different current density where the two different degradation modes were observed. Thus, the third part of this chapter discusses about the two different degradation modes due to different source of oxygen. Some experiments were done to prove this hypothesis. This is important because these two degradation modes will be further discussed in the subsequent sections and also chapter 6. In the last part, the correlation between current density and pit formation is discussed.

5.2 Experimental Details

In order to study the effect of current density, the effects of other factors that can accelerate degradation have to be minimized. The AlGaN/GaN HEMT devices used in this study have the same dimensions and come from the same wafer. Therefore, they have the same electric field when same bias is applied and the same threading dislocation density. Thermo-reflectance and thermal simulation were used to calculate the junction temperature of the device during ON-state stressing. Thus, different current density stressing conditions with the same junction temperature can be obtained by adjusting the base temperature

correspondingly. The drain bias was kept constant and gate bias was fine-tuned until the desired current densities were obtained. After the stressing conditions were determined, the devices were electrically stressed under ON-state condition followed by microstructure characterization.

5.2.1 Thermo-reflectance Measurement

The junction temperature during the ON-state stressing was calculated using the thermal model. This model has to be calibrated first in order to obtain accurate junction temperature. Thermo-reflectance measurement was used to calibrate the model. The measurements were done on an unstressed device at various ON-state biasing conditions.

Table 5.1 Device dimensions and parameters used in thermo-reflectance measurements

Device Dimensions/Parameters	Calibration
V_{DS} (V)	20
V_{GS} (V)	-2, -1.5, -1, -0.5, 0
L_{GS} (μm)	1.5
L_G (μm)	3.5
L_{GD} (μm)	2.5
H_G (μm)	0.51
W_G (μm)	100
Base temperature (^oC)	25, 40, 60

Table 5.1 shows the device dimension and parameters used in the thermo-reflectance measurements. The base temperatures used were 25, 40 and 60^oC. There were 5 different bias conditions for each base temperature. Thus, there were total of 15 junction temperature measurements obtained in this experiment. The collection time for each measurement was 5 minutes. Device characteristics were checked before and after the measurements to ensure there was no degradation caused by the measurements. These measurements were then compared to the junction temperature calculation from the thermal finite element simulation.

5.2.2 Thermal Finite Element Simulation

The thermal finite element simulation is used to calculate the junction temperature of the device during ON-state stressing. This simulation has to be calibrated against junction temperature measurements by thermo-reflectance. The device dimensions used for the simulation can be found in the Table 5.1 and the simulation details can be found in section 3.3.2. For this thermal simulation, power density was calculated using equation 3.1 and keyed into the heat source.

Table 5.2 Power density calculation for thermal finite element simulation

Base Temperature (°C)	V_{GS} (V)	V_{DS} (V)	I_{DS} (mA)	P (W)	Heat Source Volume (μm^3)	Power Density* (W/μm^3)
25	0	20	21.3	0.425	178.5	0.00238
25	-0.5	20	18.3	0.366	178.5	0.00205
25	-1	20	15.2	0.304	178.5	0.00170
25	-1.5	20	11.8	0.236	178.5	0.00132
25	-2	20	8.6	0.172	178.5	0.00096
40	0	20	19.8	0.396	178.5	0.00222
40	-0.5	20	16.6	0.332	178.5	0.00186
40	-1	20	13.5	0.270	178.5	0.00151
40	-1.5	20	10.3	0.206	178.5	0.00115
40	-2	20	7.3	0.146	178.5	0.00082
60	0	20	15.7	0.314	178.5	0.00176
60	-0.5	20	13.0	0.260	178.5	0.00146
60	-1	20	10.3	0.206	178.5	0.00115
60	-1.5	20	7.7	0.154	178.5	0.00086
60	-2	20	5.3	0.106	178.5	0.00059

*calculated using equation 3.1

Table 5.2 shows the power densities for all the 15 bias conditions for the thermal simulation. The drain current was measured during thermo-reflectance measurements. The maximum

junction temperature was calculated and compared with the thermo-reflectance measurements.

After the thermal model was calibrated, this model was used to calculate the junction temperatures for the ON-state stressing conditions. Table 5.3 shows the device dimensions and parameters used in the ON-state stressing. Junction temperatures were calculated for 5 different power densities for each base temperature. A total of 10 junction temperatures were calculated using the model.

Table 5.3 Device dimensions and parameters used in ON-state stressing

Device Dimensions/Parameters	ON-State Stressing
L_{GS} (µm)	0.8
L_G (µm)	2
L_{GD} (µm)	4
H_G (µm)	0.51
W_G (µm)	100
Heat source volume (µm^3)	102
Base temperature (^oC)	175, 200
Power density (10^{-3} W/µm^3)	0.98, 1.96, 2.94, 3.92, 4.90

5.2.3 Electric Field Finite Element Simulation

The devices used in this experiment are normally-ON devices with a threshold voltage of approximately -3 V. In this experiment, different current densities were obtained by applying different V_{GS} ranges from -3 V to 0 V at constant V_{DS}. When V_{DG} varies, the electric field at gate-drain access region will change. In the current density experiment, the effect of electric field has to be minimized. Thus, it is important to know the change in electric field within the range $-3 < V_{GS} < 0$. This 2D finite element simulation was used to simulate the electric field distribution at different V_{GS}. Table 5.4 shows the device details used in this electric field simulation. The AlGaN composition used in this simulation is $Al_{0.3}Ga_{0.7}N$. The device dimensions were the same as the device used in the current density

experiment. The electric field in both lateral and vertical directions were simulated from V_{GS} = -3 V to V_{GS} = 0 V with an interval of 1 V.

Table 5.4 Device dimensions and parameters for electric field finite element simulation

Device Dimensions/Parameters	Value
V_{DS} (V)	20
V_{GS} (V)	-3 to 0
L_{GS} (μm)	0.8
L_G (μm)	2
L_{GD} (μm)	4
AlGaN thickeness (nm)	18
GaN thickness (nm)	2200

5.2.4 Electrical Stressing

After the junction temperature and electric field were calculated, the devices were stressed under ON-state condition with different current densities. This experiment was done using the in-house-built system shown in Figure 3.4. The purpose of this experiment is to examine the effect of different current density, i.e. the amount of hot electrons in the channel, on AlGaN/GaN HEMT degradation under ON-state condition.

Table 5.5 Stressing parameters for different current density

Device Code	V_{GS} (V)	V_{DS} (V)	J_{DS}* (A/mm)	Base T (°C)	Max T_{junc}** (°C)
HC1	-0.49	20	0.1688	175	230
HC2	-0.55	20	0.1698	175	230
HC3	-0.74	20	0.1686	175	230
LC1	-1.40	20	0.0885	200	230
LC2	-1.55	20	0.0892	200	230
LC3	-1.45	20	0.0891	200	230

*Measured current density at t = 0

**Max junction temperature is calculated using thermal simulation at t = 0

Table 5.5 shows the stressing parameters used in the ON-state stressing. Identical devices were stressed with constant V_{DS} and V_{GS} for 120 hours. Due to limited number of samples, only two different current densities were used and 3 samples were stressed for each current density. The high current density (0.1686 – 0.1698 A/mm) was about twice of that of the low current density (0.0885 – 0.0892 A/mm). The V_{GS} was fine-tuned in order to obtain the desired current density at V_{DS} = 20 V. The junction temperature and electric field were kept approximately constant throughout the stressing. 230°C was chosen as maximum junction temperature in this experiment as this temperature was high enough to accelerate the degradation without the possibility of activating other degradation at higher temperature such as in Ohmic contact degradation [25] or Schottky contact degradation [84].

In addition to the current density stressing, there were additional experiments done to investigate other matters that were related to the ON-state degradation. Table 5.6 shows the stressing parameters for the additional experiments under ON-state condition. Stressing conditions 1 and 2 were used to investigate the role of oxygen from environment in AlGaN/GaN HEMT degradation under ON-state condition. In this experiment, the device stressed in high vacuum condition was compared to device stressed in ambient condition. The stressing was done with constant ON-state bias condition V_{DS} = 30 V, V_{GS} = 0 V at base temperature of 150°C. The vacuum level used in this experiment was 1×10^{-5} Torr and the stressing duration was 500 hours.

Table 5.6 Stressing parameters for additional experiment under ON-state condition

Stressing condition	1	2	3
V_{DS} (V)	30	30	0
V_{GS} (V)	0	0	0
Stressing duration (hr)	500	500	120
Base temperature (°C)	150	150	260
Vacuum level (Torr)	Ambient	1×10^{-5}	Ambient

Stressing condition 3 was used to investigate the effect of thermal stressing without any bias applied on AlGaN/GaN HEMT degradation. In this experiment, the device was

stressed at 260°C without any bias applied for 120 hours and then the $I_{D\text{-}max}$ evolution was compared with the other 6 devices stressed with different current densities. The base temperature for stressing condition 3 was 30°C higher than the maximum junction temperature of the other 6 devices stressed under ON-state condition.

5.2.5 Microstructural Characterization

In this chapter, cross-sectional TEM was done to analyze the physical defects and AlGaN/Si_xN_{1-x} interface of the stressed and fresh device, respectively. EDX and EELS analysis were used for elemental analysis on AlGaN/Si_xN_{1-x} interface. Metallization and passivation layers were removed for some of the stressed devices to analyze the pit distribution at the drain-gate access region under SEM.

5.3 Results and Discussions

5.3.1 Stressing Condition Determination

Appropriate stressing condition has to be determined before starting the current density stressing. This involved calculating the junction temperature and electric field using simulation for ON-state condition. Thermal model calibration was done before using the thermal model for junction temperature calculation. Then, electric field difference within the range $-3 < V_{GS} < 0$ will be discussed. At the end of this sub-section, different current densities used for the AlGaN/GaN HEMT stressing under ON-state condition are discussed.

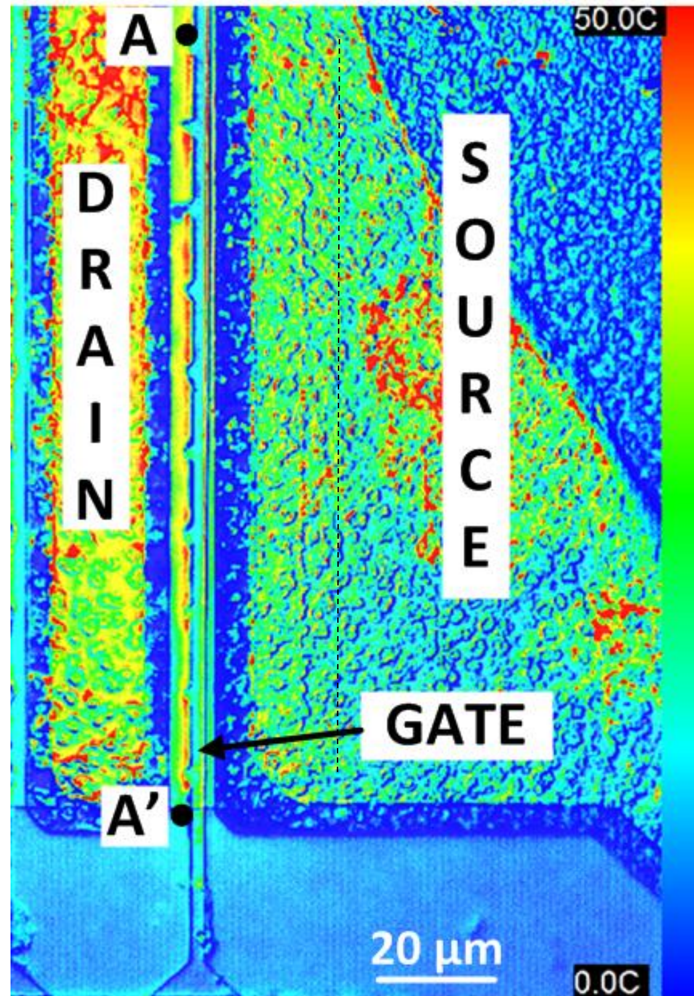

Figure 5.1 Temperature increase distribution under V_{DS} = 20 V, V_{GS} = 0 V, I_{DS} = 21.3 mA and T_{Base} = 25°C measured by thermo-reflectance method

Figure 5.1 shows a typical thermal map from thermo-reflectance measurement. This thermal map shows the temperature increase due to joule heating under ON-state condition V_{DS} = 20 V, V_{GS} = 0 V, I_{DS} = 21.3 mA and T_{Base} = 25°C. In this measurement, only the right gate was turned ON. It was observed that the hottest region between source and drain pad is the gate edge of the drain side. This corresponds to the location where electric field and power dissipation are the highest [154-156]. The temperature increase in this region was about 50°C. The maximum junction temperature was the summation of maximum temperature increase along the vertical line A-A' and the applied base temperature. The measured maximum junction temperature was then compared with the calculated maximum temperature from the thermal simulation at the same location.

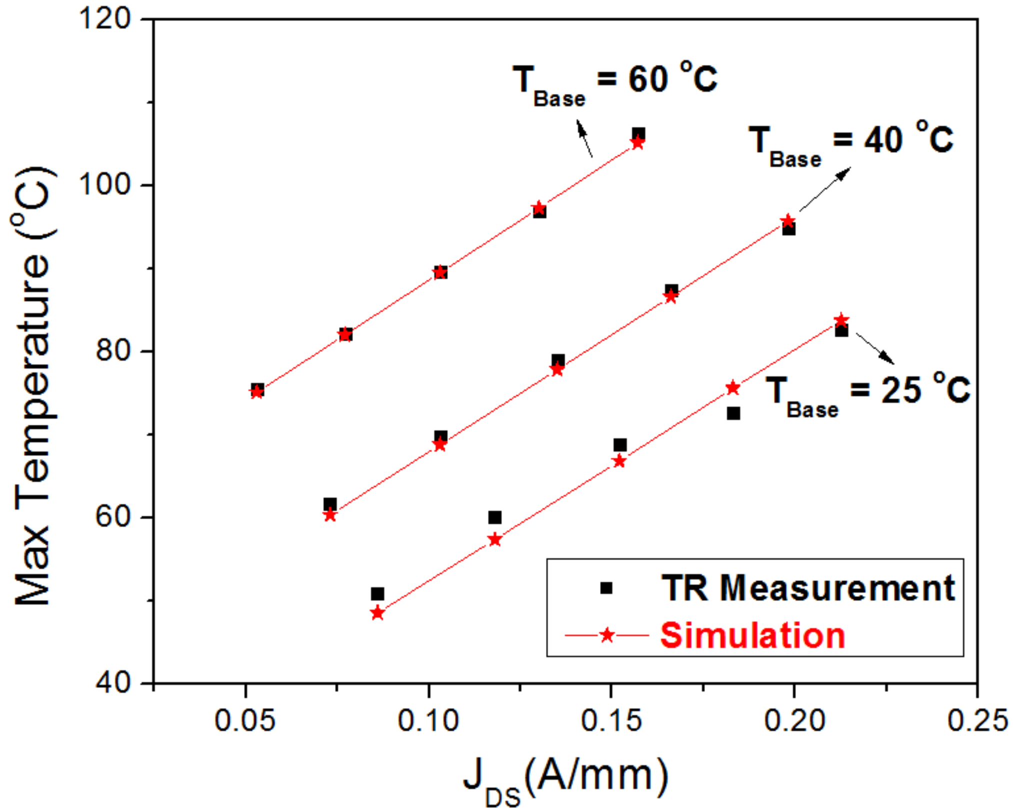

Figure 5.2 Comparison between maximum junction temperatures obtained by thermo-reflectance (TR) measurement and thermal simulation at different current densities and base temperatures

Figure 5.2 shows the maximum junction temperature comparison between thermo-reflectance measurement and thermal simulation at different current densities and base temperatures. It was observed that maximum junction temperature increases linearly for the same base temperature with a slope of 2.84°C mm/A. When the base temperature increased, the points shifted upward but the slope remained constant. The maximum junction temperatures calculated by thermal simulation correlated well with the thermo-reflectance measurements. This result validated the thermal simulation done using TAS. Therefore, the same model could be used to calculate the junction temperature for the current density stressing experiments assuming that the relationship between current density and maximum temperature is linear for all base temperatures. This assumption is supported by Martin-Horcajo *et al.* who reported linear relationship up to ambient temperature of 225°C [149].

The next step is to determine the stressing conditions for the current density stressing. Table 5.3 shows the device dimensions used for this experiment. The base temperatures were 200°C and 175°C for low and high current densities, respectively. Five different power densities were simulated for each base temperature. The five points were then linearly fitted.

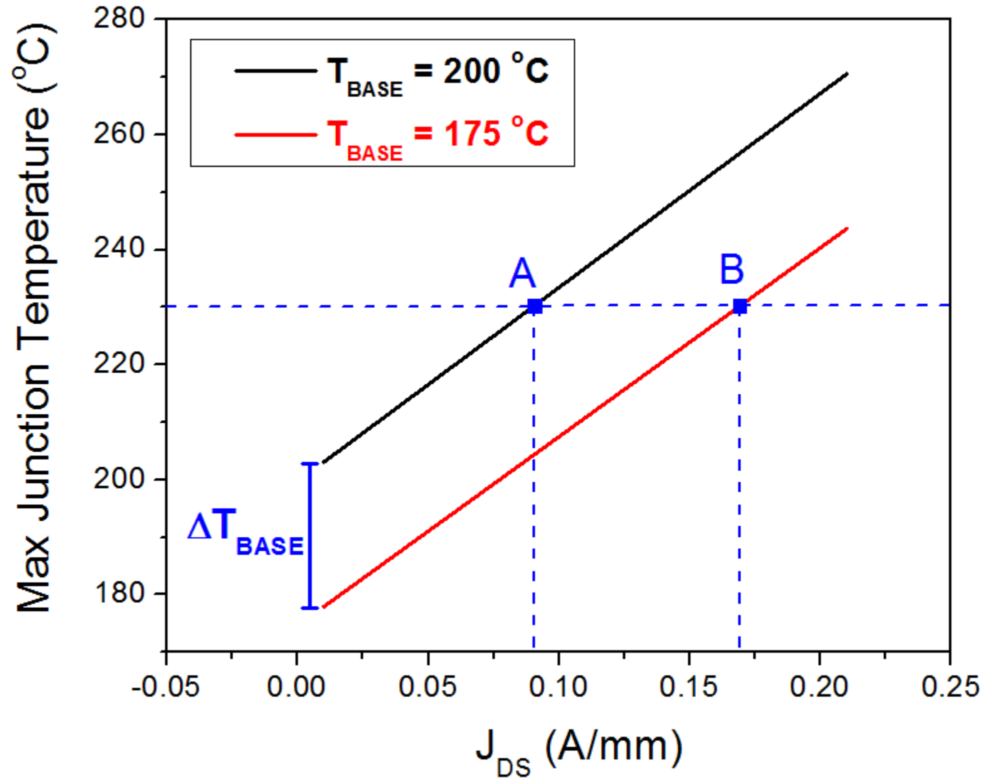

Figure 5.3 Calculated maximum junction temperature for different current densities at base temperature 200°C and 175°C

Figure 5.3 shows the fitting lines of maximum temperature calculation from the thermal simulation for different current densities at base temperature 200°C and 175°C. From this plot, a horizontal line was drawn for the maximum temperature of 230°C. This temperature would be the stressing junction temperature in the current density experiment. The intercepts between the horizontal line and the two fitting lines were the stressing conditions labeled as point A and B on Figure 5.3. Point A and B were the stressing conditions required for low and high current densities, respectively. For point A, the current density is 0.090 A/mm and T_{Base} = 200°C whereas for point B, the current density is 0.169 A/mm and T_{Base}

= 175°C. The higher joule heating caused by the higher current density was compensated with a lower base temperature in order to get the same stressing temperature.

In order to obtain the desired current densities, V_{GS} was fine-tuned at constant V_{DS} = 20 V for each condition. It is important to ensure that the electric field does not change significantly when V_{GD} changes because electric field is one of the factors that can affect the AlGaN/GaN HEMT degradation [17, 81, 82, 114, 153]. Electric field simulation was used to investigate this problem.

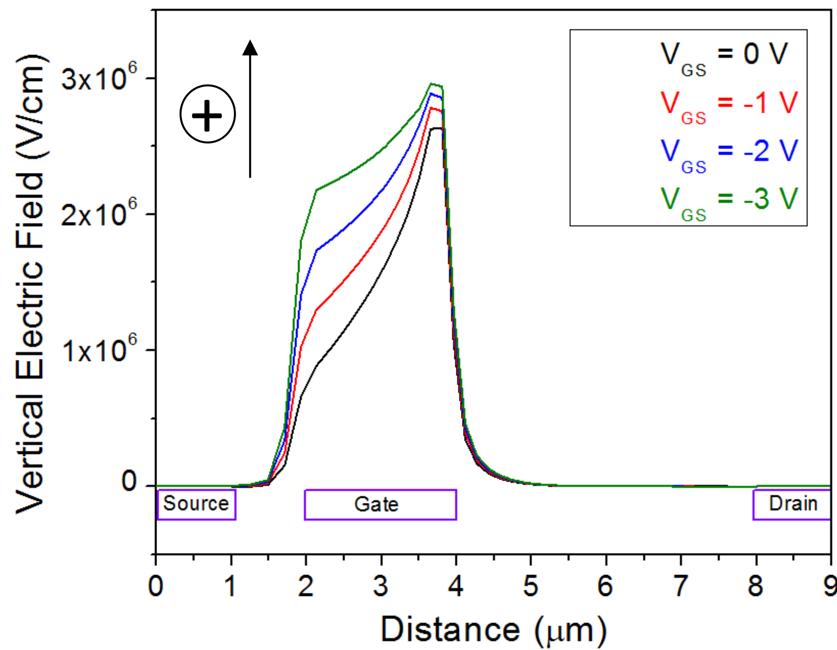

Figure 5.4 Vertical electric field distribution for V_{DS} = 20 V and different V_{GS} at the top AlGaN layer

Figure 5.4 and Figure 5.5 show the electric field distributions for vertical and horizontal directions respectively under ON-state condition V_{DS} = 20 V. In the vertical direction, change in V_{GS} affected the electric field under the gate the most whereas in the horizontal direction, change in V_{GS} affected the electric field at the gate edges. The maximum electric-field in the top AlGaN layer was located at the gate edge on the drain side of the device for both vertical and horizontal directions. This high electric field at the gate edge accelerates the electrons in 2DEG channel that leads to pit formation at the drain-gate access region in

ON-state degradation. Therefore, it is important to take note how much the electric field changes with V_{GS} to minimize the effect of electric field during the current density stressing.

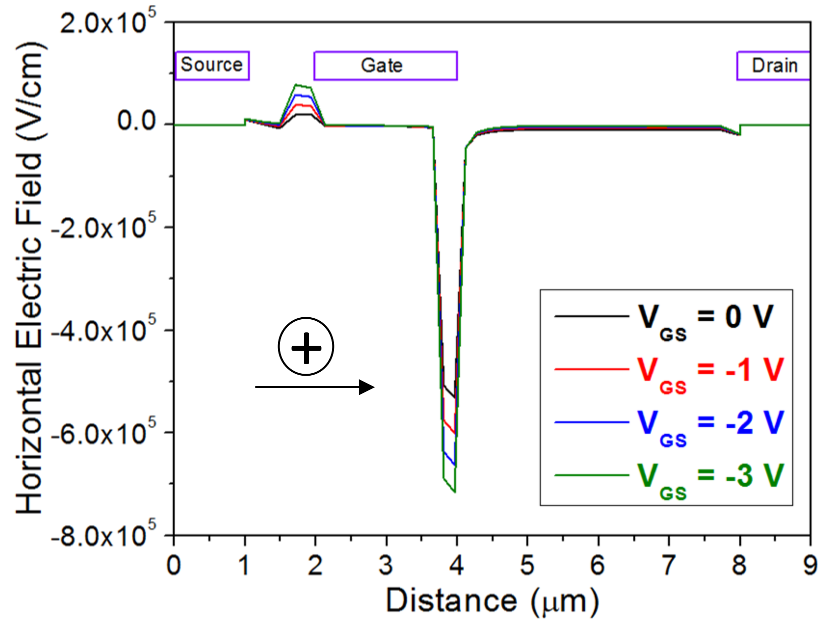

Figure 5.5 Horizontal electric field distribution for V_{DS} = 20 V and different V_{GS} at the top AlGaN layer

Figure 5.6 shows the maximum vertical and horizontal electric fields at different V_{GS} with constant V_{DS} = 20 V. The maximum electric field decreases with increasing V_{GS} from -3 V to 0 V for both directions because the voltage difference between gate and drain decreases. The same trend was observed for the maximum electric field at the SiN passivation layer, top AlGaN layer and 2DEG.

V_{GS} used in the current density stressing ranges from -1.55 V to -0.45 V (Table 5.5). Within this range, the maximum electric field difference was up to 15% in both directions at all layers. This electric field difference is small and this difference creates negligible additional physical degradation [16]. Therefore, this justifies current density stressing condition.

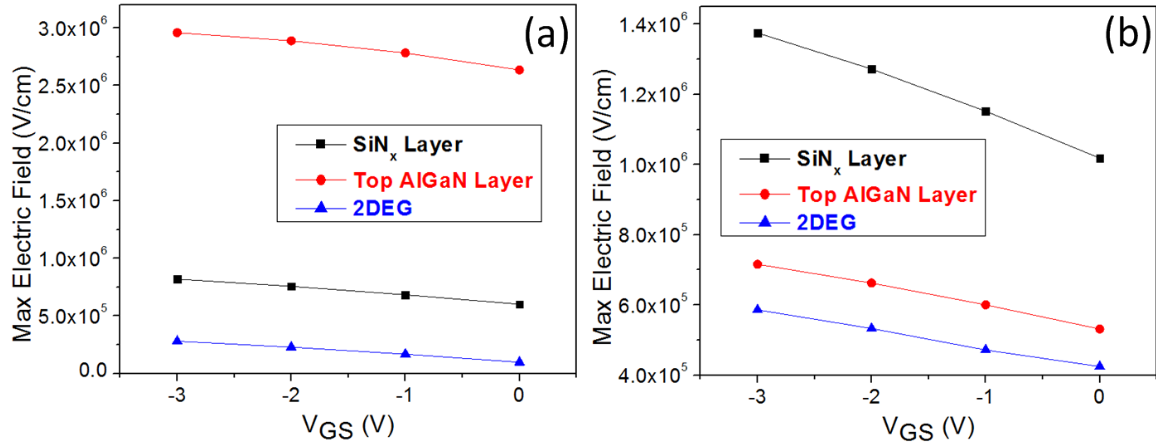

Figure 5.6 Maximum (a) vertical and (b) horizontal electric field for V_{DS} = 20 V and different V_{GS} at various locations

In this section, the thermal model used to calculate the junction temperature and the electric field simulation to check the change in electric field with V_{GS} have been elaborated. The results justified the current density stressing conditions where the maximum junction temperature was 230°C and the electric field difference was capped at 15%.

5.3.2 Current Density Stressing

After the stressing parameters were carefully determined, the devices were stressed under the ON-state with high and low current densities. In this section, the results of ON-state stressing are discussed. Table 5.7 shows the stressing parameters and results for devices stressed under ON-state condition with different current densities. Devices were stressed under ON-state condition with constant V_{DS} and V_{GS}. When the devices degraded, $I_{D\text{-}max}$ and current density decreased over time. Average current density (J_{DS}) was calculated by averaging the current density throughout stressing duration. The average current density for high current density devices was higher than that of low current density devices. This confirmed that the current density for the high current density devices was always higher than that of low current density devices throughout the stressing duration.

Table 5.7 Stressing parameters and results for devices stressed under ON-state condition with different current densities

Device Code	V_{GS} (V)	V_{DS} (V)	J_{DS}* (A/mm)	Base T (°C)	Max T_{junc}** (°C)	Average J_{DS} (A/mm)	Max E-field (MV/cm)	Final $I_{D\text{-}max}$ Deg (%)
LC1	-1.40	20	0.0885	200	230	0.0882 ± 0.003	2.89	9.9
LC2	-1.55	20	0.0892	200	230	0.0772 ± 0.003	2.91	12.2
LC3	-1.45	20	0.0891	200	230	0.0806 ± 0.001	2.90	14.1
HC1	-0.49	20	0.1688	175	230	0.1551 ± 0.004	2.77	32.2
HC2	-0.55	20	0.1698	175	230	0.1276 ± 0.020	2.78	48.3
HC3	-0.74	20	0.1686	175	230	0.1352 ± 0.008	2.81	19.4
T	0	0	0	260	260	0	0	-1.4

*Measured current density at t = 0

**Max junction temperature is calculated using thermal simulation at t = 0

The high current density devices showed 21.2% larger degradation on average as compared to the low current density devices. This suggests that stressing current density correlates well with $I_{D\text{-}max}$ degradation. This further supports the ON-state degradation model proposed in chapter 4. Higher current density means that there are more electrons flowing at the 2DEG channel. Larger number of electrons at the 2DEG channel leads to more hot electrons being injected to AlGaN/Si_xN_{1-x} interface which leads to more AlGaN oxidation and larger $I_{D\text{-}max}$ degradation. This further emphasizes the importance of 2DEG electrons in AlGaN/GaN HEMT ON-state degradation. Moreover, the maximum electric field difference between high and low current densities devices was small (i.e. 0.14 MV/cm). This is important because the effect of other factors has to be minimized.

Figure 5.7 shows the $I_{D\text{-}max}$ over time plot for devices stressed under temperature stressing (T_{base} = 260°C) and ON-state condition with different current densities. It was observed that most of the stressed devices underwent two degradation phases. The first phase is defined as fast degradation mode which can be observed approximately the first 20 hours of stressing for device HC2. The second phase is defined as slow degradation mode which refers to the less steep portion of decreasing $I_{D\text{-}max}$. These two degradation modes will be

discussed more in details the next section. Devices LC1 and HC3 showed flatter fast degradation mode as compared to the other two devices stressed under the same condition. This phenomenon might occur due to small amount of pre-existing oxygen at the AlGaN/Si_xN_{1-x} interface. It is worth noting that there was no current spike for all the samples during the stressing. Therefore, there was no sudden severe $I_{D\text{-}max}$ degradation observed.

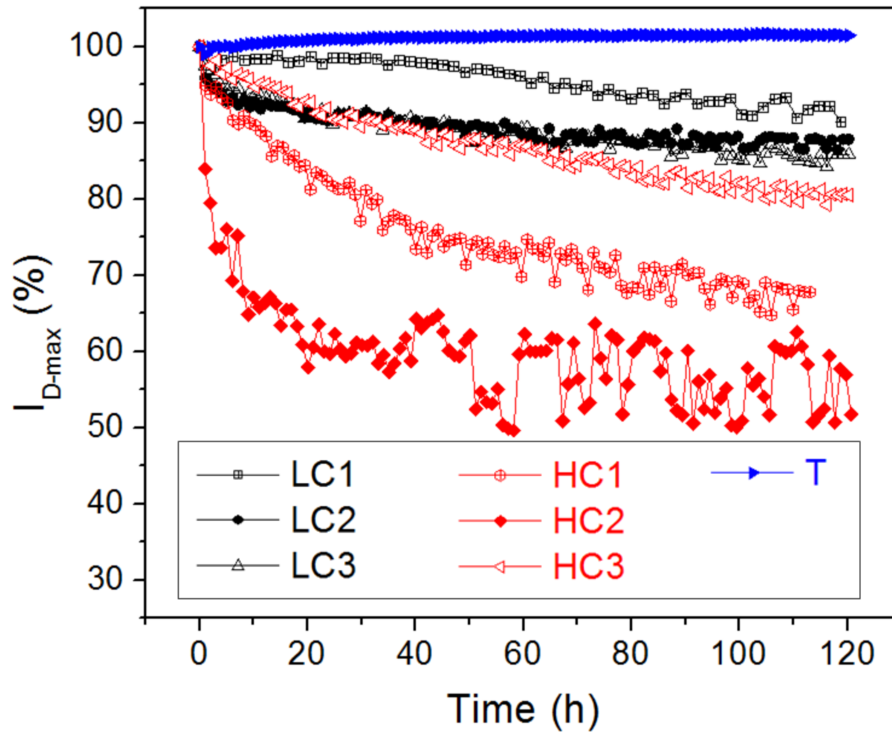

Figure 5.7 $I_{D\text{-}max}$ versus time for the devices stressed under ON-state condition V_{DS} = 20 V high (J_{DS}-initial = 0.168 A/mm, T_{base} = 175°C), low current densities (J_{DS}-initial = 0.089 A/mm, T_{base} = 200°C) and temperature only (T_{base} = 260°C) stressing.

One device was stressed only with temperature at T_{base} = 260°C without any bias. The result showed no $I_{D\text{-}max}$ degradation for 120 hours despite 30°C higher temperature than the 6 other devices. In fact, the $I_{D\text{-}max}$ increased about 1.4%. This suggests that electrical bias is required to cause the degradation. Temperature can accelerate the degradation rate [77] but temperature itself is not enough to cause the $I_{D\text{-}max}$ degradation. This device showed 1.4% $I_{D\text{-}max}$ improvement after 120 hours temperature stressing. This might be due to the improvement of ohmic contact. The ohmic contact in the AlGaN/GaN HEMT devices used in this study was made of Ti/Al/Ni/Au. After the deposition of each metal, ohmic contact

was formed by annealing at high temperature [107, 157-159]. During the annealing process, the contact resistance decreases and the drain current increases. Similarly, the increase in $I_{D\text{-}max}$ for the device stressed at T_{Base} = 260°C could be due to decreasing ohmic contact resistance during the temperature stressing.

5.3.3 Two ON-State Degradation Modes

After the ON-state electrical stressing, two different degradation modes were observed in $I_{D\text{-}max}$ vs stressing time plot for all devices. These two degradation modes were not observed in chapter 4 might be because the stressing time was too short (i.e. 20 hrs). In this section, the origin of the two degradation modes will be discussed.

Figure 5.8a shows the typical $I_{D\text{-}max}$ evolution during ON-state stressing. It was observed that the $I_{D\text{-}max}$ degraded rapidly at the beginning, then it slowed down upon reaching conversion point and continued to degrade at a constant rate. The first part of the degradation curve from t = 0 h up to conversion point is defined as fast mode degradation. The part beyond conversion point is defined as slow mode degradation.

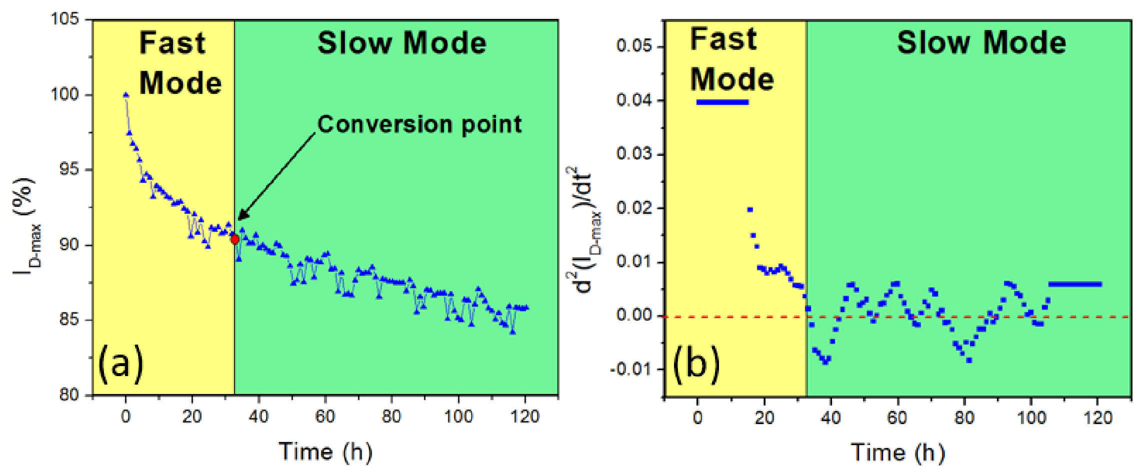

Figure 5.8 (a) Typical $I_{D\text{-}max}$ vs. time graph and (b) second derivative graph with the two degradation modes

Conversion point was defined by using the second derivative curve of the $I_{D\text{-}max}$ vs time graph (Figure 5.8b). In slow mode degradation, the $I_{D\text{-}max}$ degraded linearly during the

stressing. A linear portion of the graph will give $\frac{d^2(I_{D-\max})}{dt^2} = 0$ as it has a constant gradient. In Figure 5.8b, it was observed that the second derivative reaches 0 at t = 33 h and it fluctuates around 0 beyond this point. This point is defined as the conversion point. The fluctuation in the second derivative curve is due to small noise in I_{D-max} vs time graph beyond the conversion point as can be seen in Figure 5.8a.

The hypothesis is that the two degradation modes are due to the different source of oxygen in the electro-chemical oxidation. It was proposed in Chapter 4 that oxygen comes from the ambient and penetrates through the Si_xN_{1-x} passivation layer. When the oxygen reaches AlGaN/Si_xN_{1-x} interface, AlGaN will be oxidized and this leads to I_{D-max} degradation. Higher oxygen concentration at the AlGaN/Si_xN_{1-x} interface will lead to faster oxidation rate and thus larger I_{D-max} degradation rate. Therefore, there might be two different sources of oxygen that lead to the two degradation modes.

In order to prove this hypothesis, cross-sectional TEM analysis was done on a fresh device. STEM-EELS line-scans were done at various locations to characterize the chemical elements present at the interfaces. Figure 5.9a shows the schematics of the AlGaN/GaN HEMT. Four STEM-EELS line-scans were done at location 1, 2, 3 and 4 in Figure 5.9a to characterize nitrogen, oxygen and carbon content. The STEM-EELS line-scans showed the presence of oxygen and carbon at the AlGaN/Si_xN_{1-x} interface both near the gate edge (Figure 5.9c) and further away from the gate edge (Figure 5.9b). However, no oxygen and carbon was detected at top (Figure 5.9d) and bottom (Figure 5.9e) of the gate metal.

The oxygen and carbon contamination at the AlGaN/Si_xN_{1-x} interface might be due to the imperfect lift-off process of organic photoresist before Si_xN_{1-x} passivation deposition [160-162]. This organic photoresist is hydrocarbon with OH^- ligand. Unfortunately, hydrogen is not detectable under EELS. Oxygen and carbon were also detected at AlGaN/Si_xN_{1-x} interface on the source side. The oxygen at the AlGaN/Si_xN_{1-x} interface could react directly with AlGaN in the presence of electrons and holes during electrical stressing. This leads to the fast I_{D-max} degradation i.e. the fast degradation mode.

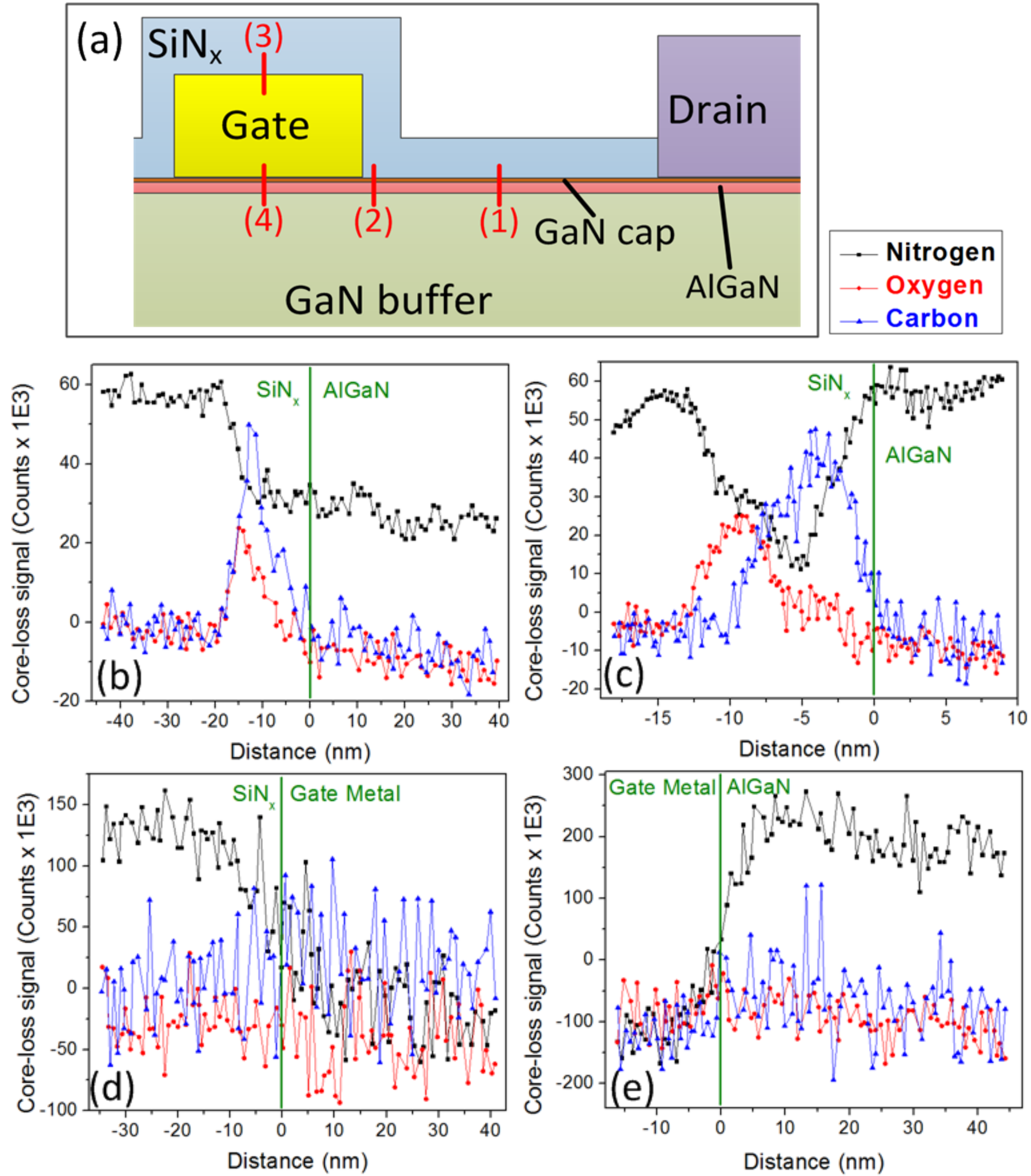

Figure 5.9 (a) schematics of AlGaN/GaN HEMT device at the drain side and STEM-EELS line-scans at location (b) 1, (c) 2, (d) 3 and (e) 4 to characterize nitrogen, oxygen and carbon.

Another experiment was done to investigate the role of the pre-existing oxygen in the ON-state degradation. Two fresh devices were stressed under ON-state state in different ambient conditions. The first device was stressed under vacuum condition at 1×10^{-5} Torr and the second device was stressed under normal ambient condition. The applied bias was the same for both devices V_{DS} = 30 V and V_{GS} = 0 V at T_{base} = 150°C. Both devices were stressed for 500 hours and $I_{D\text{-}max}$ was monitored.

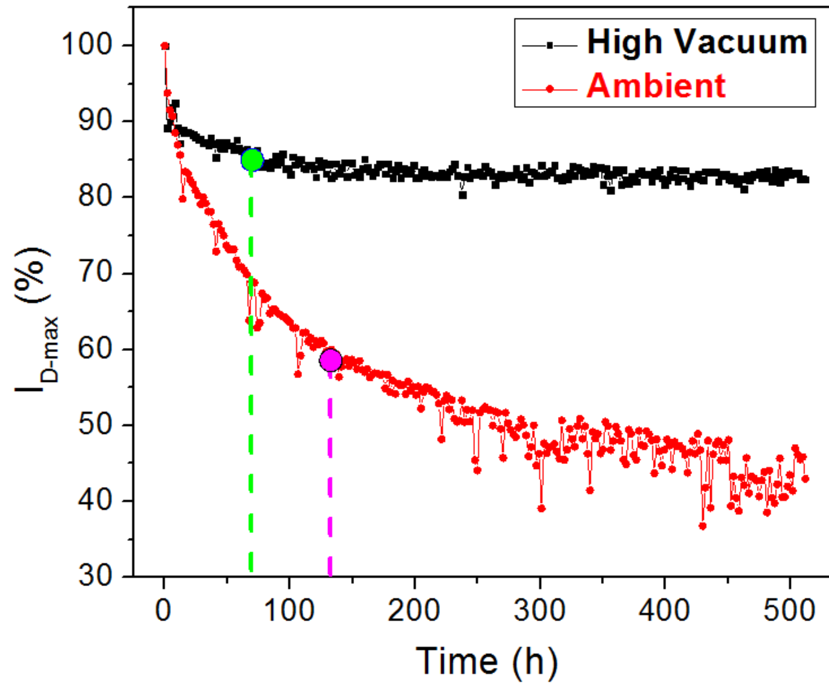

Figure 5.10 I_{D-max} evolutions of AlGaN/GaN HEMT devices stressed under ON-state condition V_{DS} = 30 V, V_{GS} = 0 V with high vacuum (1×10^{-5} Torr) and ambient at T_{base} = 150ºC for 500 hours

Figure 5.10 shows the result for ON-state stressing under vacuum and ambient conditions. It was observed that the device stressed under ambient condition degraded 40% more than the device stressed under vacuum condition. For the device stressed under vacuum condition, I_{D-max} immediately dropped 10% in the first few hours. After that it continued to degrade at a much slower rate and eventually stopped degrading at 70 hours (green dot). On the other hand, the device stressed in ambient showed fast degradation up to 135 hours (pink dot) and then it degraded linearly for the rest of the ON-state stressing. In this case, green and pink dots are the conversion point for the device stressed under vacuum and ambient, respectively.

Before the conversion point, the stressed devices underwent fast mode degradation due to electro-chemical oxidation of AlGaN layer in the presence of pre-existing oxygen at the AlGaN/Si_xN_{1-x} interface. The device stressed in ambient showed more severe fast mode degradation might be because the device had higher pre-existing oxygen content at AlGaN/Si_xN_{1-x} interface. Beyond the conversion point, both devices went into slow

degradation mode after most of the pre-existing oxygen has reacted with AlGaN. After the conversion point, the device stressed under vacuum stop degrading whereas the device stressed under ambient continued to degrade. This implies that oxygen from the ambient is the dominant source of oxygen in the slow mode degradation which causes the device stressed in ambient to degrade further. On the other hand, the device stressed in vacuum stopped degrading because there was no oxygen supply from the environment and most of the pre-existing oxygen had been used.

In this section, the two degradation modes of AlGaN/GaN HEMT have been introduced. The evidence of pre-existing oxygen and the importance of oxygen from the ambient have been discussed. The pre-existing oxygen is the dominant source of oxidant in the fast degradation mode whereas the oxygen from the ambient is the dominant source of oxidant in the slow degradation mode. It is worth noting that these two degradation modes were also observable in the AlGaN/GaN HEMT devices stressed under OFF-state condition.

5.3.4 Role of Current Density in ON-state Degradation

It has been shown that higher current density leads to higher ON-state degradation. Most of the stressed devices showed both fast and slow degradation modes. The fast degradation in the beginning was predominantly due to the pre-existing oxygen at AlGaN/Si_xN_{1-x} interface. Upon reaching conversion point, the devices continued to degrade linearly in the presence of oxygen penetrating through the Si_xN_{1-x} passivation from the ambient. In this section, the role of current density in both fast and slow ON-state degradation modes will be discussed.

Slow degradation mode is defined as $I_{D\text{-}max}$ degradation beyond the conversion point in the $I_{D\text{-}max}$ vs time graph (Figure 5.8a). This degradation mode occurs when the oxygen from the ambient becomes the dominant factor in AlGaN oxidation. This portion of the graph was fitted linearly and the slope was compared. Figure 5.11 shows that the average slow mode slope for devices stressed under high current density condition was about twice steeper than the average slope for devices stressed under low current density condition. The

slow mode slope increases proportionally with the increase in current density between the two stressing conditions.

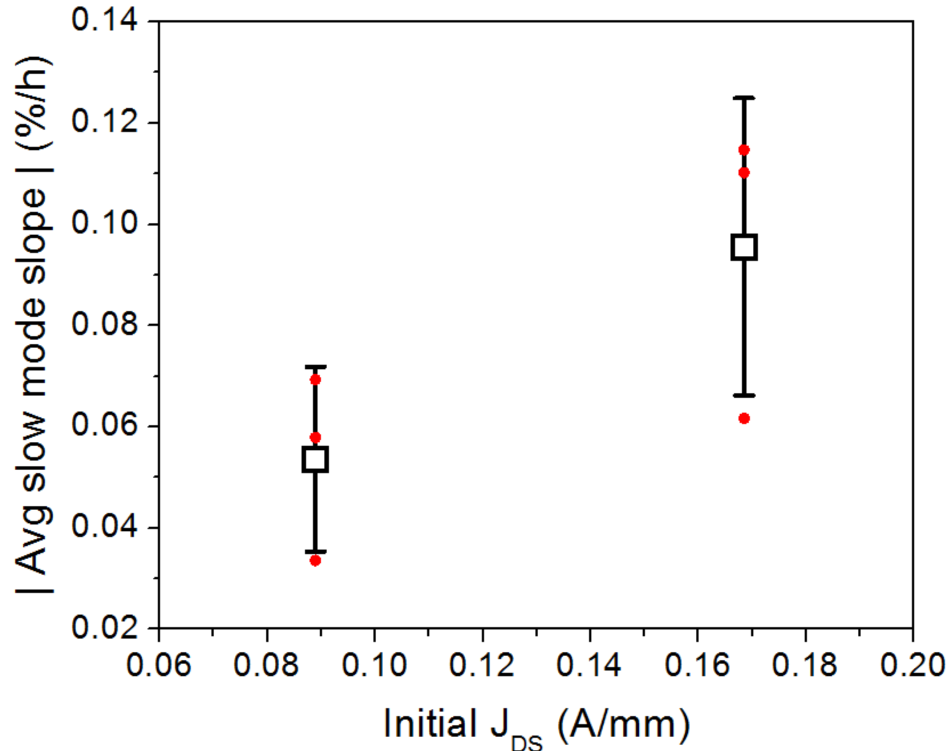

Figure 5.11 Average slow mode slopes of AlGaN/GaN HEMT devices stressed under ON-state condition with different current densities.

In slow degradation mode, there are two processes occurred. The first process is the oxygen diffusion through degraded Si_xN_{1-x} passivation from the ambient to the AlGaN/Si_xN_{1-x} interface. Si_xN_{1-x} passivation degradation will be thoroughly discussed in chapter 6. Upon reaching AlGaN/Si_xN_{1-x} interface, the oxygen will react with AlGaN in the presence of electrons and holes. The slow mode degradation rate is either limited by oxygen diffusion process or number of electrons and holes present. If the degradation rate is limited by oxygen diffusion through Si_xN_{1-x} passivation, the slow mode slope should be independent of current density. However, Figure 5.12 showed that higher current density led to faster slow mode degradation. This implies that slow degradation rate is limited by reaction between oxygen, AlGaN, electrons and holes at AlGaN/Si_xN_{1-x} interface rather than oxygen diffusion. Devices stressed under high current density have more electrons and

holes at the AlGaN/Si_xN_{1-x} interface which leads to faster I_{D-max} slow mode degradation as compared to devices stressed under low current density.

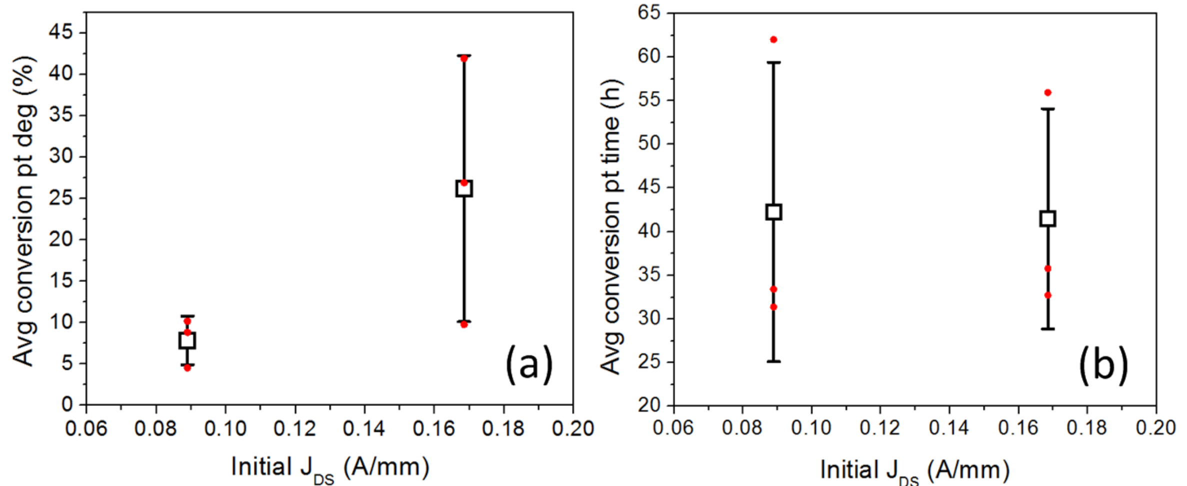

Figure 5.12 Average (a) conversion point degradation and (b) conversion point time of AlGaN/GaN HEMT devices stressed under ON-state condition with different current densities.

Figure 5.12a and b shows the average conversion point degradation and average conversion point time of devices stressed under different current density conditions, respectively. Conversion point is the point where the fast degradation mode transits to the slow degradation mode. High current density devices showed higher average conversion point degradation than low current density devices but the average conversion point times were similar for both conditions. This means that there is more AlGaN oxidation for high current density devices than low current density devices for the first 42 hours of the stressing. One possible reason is in high current density devices, there is a larger pit formation area compared to low current density devices. It was hypothesized that current density controls the maximum distance for pit formation from the gate edge on the drain side as the number of electrons that are injected into AlGaN/Si_xN_{1-x} interface increases proportionally with current density. In order to prove this hypothesis, some devices from one chip were stressed under ON-state condition with various current densities for 20 hours. After electrical stressing, the metallization and passivation layers were removed by etching. These devices were then analyzed under SEM.

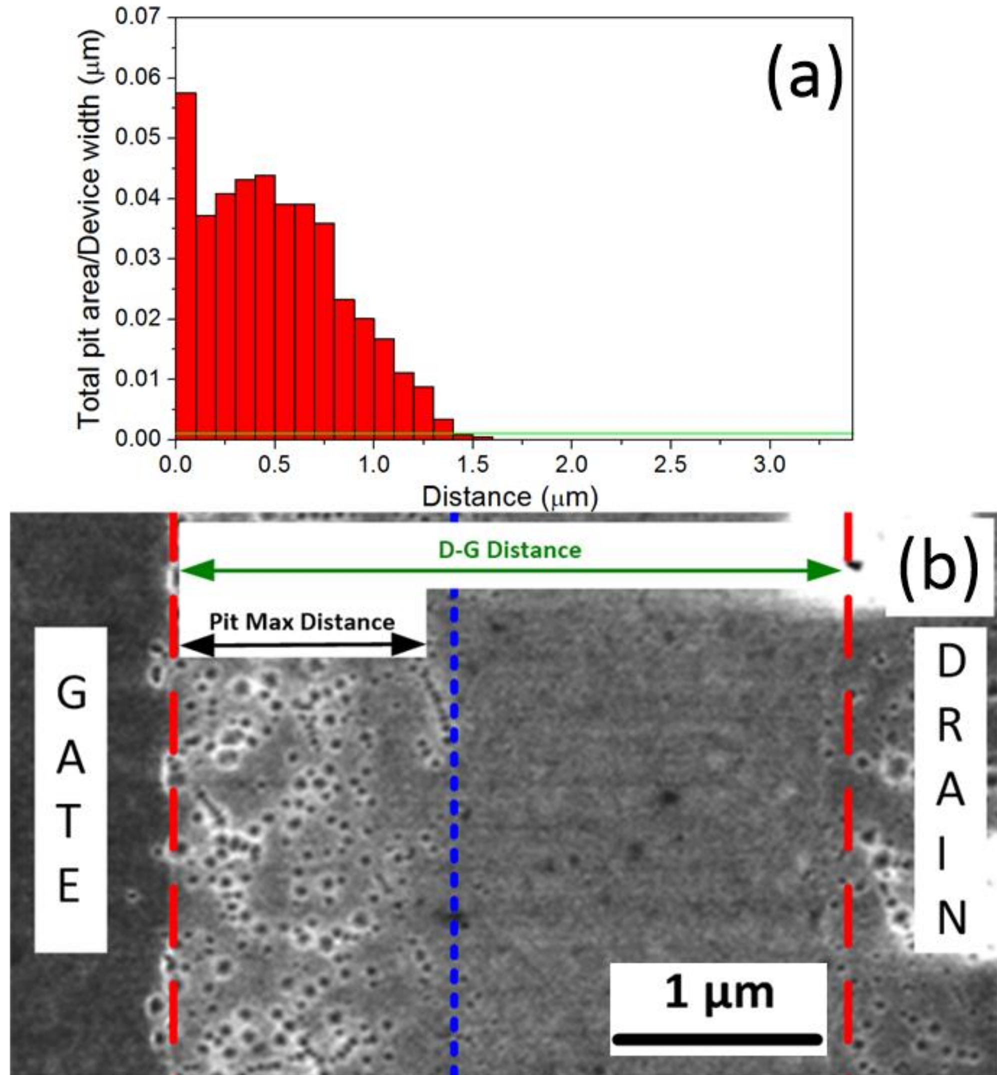

Figure 5.13 (a) Total pit area per unit device width as a function of distance from the gate edge and (b) top-view SEM image of the device stressed under V_{DS} = 20 V, V_{GS} = 0 V, T_{Base} = 150°C with average J_{DS} = 0.194 A/mm for 20 h after metallization/passivation removal

Figure 5.13b shows the top-view SEM image of the device stressed under ON-state condition V_{DS} = 20 V, V_{GS} = 0 V, T_{Base} = 150°C, average J_{DS} = 0.194 A/mm for 20 h. The image was taken after metallization and passivation layers were removed. It was observed that the pit formation stopped at a certain distance from the gate edge. In order to determine the maximum pit distance, the drain-gate access region was divided into smaller areas of 100 nm × device width. Then, the total pit area of each area was calculated and normalized against the device width. Figure 5.13a shows the normalized pit area distribution in the drain-gate access region. The maximum pit distance was defined as the distance beyond

which the normalized pit area fell below 0.001 μm. This value is obtained from the normalized pit area in the drain-gate access region of device stressed under OFF-state condition. For the device shown in Figure 5.13, the maximum pit distance was about 1.3 μm.

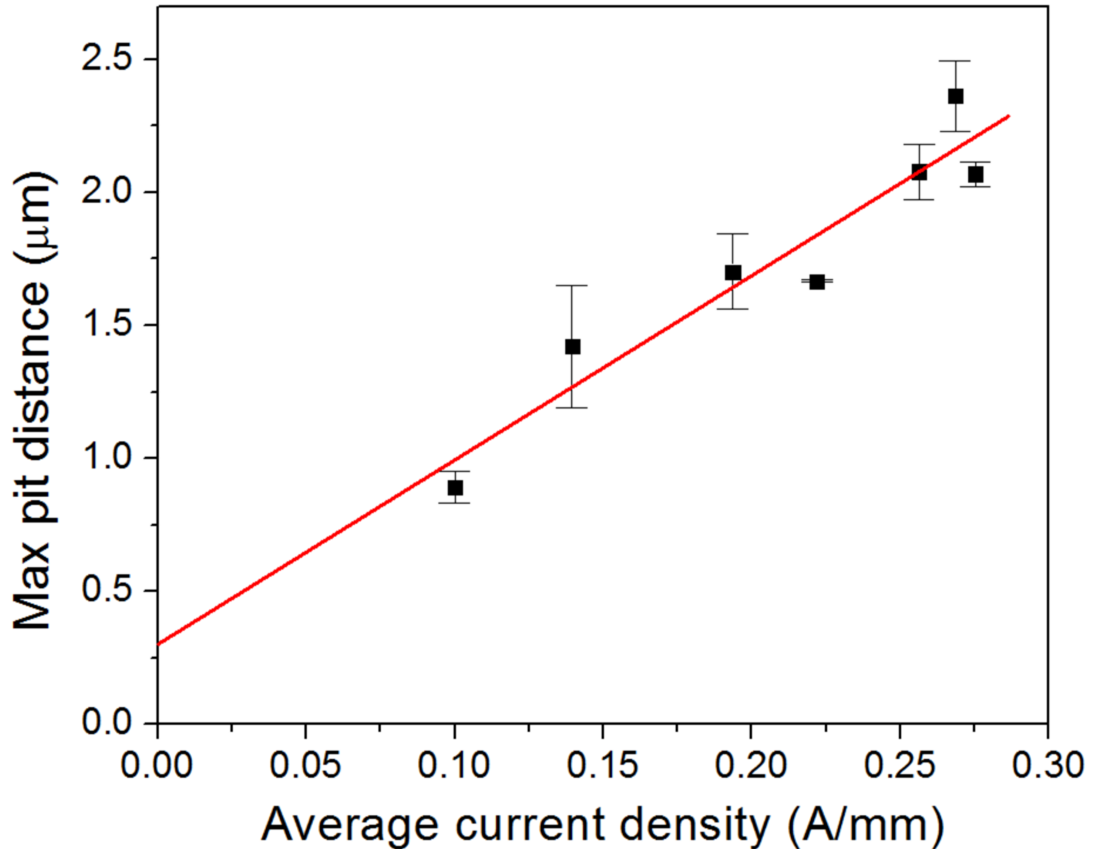

Figure 5.14 Maximum pit distance vs. average current density plot for devices stressed under ON-state condition for 20 h with different current densities at various base temperatures

Figure 5.14 shows the maximum pit distance plotted against average current density for devices stressed under different current densities. The maximum pit distance increases linearly with the average current density. This result supports the hypothesis that current density controls the maximum distance for pit formation. Higher current density translates into larger number of electrons in 2DEG channel and thus larger number of hot electrons that can be injected to AlGaN/Si_xN_{1-x} interface. The fitting line has y-intercept at 0.3 μm. This means that at zero current density, pits will be formed up to 0.3 μm away from the gate edge. Zero current density refers to OFF-state operation. Pits have been observed at

small distance away from the gate edge for AlGaN/GaN HEMT stressed under OFF-state condition due to the presence of threading dislocations away from the gate edge [75].

Figure 5.15 shows the correlation between the total pit areas at the drain-gate access region with $I_{D\text{-}max}$ degradation of the stressed devices. It was found that the $I_{D\text{-}max}$ degradation correlates well with the total pit area at the drain-gate access region for these devices. This result is consistent with the result in chapter 4 which shows that pit formation at the drain-gate access region leads to $I_{D\text{-}max}$ degradation after ON-state stressing.

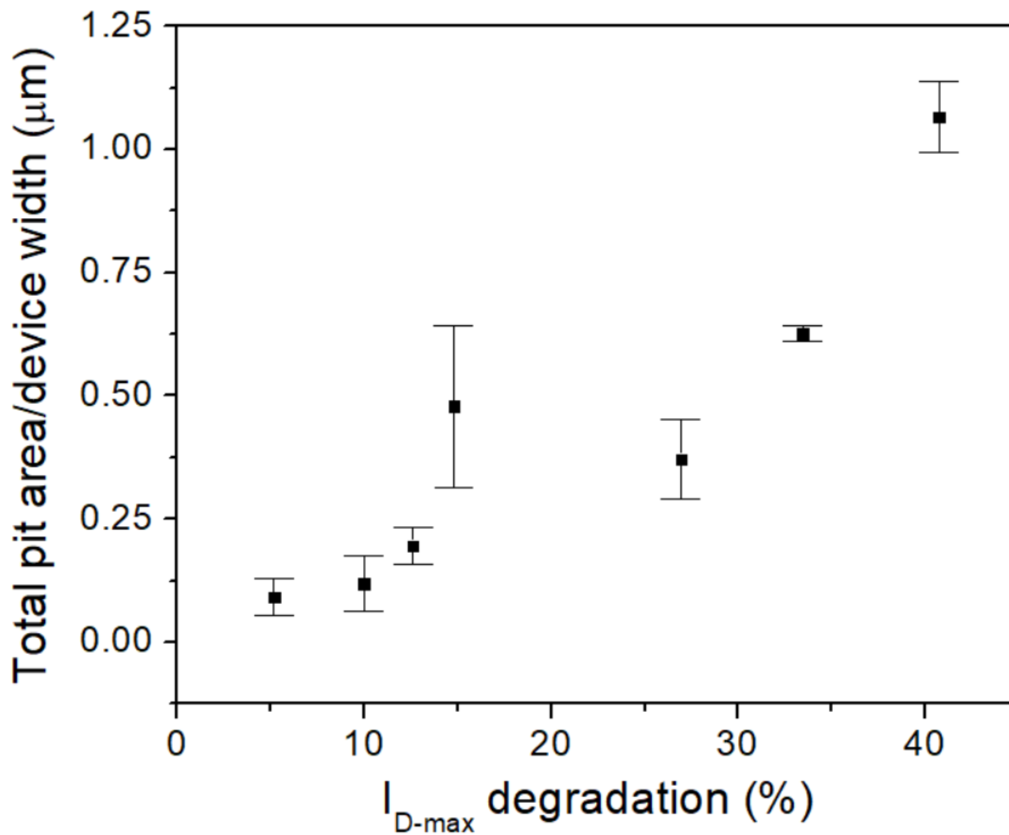

Figure 5.15 Total pit areas at the drain-gate access region plotted against $I_{D\text{-}max}$ degradation of the devices stressed under different current densities. $I_{D\text{-}max}$ degradation is normalized to individual device regardless of the stressing current density

5.3.5 Fast Degradation Mode Analysis

Fast degradation mode refers to the early degradation of the AlGaN/GaN HEMT devices up to the conversion point (Figure 5.8a). In the fast degradation mode, pre-existing oxygen at the AlGaN/Si_xN_{1-x} interface plays a dominant role in AlGaN oxidation. In this section, a kinetic model is proposed based on Johnson-Mehl-Avrami (JMA) analysis to explain the pit growth at drain-gate access region during fast degradation mode. Johnson-Mehl-Avrami (JMA) analysis combines both nucleation and growth effects [163].

Figure 5.16 shows the schematics of the proposed kinetic model. It is assumed that pits nucleate only at the threading dislocations and thus, the nucleation sites are saturated at the beginning of the pit formation and growth process. This is a reasonable assumption because, in chapter 4, it was observed that threading dislocation density (8.52×10^9 cm^{-2}) was comparable to the pit density (8.18×10^9 cm^{-2}) in the activated region of the stressed devices. Activated region is defined as the region where hot electrons are injected to the AlGaN/Si_xN_{1-x} interface from 2DEG channel and where the degradation pits are found

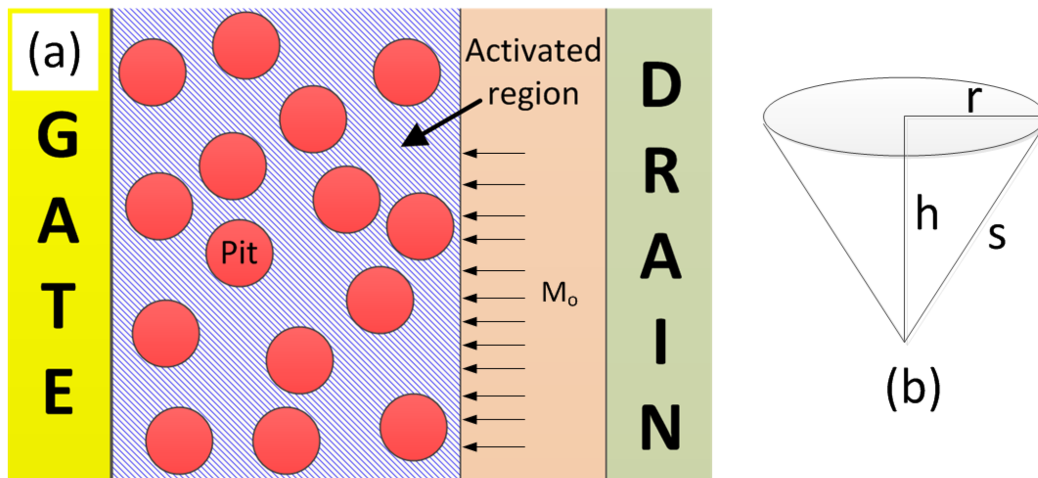

Figure 5.16 (a) Top view of the drain-gate access region and oxygen diffuses towards the activated region. (b) Each pit is assumed to have conical shape

There are two possible cases that will be considered. The first case is that the pit growth rate is limited by oxygen diffusion along the AlGaN/Si_xN_{1-x} interface towards the activated

region. The second case is that the pit growth rate is limited by the reaction at the perimeter of the pit.

In this model, individual pit is assumed to have a conical shape (Figure 5.17b). In this calculation, the height (*h*)/radius (*r*) and side (*s*)/radius (*r*) ratios are assumed to be constant for all pits. The volume of a pit (*V*) is given by

$$V = \frac{1}{3}\pi r^2(\chi_1 r) \tag{5.1}$$

In chapter 4, it was found that pits were filled with oxide particles as a result of oxidation of AlGaN layer. Thus, the total number of oxide particles (N_o) is

$$N_o = \frac{1}{\Psi}\chi_2 r^3 \tag{5.2}$$

Differentiating both sides against time,

$$\frac{dN_o}{dt} = \frac{3}{\Psi}\chi_2 r^2 \frac{dr}{dt} \tag{5.3}$$

where ψ is the volume of an oxide particle.

For the diffusion limited case, the number of oxygen molecules per unit area (M_o) reaching the activated region is constant over time. Therefore,

$$\frac{dM_o^1}{dt} = \chi_3 = \frac{dN_o}{dt} = \frac{3}{\Psi}N_p\chi_2 r^2 \frac{dr}{dt} \tag{5.4}$$

where N_p is the number of pits per unit area of the activated region. Simplifying equation 5.4 gives,

$$\chi_4 dt = N_p r^2 dr \tag{5.5}$$

Integrating both sides,

$$\int_0^t \chi_4 dt = \int_0^r N_p r^2 dr \tag{5.6}$$

it becomes

$$r_1 = \chi_5 N_p^{-\frac{1}{3}} t^{\frac{1}{3}} \tag{5.7}$$

In order to model the ON-state degradation, JMA equation for two-dimensional growth with nucleation site saturation is derived [163]. The area fraction of the activated region covered by pits is given by,

$$A = 1 - \exp(-N_p \pi r^2) \quad (5.8)$$

Substituting equation 5.7 into 5.8,

$$A_1 = 1 - \exp(-\chi_6 N_p^{\frac{1}{3}} t^{\frac{2}{3}}) \quad (5.9)$$

where χ_1 to χ_6 are constants. From equation 5.9, the Avrami exponent for case 1 is $n_1 = 2/3$.

For case 2, the pit growth rate is limited by the reaction at the perimeter of the pit. Thus, the rate of oxide molecule formation is given by

$$\frac{dM_O^2}{dt} = N_p 2\pi k s = N_p 2\pi k(\chi_7 r) \quad (5.10)$$

where k is the rate constant of the reaction between oxygen molecules and AlGaN.

Following the derivation from equation 5.4 to 5.9, the area faction of activated region covered by pits for case 2 is obtained as follow,

$$A_1 = 1 - \exp(-\chi_8 t^1) \quad (5.11)$$

where χ_7 and χ_8 are constants. From the equation 5.11 above, the Avrami exponent for case 2 is $n_2 = 1$.

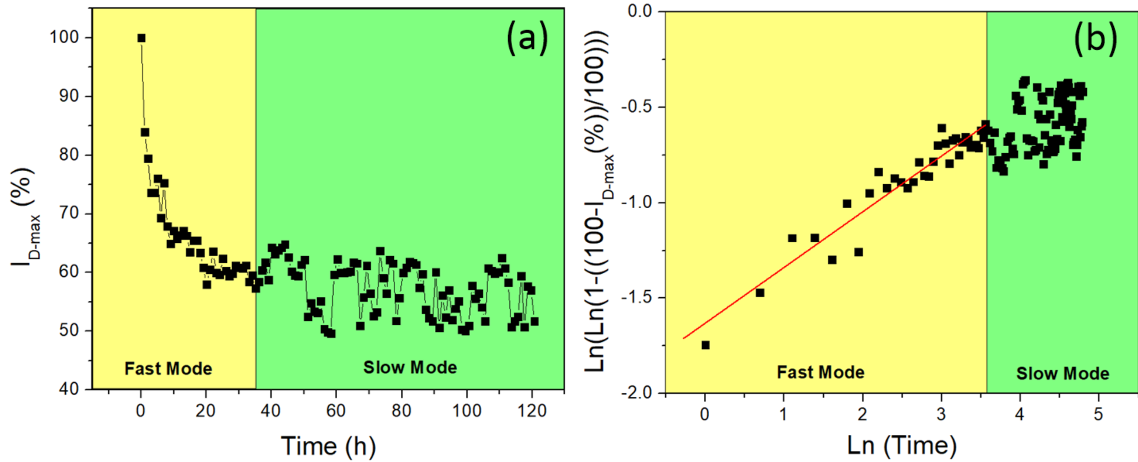

Figure 5.17 (a) I_{D-max} vs time plot for one of the devices stressed under different current density and (b) $Ln\left(Ln\left(1 - \frac{I_{D-max}\, degradation\,(\%)}{100}\right)\right)$ vs $Ln\, t$ plot to extract Avrami exponent

Previously, it has been shown that I_{D-max} degradation is proportional to the total pit area at the drain-gate access region (Figure 5.15). Figure 5.17a shows I_{D-max} vs time plot of one of

the stressed devices. Avrami exponent can be extracted by calculating the linear slope of $Ln\left(Ln\left(1-\frac{I_{D-max}\,degradation\,(\%)}{100}\right)\right)$ vs $Ln\,t$ graph for the fast degradation mode as shown in Figure 5.17b. The result is shown in Table 5.8.

Table 5.8 Avrami exponent for devices stressed under high and low current densities

Stressing condition	Avrami exponent (n)
High current density	0.53 ± 0.23
Low current density	0.28 ± 0.10

Avrami exponent for both high and low current densities were closer to 2/3, which is the first case. This means that the pit growth rate is limited by oxygen diffusion towards the activated region for both high and low current density stressing conditions.

5.3.6 Proposed Degradation Mechanism Based on Current Density

In this last section of the discussion, an ON-state degradation model for AlGaN/GaN HEMT devices based on current density is proposed. High current density means more electrons flowing at the 2DEG channel which in turn increases the number of hot electrons being injected to the AlGaN/Si_xN_{1-x} interface.

Hot electrons in AlGaN/GaN HEMT devices during ON-state operation can be characterized using electroluminescence (EL) [20, 164, 165]. Under ON-state condition, hot electrons are observed at the drain-gate access region and it correlates with the drain current thus, the EL signal will decrease as drain current decreases [20]. Kuball *et al.* studied the drain current degradation using EL [36]. EL measurements were done at V_{DS} = 30 V, V_{GS} = 0 V before and after the stressing. They found that EL signal decreases from the black curve to the blue curve because of decreasing drain current after stressing (Figure 5.18). It was also observed that hot electrons were spread in a shorter distance from the gate edge into the gate-drain access region as when the drain current decreased after the stressing. This observation supports the correlation between current density and maximum pit distance from the gate edge to the drain-gate access region.

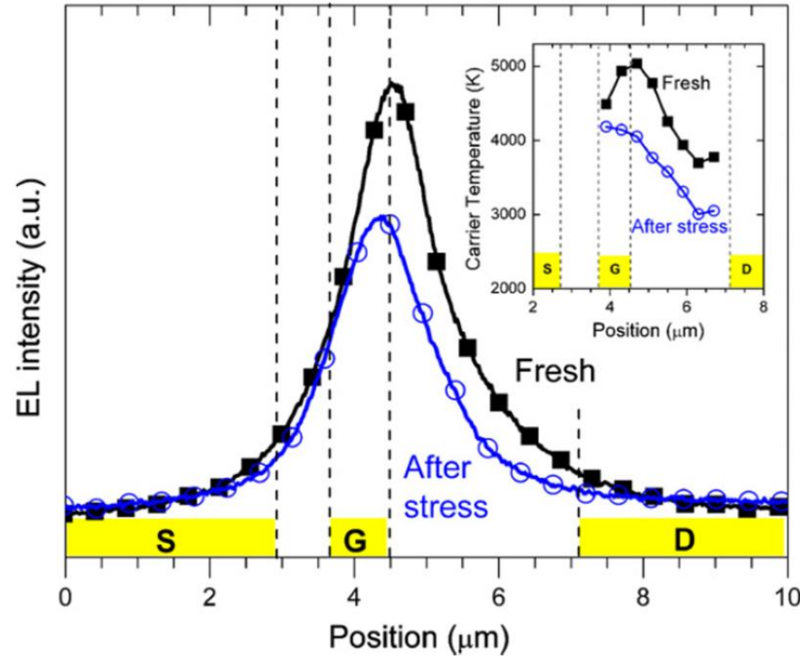

Figure 5.18 Electroluminescence (EL) intensity distributions in AlGaN/GaN HEMT before and after electrical stressing which represent drain current degradation [36]

Figure 5.19 schematically illustrates the degradation model based on current density difference. The activated region is defined as the region where hot electrons are injected to the AlGaN/Si_xN_{1-x} interface from 2DEG channel. Number of hot electrons injected into AlGaN/Si_xN_{1-x} interface and their spread distance from the gate edge increases proportionally with current density. These hot electrons can cause impact ionization which makes electro-chemical oxidation of AlGaN possible at location further away from gate edge. This leads to pit formation further away from the gate edge for high current density devices.

In the fast mode degradation, the longer activated region for high current density (Figure 5.19a) allows more electro-chemical oxidation reaction between electrons, pre-existing oxygen and AlGaN. As a result, high current density devices have higher conversion point degradation than low current density devices (Figure 5.12a) for the first 40 hours of stressing. This is supported by the physical evidence that showed pits formed further away from the gate edge for the devices stressed under high current density.

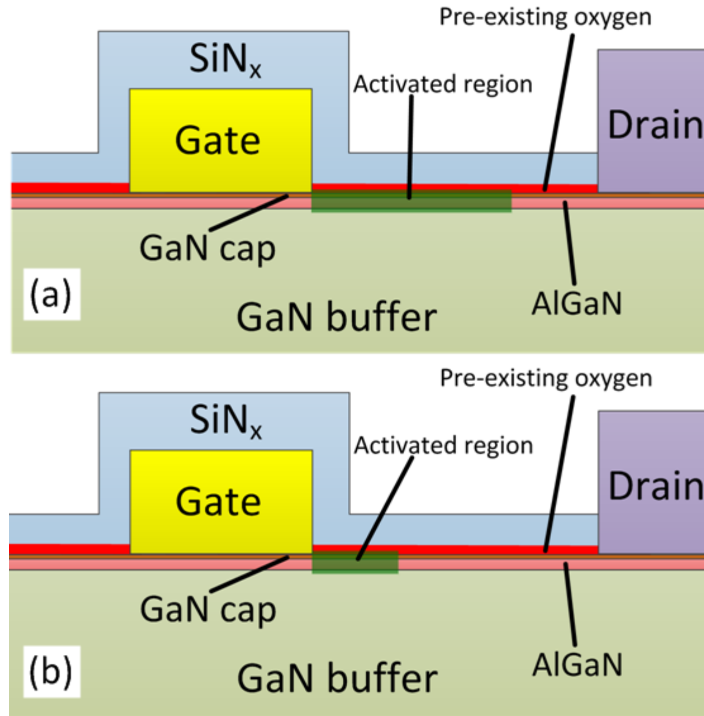

Figure 5.19 Proposed degradation model to illustrate the effect of (a) high current density and (b) low current density in AlGaN/GaN HEMT ON-state degradation

As the pre-existing oxygen at the activated region deplete, there will be oxygen concentration gradient between the activated region and the ambient. This will induce oxygen diffusion from the ambient to the AlGaN/Si_xN_{1-x} interface through the Si_xN_{1-x} passivation, i.e. slow degradation mode. Upon reaching AlGaN/Si_xN_{1-x} interface, the oxygen from the ambient will react with AlGaN in the presence of electrons and holes. Devices stressed under high current density condition have larger number of electrons and holes at AlGaN/Si_xN_{1-x} interface that results in higher slow mode slope than the devices stressed under low current condition (Figure 5.11).

5.4 Summary

In this chapter, the effect of different current density on $I_{D\text{-}max}$ degradation and pit formation at the drain-gate access region was investigated. AlGaN/GaN HEMT devices were stressed under ON-state condition with different current densities but similar electric field and temperature. This experiment was done by stressing the devices with constant V_{DS} and V_{GS}.

The desired current density was obtained by fine-tuning the V_{GS}. Electric field simulation was used to ensure that the electric field difference is very small within the stressing V_{GS} range. Junction temperature was calculated using thermal simulation in order to ensure the devices were stressed at the same junction temperature.

All stressed devices underwent two degradation modes, i.e. fast and slow degradation modes. Pre-existing oxygen at AlGaN/Si_xN_{1-x} interface is the dominant oxygen source in the fast degradation mode as it can oxidize the AlGaN layer instantly in the presence of holes and electrons during ON-state operation. Once the pre-existing oxygen depletes, the ambient oxygen will become the dominant source of oxygen i.e. slow degradation mode. The rate of electro-chemical oxidation will slow down as the oxygen has to diffuse through the Si_xN_{1-x} passivation layer to reach AlGaN/Si_xN_{1-x} interface before they can oxidize AlGaN layer during slow degradation mode.

It was also found that current density correlates with the maximum distance of pit formation at the drain-gate access region. In the high current density devices, more hot electrons are injected to AlGaN/Si_xN_{1-x} interface from 2DEG channel. Also, the hot electrons are spread further away from the gate edge into the drain gate access region which leads to longer activated region for high current density devices. Longer activation region means that pits can be formed at location further away from the gate edge. In addition, JMA analysis results show that the pit growth rate is limited by the oxygen diffusion towards the activated region during fast mode degradation for both high and low current densities.

In chapter 4, it was found that 2DEG electrons play an important role in ON-state degradation. In this chapter, the knowledge is extended by showing the effect of different amount of 2DEG electrons (current density) to the $I_{D\text{-}max}$ degradation and pit formation.

Chapter 6

Effect of Passivation Density on AlGaN/GaN High Electron Mobility Transistor Degradation under ON-State Stressing

AlGaN/GaN HEMT ON-state degradation consists of two degradation modes. The fast mode degradation is due to the pre-existing oxygen at AlGaN/Si_xN_{1-x} interface whereas the slow mode degradation is due to oxygen from the ambient. Two sets of AlGaN/GaN HEMTs with different passivation densities were stressed under ON-state condition and the result is discussed in this chapter. It was found that high density passivation showed longer conversion time than low density passivation where conversion time is defined as the time beyond which slow mode degradation dominates. This is because it takes a longer time to degrade the high density passivation. Once it degrades, oxygen from the ambient can diffuse through the degraded Si_xN_{1-x} and oxidize AlGaN layer. The slow mode degradation rate of high and low passivation densities were found to be comparable. This shows that once the passivation degrades, the passivation density does not affect the oxygen diffusion rate in slow mode degradation. Lastly, an ON-state slow mode degradation model is proposed based on electro-chemical oxidation and oxygen diffusion through passivation layer.

6.1 Introduction

Up to this point, it is understood that hot electrons in 2DEG channel play a big role in AlGaN/GaN HEMT ON-state degradation. This leads to larger degradation for ON-state condition compared to OFF-state condition. Degradation pits were found away from the gate edge into the access region on the drain side for ON-state degradation and the maximum pit distance correlated well with the current density.

It was also found that the ON-state degradation can be divided into two stages, i.e. fast and slow degradation modes. These two modes were characterized by different sources of oxygen. The pre-existing oxygen at the AlGaN/Si_xN_{1-x} interface is the dominant source of oxygen for the fast mode degradation as it can oxidize AlGaN instantly in the presence of holes and electrons. Once most of the pre-existing oxygen is used up, the device will go into slow degradation mode where ambient oxygen becomes the dominant source of oxygen.

In this chapter, the effect of passivation layer density in AlGaN/GaN HEMT degradation under ON-state condition is discussed. Two set of AlGaN/GaN HEMTs on Si with different Si_xN_{1-x} passivation density were used in the experiment. These devices were stressed at different temperatures. The effects of temperature and passivation density in device degradation under ON-state condition were discussed. Finally, slow mode degradation model is proposed based on oxygen diffusion through Si_xN_{1-x} passivation layer.

6.2 Experimental Details

Two sets of AlGaN/GaN HEMTs with different passivation densities were stressed under ON-state condition to investigate the effect of passivation layer density on device degradation under ON-state condition. The two different Si_xN_{1-x} passivation layers were characterized using X-ray reflectometry. The two sets of devices were then electrically stressed and followed by microstructure characterization.

6.2.1 Material Properties of Low and High Density Passivation Layers

X-ray Reflectivity (XRR) measurements were done on two different Si_xN_{1-x} passivation layers. Reflected ray intensity was collected for incident angle from 0 to 4.5°. The XRR measurement results were then compared with the simulated curves in Leptos software. The density, thickness and surface roughness of the two passivation layers were then extracted from the software. The working principle of the technique can be found in section 3.6.4.

Table 6.1 Parameters extracted from XRR measurements for low and high density Si_xN_{1-x} passivation

	Low Density Si_xN_{1-x}	High Density Si_xN_{1-x}
Density (g/cm^3)	2.26	2.48
Thickness (nm)	122.6	119.5
Surface roughness (nm)	0.96	0.90
Composition	$Si_{43}N_{57}$	$Si_{36}N_{64}$
Breakdown field of capacitor (MV/cm)[166]	3.3	7.2

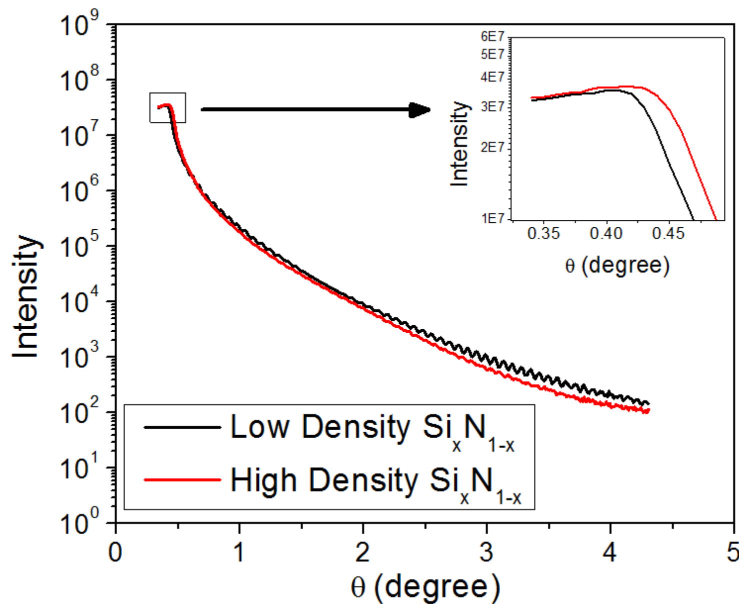

Figure 6.1 XRR measurement plots for low and high density Si_xN_{1-x} passivation layers

Figure 6.1 shows the result of XRR measurements and Table 6.1 shows the extracted parameters for two Si_xN_{1-x} passivation layers. High density Si_xN_{1-x} has about 10% higher density than low density Si_xN_{1-x}. This is because high density Si_xN_{1-x} (0.43°) has higher critical angle ϑ_c than low density Si_xN_{1-x} (0.41°) as can be seen in Figure 6.1 inset. Both passivation layers showed similar large drop at 0.5° which translated into similar surface roughness. Lastly, the data showed that the high density Si_xN_{1-x} is slightly thinner than the low density Si_xN_{1-x}. This result was consistent with the thickness measurement by cross-sectional TEM. The breakdown field for high density passivation is about 2 times of that of low density passivation.

The composition of the passivation layers was obtained by EELS. The EELS experimental details can be found in section 3.6.3. The high density Si_xN_{1-x} has lower Si/N ratio than the low density Si_xN_{1-x}. Smaller atomic size of nitrogen allows more packed S_xN_{1-x} structure which leads to higher density. The S_xN_{1-x} passivation layers were deposited by plasma-enhanced chemical vapor deposition (PECVD). Different Si/N ratio was obtained by varying the gas flow ratio between SiH_4 and NH_3 gases.

6.2.2 Electrical Stressing

In this experiment, the electrical stressing was done in batches using 32-SMU National Instrument (NI) attached to the EM system (Figure 3.5). Table 6.2 shows the device dimensions used in each batch. Each batch contained a few devices with the same dimensions but different passivation.

2D electric field simulation was used to calculate the maximum electric field for devices used in the batch stressing. The maximum electric field was similar for all the devices despite the different dimensions of the device. The maximum electric field was located at the gate edge on the drain side of the device. This result ensures that the electric field difference between batches was not significant. It is worth noting that the maximum electric field for all three batches is close to the breakdown field of low and high density passivation (Table 6.1).

Table 6.2 Device dimensions used in the experiment and the simulated maximum electric field under ON-state condition V_{DS} = 20 V and V_{GS} = 0 V

Batch Number	W_G (µm)	L_G (µm)	L_{GD} (µm)	L_{GS} (µm)	Max E-field (MV/cm)
Batch 1	100	2.30	2.40	1.70	2.79
Batch 2	100	3.60	2.40	1.50	2.86
Batch 3	100	1.70	2.40	1.25	2.75

Table 6.3 Stressing parameters for different temperatures and passivation densities

Batch Number	Passivation Density (g/cm3)	V_{DS} (V)	V_{GS} (V)	$T_{Surrounding}$ (°C)	$T_{Junction}$ (°C)	Number of Devices
Batch 1	2.26	20	0	150	202	6
Batch 1	2.48	20	0	150	202	4
Batch 2	2.26	20	0	175	221	5
Batch 2	2.48	20	0	175	221	6
Batch 3	2.26	20	0	225	260	4
Batch 3	2.48	20	0	225	260	5

Table 6.3 shows the stressing parameters for different temperatures and different Si_xN_{1-x} passivation densities. The junction temperatures were obtained by the same thermal model used in chapter 5. The device characteristics were monitored every 5 hour throughout the stressing duration. The number of stressed devices included in the analysis for batch 3 is very small because there were a lot of bad devices in the batch. The detailed explanation of the bad devices can be found in appendix. The effect of stressing temperature and passivation density on AlGaN/GaN HEMT ON-state degradation will be analyzed and discussed in this chapter.

6.3 Results and Discussions

6.3.1 Si_xN_{1-x} Degradation

AlGaN/GaN HEMT I_{D-max} degradation consists of two parts, i.e. fast and slow mode degradation under both ON-state and OFF-state stressing conditions. In the previous chapter, oxygen from the ambient has been shown to be the dominant source of oxygen in the slow degradation mode. It was hypothesized that Si_xN_{1-x} passivation degrades during electrical stressing and oxygen from the ambient diffuses through the degraded part of the Si_xN_{1-x} passivation to reach AlGaN/Si_xN_{1-x} interface.

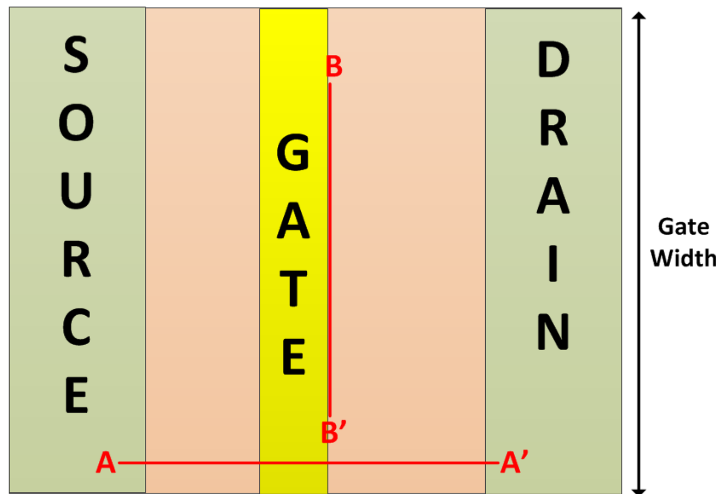

Figure 6.2 Top-view schematics of AlGaN/GaN HEMT device to show cross-sectional TEM sample cut directions

Cross-sectional TEM analysis was done on the stressed devices in order to prove this hypothesis. Figure 6.2 shows the cut directions for cross-sectional TEM. No appealing evidence of Si_xN_{1-x} degradation was found on devices stressed under ON-state and OFF-state conditions along the line A-A'. Another TEM sample was done along the gate width at the gate edge on the drain side (line B-B') where maximum electric field is located. Cross-sectional TEM samples were prepared for both ON- and OFF-state-stressed devices using SEM/FIB. Unfortunately, the ON-state sample preparation failed so only the TEM analysis for OFF-state sample is shown in Figure 6.3a.

Figure 6.3a shows the cross-section TEM image along the gate width of the device stressed under OFF-state condition. The OFF-state stressing condition was $V_{DS} = 0$ V, $V_{GS} = -50$ V at $T_{Base} = 200^{o}$C and the device showed 24% $I_{D\text{-}max}$ degradation. White circular features named as nano-globes were observed at the Si_xN_{1-x} passivation layer. Figure 6.3b shows the relative density, oxygen line-scan and nitrogen line-scan obtained by EELS analysis from line C-C' in Figure 6.3a. It was found that nitrogen amount decreased while oxygen amount increased at the vicinity of the nano-globes. This suggests that Si_xN_{1-x} has been oxidized. In addition, these nano-globes have lower density than the Si_xN_{1-x} further away from the degraded area. Figure 6.3c and 6.3d shows the oxygen/nitrogen EELS line-scans for line E-E' and D-D' in Figure 6.3a, respectively. Oxygen was observed in Si_xN_{1-x} layer along the line E-E' which means that the Si_xN_{1-x} passivation degrades throughout the whole Si_xN_{1-x} film thickness. On the other hand, there is no oxygen observed along line D-D' except for the small region near the surface which is the pre-existing oxygen due to imperfect lift-off process. This supports the hypothesis that the Si_xN_{1-x} degrades during electrical stressing to become silicon oxide with lower density. Oxygen from the ambient can easily diffuse through the degraded Si_xN_{1-x} to reach AlGaN/Si_xN_{1-x} interface. A degraded spot was found about every 6 µm of the gate width. This is likely to be the reason why no Si_xN_{1-x} degradation was found in the TEM sample along line A-A'.

Previous studies reported that crystalline and amorphous Si_3N_4 film gets oxidized into SiO_2 at high temperature above 1100°C [167-170]. Although the maximum stressing temperature used in this study was only 260°C, Si_xN_{1-x} oxidation is still possible in the presence of high electric field [171]. The cross-section TEM sample was cut from the gate edge on the drain side of the device. The electric field in this location is very high, about 1-3 MV/cm under both ON-state and OFF-state conditions. This electric field is close to the breakdown field of both high and low density passivation. Therefore, the Si_xN_{1-x} oxidation is possible at the gate edge on the drain side of the device stressed under both ON- and OFF-state conditions.

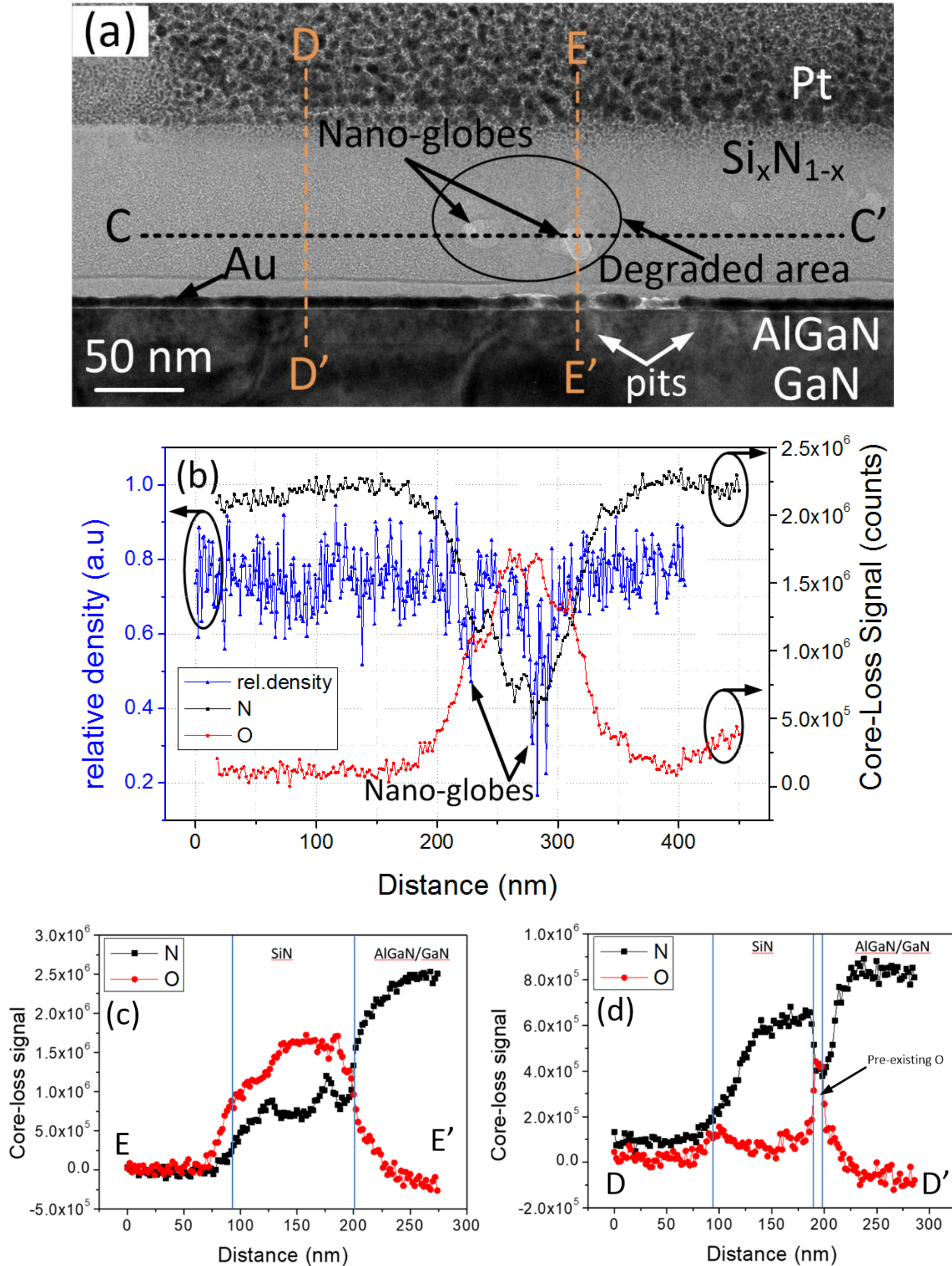

Figure 6.3 (a) Cross-sectional TEM image along the gate width from the OFF-state stressed device $V_{DS} = 0$ V, $V_{GS} = -50$ V at 200°C with 24% $I_{D\text{-}max}$ degradation; (b) relative density, oxygen line-scan and nitrogen line-scan obtained by EELS analysis from line C-C’; oxygen and nitrogen line-scan obtained by EELS analysis from line (c) E-E’ and (d) D-D’

6.3.2 Electrical Stressing Results

Electrical stressing result of AlGaN/GaN HEMT devices under ON-state condition V_{DS} = 20 V, V_{GS} = 0 V at different temperatures is discussed in this section. Figure 6.4a and b show typical $I_{D\text{-}max}$ vs. time plot and $I_{D\text{-}stress}$ vs. time plot for the stressed devices, respectively. It was observed that both $I_{D\text{-}max}$ and $I_{D\text{-}stress}$ decreased over time and there were two degradation modes as discussed in chapter 5. Fast and slow degradation modes were observed for all the devices regardless of Si_xN_{1-x} density. Fast and slow degradation modes are separated by the conversion point. Conversion point is the point beyond which the device degrades linearly, i.e. slow mode slope. In chapter 5, it was shown that in fast degradation mode pre-existing oxygen was the dominant factor in AlGaN electro-chemical oxidation whereas in slow degradation mode, oxygen from ambient was dominant factor.

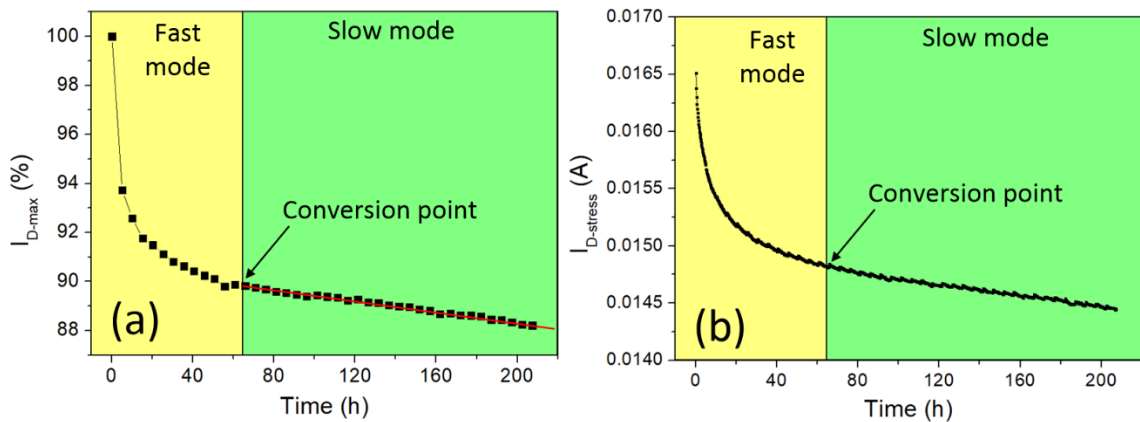

Figure 6.4 Typical (a) $I_{D\text{-max}}$ vs time and (b) $I_{D\text{-stress}}$ vs time plot for device stressed under ON-state condition V_{DS} = 20 V, V_{GS} = 0 V for 200 hours in this experiment

Conversion point is obtained by plotting the second derivative curve of $I_{D\text{-}stress}$ vs time. $I_{D\text{-}stress}$ vs time plot instead of $I_{D\text{-}max}$ vs time plot because the former has more points than the latter and thus conversion time can be more accurately determined. Figure 6.5 shows the $\frac{d^2(I_{D-stress})}{dt^2}$ vs time plot. The conversion point is defined as the first point where $\frac{d^2(I_{D-stress})}{dt^2} = 0$ because the device degrades linearly in slow degradation mode. Slow mode slope is defined as linear gradient of slow mode portion of $I_{D\text{-}max}$ vs time plot (red

line in Figure 6.4a). The effect of temperature and Si_xN_{1-x} passivation density will be discussed based on slow mode slope and conversion time.

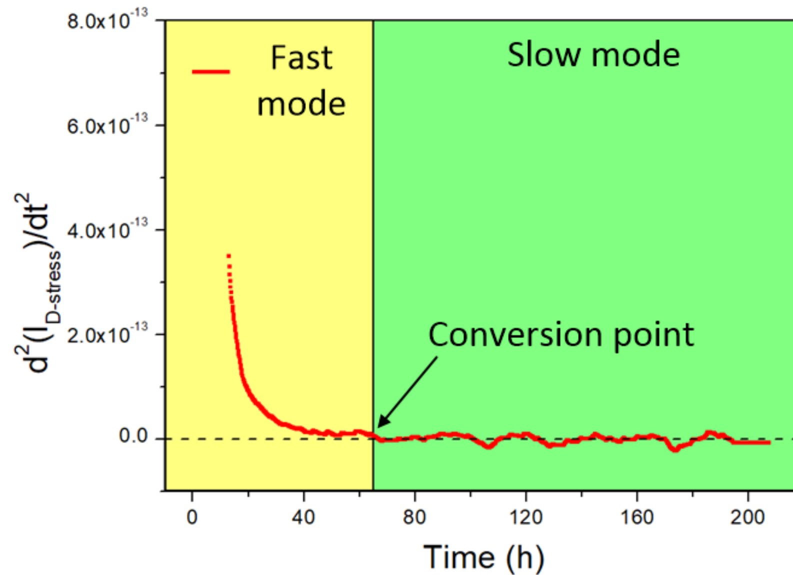

Figure 6.5 Second derivative plot from $I_{D\text{-stress}}$ vs time plot of the device stressed under ON-state condition V_{DS} = 20 V, V_{GS} = 0 V

6.3.2.1 Conversion Time

In section 6.3.1, it has been shown that Si_xN_{1-x} passivation oxidized to silicon oxide upon ON-state stressing due to high electric field at the gate edge of the drain side. It is then hypothesized that high density Si_xN_{1-x} requires longer time to degrade compared to low density Si_xN_{1-x} because the breakdown field of high density Si_xN_{1-x} is 2 times higher than low density Si_xN_{1-x} (Table 6.1). In order to prove this hypothesis, conversion time was extracted for all the devices stressed under ON-state and then compared.

Figure 6.6 shows the average conversion time for all devices stressed under ON-state condition at different surrounding temperatures. In general, it was observed that high density passivation showed higher conversion time than low density passivation although the difference became less apparent at high surrounding temperatures. It is worth noting that the devices with high and low passivation densities were stressed at three different

surrounding temperatures (150°C, 175°C and 225°C). High and low density passivation data are plotted side by side in Figure 6.6 for clearer presentation. This result supports the hypothesis that it takes longer time to degrade high density passivation compared to the low density passivation as conversion time shows the time beyond which oxygen from the ambient becomes the dominant source of oxygen for electro-chemical oxidation of AlGaN. After the conversion time, the oxygen can diffuse through the degraded Si_xN_{1-x} passivation.

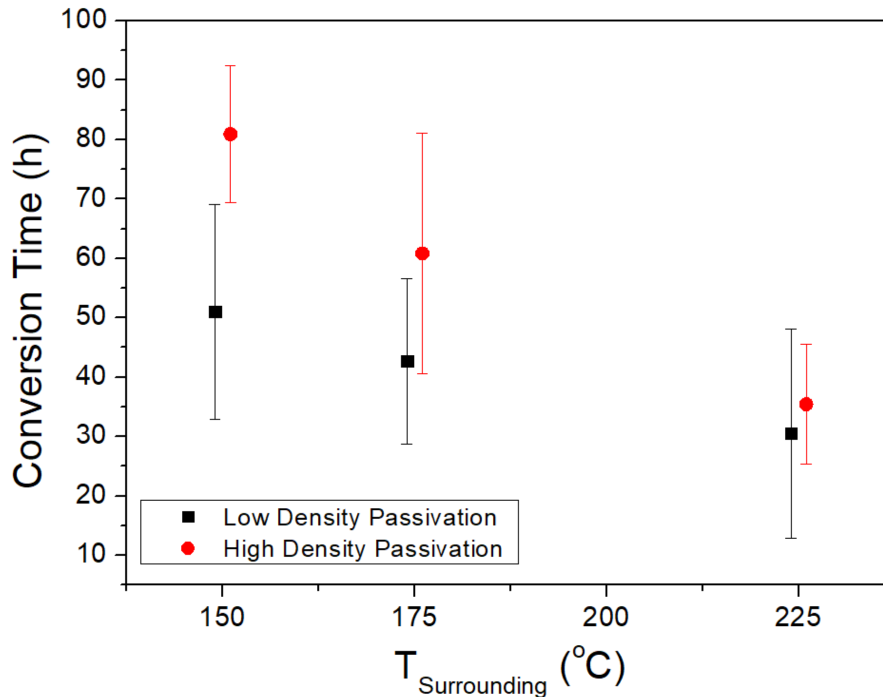

Figure 6.6 Average conversion time vs surrounding temperature for devices with high and low density passivation stressed under ON-state condition V_{DS} = 20 V, V_{GS} = 0 V

At high surrounding temperatures, the difference in conversion time between two passivation densities became less apparent. One possible reason is because at high surrounding temperatures, in addition to high electric field, the energy required to degrade the Si_xN_{1-x} passivation is easily overcome even for the high density passivation. Therefore, the difference in breakdown time between high and low density passivation is smaller at high temperatures.

6.3.2.2 Slow Mode Slope

In the previous section, it has been shown that high density passivation has a longer conversion time than low density passivation which implies that high density passivation is harder to degrade. The next question is whether the slow mode degradation rate depends on passivation density. This question can be answered by analyzing the slow mode slope from $I_{D\text{-}max}$ vs time plot of the stressed devices.

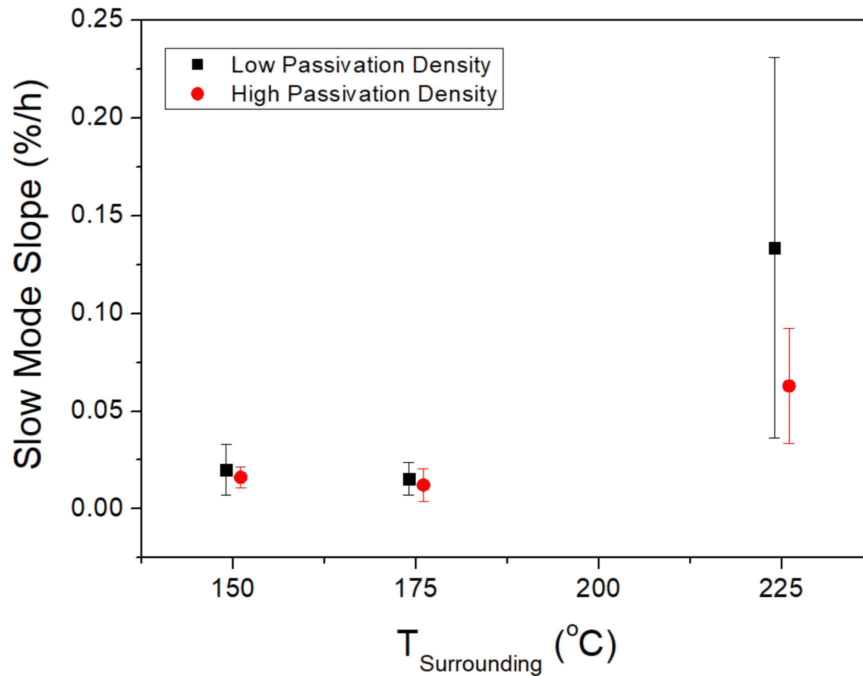

Figure 6.7 Average slow mode slope vs surrounding temperature for devices with high and low density passivation stressed under ON-state condition V_{DS} = 20 V, V_{GS} = 0 V

Figure 6.7 above shows that there is no apparent difference in average slow mode slope between high and low density passivation for all 3 different surrounding temperatures. This result suggests that slow mode degradation rate is independent of passivation density. This means that once the passivation degrades, the oxygen diffuses through the degraded passivation at the same rate regardless the passivation density. Figure 6.7 also shows that the slow mode slope increases with temperature. This is consistent as diffusion is thermally-activated process. In the next section, the temperature dependence of slow mode slope will be used to derive the ON-state degradation model.

6.4 ON-State Degradation Model

Up to this point, it is understood that ambient oxygen is the dominant source of oxygen in the slow degradation mode. Oxygen diffusion rate through the degraded Si_xN_{1-x} passivation is independent of passivation density but dependent on surrounding temperatures during ON-state stressing. Since slow mode degradation rate is independent of passivation density, the devices stressed at the same temperature will be grouped together in this model regardless their passivation density. In this section, ON-state slow mode degradation is modeled based on oxygen diffusion through passivation. It is more crucial to model the slow mode degradation because the slow mode degradation will still exist even if the device is fabricated perfectly with no pre-existing oxygen. On the other hand, fast mode degradation will cease if there is no pre-existing oxygen at AlGaN/ Si_xN_{1-x} interface from imperfect lift-off process.

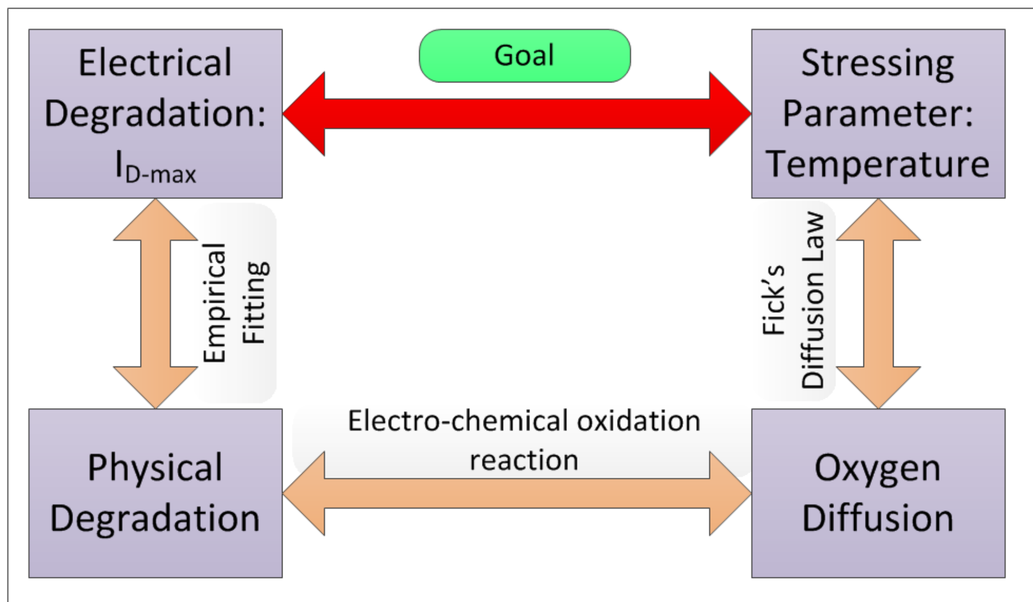

Figure 6.8 Modeling map for AlGaN/GaN HEMT slow degradation mode under ON-state stressing condition

Figure 6.8 shows the modeling map used in this section. The goal of this section is to obtain mathematical relationship between electrical degradation and stressing parameter which are I_{D-max} degradation and temperature, respectively. This section is divided into three sub-

sections. Firstly, the electrical and physical degradation is correlated by empirical fitting. The physical degradation here is the pits at the drain-gate access region. Secondly, physical degradation is correlated to amount of diffusing oxygen based on electro-chemical oxidation reaction. Lastly, oxygen diffusion is correlated to temperature based on Fick's law of diffusion which includes calculation of diffusion activation energy.

6.4.1 $I_{D\text{-}max}$ Degradation and Pit Volume Correlation

The total pit area and pit number were calculated from the top-view SEM images of stressed devices after metallization and passivation layer removal. The pit counting method was explained in section 3.6.5. In this model, it was assumed that the amount of AlGaN/GaN oxidized is equivalent to the total volume of the degradation pits. Thus, it is important to obtain the total pit volume.

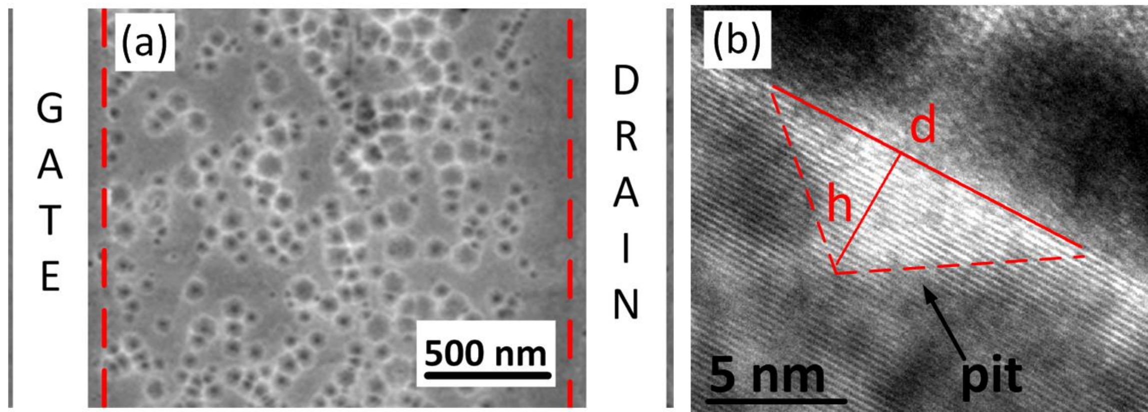

Figure 6.9 (a) Top-view SEM image and (b) cross-sectional TEM image of the degradation pits at the drain-gate access region

Figure 6.9a shows the top-view image of the pits at drain-gate access region. It was observed that most of the pits have circular shape. Cross-sectional TEM images show that most of the pits have a triangular shape (Figure 6.9b). Thus, it is assumed that all pits have inverted cone shape. The pit radius (r) is calculated using equation 6.1 below where A is the pit area obtained from the pit counting method.

$$r = \sqrt{\frac{A}{\pi}} \tag{6.1}$$

In order to obtain the pit volume, the height of the pit was obtained from radius/height (*r/h*) ratio. This ratio was calculated from cross-sectional TEM images from both stressed samples in this study and literature. Table 6.4 shows the calculation result from cross-sectional TEM images with average *r/h* = 1.611. This average ratio is used to calculate the pit volume assuming that the *r/h* ratio is constant for all the degradation pits.

Table 6.4 Degradation pit radius/height (r/h) ratio from cross-sectional TEM images

Source/ Device Code	Pit Diameter (nm)	Pit Radius (nm)	Pit Height (nm)	r/h ratio
Device 1	12.37	6.19	4.65	1.330
Device 1	5.19	2.59	3.27	0.794
Device 2	16.60	8.30	2.34	3.547
Device 3	17.50	8.75	4.30	2.035
Device 3	7.49	3.75	1.79	2.092
Device 4	12.00	6.00	5.00	1.200
Device 5	13.00	6.50	4.00	1.625
Device 6	20.00	10.00	7.00	1.429
Device 7	28.00	14.00	8.00	1.750
Ref [75]	109.00	54.50	33.00	1.652
Ref [75]	61.00	30.50	39.78	0.767
Ref [75]	75.88	37.94	19.28	1.968
Ref [16]	31.41	15.71	10.75	1.461
Ref [16]	11.12	5.56	3.00	1.853
Ref [16]	24.91	12.45	12.86	0.968
Ref [22]	11.00	5.50	3.00	1.833
Ref [22]	13.00	6.50	6.00	1.083

The pit volume (*V*) is then calculated using the equation below

$$V = \pi r^2 \frac{h}{3} \tag{6.2}$$

Figure 6.10 shows the $I_{D\text{-}max}$ degradation vs. normalized pit volume from the stressed devices. It can be observed that the total pit volume is linearly correlated to the $I_{D\text{-}max}$ degradation. This suggests that $I_{D\text{-}max}$ degradation is caused by the pits which is consistent with the results in previous chapters.

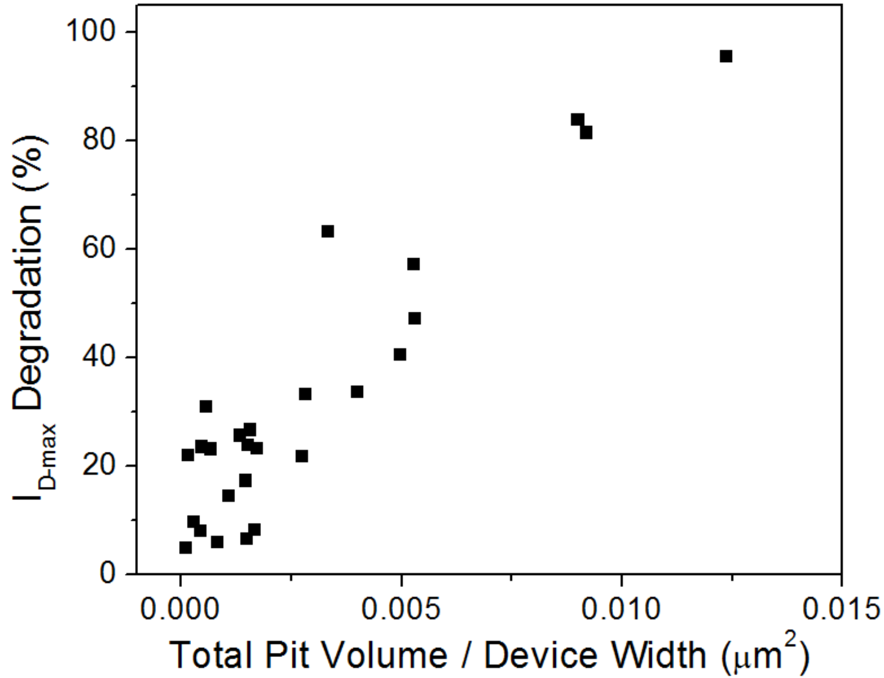

Figure 6.10 $I_{D\text{-}max}$ degradation plotted against normalized total pit volume calculated from the stressed devices

6.4.2 Electro-chemical Oxidation Reaction

The correlation between $I_{D\text{-}max}$ degradation and pit volume was shown in previous section. The next step is to relate $I_{D\text{-}max}$ degradation with the amount of oxygen diffusing through the Si_xN_{1-x} passivation. It is assumed that the amount of AlGaN oxidized is equal to the total pit volume in drain-gate access region and oxygen from the ambient is the only source of oxygen for AlGaN electro-chemical oxidation. The Al and Ga composition in $Al_xGa_{1-x}N$ are 0.26 and 0.74, respectively [107]. The diffusing oxygen species is assumed to be oxygen molecules instead of water vapor because of the high stressing temperature about 150-225°C. At this range of temperature, the humidity in the device vicinity is only about 2%. The electro-chemical oxidation reaction of AlGaN can be seen in equation 6.3.

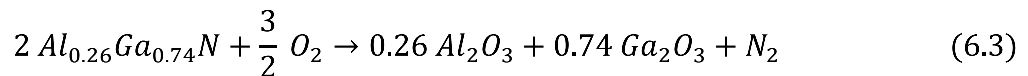

$$2\,Al_{0.26}Ga_{0.74}N + \frac{3}{2}\,O_2 \rightarrow 0.26\,Al_2O_3 + 0.74\,Ga_2O_3 + N_2 \qquad (6.3)$$

The molecular mass of $Al_{0.26}Ga_{0.74}N$ is calculated using equation 6.4. The atomic mass of Al, Ga and N are 27, 69.7 and 14, respectively. The molecular mass of $Al_{0.26}Ga_{0.74}N$ is 72.6 g/mol.

$$MR_{Al_xGa_{1-x}N} = (AR_{Al})(x) + (AR_{Ga})(1-x) + (AR_N)(1) \quad (6.4)$$

The density of pure AlN and GaN are 3.26 g/cm^3 [172, 173] and 6.15 g/cm^3 [174]. The density of $Al_xGa_{1-x}N$ was assumed to be a fraction of AlN and GaN densities. Using equation 6.5, the density of $Al_{0.26}Ga_{0.74}N$ is 5.40 g/cm^3.

$$\rho_{Al_xGa_{1-x}N} = (\rho_{AlN})(x) + (\rho_{GaN})(1-x) \quad (6.5)$$

Let V be the total pit volume (in µm^3) in the drain-gate access region of the stressed devices. The number of moles of $Al_{0.26}Ga_{0.74}N$ can be represented as

$$No\ of\ moles_{Al_{0.26}Ga_{0.74}N} = \frac{\rho_{Al_{0.26}Ga_{0.74}N}V}{MR_{Al_{0.26}Ga_{0.74}N}} \quad (6.6)$$

By stoichiometry in equation 6.3,

$$2Al_{0.26}Ga_{0.74}N \equiv \frac{3}{2}O_2 \quad (6.7)$$

$$No\ of\ moles_{O_2} = \left(\frac{3}{2}\right)\left(\frac{1}{2}\right)No\ of\ moles_{Al_{0.26}Ga_{0.74}N} \quad (6.8)$$

Substituting equation (6.6) into (6.8),

$$No\ of\ moles_{O_2} = \left(\frac{3}{2}\right)\left(\frac{1}{2}\right)\frac{\rho_{Al_{0.26}Ga_{0.74}N}V}{MR_{Al_{0.26}Ga_{0.74}N}} \quad (6.9)$$

The total number of moles of O_2 reacted in the electro-chemical oxidation is calculated by substituting the total pit volume for each stressed device into equation 6.9.

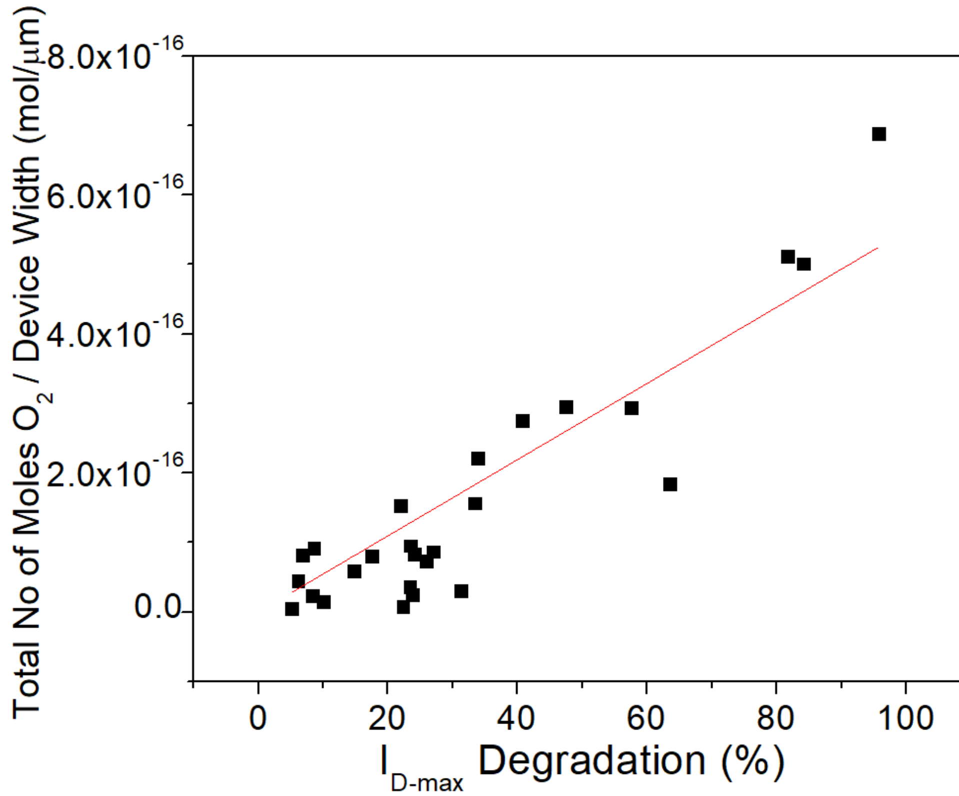

Figure 6.11 Total numbers of moles O_2 used in electro-chemical oxidation plotted as a function of $I_{D\text{-}max}$ degradation for all the stressed devices

Figure 6.11 shows the total number of moles of O_2 reacted as a function of $I_{D\text{-}max}$ degradation. The data is then linearly fitted to obtain the relationship between number of moles of O_2 used and $I_{D\text{-}max}$ degradation. The linear relationship can be represented as

$$\frac{No\ of\ moles\ O_2}{W_G}\ \left(\frac{mol}{\mu m}\right) = m[I_{D-max}\,\deg(\%)] \tag{6.10}$$

where m is the slope of the fitting line and W_G is the device width.

Equation 6.10 connects the electrical degradation with the amount of oxygen used in AlGaN electro-chemical oxidation during the slow degradation mode. In the next sub-section, this equation is used to calculate the oxygen diffusion through Si_xN_{1-x} passivation layer.

6.4.3 Oxygen Diffusion through Si_xN_{1-x} Passivation

In slow degradation mode, the oxygen diffuses through the degraded Si_xN_{1-x} passivation layer and reacts with AlGaN upon reaching AlGaN/Si_xN_{1-x} interface. Oxygen from ambient becomes the dominant source of oxygen once the pre-existing oxygen depletes. The lack of oxygen at the AlGaN/Si_xN_{1-x} interface generates the concentration gradient which leads to oxygen diffusion from the ambient to the AlGaN/Si_xN_{1-x} interface through the Si_xN_{1-x} passivation layer. For all the stressed devices, $I_{D\text{-}max}$ decreases linearly in the slow degradation mode. This suggests that oxygen diffusion is at steady-state.

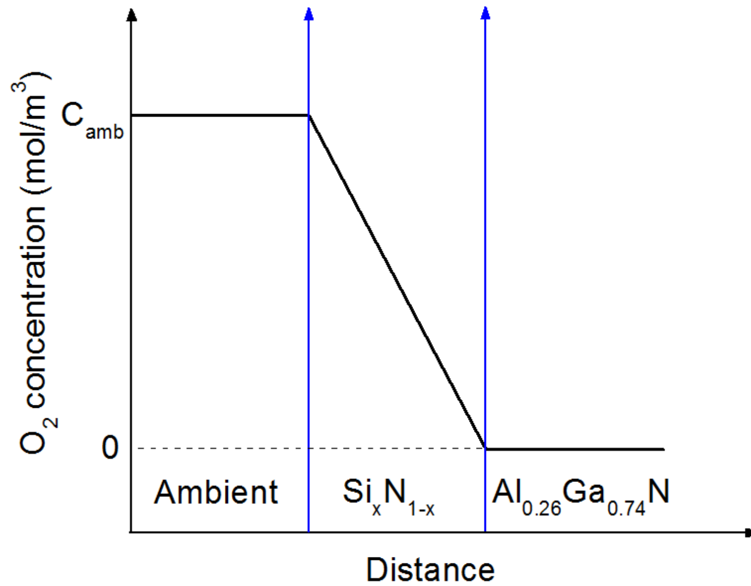

Figure 6.12 O_2 concentration profile in the steady-state diffusion through Si_xN_{1-x} passivation

Figure 6.12 shows O_2 concentration profile for steady-state diffusion through Si_xN_{1-x} passivation. Oxygen diffuses through Si_xN_{1-x} passivation and it immediately reacts with AlGaN upon reaching AlGaN/Si_xN_{1-x} interface, i.e. the oxygen concentration at AlGaN/Si_xN_{1-x} interface is always zero. Since, the oxygen concentration in the ambient is constant, the concentration gradient between ambient and AlGaN surface is constant. The steady-state diffusion can be represented by Fick's first law equation as follow,

$$J = -D\,\frac{\Delta C}{\Delta x} \tag{6.11}$$

where J is the diffusion flux (mol/m^2.s), D is the diffusivity (m^2/s) and $\frac{\Delta C}{\Delta x}$ is the concentration gradient (mol/m^4). Fick's first law states that diffusion flux is proportional to the concentration gradient. The negative sign indicates that J is positive when the movement is down the gradient. This negative sign will cancel the negative gradient along the direction of the positive flux.

The next step is to calculate the oxygen concentration in ambient. Assuming that air is an ideal gas and oxygen is 20% of the gases in the air, the oxygen concentration in the ambient air can be represented as

$$C_{amb} = \frac{n}{V} = B\frac{P}{RT_s} \tag{6.12}$$

where P is the ambient air pressure (1 atm), B is the oxygen concentration in air (%), T_s is the surrounding temperature (K) during ON-state stressing and R is gas constant (8.206 m^3.atm.K^{-1}.mol^{-1}).

The length of diffusion medium, Δx, is the Si_xN_{1-x} passivation layer thickness. The Si_xN_{1-x} passivation layer thickness is 120 nm measured by cross-sectional TEM. Therefore, the concentration gradient can be expressed as

$$\frac{\Delta C}{\Delta x} = \frac{C_{amb} - C_{AlGaN/Si_xN_{1-x}\, interface}}{X_{Si_xN_{1-x}}} \tag{6.13}$$

where $X_{Si_xN_{1-x}}$ is Si_xN_{1-x} passivation layer thickness (m).

Substituting equation 6.12 to 6.13,

$$\frac{\Delta C}{\Delta x} = \frac{B}{X_{Si_xN_{1-x}}}\frac{P}{RT_s} \tag{6.14}$$

Equation 6.14 shows that the concentration gradient is dependent on the ambient temperature during stressing. This temperature is taken as the chamber temperature during the stressing. The concentration gradients for all the stressing batches were calculated using equation 6.14 and the result is summarized in Table 6.5.

Table 6.5 Concentration gradients for all three stressing batches under ON-state condition V_{DS} = 20 V, V_{GS} = 0 V with 2 different Si_xN_{1-x} densities

Batch Number	Stressing Temperature (K)	Concentration Gradient (mol/m^4)
Batch 1	423	4.802×10^7
Batch 2	448	4.534×10^7
Batch 3	498	4.079×10^7

Diffusion flux (J) is the rate at which amount of substance (mol) diffuses through an area of the diffusion medium. In this case, diffusion flux is the number of moles of O_2 that diffuses through Si_xN_{1-x} passivation layer per second. Figure 6.13 shows a typical no of moles O_2 over stressing time for stressed device. Equation 6.10 was used to convert $I_{D\text{-}max}$ degradation into number of moles O_2.

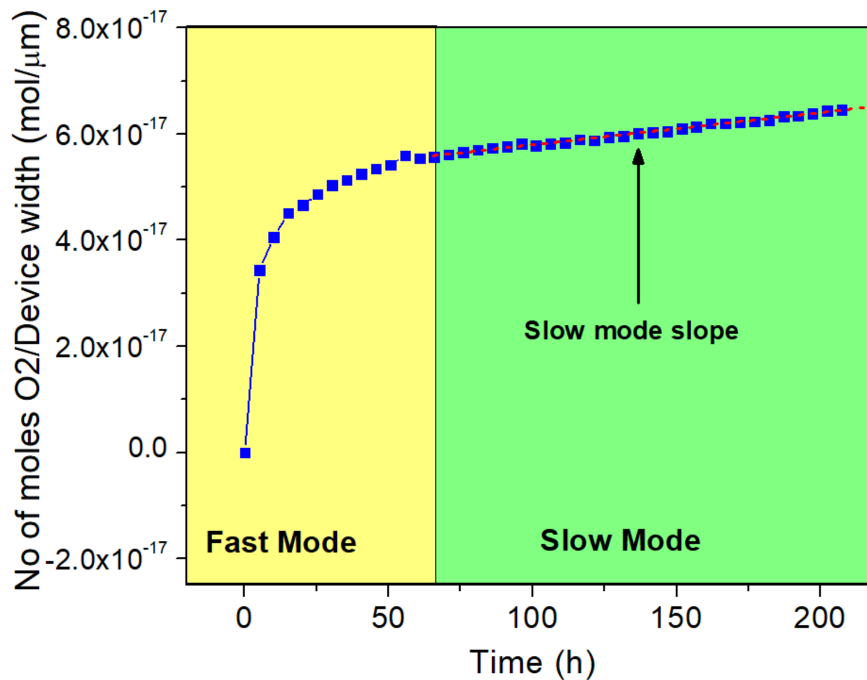

Figure 6.13 Number of moles O_2 distribution plot for AlGaN/GaN HEMT device stressed under ON-state condition

The number of moles O_2 increases linearly in the slow degradation mode. The slow mode slope becomes the rate of ambient O_2 reacted with AlGaN per unit device width. Slow mode slope can be expressed as

$$Slow\ mode\ slope = \frac{No\ of\ moles\ O_2}{W_G\ t} \tag{6.15}$$

where W_G is the device width (μm) and t is stressing time (s).

In order to convert this rate to flux, the slow mode slope is normalized against the distance L from the gate edge where the Si_xN_{1-x} passivation layer is likely to degrade due to high electric field (Figure 6.14). For this calculation, L was fixed at 300 nm as this is the distance where the electric field is at least 1 MV/cm. Therefore, diffusion flux (J) can be represented as

$$J = \frac{No\ of\ moles\ O_2}{L\ W_G\ t} \tag{6.16}$$

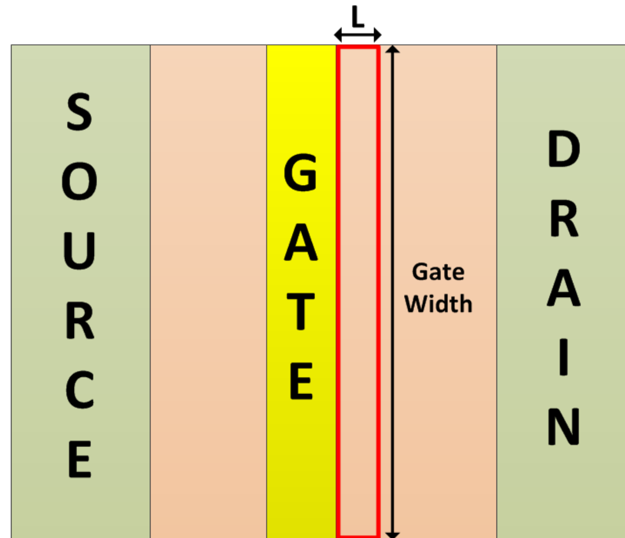

Figure 6.14 Top-view schematic of AlGaN/GaN HEMT device to show the distance L where the Si_xN_{1-x} passivation is likely to degrade due to high electric field

After concentration gradient and diffusion flux of all the stressed devices were computed, diffusivity can be calculated by equation 6.11. Diffusivity can be expressed as Arrhenius equation,

$$D = D_0 \exp\left(-\frac{Q_d}{RT_j}\right) \quad (6.17)$$

where D is the diffusivity, D_0 is the pre-exponent factor, T_j is stressing/junction temperature, R is gas constant and Q_d is the activation energy.

Re-arranging equation 6.17 gives,

$$\ln D = \ln D_0 - \frac{Q_d}{R}\left(\frac{1}{T_j}\right) \quad (6.18)$$

Activation energy (Q_d) and pre-exponent factor (D_0) can be estimated by linear plotting (D) versus $\left(\frac{1}{T_j}\right)$.

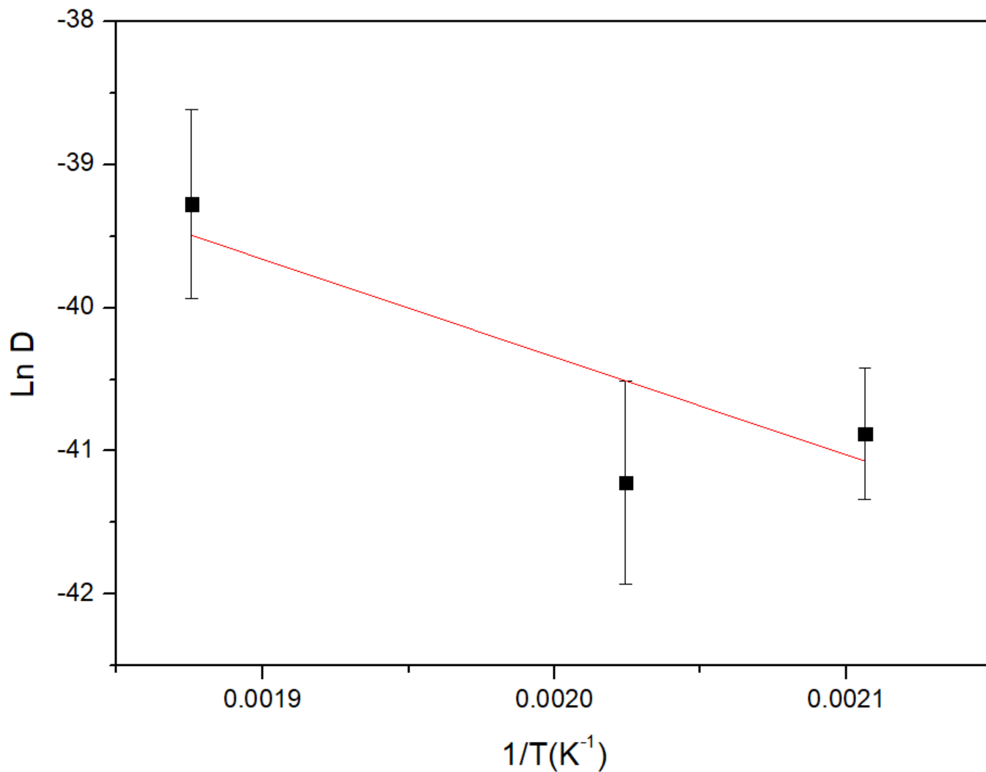

Figure 6.15 Arrhenius plot of the O_2 diffusivity through degraded Si_xN_{1-x} passivation layer

Figure 6.15 shows the Arrhenius plots for oxygen diffusion through the degraded passivation layer. Activation energy Q_d and pre-exponent factor D_0 were extracted and summarized in Table 6.6.

Table 6.6 Activation energy Q_d and pre-exponent factor D_0 for O_2 diffusion through degraded Si_xN_{1-x} passivation layer

Activation Energy (eV)	Pre-exponent Factor (m^2/s)
0.59 ± 0.34	2.59×10^{-12}

There is no activation energy reported for oxygen diffusion through amorphous silicon nitride. The closest case is nitrogen diffusion through silicon nitride as the size difference between nitrogen and oxygen atoms is small. The activation energy for nitrogen diffusion through crystalline silicon nitride varies from 1.46 eV to 6.85 eV [175] and for amorphous silicon nitride is 3.6 eV [176]. However, these values are much higher than the energy calculated in this study.

Perez-Bueno *et al.* reported activation energy of 0.73 eV for oxygen diffusion through porous amorphous silicon dioxide [177]. This value is close to the result obtained in this study. This suggests that the oxygen from the ambient penetrates through silicon dioxide rather than silicon nitride. This is consistent with the silicon nitride degradation observation. The silicon nitride at the gate edge degraded into silicon dioxide and oxygen from the ambient can easily diffuse through this degraded portion of the passivation layer to reach AlGaN/Si_xN_{1-x} interface. For high density passivation, it takes longer to degrade the silicon nitride due to higher breakdown field but once it degrades into silicon dioxide, the rate of oxygen diffusing through is the same for both high and low density passivation.

6.4.4 Temperature Dependence of $I_{D\text{-}max}$ Degradation

First of all, the relationship between $I_{D\text{-}max}$ degradation and degradation pits was determined empirically. The pit volume was then correlated with the amount of oxygen diffusion based on electro-chemical oxidation reaction of AlGaN. After that, temperature dependence of oxygen diffusion was explained based on Fick's first law of diffusion. These results are combined in this sub-section in order to obtain the temperature dependence of $I_{D\text{-}max}$ degradation. Starting from Fick's first law equation,

$$J = D\,\frac{\Delta C}{\Delta x} \tag{6.19}$$

Substituting equations 6.10, 6.14, 6.16 and 6.17 into equation 6.19,

$$\frac{m[I_{D-max}\,\mathrm{deg}(\%)]}{L\,t} = D_0 \exp\left(-\frac{Q_d}{RT_j}\right)\frac{B}{X_{Si_xN_{1-x}}}\,\frac{P}{RT_S} \tag{6.20}$$

Re-arranging equation (6.20),

$$I_{D-max}Deg\ (\%) = \left[\frac{B.P.L.D_0}{R.T_S.m.X_{Si_xN_{1-x}}}\exp\left(-\frac{Q_d}{RT_j}\right)\right]t \tag{6.21}$$

where t is stressing time (s)

T_S is surrounding temperature (K)

T_j is stressing/junction temperature (K)

Q_d is activation energy (eV)

R is gas constant

D_0 is the diffusion pre-exponent factor (m^2/s)

P is atmospheric pressure (atm)

B is oxygen concentration in air (%)

L is length of degraded passivation layer (m)

m is the fitting line slope from Figure 6.11 (mol/µm.%)

$X_{Si_xN_{1-x}}$ is passivation thickness (m)

The equation 6.21 shows the I_{D-max} degradation as a function of stressing temperature and stressing time. This equation can be used to predict the I_{D-max} slow mode degradation after stressing the device for t seconds under ON-state condition, V_{DS} = 20 V and V_{GS} = 0 V, at surrounding temperature T_S K. However, there are limitations to this model. Firstly, this model is limited to one bias condition as the effect of stressing voltage is not included in the equation. Secondly, this model is only based on the slow mode degradation as this model did not take into account the pre-existing oxygen caused by imperfect lift-off process.

6.5 Summary

The effect of passivation density on the AlGaN/GaN HEMT degradation under ON-state stressing condition was discussed in this chapter. Two sets of AlGaN/GaN HEMT devices with different Si_xN_{1-x} densities were stressed under ON-state condition V_{DS} = 20 V, V_{GS} = 0 V at three different temperatures. XRR measurement showed that the high density Si_xN_{1-x} is 10% denser than the low density Si_xN_{1-x}.

Cross-sectional TEM image showed nano-globes in the Si_xN_{1-x} layer on the gate edge of the drain side after electrical stressing. EELS analysis showed that the nano-globes had a lower density and the area around them had high oxygen concentration and low nitrogen concentration. This suggests that silicon nitride is oxidized into silicon oxide during electrical stressing. High electric field at the gate edge on the drain side is likely to be the reason for this silicon nitride oxidation. Oxygen from the ambient can easily diffuse through the degraded Si_xN_{1-x} to the AlGaN surface.

High density passivation had a longer conversion time than low density passivation for all temperatures. The difference in conversion time became less apparent at high temperature because the energy required to degrade the passivation was easily overcome by the combination of high temperature and high electric field. This result suggests that high density passivation is harder to degrade as it has higher breakdown field than low density passivation. Once it degrades, the oxygen from ambient can diffuse through the degraded passivation at a comparable rate between high and low density passivation. This was supported by comparable slow mode slopes between the two passivation densities.

A slow mode degradation model is proposed based on the electro-chemical oxidation and oxygen diffusion through degraded passivation layer. The activation energy obtained from the calculation is 0.59 eV. This value are close to the reported value for oxygen diffusion through porous silicon dioxide [177]. This is consistent with the cross-sectional TEM and EELS analysis which showed that the degraded area had high oxygen content and low nitrogen content. This suggests that silicon nitride degraded into silicon dioxide and this

degraded region becomes preferable diffusion path for oxygen from ambient to AlGaN/Si_xN_{1-x} interface. This model can be used to predict the $I_{D\text{-}max}$ slow mode degradation for AlGaN/GaN HEMT on Si stressed under ON-state bias V_{DS} = 20 V and V_{GS} = 0 V.

Chapter 7

Summary and Future Works

This chapter concludes the AlGaN/GaN HEMT-on-Si ON-state degradation study presented in the previous chapters. Key achievements of the thesis are summarized and linked to the objectives of the reliability study. This study has improved the understanding of AlGaN/GaN HEMT ON-state reliability which complements the OFF-state reliability knowledge. However, there are some issues such as small number of samples that limit the scope of this study. The implications and limitations of the study are thoroughly discussed in this chapter. Last but not least, some possibilities for future work are discussed such as statistical analysis and studying the effect of growth orientation on the device reliability.

7.1 Summary

The main objective of this project is to understand ON-state degradation of AlGaN/GaN HEMT devices grown on Si substrate in order to improve the reliability of AlGaN/GaN HEMT-on-Si technology. In Chapter 4, OFF-state degradation was compared to ON-state degradation with a starting hypothesis that the role of 2DEG current in ON-state degradation is just to increase junction temperature via joule heating. This hypothesis was proven wrong as I_{D-max} degradation under ON-state stressing was 30% higher than under OFF-state stressing despite having 33°C lower stressing temperature during ON-state stressing. Microstructure characterization on the de-processed devices after electrical stressing revealed that pits had formed in the drain-gate access region for devices stressed under ON-state condition whereas pits were confined at the gate edge for the devices stressed under OFF-state condition. Cross-sectional TEM analysis on device stressed under ON-state condition showed dark features at the AlGaN/Si_xN_{1-x} interface away from the gate edge on the drain side of the device. These dark features contained oxygen, gallium and aluminum, which indicated AlGaN oxidation during the electrical stressing.

More pits were found at the drain-gate access region of the devices stressed under ON-state condition with negative substrate bias. This suggested that electrons from 2DEG were involved in the AlGaN oxidation away from the gate edge as the negative substrate bias forced electrons from 2DEG to move upward. Based on these findings, a qualitative ON-state degradation model was proposed. The hot electrons from 2DEG were injected to AlGaN/Si_xN_{1-x} interface and, at the same time, produced holes via impact ionization. These electrons reacted with oxygen at the AlGaN/Si_xN_{1-x} interface to form oxygen ions. These oxygen ions then oxidized AlGaN layer away from the gate edge in the presence of holes to produce aluminum and gallium oxides which were observed as dark features. The oxidized AlGaN was removed during the metallization and passivation layer etching, leaving behind pits at the drain-gate access region.

The effect of different current densities in AlGaN/GaN HEMT ON-state degradation was thoroughly discussed in Chapter 5. The stressing parameters were chosen carefully to

ensure that devices were stressed at different current densities and kept the other parameters constant. Thermal and electrical simulations were used to ensure that the stressing temperatures were the same and negligible electric field difference between the two current density stressing conditions. The results showed that current density correlated well with the maximum pit distance at the drain-gate access region. This was because the amount of hot electrons being injected to the AlGaN/Si_xN_{1-x} interface increased proportionally with increasing current density, i.e. amount of electrons at 2DEG channel. Hot electrons were also spread further away from the gate edge for higher current density devices. This led to pit formation further away from the gate edge in the drain-gate access region.

In Chapter 5, it also was discovered that AlGaN/GaN HEMT ON-state degradation consisted of two degradation modes i.e. fast and slow degradation modes. These two degradation modes were differentiated by the source of oxygen. In fast degradation mode, the major source of oxygen was pre-existing oxygen at the AlGaN/Si_xN_{1-x} interface due to imperfect lift-off process. This was supported by EELS line-scans at the AlGaN/Si_xN_{1-x} interface of fresh device which showed oxygen presence. In contrast, the predominant source of oxygen in slow degradation mode was oxygen from the ambient. This was supported by comparison between the ON-state stressing under high vacuum and under normal ambient. The device stressed under vacuum stopped degrading after fast degradation mode whereas the device stressed under normal ambient continued to degrade linearly.

In Chapter 6, the effect of passivation density on AlGaN/GaN HEMT ON-state degradation was investigated using two different Si_xN_{1-x} densities. The high density passivation has 2 times higher breakdown field compared to low density passivation. All the devices were stressed under ON-state condition V_{DS} = 20 V, V_{GS} = 0 V at three different temperatures. These devices were then analyzed and compared based on conversion time and slow mode slope. Conversion time is the time beyond which the device degrades linearly over time and slow mode slope is the gradient of the linear portion of $I_{D\text{-}max}$ vs time plot after conversion point. It was observed that high density passivation had a longer conversion time than low density passivation for all temperatures. This was expected as high density

passivation required more time to degrade due to its higher breakdown field compared to low density passivation. It was also found that the slow mode slope of high density passivation was comparable to that of low density passivation and it increased with temperature. This suggested that oxygen diffused through at the same rate for both passivation densities after the passivation degraded and it was thermally-activated process. Therefore, the slow mode degradation rate depends on temperature but not passivation density.

Cross-sectional TEM showed that Si_xN_{1-x} at the gate edge on the drain side degraded into silicon oxide upon electrical stressing. The degraded area contained high concentration of oxygen and low concentration of nitrogen. Nano-globes were also found in the degraded area and they had lower relative density than non-degraded location. The high electric field at the gate edge on the drain side (1-3 MV/cm) made Si_xN_{1-x} oxidation possible. The oxygen from the ambient could easily diffuse through the degraded Si_xN_{1-x} and contributed to AlGaN oxidation at AlGaN/Si_xN_{1-x} interface.

Finally, a quantitative model for ON-state slow degradation mode was proposed based on electro-chemical oxidation and oxygen diffusion through Si_xN_{1-x} passivation. Activation energy for oxygen diffusion obtained from the model is 0.59 eV. This value is close to the activation energy for oxygen diffusion through porous silicon dioxide reported by Perez-Bueno *et al.* [177]. This suggests that oxygen diffuses from the degraded portion of Si_xN_{1-x} passivation and this is consistent with the cross-sectional TEM which showed that degraded Si_xN_{1-x} had high oxygen content and low nitrogen content.

The new findings mentioned above have fulfilled the main objectives of the study. This thesis improves the understanding on electrical and physical degradation mechanisms in AlGaN/GaN HEMT-on–Si devices stressed under ON-state condition. The stressing parameters such as current density, passivation density and temperature were varied and the effect of each parameter was discussed. Last but not least, AlGaN/GaN HEMT ON-state degradation model was developed based on electro-chemical oxidation of AlGaN.

7.2 Implications and Limitations

This thesis presented several key achievements. The implications and limitations of these key achievements will be discussed in this section.

First and foremost, this work presented a direct comparison between OFF-state and ON-state degradation of AlGaN/GaN HEMT. The results showed that the degradation under ON-state condition was more severe than OFF-state condition due to the presence of hot electron flow in 2DEG channel. The implication of this finding is that it is crucial to tackle the ON-state reliability problem first before the OFF-state reliability, especially so as enhancement-mode (E-mode) AlGaN/GaN HEMT has drawn a lot of interest recently. E-mode AlGaN/GaN HEMT allows circuit simplicity, low standby power dissipation and better system safety [11, 178, 179]. In E-mode devices, a higher voltage has to be applied during ON-state condition due to the positive threshold voltage. This may lead to higher ON-state degradation in E-mode devices. Thus it is very important to solve ON-state reliability problems.

The second key finding was the two $I_{D\text{-}max}$ degradation modes. These two degradation modes were observed in devices stressed under ON-state and OFF-state conditions. Pre-existing oxygen caused the fast degradation mode whereas slow degradation mode was caused by oxygen diffusion from the ambient through the Si_xN_{1-x} passivation layer. This result showed the importance of good lift-off process to minimize amount of pre-existing oxygen at AlGaN/Si_xN_{1-x} interface. It is even more important to note that denser passivation can mitigate Si_xN_{1-x} degradation and thus, preventing oxygen from ambient to diffuse to AlGaN/Si_xN_{1-x} interface to oxidize AlGaN layer and degrade the device performance.

Lastly, ON-state degradation model was presented in this thesis based on the electro-chemical oxidation. This was the first reported model for AlGaN/GaN HEMT ON-state degradation. This model complements the OFF-state model based on the same mechanism proposed by Feng *et al.* [16]. In chapter 6, the relationship between temperature and $I_{D\text{-}max}$ degradation under ON-state condition was proposed. This relationship can be used to

predict I_{D-max} ON-state slow degradation at different stressing temperatures with constant bias. However, there are some limitations to this model. First, this relationship is limited to slow degradation mode and it does not take into account the fast degradation mode. Secondly, there are other stressing and process parameters that have to be included in this mathematical equation such as electric field, current density and threading dislocation density.

7.3 Future Work

Despite the key findings made in this thesis, there are still a lot of questions to be answered about AlGaN/GaN HEMT ON-state reliability. Possibilities of future works are discussed in this section.

The main limitation of this project is sample availability. Large device-to-device variations were observed for the same stressing condition. Stressing more devices for each condition can show a clearer effect of each stressing/process parameter in ON-state degradation. Also, different stressing conditions can be explored with abundant samples. Firstly, the ON-state degradation study can be done with different composition of SiN passivation. This will complete the study of different passivation density and thus a clearer correlation between I_{D-max} degradation and passivation density can be obtained. From this study, one can obtain the best SiN composition to prevent device degradation.

Secondly, an ON-state stressing can be done at different environments such as high humidity, high oxygen level and ozone environment. This study will give correlation between different sources of oxygen (H_2O, O_2 and O_3) and I_{D-max} degradation under ON-state stressing. In addition, ON-state stressing under different environments can simulate the harsh environment in which AlGaN/GaN HEMT will be used.

ON-state stressing with devices grown with different crystal orientation can be another potential future work. Figure 7.1 shows the design of AlGaN/GaN HEMT grown in the same chip with different orientations i.e. [1100] and [1120]. The rationale behind this is

that ON-state bias stressing may induce mechanical stress because of the inverse-piezoelectric phenomenon. This mechanical stress is anisotropic in lateral direction. These structures can be used to investigate the effect of mechanical stress in AlGaN/GaN HEMT ON-state degradation. The correlation between $I_{D\text{-}max}$ degradation and these parameters can be incorporated into the model proposed in Chapter 6 in order to obtain more complete model for slow degradation mode.

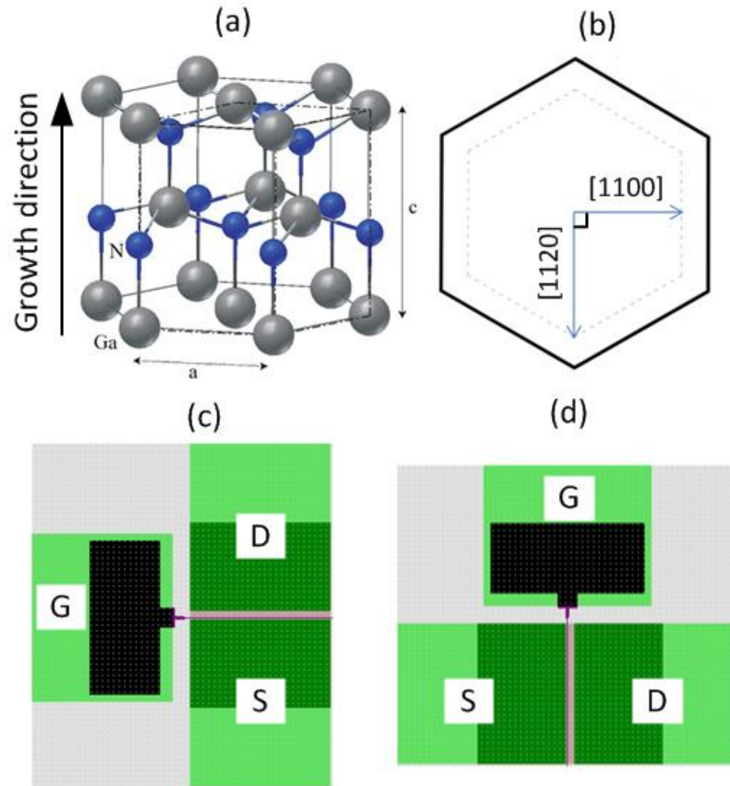

Figure 7.1 (a) Unit cell of GaN hexagonal-wurzite structure [37], (b) top view of the unit cell, and AlGaN/GaN HEMT devices grown in the same chip in (c) [1100], (d) [1120] orientations

Moreover, the ON-state electrical degradation discussed in this thesis was based on $I_{D\text{-}max}$ degradation. There are other electrical parameters that can be investigated such as $I_{G\text{-}leak}$ and V_{TH}. These parameters were out of the thesis scope as they may induce different degradation mechanism such as gate metal inter-diffusion driven by local strain [180]. This study will advance the understanding of AlGaN/GaN HEMT ON-reliability even further.

Last but not least, after understanding the effect of various parameters on AlGaN/GaN HEMT ON-state degradation with a large number of samples, statistical model needs to be develop in order to predict the life-time of AlGaN/GaN HEMT devices on silicon substrate.

7.4 List of Publication

1) "ON-State Reliability of AlGaN/GaN High Electron Mobility Transistor (HEMT) on Silicon Substrate" presented in student presentation session in European Symposium on Reliability of Electron Devices, Failure Physics and Analysis (ESREF) 2016.

2) "Role of two-dimensional electron gas (2DEG) in AlGaN/GaN high electron mobility transistor (HEMT) ON-state degradation" presented as poster in ESREF 2016 and published as a special journal issue in Microelectronics Reliability.

References

[1] A. Vescan *et al.*, "AlGaN/GaN HFETs on 100 mm silicon substrates for commercial wireless applications," *physica status solidi (c),* no. 1, pp. 52-56, 2003.

[2] L. Liu and J. H. Edgar, "Substrates for gallium nitride epitaxy," *Materials Science and Engineering: R: Reports,* vol. 37, no. 3, pp. 61-127, 2002.

[3] A. Krost and A. Dadgar, "GaN-based optoelectronics on silicon substrates," *Materials Science and Engineering: B,* vol. 93, no. 1, pp. 77-84, 2002.

[4] L. F. Eastman *et al.*, "Undoped AlGaN/GaN HEMTs for microwave power amplification," *IEEE Transactions on Electron Devices,* vol. 48, no. 3, pp. 479-485, 2001.

[5] M. Hao *et al.*, "Study of threading dislocations in wurtzite GaN films grown on sapphire by metalorganic chemical vapor deposition," *Japanese journal of applied physics,* vol. 37, no. 3A, p. L291, 1998.

[6] T. Hino, S. Tomiya, T. Miyajima, K. Yanashima, S. Hashimoto, and M. Ikeda, "Characterization of threading dislocations in GaN epitaxial layers," *Applied Physics Letters,* vol. 76, no. 23, pp. 3421-3423, 2000.

[7] S. Kaiser *et al.*, "Structural properties of AlGaN/GaN heterostructures on Si (111) substrates suitable for high-electron mobility transistors," *Journal of Vacuum Science & Technology B: Microelectronics and Nanometer Structures Processing, Measurement, and Phenomena,* vol. 18, no. 2, pp. 733-740, 2000.

[8] GATAN. (2017, 22 August). *EELS Atlas*. Available: http://www.eels.info/atlas

[9] S. Taranovich. (2013, 11 September 2016). *Si vs. GaN vs. SiC: Which process and supplier are best for my power design?* Available: http://www.edn.com/design/power-management/4409627/2/Si-vs--GaN-vs--SiC--Which-process-and-supplier-are-best-for-my-power-design-

[10] O. Ambacher *et al.*, "Two dimensional electron gases induced by spontaneous and piezoelectric polarization in undoped and doped AlGaN/GaN heterostructures," *Journal of Applied Physics,* vol. 87, no. 1, pp. 334-344, 2000.

[11] D. Ueda, "Properties and Advantages of Gallium Nitride," in *Power GaN Devices*: Springer, 2017, pp. 1-26.

[12] J. Joh, J. A. Del Alamo, K. Langworthy, S. Xie, and T. Zheleva, "Role of stress voltage on structural degradation of GaN high-electron-mobility transistors," *Microelectronics Reliability,* vol. 51, no. 2, pp. 201-206, 2011.

[13] J. Joh, F. Gao, T. Palacios, and J. A. del Alamo, "A model for the critical voltage for electrical degradation of GaN high electron mobility transistors," *Microelectronics Reliability,* vol. 50, no. 6, pp. 767-773, 2010.

[14] P. Makaram, J. Joh, J. A. del Alamo, T. Palacios, and C. V. Thompson, "Evolution of structural defects associated with electrical degradation in AlGaN/GaN high electron mobility transistors," *Applied Physics Letters,* vol. 96, no. 23, pp. 233509-3, 2010.

[15] F. Gao *et al.*, "Role of oxygen in the OFF-state degradation of AlGaN/GaN high electron mobility transistors," *Applied Physics Letters,* vol. 99, no. 22, pp. 223506-3, 2011.

[16] G. Feng, T. Swee Ching, J. A. del Alamo, C. V. Thompson, and T. Palacios, "Impact of Water-Assisted Electrochemical Reactions on the OFF-State Degradation of AlGaN/GaN HEMTs," *Electron Devices, IEEE Transactions on,* vol. 61, no. 2, pp. 437-444, 2014.

[17] M. Meneghini *et al.*, "Time-dependent degradation of AlGaN/GaN high electron mobility transistors under reverse bias," *Applied Physics Letters,* vol. 100, no. 3, pp. -, 2012.

[18] M. Montes Bajo, C. Hodges, M. Uren, and M. Kuball, "On the link between electroluminescence, gate current leakage, and surface defects in AlGaN/GaN high electron mobility transistors upon off-state stress," *Applied Physics Letters,* vol. 101, no. 3, p. 033508, 2012.

[19] D. Marcon *et al.*, "Reliability analysis of permanent degradations on AlGaN/GaN HEMTs," *IEEE Transactions on Electron Devices,* vol. 60, no. 10, pp. 3132-3141, 2013.

[20] M. Meneghini, A. Stocco, R. Silvestri, G. Meneghesso, and E. Zanoni, "Degradation of AlGaN/GaN high electron mobility transistors related to hot electrons," *Applied Physics Letters,* vol. 100, no. 23, pp. 233508-3.

[21] D. Pavlidis, P. Valizadeh, and S. Hsu, "AlGaN/GaN high electron mobility transistor (HEMT) reliability," in *Gallium Arsenide and Other Semiconductor Application Symposium, 2005. EGAAS 2005. European*, 2005, pp. 265-268: IEEE.

[22] S. Y. Park *et al.*, "Physical degradation of GaN HEMT devices under high drain bias reliability testing," *Microelectronics Reliability,* vol. 49, no. 5, pp. 478-483, 2009.

[23] Y. Wu, C.-Y. Chen, and J. A. del Alamo, "Electrical and structural degradation of GaN high electron mobility transistors under high-power and high-temperature Direct Current stress," *Journal of Applied Physics,* vol. 117, no. 2, p. 025707, 2015.

[24] Z. Dong *et al.*, "High temperature induced failure in Ti/Al/Ni/Au Ohmic contacts on AlGaN/GaN heterostructure," *Microelectronics Reliability,* vol. 52, no. 2, pp. 434-438, 2012.

[25] M. Piazza, C. Dua, M. Oualli, E. Morvan, D. Carisetti, and F. Wyczisk, "Degradation of TiAlNiAu as ohmic contact metal for GaN HEMTs," *Microelectronics Reliability,* vol. 49, no. 9, pp. 1222-1225, 2009.

[26] G. Feng, L. Hsin-Yi, R. Ram, and T. Palacios, "Self-consistent electro-thermal simulation of AlGaN/GaN HEMTs for reliability prediction," in *Device Research Conference (DRC), 2010*, 2010, pp. 127-128.

[27] S. Atlas, "Device simulation software," *User's manual,* 1998.

[28] D. Henry. (24 August 2012). *Electron-Sample Interactions*. Available: http://serc.carleton.edu/research_education/geochemsheets/electroninteractions.html

[29] H. Iwai *et al.*, "Quantification of SOFC anode microstructure based on dual beam FIB-SEM technique," *Journal of Power Sources,* vol. 195, no. 4, pp. 955-961, 2010.

[30] (2012, 2 May 2017). *TEM*. Available: http://research.ntu.edu.sg/facts/Facilities/Pages/TEM.aspx

[31] P. D. Ngo, "Energy dispersive spectroscopy," in *Failure Analysis of Integrated Circuits*: Springer, 1999, pp. 205-215.

[32] D. H. Shin, "Scanning transmission electron microscopy studies of high temperature superconducting yttrium barium copper oxide thin films," ed, 1992.

[33] R. F. Egerton, "TEM Applications of EELS," in *Electron Energy-Loss Spectroscopy in the Electron Microscope*Boston, MA: Springer US, 2011, pp. 293-397.

[34] (2017, 17 April 2017). *X-ray Reflectivity (XRR)*. Available: https://www.bruker.com/products/x-ray-diffraction-and-elemental-analysis/x-ray-metrology/d8-fabline/metrology-knowledge/x-ray-metrology-knowledge/xrr.html

[35] (2012, 19 April 2017). *XRD*. Available: http://research.ntu.edu.sg/facts/Facilities/Pages/XRD.aspx

[36] M. Kuball, M. Ťapajna, R. J. T. Simms, M. Faqir, and U. K. Mishra, "AlGaN/GaN HEMT device reliability and degradation evolution: Importance of diffusion processes," *Microelectronics Reliability,* vol. 51, no. 2, pp. 195-200, 2// 2011.

[37] M.-T. Hoang, J. Yvonnet, A. Mitrushchenkov, and G. Chambaud, "First-principles based multiscale model of piezoelectric nanowires with surface effects," *Journal of Applied Physics,* vol. 113, no. 1, p. 014309, 2013.

[38] U. K. Mishra, P. Parikh, and W. Yi-Feng, "AlGaN/GaN HEMTs-an overview of device operation and applications," *Proceedings of the IEEE,* vol. 90, no. 6, pp. 1022-1031, 2002.

[39] H. Hommel and H.-P. Feldle, "Current status of airborne active phased array (AESA) radar systems and future trends," in *Microwave Conference, 2004. 34th European*, 2004, vol. 3, pp. 1517-1520: IEEE.

[40] J. Würfl, "Technology and perspectives of GaN devices for innovative microwave applications," in *Microwave Conference (GeMIC), 2008 German*, 2008, pp. 1-4: VDE.

[41] S. K. O'leary, B. E. Foutz, M. S. Shur, and L. F. Eastman, "Steady-state and transient electron transport within the III–V nitride semiconductors, GaN, AlN, and InN: a review," *Journal of Materials Science: Materials in Electronics,* vol. 17, no. 2, pp. 87-126, 2006.

[42] A. Pérez-Tomás *et al.*, "2DEG HEMT Mobility vs Inversion Channel MOSFET Mobility," *Materials Science Forum,* p. 1207, 2010.

[43] F. A. Marino, N. Faralli, D. K. Ferry, S. M. Goodnick, and M. Saraniti, "Figures of merit in high-frequency and high-power GaN HEMTs," *Journal of Physics: Conference Series,* vol. 193, no. 1, p. 012040, 2009.

[44] R. S. Pengelly, S. M. Wood, J. W. Milligan, S. T. Sheppard, and W. L. Pribble, "A review of GaN on SiC high electron-mobility power transistors and MMICs," *IEEE Transactions on Microwave Theory and Techniques,* vol. 60, no. 6, pp. 1764-1783, 2012.

[45] T. Mimura, S. Hiyamizu, T. Fujii, and K. Nanbu, "A New Field-Effect Transistor with Selectively Doped GaAs/n-Al$_{x}$Ga$_{1-x}$As Heterojunctions," *Jpn. J. Appl. Phys.,* vol. 19, p. 3, 1980.

[46] M. Asif Khan, A. Bhattarai, J. Kuznia, and D. Olson, "High electron mobility transistor based on a GaN‐ Al x Ga1− x N heterojunction," *Applied Physics Letters,* vol. 63, no. 9, pp. 1214-1215, 1993.

[47] O. Ambacher *et al.*, "Two-dimensional electron gases induced by spontaneous and piezoelectric polarization charges in N- and Ga-face AlGaN/GaN heterostructures," *Journal of Applied Physics,* vol. 85, no. 6, pp. 3222-3233, 1999.

[48] L. Frenzel. (2012, 27 October 2016). *What's The Difference Between GaAs And GaN RF Power Amplifiers?* Available: http://electronicdesign.com/communications/what-s-difference-between-gaas-and-gan-rf-power-amplifiers

[49] W. Patrick, P. Christiane, R. Siddharth, W. Feng, K. M. Umesh, and S. S. James, "Structural Properties of GaN Buffer Layers on 4H-SiC(0001) Grown by Plasma-Assisted Molecular Beam Epitaxy for High Electron Mobility Transistors," *Japanese Journal of Applied Physics,* vol. 43, no. 12A, p. L1520, 2004.

[50] J. S. Moon *et al.*, "GaN/AlGaN HEMTs operating at 20 GHz with continuous-wave power density >6 W/mm," *Electronics Letters,* vol. 37, no. 8, pp. 528-530, 2001.

[51] D. S. Katzer, S. C. Binari, D. F. Storm, J. A. Roussos, B. V. Shanabrook, and E. R. Glaser, "MBE growth of AlGaN/GaN HEMTs with high power density," *Electronics Letters,* vol. 38, no. 25, pp. 1740-1741, 2002.

[52] N. G. Weimann, M. J. Manfra, and T. Wachtler, "Unpassivated AlGaN-GaN HEMTs with minimal RF dispersion grown by plasma-assisted MBE on semi-

insulating 6H-SiC substrates," *Electron Device Letters, IEEE,* vol. 24, no. 2, pp. 57-59, 2003.

[53] R. Behtash *et al.*, "AlGaN/GaN HEMTs on Si(111) with 6.6 W/mm output power density," *Electronics Letters,* vol. 39, no. 7, pp. 626-627, 2003.

[54] A. P. Zhang *et al.*, "9.2 W/mm (13.8 W) AlGaN/GaN HEMTs at 10 GHz and 55 V drain bias," *Electronics Letters,* vol. 39, no. 2, pp. 245-247, 2003.

[55] L. Shen *et al.*, "High-power polarization-engineered GaN/AlGaN/GaN HEMTs without surface passivation," *Electron Device Letters, IEEE,* vol. 25, no. 1, pp. 7-9, 2004.

[56] L. Taehun, P. Saunier, Y. Jinwei, and M. A. Khan, "AlGaN-GaN HEMTs on SiC with CW power performance of >4 W/mm and 23% PAE at 35 GHz," *Electron Device Letters, IEEE,* vol. 24, no. 10, pp. 616-618, 2003.

[57] S. Heikman, S. Keller, D. S. Green, S. P. DenBaars, and U. K. Mishra, "High conductivity modulation doped AlGaN/GaN multiple channel heterostructures," *Journal of Applied Physics,* vol. 94, no. 8, pp. 5321-5325, 2003.

[58] J. R. Shealy *et al.*, "An AlGaN/GaN high-electron-mobility transistor with an AlN sub-buffer layer," *Journal of Physics: Condensed Matter,* vol. 14, no. 13, p. 3499, 2002.

[59] T. Palacios *et al.*, "High-power AlGaN/GaN HEMTs for Ka-band applications," *Electron Device Letters, IEEE,* vol. 26, no. 11, pp. 781-783, 2005.

[60] O. Ambacher, "Growth and applications of group III-nitrides," *Journal of Physics D: Applied Physics,* vol. 31, no. 20, p. 2653, 1998.

[61] M. Sumiya and S. Fuke, "Review of polarity determination and control of GaN," *MRS Internet Journal of Nitride Semiconductor Research,* vol. 9, p. e1, 2004.

[62] C. Wood and D. Jena, *Polarization effects in semiconductors: from ab initio theory to device applications*. Springer Science & Business Media, 2007.

[63] P. Asbeck, E. Yu, S. Lau, G. Sullivan, J. Van Hove, and J. Redwing, "Piezoelectric charge densities in AlGaN/GaN HFETs," *Electronics letters,* vol. 33, no. 14, pp. 1230-1231, 1997.

[64] E. Yu, G. Sullivan, P. Asbeck, C. Wang, D. Qiao, and S. Lau, "Measurement of piezoelectrically induced charge in GaN/AlGaN heterostructure field-effect transistors," *Applied Physics Letters,* vol. 71, no. 19, pp. 2794-2796, 1997.

[65] M. B. Nardelli, K. Rapcewicz, and J. Bernholc, "Polarization field effects on the electron-hole recombination dynamics in In0. 2Ga0. 8N/In1-xGaxN multiple quantum wells," *Applied physics letters,* vol. 71, no. 21, pp. 3135-3137, 1997.

[66] T. Takeuchi, H. Takeuchi, S. Sota, H. Sakai, H. Amano, and I. Akasaki, "Optical properties of strained AlGaN and GaInN on GaN," *Japanese journal of applied physics,* vol. 36, no. 2B, p. L177, 1997.

[67] H. Xiao-Guang, Z. De-Gang, and J. De-Sheng, "Formation of two-dimensional electron gas at AlGaN/GaN heterostructure and the derivation of its sheet density expression," *Chinese Physics B,* vol. 24, no. 6, p. 067301, 2015.

[68] J. Ibbetson, P. Fini, K. Ness, S. DenBaars, J. Speck, and U. Mishra, "Polarization effects, surface states, and the source of electrons in AlGaN/GaN heterostructure field effect transistors," *Applied Physics Letters,* vol. 77, no. 2, pp. 250-252, 2000.

[69] I. P. Smorchkova *et al.*, "Polarization-induced charge and electron mobility in AlGaN/GaN heterostructures grown by plasma-assisted molecular-beam epitaxy," *Journal of Applied Physics,* vol. 86, no. 8, pp. 4520-4526, 1999.

[70] A. Dadgar, C. Hums, A. Diez, F. Schulze, J. Bläsing, and A. Krost, "Epitaxy of GaN LEDs on large substrates: Si or sapphire?," in *Asia-Pacific Optical Communications*, 2006, pp. 63550R-63550R-8: International Society for Optics and Photonics.

[71] W. E. Hoke *et al.*, "Monolithic integration of silicon CMOS and GaN transistors in a current mirror circuit," *Journal of Vacuum Science & Technology B,* vol. 30, no. 2, p. 02B101, 2012.

[72] E. A. Fitzgerald *et al.*, "Enabling the integrated circuits of the future," in *Electron Devices and Solid-State Circuits (EDSSC), 2015 IEEE International Conference on*, 2015, pp. 1-4.

[73] E. A. Fitzgerald *et al.*, "(Invited) Novel Integrated Circuit Platforms Employing Monolithic Silicon CMOS+ GaN Devices," *ECS Transactions,* vol. 75, no. 12, pp. 31-37, 2016.

[74] G. Meneghesso *et al.*, "Reliability of GaN high-electron-mobility transistors: state of the art and perspectives," *Device and Materials Reliability, IEEE Transactions on,* vol. 8, no. 2, pp. 332-343, 2008.

[75] W. A. Sasangka, G. J. Syaranamual, C. L. Gan, and C. V. Thompson, "Origin of physical degradation in AlGaN/GaN on Si high electron mobility transistors under reverse bias stressing," in *Reliability Physics Symposium (IRPS), 2015 IEEE International*, 2015, pp. 6C.3.1-6C.3.4.

[76] W. Sasangka, G. Syaranamual, R. Made, C. Thompson, and C. Gan, "Threading dislocation movement in AlGaN/GaN-on-Si high electron mobility transistors under high temperature reverse bias stressing," *AIP Advances,* vol. 6, no. 9, p. 095102, 2016.

[77] L. Li, J. Joh, J. A. del Alamo, and C. V. Thompson, "Spatial distribution of structural degradation under high-power stress in AlGaN/GaN high electron mobility transistors," *Applied Physics Letters,* vol. 100, no. 17, pp. 172109-3.

[78] M. M. Bajo, H. Sun, M. Uren, and M. Kuball, "Time evolution of off-state degradation of AlGaN/GaN high electron mobility transistors," *Applied Physics Letters,* vol. 104, no. 22, p. 223506, 2014.

[79] G. Meneghesso, F. Rampazzo, P. Kordos, G. Verzellesi, and E. Zanoni, "Current collapse and high-electric-field reliability of unpassivated GaN/AlGaN/GaN HEMTs," *IEEE Transactions on Electron Devices,* vol. 53, no. 12, pp. 2932-2941, 2006.

[80] J. Joh and J. A. Del Alamo, "RF power degradation of GaN high electron mobility transistors," in *Electron Devices Meeting (IEDM), 2010 IEEE International*, 2010, pp. 20.2. 1-20.2. 4: IEEE.

[81] J. Jungwoo and J. A. del Alamo, "Critical Voltage for Electrical Degradation of GaN High-Electron Mobility Transistors," *Electron Device Letters, IEEE,* vol. 29, no. 4, pp. 287-289, 2008.

[82] J. Joh and J. A. del Alamo, "Mechanisms for Electrical Degradation of GaN High-Electron Mobility Transistors," in *Electron Devices Meeting, 2006. IEDM '06. International*, 2006, pp. 1-4.

[83] M. Ťapajna, N. Killat, U. Chowdhury, J. L. Jimenez, and M. Kuball, "The role of surface barrier oxidation on AlGaN/GaN HEMTs reliability," *Microelectronics Reliability,* vol. 52, no. 1, pp. 29-32, 2012.

[84] S. Singhal *et al.*, "GaN-on-Si failure mechanisms and reliability improvements," in *Reliability Physics Symposium Proceedings, 2006. 44th Annual., IEEE International*, 2006, pp. 95-98: IEEE.

[85] M. Tajima, J. Kotani, and T. Hashizume, "Effects of surface oxidation of AlGaN on DC characteristics of AlGaN/GaN high-electron-mobility transistors," *Japanese Journal of Applied Physics,* vol. 48, no. 2R, p. 020203, 2009.

[86] U. Chowdhury *et al.*, "TEM Observation of Crack- and Pit-Shaped Defects in Electrically Degraded GaN HEMTs," *IEEE Electron Device Letters,* vol. 29, no. 10, pp. 1098-1100, 2008.

[87] J. Jimenez and U. Chowdhury, "X-band GaN FET reliability," in *Reliability Physics Symposium, 2008. IRPS 2008. IEEE International*, 2008, pp. 429-435: IEEE.

[88] N. Cabrera and M. Levine, "XLV. On the dislocation theory of evaporation of crystals," *Philosophical Magazine,* vol. 1, no. 5, pp. 450-458, 1956.

[89] D. Marcon *et al.*, "Reliability of AlGaN/GaN HEMTs: Permanent leakage current increase and output current drop," *Microelectronics Reliability,* vol. 52, no. 9, pp. 2188-2193, 2012.

[90] B. D. Christiansen *et al.*, "Reliability testing of AlGaN/GaN HEMTs under multiple stressors," in *Reliability Physics Symposium (IRPS), 2011 IEEE International*, 2011, pp. CD. 2.1-CD. 2.5: IEEE.

[91] J. Joh and J. A. Del Alamo, "Time evolution of electrical degradation under high-voltage stress in GaN high electron mobility transistors," in *Reliability Physics Symposium (IRPS), 2011 IEEE International*, 2011, pp. 4E. 3.1-4E. 3.4: IEEE.

[92] D. Marcon *et al.*, "A comprehensive reliability investigation of the voltage-, temperature-and device geometry-dependence of the gate degradation on state-of-the-art GaN-on-Si HEMTs," in *Electron Devices Meeting (IEDM), 2010 IEEE International*, 2010, pp. 20.3. 1-20.3. 4: IEEE.

[93] D. A. Cullen *et al.*, "Electroluminescence and transmission electron microscopy characterization of reverse-biased AlGaN/GaN devices," *IEEE Transactions on Device and Materials Reliability,* vol. 13, no. 1, pp. 126-135, 2013.

[94] A. Chini, M. Esposto, G. Meneghesso, and E. Zanoni, "Evaluation of GaN HEMT degradation by means of pulsed I–V, leakage and DLTS measurements," *Electronics letters,* vol. 45, no. 8, pp. 426-427, 2009.

[95] A. Sozza, C. Dua, E. Morvan, B. Grimber, and S. L. Delage, "A 3000 hours DC Life Test on AlGaN/GaN HEMT for RF and microwave applications," *Microelectronics Reliability,* vol. 45, no. 9–11, pp. 1617-1621, 2005.

[96] S. Khemiri, M. Kadi, and A. Louis, "Reliability study of AlGaN/GaN HEMT under electromagnetic, RF and DC stress," *Microelectronics Reliability,* vol. 51, no. 9, pp. 1783-1787, 2011.

[97] A. Sozza *et al.*, "Evidence of traps creation in GaN/AlGaN/GaN HEMTs after a 3000 hour on-state and off-state hot-electron stress," in *Electron Devices Meeting, 2005. IEDM Technical Digest. IEEE International*, 2005, pp. 4 pp.-593.

[98] M. Meneghini *et al.*, "Extensive analysis of the luminescence properties of AlGaN/GaN high electron mobility transistors," *Applied Physics Letters,* vol. 97, no. 6, p. 063508, 2010.

[99] M. J. Anand, G. I. Ng, S. Arulkumaran, B. Syamal, and X. Zhou, "Distribution of trap energy level in AlGaN/GaN high-electron-mobility transistors on Si under ON-state stress," *Applied Physics Express,* vol. 8, no. 10, p. 104101, 2015.

[100] Y. Wu, C.-Y. Chen, and J. A. Del Alamo, "Temperature-Accelerated Degradation of GaN HEMTs under High-Power Stress: Activation Energy of Drain-Current Degradation," *ROCS, May,* vol. 19, 2014.

[101] Y. Wu, C.-Y. Chen, and J. A. del Alamo, "Activation energy of drain-current degradation in GaN HEMTs under high-power DC stress," *Microelectronics Reliability,* vol. 54, no. 12, pp. 2668-2674, 2014.

[102] A. Soltani *et al.*, "Development and analysis of low resistance ohmic contact to n-AlGaN/GaN HEMT," *Diamond and related materials,* vol. 16, no. 2, pp. 262-266, 2007.

[103] F. Iucolano, F. Roccaforte, A. Alberti, C. Bongiorno, S. Di Franco, and V. Raineri, "Temperature dependence of the specific resistance in Ti⁄ Al⁄ Ni⁄ Au contacts on n-type GaN," *Journal of applied physics,* vol. 100, no. 12, p. 123706, 2006.

[104] F. M. Mohammed, L. Wang, H. J. Koo, and I. Adesida, "Anatomy-performance correlation in Ti-based contact metallizations on Al Ga N⁄ Ga N heterostructures," *Journal of applied physics,* vol. 101, no. 3, p. 033708, 2007.

[105] B. Jacobs, M. Kramer, E. Geluk, and F. Karouta, "Optimisation of the Ti/Al/Ni/Au ohmic contact on AlGaN/GaN FET structures," *Journal of Crystal Growth,* vol. 241, no. 1, pp. 15-18, 2002.

[106] T.-L. Wu *et al.*, "Stability evaluation of Au-free Ohmic contacts on AlGaN/GaN HEMTs under a constant current stress," *Microelectronics Reliability,* vol. 54, no. 9, pp. 2232-2236, 2014.

[107] A. Subramaniam, V. Sahmuganathan, I. Ng Geok, S. Susai Lawrence, and E. Takashi, "Improved Power Device Figure-of-Merit (4.0×10 8 V 2 Ω -1 cm -2) in AlGaN/GaN High-Electron-Mobility Transistors on High-Resistivity 4-in. Si," *Applied Physics Express,* vol. 4, no. 8, p. 084101, 2011.

[108] E. Feltin *et al.*, "Stress control in GaN grown on silicon (111) by metalorganic vapor phase epitaxy," *Applied Physics Letters,* vol. 79, no. 20, pp. 3230-3232, 2001.

[109] H. Guo, W. Tang, W. Zhou, and C. M. Li, "Effect of GaN Cap Layer on the Electrical Properties of AlGaN/GaN HEMT," *Applied Mechanics and Materials,* vol. 217-219, pp. 2393-2396, 2012.

[110] A. Subramaniam, E. Takashi, and I. Hiroyasu, "Studies on the Influences of i -GaN, n -GaN, p -GaN and InGaN Cap Layers in AlGaN/GaN High-Electron-Mobility Transistors," *Japanese Journal of Applied Physics,* vol. 44, no. 5R, p. 2953, 2005.

[111] A. Asgari, M. Kalafi, and L. Faraone, "The effects of GaN capping layer thickness on two-dimensional electron mobility in GaN/AlGaN/GaN heterostructures," *Physica E: Low-dimensional Systems and Nanostructures,* vol. 25, no. 4, pp. 431-437, 1// 2005.

[112] J. Jungwoo, X. Ling, and J. A. del Alamo, "Gate Current Degradation Mechanisms of GaN High Electron Mobility Transistors," in *Electron Devices Meeting, 2007. IEDM 2007. IEEE International*, 2007, pp. 385-388.

[113] G. Syaranamual *et al.*, "Role of two-dimensional electron gas (2DEG) in AlGaN/GaN high electron mobility transistor (HEMT) ON-state degradation," *Microelectronics Reliability,* vol. 64, pp. 589-593, 2016.

[114] D. Marcon *et al.*, "A comprehensive reliability investigation of the voltage-, temperature- and device geometry-dependence of the gate degradation on state-of-the-art GaN-on-Si HEMTs," in *Electron Devices Meeting (IEDM), 2010 IEEE International*, 2010, pp. 20.3.1-20.3.4.

[115] M. Faqir, G. Verzellesi, G. Meneghesso, E. Zanoni, and F. Fantini, "Investigation of High-Electric-Field Degradation Effects in AlGaN/GaN HEMTs," *Electron Devices, IEEE Transactions on,* vol. 55, no. 7, pp. 1592-1602, 2008.

[116] J. Ling, A. Tay, K. Choo, W. Chen, and D. Kendig, "Measurement of MMIC gate temperature using infrared and Thermoreflectance thermography," in *Electronics Packaging Technology Conference (EPTC), 2012 IEEE 14th*, 2012, pp. 515-518: IEEE.

[117] M. Farzaneh *et al.*, "CCD-based thermoreflectance microscopy: principles and applications," *Journal of Physics D: Applied Physics,* vol. 42, no. 14, p. 143001, 2009.

[118] F. Gao, "Degradation study of AIGaN/GaN HEMT through electro-thermo-mechanical calculations and thermo-reflectance measurements," 2010.

[119] Microsanj. (2017, 1 May 2017). *NT200 Thermal Imaging System*. Available: https://www.microsanj.com/products/200-series/

[120] ANSYS. (2005, 22 August). *Thermal Analysis System* Available: https://www.yumpu.com/en/document/view/10750239/thermal-analysis-system-tas-users-manual-ansys

[121] J. A. del Alamo and J. Joh, "GaN HEMT reliability," *Microelectronics reliability,* vol. 49, no. 9, pp. 1200-1206, 2009.

[122] C. Chih-Yang *et al.*, "Electric-Field-Driven Degradation in off-State Step-Stressed AlGaN/GaN High-Electron Mobility Transistors," *Device and Materials Reliability, IEEE Transactions on,* vol. 11, no. 1, pp. 187-193, 2011.

[123] Silvaco. (2015, 1 May 2017). *AlGaN/GaN HEMT Id-Vgs and Id-Vds Characterization*. Available: http://www.silvaco.com.sg/examples/tcad/section20/example3/index.html

[124] J. Chen *et al.*, "Measurement of threading dislocation densities in GaN by wet chemical etching," *Semiconductor Science and Technology,* vol. 21, no. 9, p. 1229, 2006.

[125] L. zhang *et al.*, "Characterization of dislocation etch pits in HVPE-grown GaN using different wet chemical etching methods," *Journal of Alloys and Compounds,* vol. 504, no. 1, pp. 186-191, 8/13/ 2010.

[126] P. Visconti, K. M. Jones, M. A. Reshchikov, R. Cingolani, H. Morkoc, and R. J. Molnar, "Dislocation density in GaN determined by photoelectrochemical and hot-wet etching," *Applied Physics Letters,* vol. 77, no. 22, pp. 3532-3534, 11/27/ 2000.

[127] D. Hull and D. J. Bacon, "2 - Observation of Dislocations," in *Introduction to Dislocations (Fourth Edition)*, D. Hull and D. J. Bacon, Eds. Oxford: Butterworth-Heinemann, 2001, pp. 22-41.

[128] S. Swapp. (24 August 2012). *Scanning Electron Microscopy (SEM)*. Available: http://serc.carleton.edu/research_education/geochemsheets/techniques/SEM.html

[129] L. A. Giannuzzi and F. A. Stevie, "A review of focused ion beam milling techniques for TEM specimen preparation," *Micron,* vol. 30, no. 3, pp. 197-204, 1999.

[130] T. Ishitani, H. Tsuboi, T. Yaguchi, and H. Koike, "Transmission electron microscope sample preparation using a focused ion beam," *Journal of Electron Microscopy,* vol. 43, no. 5, pp. 322-326, 1994.

[131] J. Mayer, L. A. Giannuzzi, T. Kamino, and J. Michael, "TEM sample preparation and FIB-induced damage," *MRS bulletin,* vol. 32, no. 05, pp. 400-407, 2007.

[132] A. Marshall and A. L. Koh. (24/08/2012). *Transmission Electron Microscope (TEM) Facility*. Available: http://www.stanford.edu/group/snl/tem.htm

[133] P. D. Nellist, "The Principles of STEM Imaging," in *Scanning Transmission Electron Microscopy: Imaging and Analysis*, S. J. Pennycook and P. D. Nellist, Eds. New York, NY: Springer New York, 2011, pp. 91-115.

[134] S. Pennycook *et al.*, "Scanning Transmission Electron Microscopy for Nanostructure Characterization."

[135] M. Watanabe, "X-ray energy-dispersive spectrometry in scanning transmission electron microscopes," in *Scanning Transmission Electron Microscopy*: Springer, 2011, pp. 291-351.

[136] D. Williams and C. B. Carter, "Weak-Beam Dark-Field Microscopy," in *Transmission Electron Microscopy*: Springer US, 2009, pp. 463-481.

[137] F. Ponce, D. Cherns, W. Young, and J. Steeds, "Characterization of dislocations in GaN by transmission electron diffraction and microscopy techniques," *Applied physics letters,* vol. 69, no. 6, pp. 770-772, 1996.

[138] R. F. Egerton, "Electron energy-loss spectroscopy in the TEM," *Reports on Progress in Physics,* vol. 72, no. 1, p. 016502, 2009.

[139] H. S. von Harrach, D. Klenov, B. Freitag, P. Schlossmacher, P. C. Collins, and H. L. Fraser, "Comparison of the detection limits of EDS and EELS in S/TEM," *Microscopy and Microanalysis,* vol. 16, no. S2, pp. 1312-1313, 2010.

[140] (2017, 19 April 2017). *Gatan Microscopy Suite Software*. Available: http://www.gatan.com/products/tem-analysis/gatan-microscopy-suite-software

[141] M. Yasaka, "X-ray thin-film measurement techniques," *The Rigaku Journal,* vol. 26, no. 2, 2010.

[142] D. Windover *et al.*, "Thin film density determination by multiple radiation energy dispersive X-ray reflectivity," *International Centre for Diffraction Data, Advances in X-ray Analysis,* vol. 42, pp. 590-600, 2000.

[143] L. G. Parratt, "Surface studies of solids by total reflection of X-rays," *Physical review,* vol. 95, no. 2, p. 359, 1954.

[144] I. Kojima and B. Li, "Structural characterization of thin films by X-ray reflectivity," *The Rigaku Journal,* vol. 16, no. 2, p. 31, 1999.

[145] E. Chason and T. Mayer, "Thin film and surface characterization by specular X-ray reflectivity," *Critical Reviews in Solid State and Material Sciences,* vol. 22, no. 1, pp. 1-67, 1997.

[146] (2017, 19 April 2017). *Advanced X-ray Diffraction System for Materials Research Applications*. Available: https://www.bruker.com/products/x-ray-diffraction-and-elemental-analysis/x-ray-diffraction/d8-discover/overview.html

[147] A. Ulyanenkov, "LEPTOS: a universal software for x-ray reflectivity and diffraction," 2004, vol. 5536, pp. 1-15.

[148] C. A. Schneider, W. S. Rasband, and K. W. Eliceiri, "NIH Image to ImageJ: 25 years of image analysis," *Nat Meth,* 10.1038/nmeth.2089 vol. 9, no. 7, pp. 671-675, 07//print 2012.

[149] S. Martin-Horcajo, A. Wang, M.-F. Romero, M. J. Tadjer, and F. Calle, "Simple and accurate method to estimate channel temperature and thermal resistance in AlGaN/GaN HEMTs," *IEEE Transactions on Electron Devices,* vol. 60, no. 12, pp. 4105-4111, 2013.

[150] N. Killat, M. J. Uren, S. Keller, S. Kolluri, U. K. Mishra, and M. Kuball, "Impact ionization in N-polar AlGaN/GaN high electron mobility transistors," *Applied Physics Letters,* vol. 105, no. 6, p. 063506, 2014.

[151] N. Killat, M. Tapajna, M. Faqir, T. Palacios, and M. Kuball, "Evidence for impact ionisation in AlGaN/GaN HEMTs with InGaN back-barrier," *Electronics Letters,* vol. 47, no. 6, pp. 405-406, 2011.

[152] P. S. Park and S. Rajan, "Simulation of short-channel effects in N-and Ga-polar AlGaN/GaN HEMTs," *Electron Devices, IEEE Transactions on,* vol. 58, no. 3, pp. 704-708, 2011.

[153] J. Jungwoo and J. A. del Alamo, "Impact of electrical degradation on trapping characteristics of GaN high electron mobility transistors," in *Electron Devices Meeting, 2008. IEDM 2008. IEEE International*, 2008, pp. 1-4.

[154] R. J. Simms, J. W. Pomeroy, M. J. Uren, T. Martin, and M. Kuball, "Channel temperature determination in high-power AlGaN/GaN HFETs using electrical methods and Raman spectroscopy," *IEEE Transactions on Electron Devices,* vol. 55, no. 2, pp. 478-482, 2008.

[155] A. Anwar, S. Wu, and R. T. Webster, "Temperature dependent transport properties in GaN, Al/sub x/Ga/sub 1-x/N, and In/sub x/Ga/sub 1-x/N semiconductors," *IEEE Transactions on Electron devices,* vol. 48, no. 3, pp. 567-572, 2001.

[156] M. A. der Maur, G. Romano, and A. Di Carlo, "Electro-thermo-mechanical simulation of AlGaN/GaN HEMTs," in *Computational Electronics (IWCE), 2012 15th International Workshop on*, 2012, pp. 1-4: IEEE.

[157] V. Kumar, L. Zhou, D. Selvanathan, and I. Adesida, "Thermally-stable low-resistance Ti/Al/Mo/Au multilayer ohmic contacts on n–GaN," *Journal of applied physics,* vol. 92, no. 3, pp. 1712-1714, 2002.

[158] A. Malmros, H. Blanck, and N. Rorsman, "Electrical properties, microstructure, and thermal stability of Ta-based ohmic contacts annealed at low temperature for GaN HEMTs," *Semiconductor Science and Technology,* vol. 26, no. 7, p. 075006, 2011.

[159] D. Selvanathan, L. Zhou, V. Kumar, and I. Adesida, "Low resistance Ti/Al/Mo/Au ohmic contacts for AlGaN/GaN heterostructure field effect transistors," *PHYSICA STATUS SOLIDI A APPLIED RESEARCH,* vol. 194, no. 2, pp. 583-586, 2002.

[160] P. Ye *et al.*, "GaN metal-oxide-semiconductor high-electron-mobility-transistor with atomic layer deposited Al 2 O 3 as gate dielectric," *Applied Physics Letters,* vol. 86, no. 6, p. 063501, 2005.

[161] W. Saito, Y. Takada, M. Kuraguchi, K. Tsuda, and I. Omura, "Recessed-gate structure approach toward normally off high-voltage AlGaN/GaN HEMT for power electronics applications," *IEEE Transactions on electron devices,* vol. 53, no. 2, pp. 356-362, 2006.

[162] W. Lanford, T. Tanaka, Y. Otoki, and I. Adesida, "Recessed-gate enhancement-mode GaN HEMT with high threshold voltage," *Electronics Letters,* vol. 41, no. 7, pp. 449-450, 2005.

[163] J. W. Christian, *The theory of transformations in metals and alloys*. Newnes, 2002.

[164] M. Tapajna, R. J. Simms, Y. Pei, U. K. Mishra, and M. Kuball, "Integrated optical and electrical analysis: Identifying location and properties of traps in AlGaN/GaN HEMTs during electrical stress," *IEEE Electron Device Letters,* vol. 31, no. 7, pp. 662-664, 2010.

[165] J. Pomeroy, M. Kuball, M. Uren, K. Hilton, R. Balmer, and T. Martin, "Insights into electroluminescent emission from AlGaN⁄ GaN field effect transistors using micro-Raman thermal analysis," *Applied Physics Letters,* vol. 88, no. 2, p. 023507, 2006.

[166] W. A. Sasangka, G. J. Syaranamual, Y. Gao, R. I Made, C. L. Gan, and C. V. Thompson, "Improved reliability of AlGaN/GaN-on-Si high electron mobility

transistors (HEMTs) with high density silicon nitride passivation," *Microelectronics Reliability,* vol. 76-77, pp. 287-291, 2017/09/01/ 2017.

[167] H. Du, R. E. Tressler, K. E. Spear, and C. G. Pantano, "Oxidation studies of crystalline CVD silicon nitride," *Journal of the Electrochemical Society,* vol. 136, no. 5, pp. 1527-1536, 1989.

[168] D. J. Choi, D. B. Fischbach, and W. D. Scott, "Oxidation of Chemically- Vapor-Deposited Silicon Nitride and Slnglem- Crystal Silicon," *Journal of the American Ceramic Society,* vol. 72, no. 7, pp. 1118-1123, 1989.

[169] T. Hirai, K. Niihara, and T. Goto, "Oxidation of CVD Si3N4 at 1550 to 1650 C," *Journal of the American Ceramic Society,* vol. 63, no. 7- 8, pp. 419-424, 1980.

[170] C. Greskovich and J. Rosolowski, "Sintering of covalent solids," *Journal of the American Ceramic Society,* vol. 59, no. 7- 8, pp. 336-343, 1976.

[171] F.-S. Chien, Y. Chou, T. Chen, W.-F. Hsieh, T.-S. Chao, and S. Gwo, "Nano-oxidation of silicon nitride films with an atomic force microscope: Chemical mapping, kinetics, and applications," *Journal of Applied Physics,* vol. 89, no. 4, pp. 2465-2472, 2001.

[172] I. Institute. (2001, 25 April 2017). *AlN - Aluminium Nitride Basic Parameters*. Available: http://www.ioffe.ru/SVA/NSM/Semicond/AlN/basic.html

[173] G. A. Slack, "Nonmetallic crystals with high thermal conductivity," *Journal of Physics and Chemistry of Solids,* vol. 34, no. 2, pp. 321-335, 1973/01/01 1973.

[174] I. Institute. (2001, 25 April 2017). *GaN - Gallium Nitride Basic Parameters*. Available: http://www.ioffe.ru/SVA/NSM/Semicond/GaN/basic.html

[175] K. Kijima and S. i. Shirasaki, "Nitrogen self- diffusion in silicon nitride," *The Journal of Chemical Physics,* vol. 65, no. 7, pp. 2668-2671, 1976.

[176] H. Schmidt, M. Gupta, and M. Bruns, "Nitrogen diffusion in amorphous silicon nitride isotope multilayers probed by neutron reflectometry," *Physical review letters,* vol. 96, no. 5, p. 055901, 2006.

[177] J. Perez-Bueno, R. Ramırez-Bon, Y. V. Vorobiev, F. Espinoza-Beltran, and J. González-Hernández, "Oxygen diffusion in silicon oxide films produced by different methods," *Thin Solid Films,* vol. 379, no. 1, pp. 57-63, 2000.

[178] T. Mizutani, M. Ito, S. Kishimoto, and F. Nakamura, "AlGaN/GaN HEMTs With Thin InGaN Cap Layer for Normally Off Operation," *Electron Device Letters, IEEE,* vol. 28, no. 7, pp. 549-551, 2007.

[179] A. Endoh *et al.*, "Non-recessed-gate enhancement-mode AlGaN/GaN high electron mobility transistors with high RF performance," *Japanese journal of applied physics,* vol. 43, no. 4S, p. 2255, 2004.

[180] M. Broas *et al.*, "Correlation of gate leakage and local strain distribution in GaN/AlGaN HEMT structures," *Microelectronics Reliability,* vol. 64, pp. 541-546, 2016.

APPENDIX

This appendix is to complement chapter 6 which discuss about the effect of passivation density on AlGaN/GaN HEMT-on-Si ON-state degradation.

A Bad Devices

In this chapter, batch stressing was done in 32-SMU NI system. During the analysis of the electrical stressing results, there were some of bad devices that were excluded. These bad devices will be discussed in this section.

A-1 Large Drain Leakage

Figure A.1a and b shows the $I_{D\text{-}max}$ vs time and I_{DS}-V_{GS} plots for the bad device, respectively. This device had a large drain leakage current about 2 mA in OFF-state operation regime where V_{GS} is below V_{TH} = -3.8 V.

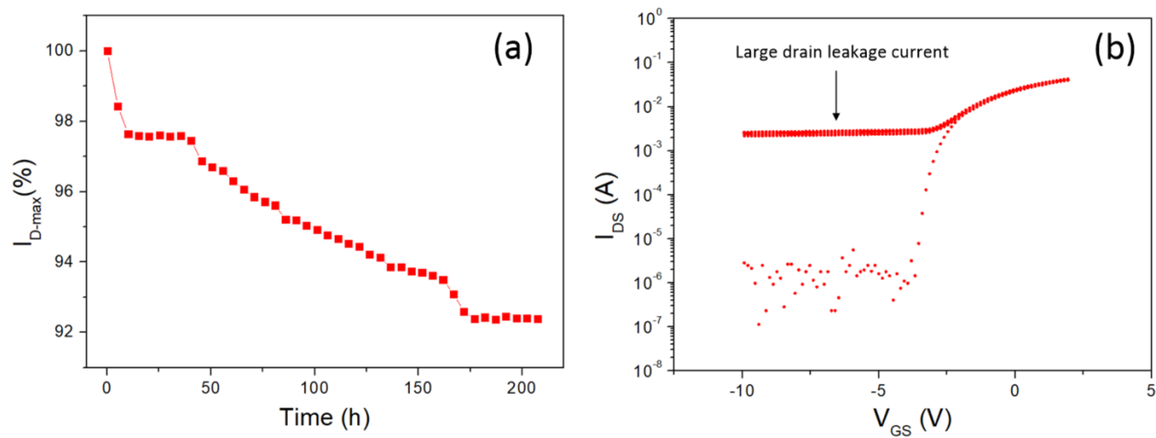

Figure A.1 (a) $I_{D\text{-}max}$ vs time and (b) I_{DS}-V_{GS} plots for bad device with large drain leakage current indicated by the arrow

A-2 Bad Gate Pad Connection

In this device, I_{DS} did not change with increasing V_{GS}. The I_{DS} stayed constant at 17 mA. One possible reason is that this device has a bad gate pad connection.

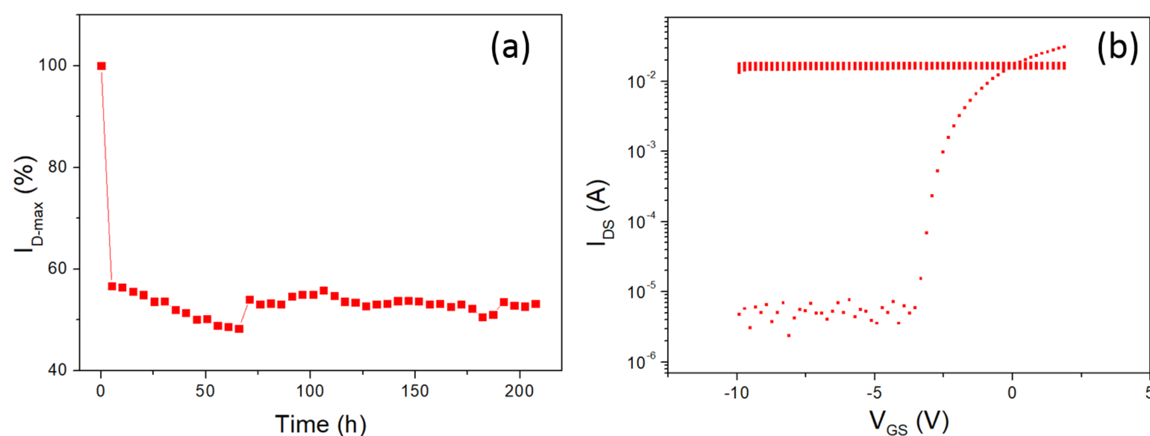

Figure A.2 (a) $I_{D\text{-max}}$ vs time and (b) I_{DS}-V_{GS} plots for bad device that lost its transistor characteristics because of bad gate pad connection

B Electrical Stressing Raw Data

B-1 V_{DS} = 20 V, V_{GS} = 0 V and $T_{surrounding}$ = 150°C

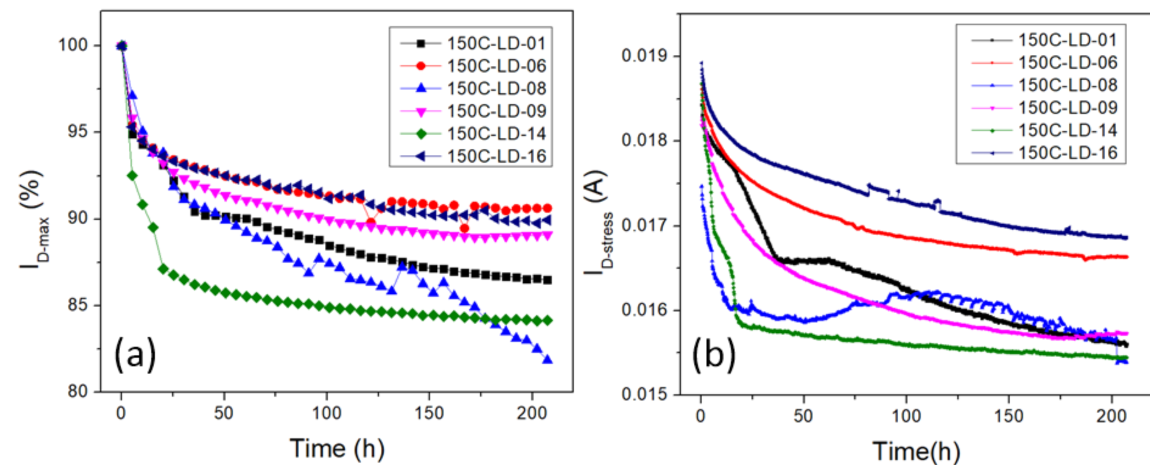

Figure A.4 (a) $I_{D\text{-max}}$ vs time and (b) $I_{D\text{-stress}}$ vs time plots for devices with low density passivation stressed under ON-state condition V_{DS} = 20 V, V_{GS} = 0 V and $T_{surrounding}$ = 150°C

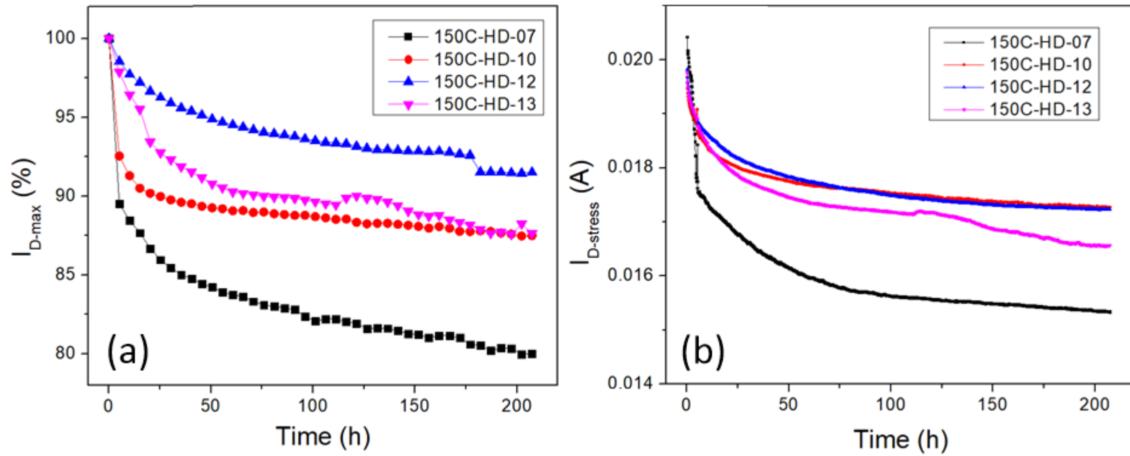

Figure A.5 (a) $I_{D\text{-}max}$ vs time and (b) $I_{D\text{-}stress}$ vs time plots for devices with high density passivation stressed under ON-state condition V_{DS} = 20 V, V_{GS} = 0 V and $T_{surrounding}$ = 150˚C

B-2 V_{DS} = 20 V, V_{GS} = 0 V and $T_{surrounding}$ = 175˚C

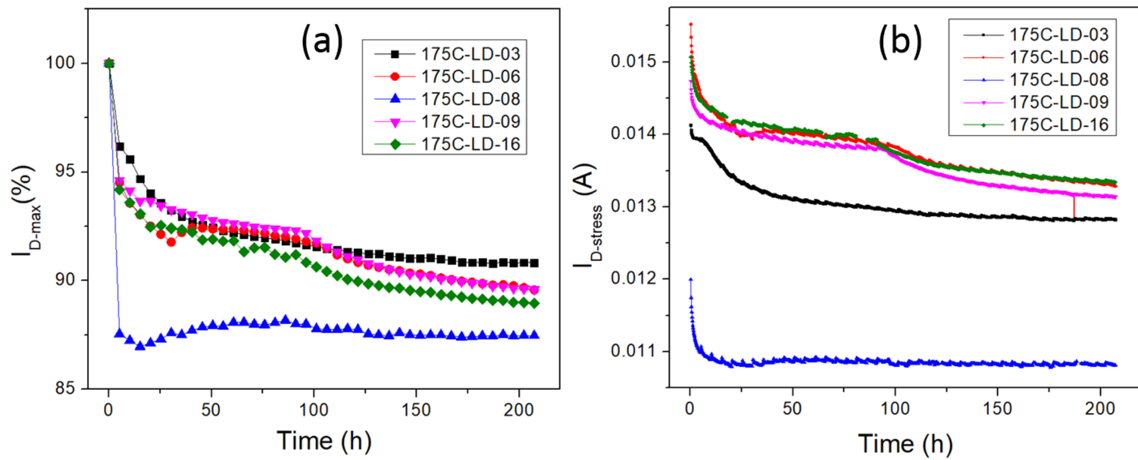

Figure A.6 (a) $I_{D\text{-}max}$ vs time and (b) $I_{D\text{-}stress}$ vs time plots for devices with low density passivation stressed under ON-state condition V_{DS} = 20 V, V_{GS} = 0 V and $T_{surrounding}$ = 175˚C

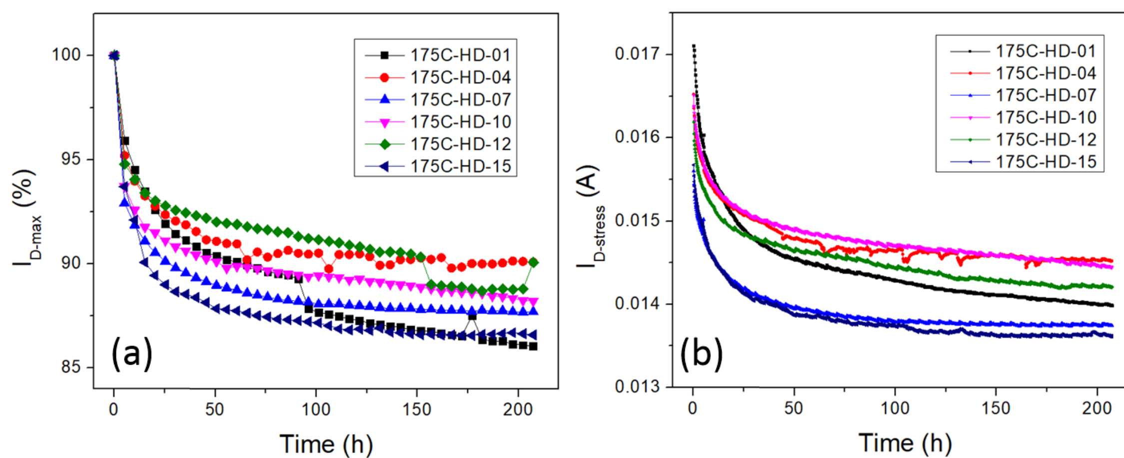

Figure A.7 (a) $I_{D\text{-}max}$ vs time and (b) $I_{D\text{-}stress}$ vs time plots for devices with high density passivation stressed under ON-state condition V_{DS} = 20 V, V_{GS} = 0 V and $T_{surrounding}$ = 175˚C

B-3 V_{DS} = 20 V, V_{GS} = 0 V and $T_{surrounding}$ = 225˚C

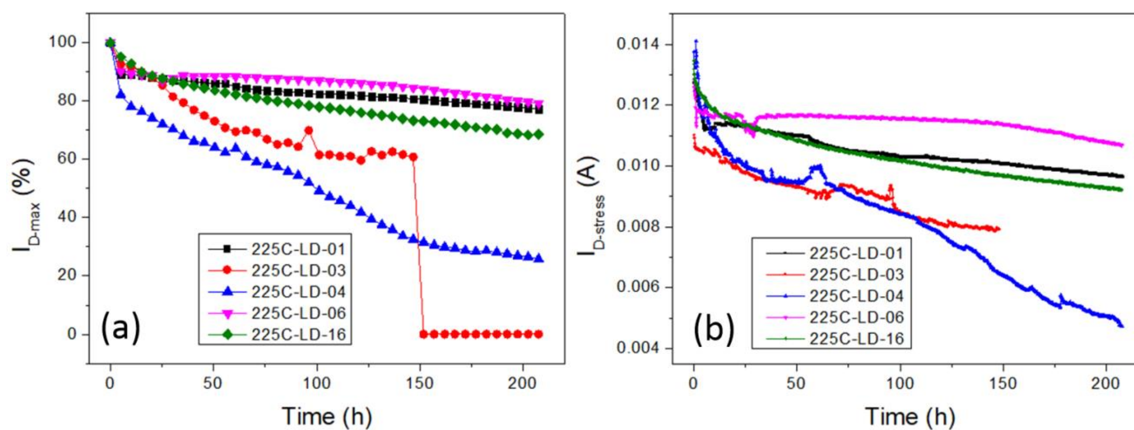

Figure A.10 (a) $I_{D\text{-}max}$ vs time and (b) $I_{D\text{-}stress}$ vs time plots for devices with low density passivation stressed under ON-state condition V_{DS} = 20 V, V_{GS} = 0 V and $T_{surrounding}$ = 225˚C

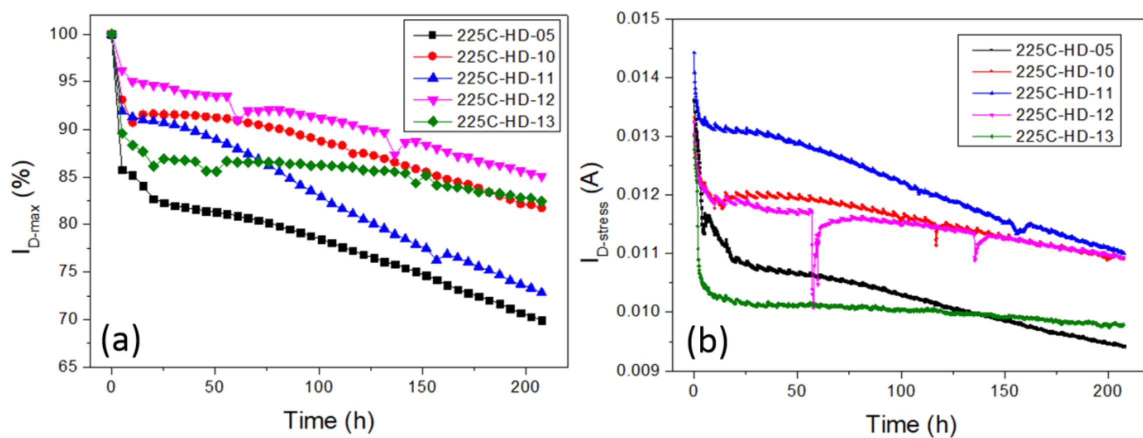

Figure A.11 (a) $I_{D\text{-max}}$ vs time and (b) $I_{D\text{-stress}}$ vs time plots for devices with high density passivation stressed under ON-state condition V_{DS} = 20 V, V_{GS} = 0 V and $T_{surrounding}$ = 225˚C